

BOREHOLE RADAR EXPERIMENTS AND
MICROSEISMIC MONITORING ON THE
UNSTABLE RANDA ROCKSLIDE
(SWITZERLAND)

Thomas Spillmann

DISS. ETH NO. 16866

BOREHOLE RADAR EXPERIMENTS AND MICROSEISMIC
MONITORING ON THE UNSTABLE RANDA ROCKSLIDE
(SWITZERLAND)

A dissertation submitted to

ETH ZURICH

for the degree of

Doctor of Sciences

presented by

THOMAS SPILLMANN

Dipl. Natw., ETH Zurich

born December 14, 1969

citizen of Niederhasli (ZH)

accepted on the recommendation of

Prof. Dr. Alan G. Green, examiner
PD Dr. Hansruedi Maurer, co-examiner
Prof. Dr. Denis Jongmans, co-examiner

2007

Content

Abstract	ix
Zusammenfassung	xi
1 Introduction	1
1.1 ROCKSLIDE HAZARD	1
1.2 BRIEF OVERVIEW OF ROCKSLIDE INVESTIGATIONS	3
1.2.1 Detection of unstable zones	3
1.2.2 Structural characterization: geophysical techniques	4
1.2.3 Kinematic and dynamic characterization: microseismic monitoring	7
1.3 THE RANDA ROCKSLIDE PROJECT	9
1.3.1 1991 Randa rockslides	10
1.3.2 Current instability	13
1.3.3 Geology and discontinuities	13
1.3.4 Boreholes and borehole experiments	13
1.3.5 Monitoring network	14
1.3.6 Surface geophysics	14
1.4 THESIS OBJECTIVES	15
1.5 STRUCTURE OF THE THESIS	15
2 Characterization of an unstable rock mass based on borehole logs and diverse borehole radar data	17
ABSTRACT	18
2.1 INTRODUCTION	18
2.2 RANDA STUDY SITE	20
2.2.1 The 1991 Randa rockslides	20
2.2.2 Continued instability	20
2.2.3 Topographic relief, rock lithologies and fracture/fault distribution	20
2.2.4 Boreholes	21
2.3 BOREHOLE RADAR METHODS	22
2.3.1 Single-hole radar	22
2.3.2 Vertical radar profiling (VRP)	22

2.3.3	Crosshole radar	23
2.4	DATA ACQUISITION	23
2.5	RADAR AND SONIC LOG DATA PROCESSING	25
2.5.1	Single-hole radar	25
2.5.2	Vertical radar profiling (VRP)	25
2.5.3	Crosshole radar	27
2.5.4	Sonic logs	28
2.6	RESULTS AND INTERPRETATION	28
2.6.1	Borehole logs	28
2.6.2	Crosshole tomogram and VRP velocity-depth models	29
2.6.3	Single-hole and VRP reflection sections	30
2.6.4	Fracture zones near SB120	31
2.6.5	Fracture zones near SB50S	32
2.6.6	Fracture zones near SB50N	33
2.7	DISCUSSION AND CONCLUSIONS	34
2.8	ACKNOWLEDGEMENTS	36
2.9	APPENDIX	36
2.9.A	Synthetic examples	36
2.9.B	Field examples	37
3	Monitoring network: design, deployment, and operation	57
3.1	INTRODUCTION	57
3.2	RANDA MONITORING NETWORKS	57
3.3	MICROSEISMIC NETWORK DESIGN	58
3.4	TECHNICAL SETUP OF THE RANDA MICROSEISMIC NETWORK	64
3.4.1	Geophones	64
3.4.2	Geophone orientation	66
3.4.3	<i>Geode</i> seismographs	68
3.4.4	Central recording site	69
3.5	MODES OF OPERATION AND DATA HANDLING	70
3.5.1	Network communication	70
3.5.2	Automatic and interactive network control	71
3.5.3	Seismic event triggering	71

3.6	ESTIMATING ARRIVAL TIMES	72
4	Microseismic investigation of an unstable mountain slope in the Swiss Alps	75
4.1	INTRODUCTION	76
4.2	RANDA STUDY SITE	79
4.2.1	The 1991 Randa rockslides	79
4.2.2	Geology and fracture/fault systems	79
4.3	RANDA MONITORING SYSTEMS	80
4.3.1	Geodetic-geotechnical-meteorological monitoring systems	80
4.3.2	Microseismic monitoring system	80
4.4	INITIAL PROCESSING OF THE RANDA MICROSEISMIC DATA	81
4.5	3-D SEISMIC MODEL	83
4.6	DETERMINING EARTHQUAKE LOCATIONS	84
4.7	PERFORMANCE OF THE RANDA MICROSEISMIC NETWORK	87
4.7.1	Effect of network size and geometry on the hypocenter estimation process	87
4.7.2	Calibration of the network using small test shots: station corrections	88
4.8	MICROEARTHQUAKE LOCATIONS AND MAGNITUDES	89
4.8.1	Two single microearthquakes	90
4.8.2	Analysis of all microearthquakes	91
4.8.3	Magnitudes	92
4.9	INTERPRETATION	93
4.9.1	Microseismogenic zones (A, B, D, E, and G)	94
4.9.2	Aseismic zones (C and F)	95
4.9.3	Extent of the unstable slope	96
4.9.4	Microseismicity and the presence of water	96
4.10	DISCUSSION AND CONCLUSIONS	96
4.11	ACKNOWLEDGEMENTS	99
4.12	APPENDIX	100
	SEMI-AUTOMATIC SEISMIC EVENT CLASSIFICATION	100
4.12.A	Step I: identification of impulsive transients	100
4.12.B	Step II: sonogram pattern recognition scheme	101
4.12.C	Step III: manual classification	102

5	Conclusions and outlook	123
5.1	BOREHOLE RADAR	123
5.2	MICROSEISMIC NETWORK AND MONITORING	124
5.3	INTEGRATED STRUCTURAL MODEL	125
5.4	SUGGESTIONS FOR FURTHER INVESTIGATIONS AT RANDA	126
5.4.1	Unresolved depth extent of instability	126
5.4.2	Reduce inaccuracies of the microseismic technique	128
5.5	SUGGESTIONS FOR METHODOLOGICAL IMPROVEMENTS	128
5.5.1	Borehole and surface radar	128
5.5.2	Research on transients	129
5.5.3	Microseismic monitoring	131
	Appendix A	133
	Polarization for two selected rockslide-related microearthquakes	133
A.1	THE COVARIANCE METHOD	133
A.2	RESULTS	134
	Appendix B	137
	Magnitudes for rockslide-related microearthquakes	137
B.1	INTRODUCTION	137
B.2	MOMENT MAGNITUDES	137
B.3	RESULTS	138
	Appendix C	143
	Multidisciplinary monitoring of progressive failure processes in brittle rock slopes – concepts and system design	143
	ABSTRACT	143
C.1	INTRODUCTION	144
C.2	CONCEPTUALIZATION	145
C.3	SITE SELECTION AND INVESTIGATION	146
C.3.1	Study site Randa	146
C.3.1	Existing data	148
C.4	INSTRUMENTATION NETWORK DESIGN	148
C.4.1	Geological model – working hypothesis	148
C.4.2	Geotechnical instrumentation	149

C.4.3	Microseismic network	151
C.4.2	Communication and data management	153
C.5	CONCLUSIONS	154
C.6	ACKNOWLEDGEMENTS	155
Appendix D		156
The Randa Rockslide Laboratory: Establishing brittle and ductile instability mechanisms using numerical modelling and microseismicity		156
	ABSTRACT	156
D.1	INTRODUCTION	157
D.2	BRITTLE FRACTURE PROCESSES IN MASSIVE ROCK SLOPES	158
D.3	NUMERICAL MODELLING OF BRITTLE AND DUCTILE MECHANISMS	160
D.3.1	The Randa Rockslide Laboratory	160
D.4	NUMERICAL FORMULATION AND MODEL SETUP	161
D.5	EXTENSIONAL STRAIN AND BRITTLE FRACTURE	162
D.6	MICROSEISMIC MONITORING	164
D.7	CONCLUSIONS	167
Appendix E		169
High-resolution geophysical techniques for improving hazard assessments of unstable rock slopes		169
	ABSTRACT	169
E.1	RANDA STUDY SITE	170
E.2	MAPPING SHALLOW-DIPPING STRUCTURES USING SURFACE GEORADAR DATA	172
E.3	MAPPING STEEP-DIPPING FRACTURES USING BOREHOLE GEORADAR DATA	174
E.4	MAPPING ULTRA-LOW P-WAVE VELOCITIES USING TOMOGRAPHIC SEISMIC DATA	177
E.5	MAPPING ROCK-SLOPE INSTABILITIES BASED ON MICROSEISMICITY	179
E.6	WHAT HAVE WE LEARNED ?	181
E.7	WHAT NEXT ?	182

E.8	SUGGESTED READING	183
E.9	ACKNOWLEDGMENTS	183
	Bibliography	185
	Acknowledgements	203
	Curriculum vitae	205

Abstract

Unstable rock slopes are major hazards to the growing number of people that live and travel through mountainous regions. In many countries, socio-economic losses due to rockslides are growing as human development expands into vulnerable areas. To mitigate the effects of slope failures, early warning systems and robust protective barriers need to be constructed. Such installations require reliable knowledge on the positions, dimensions, and geometries of the structures that promote instability. In addition to this static characterization of the ground, detailed knowledge on the kinematic and dynamic conditions of unstable slopes is essential for understanding and predicting failure.

My thesis is part of a multidisciplinary project to understand the internal structure and processes of complex crystalline rockslides. It contains two major parts, both concerned with an unstable mountain slope: (1) structural investigation based on geophysical logs and borehole radar data, and (2) a study of microseismic activity. The overall project involved geological mapping, surface geophysics, geotechnical monitoring, and numerical analyses.

The study site is located above the scarp of the 30-million m³ Randa rockslides that occurred in 1991 close to the village of Randa in the Matter Valley (Switzerland). Geodetic monitoring suggests that 2.7-9.2 million m³ of the remaining mountain slope continues to move 0.01-0.02 m/year southeastwards. These movements have been concentrated across major fracture zones and faults that likely control the instability. Three sets of brittle discontinuities affected the foliated gneisses on the unstable mountain slope, one shallow-dipping set and two steep-dipping sets.

To map and characterize fracture zones and faults within the unstable mountain slope, geophysical log, single-hole radar, vertical radar profiling (VRP), and crosshole radar data were acquired in three moderately deep boreholes (depths of 51.0-120.8 m). Spallation zones, displacements, and borehole radar velocity anomalies were observed at 16 of 46 discontinuities identified in the borehole optical televiewer images. Much useful structural information was provided by the single-hole radar reflection sections, but images provided by the other radar surveys were either disappointing (VRP sections) or surprisingly featureless (crosshole tomograms). Radar reflections were recorded primarily from steeply dipping fracture zones and faults; however, their orientations could not be derived from the radar data alone. The combined interpretation of single-hole radar reflections and fracture

zone/fault orientations measured at the surface or in the boreholes enabled six surface and four borehole fracture zones/faults to be mapped at depth. Six additional borehole radar reflections were interpreted as unmapped fracture zones. On the basis of the radar reflection sections, it was concluded that the major fracture zones/faults extended to at least 50-75 m depth.

Rockslide-related microearthquakes were recorded by a network of twelve 3-component geophones that were installed near the bottom of the three moderately deep boreholes and in nine shallow holes. The microseismic network with an aperture of ~250 m was deployed across the rugged terrain above the rockslide scarp. It was designed to operate under harsh, high-alpine conditions. Semi-automatic detection and classification routines were developed to identify rockslide-generated microseismicity out of 66,409 triggered events. During the network's 31-month lifetime, 223 microearthquakes with moment magnitudes of -2 to 0 were recorded. The frequency content of the microseismic recordings was limited to 5- 100 Hz, suggesting that attenuation of seismic energy within the fractured and faulted rock mass was substantial. Locating the recorded microearthquakes was challenging because of highly heterogeneous P-wave velocities, shortage of first-break and no reliable S-wave picks, and microearthquakes just outside the network boundaries. To derive reliable hypocenters and uncertainties, I took advantage of a comprehensive 3-D seismic velocity model and a novel probabilistic earthquake location algorithm. The observed microseismic activity was concentrated in two main zones: one that followed the rockslide scarp and extended ~35 m to north, and one that coincided with the area of highest fracture zone/fault density. Most microearthquakes occurred at shallow depths within 50-100 m of the surface. Microseismic activity was also observed near and beyond the western boundary of the microseismic network. Minor microseismicity near the base of the location model suggested that activity may extend deeper into the mountain.

My thesis includes a comprehensive model of discontinuities at the Randa site based on an integrated interpretation of borehole radar data with geological and geotechnical data. The location of microseismicity detected by the monitoring network is consistent with this model, and with displacements measured at the surface and within boreholes. The results suggest that the currently unstable volume of mountain slope at Randa is delineated by steeply dipping fracture zones and faults. Unfortunately, it is not possible to delineate a master fault at depth that could control any future rockslide.

Zusammenfassung

Hanginstabilitäten in den Alpen stellen eine bedeutende Bedrohung für die wachsende Bevölkerung und den zunehmenden Tourismus dar. In vielen Ländern sind die sozialen und ökonomischen Einbussen durch Felsrutschungen/Bergstürze am steigen, da weiterhin gefährdete Gebiete besiedelt werden. Um die Auswirkungen von solchen Instabilitäten zu entschärfen, müssen Frühwarnsysteme installiert und geeignete Schutzbauten erstellt werden. Zuverlässige Systeme erfordern dabei detailliertes Wissen über die Lage, Erstreckung und Geometrie der Strukturen im Gebirge, die destabilisierend auf den Felshang wirken. Zusammen mit dieser statischen Charakterisierung des Gebirges sind die kinematischen und dynamischen Vorgänge von Bedeutung, damit das Bruch- und Absturzverhalten der instabilen Felsmassen besser verstanden und vorhergesagt werden kann.

Meine Arbeit ist Teil eines multidisziplinären Projekts mit dem Ziel, die interne Struktur und Prozesse einer Felsrutschung im kristallinen Gebirge zu verstehen. Die Arbeit umfasst zwei Teile, die sich beide mit einer Felsrutschung in den Alpen befassen: (1) geophysikalische Bohrlochmessungen und Bohrlochgeoradar zur strukturellen Untersuchung, und (2) eine Studie zur mikroseismischen Aktivität. Im Rahmen des gesamten Projektes wurden zudem geologische Kartierung, Oberflächengeophysik, geotechnische Überwachung und numerische Modellierungen durchgeführt.

Das Untersuchungsgebiet liegt oberhalb der Abbruchkante des Bergsturzes von Randa, wo im Jahre 1991 etwa 30 mio. m³ Gestein ins Mattertal stürzten. Der Hang wird seitdem vermessungstechnisch überwacht und zeigt südostwärts gerichtete Bewegungen von 0.01-0.02 m/Jahr. Das Volumen der instabilen Felsmasse wird auf 2.7-9.2 mio. m³ geschätzt. Die beobachteten Verschiebungen konzentrieren sich an Klufzonen und grossen Störungen, die wahrscheinlich die instabile Masse begrenzen. Es handelt sich dabei um drei Gruppen von Kluft- und Störzonen in den geschieferten Gneisen des Hanges, entlang derer meist spröde Deformationen stattgefunden haben.

Um diese Klufzonen und grossen Störungen innerhalb der instabilen Masse zu charakterisieren, wurden in den drei mitteltiefen Bohrlöchern (51.0-120.8 m) geophysikalische Logs und Bohrlochradardaten (single-hole radar) aufgezeichnet. Die

Radarmessungen beinhalten auch Messungen von den Bohrlöchern zur Oberfläche (VRP) und zwischen zwei Bohrlöchern (crosshole). Anhand von Aufnahmen einer Bohrlochkamera (televiever images) wurden 46 Diskontinuitäten identifiziert, wobei an deren 16 Absplitterungen, Verschiebungszonen oder Anomalien in den Radargeschwindigkeiten beobachtet wurden. Die wertvollsten Informationen ergaben Reflexionen von Bohrlochradar (single-hole radar), die anderen Radarsektionen waren enttäuschend (VRP) oder nichts sagend (crosshole). Die Radarreflexionen stammten hauptsächlich von steil einfallenden Klüftzonen oder Störungen, deren Streichrichtung mit Bohrlochradar alleine nicht bestimmt werden konnte. Die Bohrlochradardaten erlaubten jedoch, sechs an der Oberfläche kartierte Klüft- und Störzonen vier in den Bohrlöchern beobachteten Klüft-/Störzonen zuzuordnen. Weitere sechs Reflexionen bezeugten die Existenz bisher nicht kartierter Klüftzonen. Aufgrund der Radarreflexionen konnte auf tiefgreifende Zerklüftung des Gesteins bis in Tiefen von mindestens 50-75 m geschlossen werden.

Eine Felsrutschung induziert höchstwahrscheinlich Mikroerdbeben. Um solche Mikroerdbeben zu messen, wurde ein spezielles Netzwerk von zwölf triaxialen Bohrlochgeophonen (je eines im untersten Teil der drei mitteltiefen Bohrlöcher, neun weitere in kurzen Bohrungen) errichtet. Das Netzwerk mit einem Durchmesser von ca. 250 m befand sich unmittelbar oberhalb der Abbruchkante des Bersturzes von Randa. Hohe Anforderungen wurden an die verschiedenen technischen Komponenten gestellt, damit das Netzwerk in der hochalpinen Umgebung betrieben werden konnte. Um aus den 66'409 aufgezeichneten Ereignissen die relevanten auszuwählen, habe ich halbautomatische Erkennungs- und Klassifizierungsverfahren angewandt. Während 31 Monaten wurden so 223 Mikroerdbeben mit Momentenmagnituden zwischen -2 und 0 aufgezeichnet. Die spektralen Bandbreiten der aufgezeichneten Signale beschränkten sich auf 5-100 Hz, was auf relative hohe Dämpfung von seismischen Wellen durch Klüfte und Brüche schließen lässt. Die Mikroerdbeben zu lokalisieren war schwierig. Komplikationen ergaben sich durch sehr heterogene P-Wellen Geschwindigkeiten, mittelmässige Datenqualität, schlecht detektierbare S-Wellen und durch Lokalisierungen ausserhalb des Netzwerkes. Ein dreidimensionales Geschwindigkeitsmodell und eine Lokalisierung auf Grundlage der Wahrscheinlichkeitstheorie ergaben zuverlässige Herdkoordinaten mit zugehörigen Fehlern. Die beobachtete Seismizität konzentrierte sich in zwei Zonen: Die eine folgte der Abbruchkante und erstreckte sich ca. 35 m weit nach Norden, die andere umfasste die Zone mit der höchsten

Dichte and Klüften und Störungen. Die meisten Mikroerdbeben ereigneten sich innerhalb der ersten 50-100 m unterhalb der Erdoberfläche. Geringe mikroseismische Aktivität wurde entlang und ausserhalb der westlichen Begrenzung des Netzwerkes beobachtet. Zusätzliche Mikroerdbeben wurden an der unteren Modellgrenze lokalisiert; diese Beben dürften sich jedoch in noch grösserer Tiefe ereignet haben.

Meine Arbeit beinhaltet eine umfassende Interpretation von Bohrlochradar mit geologischen und geotechnischen Daten. Ein Modell der wichtigen Kluft- und Störzonen im Untersuchungsgebiet wurde daraus abgeleitet und dargestellt. Die aufgezeichnete mikroseismische Aktivität ist konsistent mit diesem Modell und auch mit den Verschiebungsmessungen an der Oberfläche und in den Bohrlöchern. Gemäss diesen Resultaten ist die instabile Felsmasse durch steilstehende Kluft- und Störzonen begrenzt. Leider war es weder möglich, eine basale Scherzone festzustellen, noch ihre Existenz zu widerlegen.

1 Introduction

1.1 ROCKSLIDE HAZARD

Landslides and more specifically rockslides are natural hazards in mountainous regions worldwide. Many landslide/rockslide disasters have resulted in hundred's to thousand's of deaths (Table 1.1). European examples, such as the 1801 Goldau (Heim, 1932), 1886 Elm (Cooke and Doornkamp, 1990), 1963 Vaiont (Müller, 1968), and 1987 Val Pola (Govi et al., 2002) rockslides, caused heavy damage and numerous fatalities in the Alps. The tremendous power and destruction of catastrophic mass movement was highlighted by the 1970 Huascarán rock and ice avalanche (Cooke and Doornkamp, 1990; Erismann and Abele, 2001), which resulted in the loss of 25,000 lives.

In many countries, socio-economic losses due to rockslides are growing as human development expands into unstable hillslope areas (Schuster, 1996). Although the effects of global warming on rockslide hazard has yet to be established, the growing number of people that live and recreate in mountainous areas is clearly increasing the risks associated with rockslides. Society expects such risks to be quantified. The locations and volumes of unstable rock as well as the time and modes of failure need to be predicted, so that appropriate countermeasures can be taken. There is a requirement to improve our understanding of rockslide slip mechanisms in order to forecast better the behavior of unstable slopes.

Traditionally, slopes are classified as either *stable* or *unstable* on the basis of the margin of stability (i.e. factor of safety), defined as the shear strength to shear stress ratio (Hufschmidt et al., 2005). Such an approach is an effective way of quantitatively evaluating slope stability, but knowledge or assumptions about the shape of the rupture surface and its strength are required. In fractured brittle rock, the boundaries of an unstable mass are likely to be controlled by existing discontinuities. To obtain the required information on the locations, sizes, and geometries of brittle discontinuities, a wide variety of geological, geotechnical, and geophysical techniques is available (Cooke and Doornkamp, 1990; McCann and Forster, 1990; Turner and Schuster, 1996; Hack, 2000; Glade et al., 2005a).

Table 1.1: Examples of disastrous landslide/rockslide events worldwide. The 1991 Randa rockslide is highlighted. Modified after Cooke and Doornkamp (1990).

<i>Place</i>	<i>Date</i>	<i>Type of landslide</i>	<i>Impact</i>
Goldau, Switzerland	2 Sept 1806		457 fatalities
Elm, Switzerland	1881		115 fatalities
Frank Slide, Canada	1903	Rockslide	72 fatalities
Java	1919	Debris flow	5100 fatalities, 140 villages destroyed
Kansu, China	16 Dec. 1920	Loess flows	10,000 fatalities
California, USA	31 Dec. 1934	Debris flow	40 fatalities, 400 houses destroyed
Kure, Japan	1945		1154 fatalities
Khait, Tadjikistan	1949	Earthquake-triggered landslide	~12,000 fatalities
SW of Tokyo, Japan	1958		1100 fatalities
Ranrachirca, Peru	10 June 1962	Ice and rock avalanche	3500+ fatalities
Vaiont, Italy	1963	Rockslide into reservoir	about 2600 fatalities
Aberfan, UK	21 Oct. 1966	Coal tip collapse	144 fatalities
Rio de Janeiro, Brazil	1966		1000 fatalities
Rio de Janeiro, Brazil	1967		1700 fatalities
Virginia, USA	1969	Debris flow	150 fatalities
Japan	1969-72	Various	519 fatalities, 7328 houses destroyed
Huascarán, Peru	31 May 1970	Earthquake-triggered rock/ice avalanche	up to 25,000 fatalities
Chungar	1971		259 fatalities
Hong Kong	June 1972	Various	138 fatalities
Kamijima, Japan	1972		112 fatalities
S. Italy	1972-3	Various	about 100 villages abandoned affecting about 200,000 people
Mayunmarca, Peru	25 Apr. 1974	Debris flow	town destroyed, 451 fatalities
Mantaro Vally, Peru	1974		450 fatalities
Mt. Semeru	1981		500 fatalities
Yacitan, Peru	1983		233+ fatalities
W. Nepal	1983		186 fatalities
Dongxiang, China	1983		227 fatalities
Val Pola, Italy	1987	Rockslide	28 fatalities
Randa, Switzerland	1991	Rockslide	
Santa Tecla, El Salvador	2001	Earthquake-triggered landslide	
Kolka, Russian Caucasus	2002	Rock/ice avalanche	140 fatalities
Leyte, Philippines	2006	Rockslide/mudslide	~1500 fatalities

Although a detailed description of the structure of a mountain slope allows its stability and consequences of failure to be appraised, a reliable hazard assessment also needs the probability of failure to be quantified. Internal fracturing may gradually reduce slope stability until it reaches a point when a small trigger can release the unstable mass. A rising groundwater table as a result of increased precipitation or snow melt is a possible internal trigger. External triggering mechanisms include large earthquakes or the removal of lateral or underlying support by undercutting the unstable slope (Cooke and Doornkamp, 1990).

In some cases, evidence of triggering is not recognized and/or the cause of failure remains largely unresolved (e.g. Pandemonium Creek - Evans et al., 1989; Frank slide - Benko and Stead, 1998; Randa rockslide - Schindler et al., 1993). It is likely that complex mechanisms involving fracturing of intact rock and/or shearing along existing discontinuities contribute to many failures. Our knowledge about the evolutionary development of future sliding surfaces is based mainly on back-analyses of natural or engineered slope failures (Kawamoto and Takeda, 1979; Chowdhury, 1992; Einstein et al., 1995; Tanaka, 1998; Eberhardt et al., 2004a). Validation of the resulting models requires information on the displacement fields prior and during the catastrophic rockslides. Presently, standard ground-deformation measurements must be made over large periods of time to resolve key details on pre-failure deformation. A method sensitive to small displacements preceding failure would be of significant value for improving early warning systems.

1.2 BRIEF OVERVIEW OF ROCKSLIDE INVESTIGATIONS

1.2.1 Detection of unstable zones

Rockslide investigations are typically only initiated after certain unusual signals (e.g., opening fractures or increasing rock fall) have been observed. The increasing exposure of civilization and infrastructure to rockslide risk requires more systematic approaches for detecting rockslide prone areas. Improvements to catalogues of unstable slopes may be expected from applications of various remote sensing techniques (e.g., aerial photographs and ground, airborne, and/or satellite images; Metternicht et al., 2005). Recent developments of the InSAR and DInSAR techniques have improved the resolution and accuracy of space-borne interferometric radar data, such that slowly moving masses with dimensions of <100 m and displacement rates <1.6 mm/y may be detected (Canuti et al., 2004; Catani et al., 2005; Rott and Nagler, 2006). Unfortunately, several factors can limit the use of remote

sensing techniques: slope face and slip direction may be oriented in directions unfavorable to the satellite's orbit, and vegetation may cover the slope. To assess the geological structure and instability mechanisms of potentially unstable slopes in a more deterministic fashion requires the use of ground-based geological, geotechnical and geophysical investigations (Soeters and van Westen, 1996).

1.2.2 Structural characterization: geophysical techniques

Structural characterization of rockslides is a complex task, because the combination of different rocks, varying topography and diverse structures can produce very different types of slope displacement. Surface-based geophysical techniques provide the means to investigate subsurface geological structures in a fast and non-invasive manner. Seismic methods are of particular interest, because seismic velocities are directly related to the elastic parameters of materials. The overview of important geophysical studies on rockslides in Table 1.2 suggests that seismic refraction methods are becoming standard in rockslide investigations. The relatively fast and robust tomographic seismic refraction technique allows complex variations of material properties in 2-D and 3-D to be mapped, which is useful when rockslide boundaries follow lithological units (Havenith et al., 2000; Schmutz et al., 2000; Glade et al., 2005b; Meric et al., 2005).

The development of a sliding surface parallel to lithological boundaries is not always observed: rockslide slip surfaces may transect the bedding. This applies especially to slope instabilities in crystalline rock, where failure is likely to be controlled by fractures or faults. Jongmans et al. (2000), Dussauge-Peisser et al. (2003), Brückl and Brückl (2006) and Heincke et al. (2006a) have demonstrated that seismic tomographic images can distinguish highly fractured, and hence weakened, unstable zones from sound rock.

In principle, higher resolution information on the location of important discontinuities can be obtained from interpretations of seismic reflection data. In practice, it is generally very difficult to obtain detailed seismic reflection images of shallow fractures. Shallow reflections are typically overwhelmed by strong surface, guided, and air waves. Furthermore, complexities in the acquired data may originate from multiple scattering, attenuation, dispersion and wave-conversion effects. Nevertheless, at least two groups have been successful in obtaining seismic reflection images of structures that influence slope stability (Figure 1.1; Bruno and Marillier, 2000; Bichler et al., 2004).

Table 1.2: Brief review of geophysical landslide/rockslide investigations.

<i>Authors</i>	<i>Principal methods</i>	<i>Main results</i>	<i>Landslide name and type</i>
Bogoslavsky & Ogilvy (1977)	Seismic, resistivity, self-potential	Landslide body, groundwater level	Landslides in sedimentary rocks
McCann & Forster (1990)	Seismic, resistivity, electromagnetic	Review of case studies	
Gornberg et al. (1995)	Seismic monitoring, GPS	Microearthquake probability	Slungulion earthflow (USA)
Bruno & Marillier (2000)	Seismic reflection, electromagnetic, georadar	Sliding surface, disappointing georadar	Boup landslide (CH)
Cummings (2000)	Electromagnetic	Landslide thickness, fault depth	Santa Susanna Mountains (USA)
Del Gaudio et al. (2000)	Gravity	Upslope landslide enlargement	Senerchia slump-earthflow (I)
Hack (2000)	Seismic, resistivity, self-potential, electromagnetic, gravity	Review of fundamental principles	
Havenith et al. (2000)	Seismic refraction, resistivity	3-D geological model	Suusamyr debris slump/debris flow (KS)
Jongmans et al. (2000)	VSP, resistivity	Delineate fractured, unstable rock	Rockslide Bas-Oha (B)
Mauritsch et al. (2000)	Seismic refraction, resistivity	Seismic velocities and resistivities	Carnic landlides (A)
Scheikl et al. (2000)	Geotechnical, microseismic monitoring	Ground displacement and vibration	Eiblschrofen rockfall (A)
Schmutz et al. (2000)	Electromagnetic, resistivity	Soil stratification	Super Sauze earthflow (F)
Eberhardt et al. (2001, 2004b)	Geotechnical and microseismic monitoring	Installation of monitoring system	Randa rockslide (CH)
Liu et al. (2001)	VSP, seismic reflection	Landslide boundary and stability	Zhaoshuling landslide (CN)
Havenith et al. (2002)	Seismic refraction, seismic noise measurements	Amplification at mountain crest	Anavevo Rockslide (KS)
Dussauge-Peisser et al. (2003)	Seismic refraction, georadar	Mean velocities, steep fractures	Chartreuse limestone cliff (F)
Bichler et al. (2004)	Georadar, resistivity, seismic reflection, refraction	Rupture surface	Quesnel Forks landslide (earth slide) (CDN)
Amitrano et al. (2005)	Microseismic monitoring	Seismicity rate before cliff collapse	Chalk cliff in Normandie (F)
Brückl & Parotidis (2005)	Seismic refraction, microseismic monitoring, creep	Seismic velocities and microseismic activity	Four rockslides (A)
Merrien-Soukatchoff et al. (2005)	Microseismic monitoring	Microearthquake hypocenters	Rochers de Valabres (F)
Roth et al. (2005)	Microseismic monitoring	Microearthquake recordings	Åknes rockslide (N)
Glade et al. (2005b)	Seismic refraction	Lower landslide boundary	Complex slide in limestone, clay and marls (D)
Heincke et al. (2005a, 2006b)	3-D surface georadar	Images of shallow and steeply dipping fractures	Randa rockslide (CH)
Lapenna et al. (2005)	Resistivity	Map of sliding surface	Apenine landlides (I)
Heincke et al. (2006a)	3-D seismic refraction	3-D velocity model, delineate faults	Randa rockslide (CH)
Brückl & Brückl (2006)	Seismic refraction	Basal slide plane, elastic parameters	Lesachriegel and Gradenbach creeping masses (A)
Godio et al. (2006)	Resistivity, seismic refraction, borehole logs	Delineate fractured rock, elastic parameters	Rockslide in gneissic rock (I)
Jeannin et al. (2006)	Georadar	Location and orientation of steeply dipping fractures	Limestone cliffs in Chartreuse massif (F)
Spillmann et al. (2006)	Borehole radar	Location and orientation of steeply dipping fractures	Randa rockslide (CH)

Highly detailed information on the location and orientation of rock discontinuities in the shallow subsurface are provided by ground-penetrating radar (georadar or GPR) techniques (Grasmueck, 1996; Dussauge-Peisser et al., 2003; Heincke et al., 2005; 2006b; Jeannin et al., 2006). However, the depth penetration of surface-based georadar may be limited by the presence of conductive surface layers.

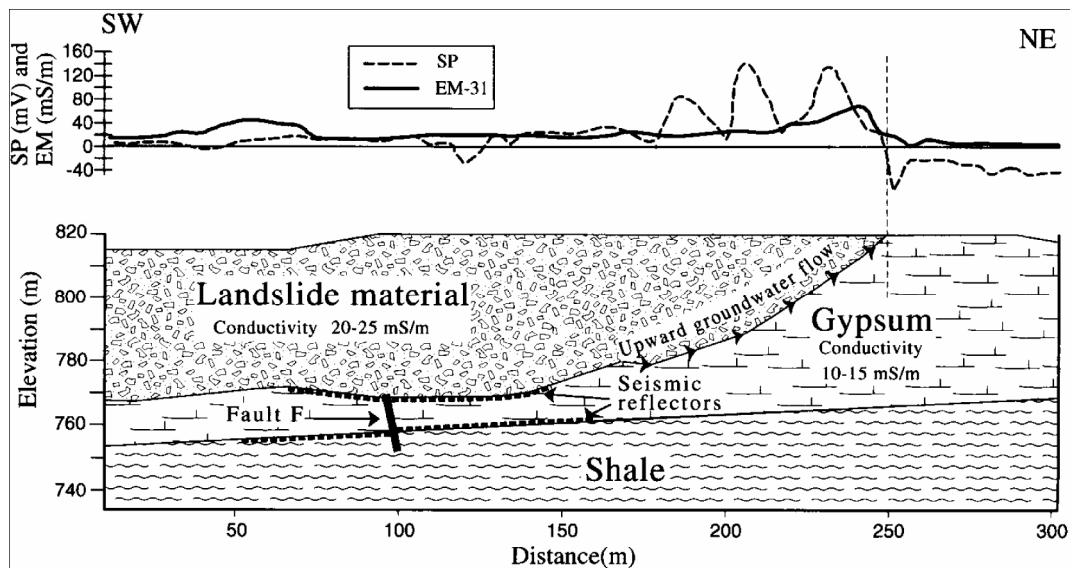


Figure 1.1: Interpretation of geophysical surveys across the Boup landslide. Landslide body and lower boundary were characterized by an electrical conductivity anomaly and seismic reflections. Information on water flow was inferred from self potential (SP) measurements (after Bruno and Marillier, 2000).

There is a variety of electrical, electromagnetic and gravimetric methods that can be used to characterize rockslides (Table 1.2, Figure 1.1). Generally, details of the rockslide mass and lower boundary have been supplied by these methods. Information on water flow has been inferred from self potential (SP) measurements (Bruno and Marillier, 2000). The resolution provided by standard applications of these methods is generally not sufficient for mapping and characterizing individual fractures in crystalline rock.

Borehole geophysical methods provide the means to extend surface-based information to greater depth. Although many boreholes have been drilled at or near rockslides, borehole geophysical investigations are uncommon. The few documented studies employed vertical seismic profile (VSP) data to derive seismic and geotechnical parameters (Jongmans et al., 2000; Liu et al., 2001; Godio et al., 2006). It is worth noting that valuable

information on the nature and distribution of fractures in brittle rock has been provided by borehole geophysical studies related to nuclear waste disposal (Olsson et al., 1992; Wänstedt et al., 2000; Serzu et al., 2004) and in an investigation of a granite quarry (Seol et al., 2004).

1.2.3 Kinematic and dynamic characterization: microseismic monitoring

To gain insight into the kinematics of instabilities, ground deformation is usually measured using surface survey markers, benchmark arrays, or inclinometer tubes installed through the potentially unstable mass (Brunsdén and Prior, 1984; Turner and Schuster, 1996; Jaboyedoff et al., 2004; Willenberg et al., 2004). Because these measurements are restricted to distinct observation points or to boreholes, assessing the displacement field of complex rockslides requires dense networks of observation points covering larger areas. Ground-based interferometric radar methods (Tarchi et al., 2003; Antonello et al., 2004) provide the opportunity to obtain kinematic information more quickly and efficiently. However, these methods do not provide insight into the physical processes that control sliding and slope failure.

Monitoring microearthquakes, caused by fracture initiation, fracture propagation or sliding along existing discontinuities, and analyzing the generated seismic waves offers an alternative method for assessing slip. The presence of an earthquake is an indication of strain within rock under stress. Local stress maxima that exceed the shear strength of a rock result in strain. Simple measurements have shown that count rates of microseismic events or acoustic emissions are good indicators of future slope failure (Chichibu et al., 1989; Hardy, 1989). Unfortunately, typical acoustic emissions are in the kHz range, a frequency band that is rapidly attenuated in fractured rock. This limits the acoustic emission technique to small-scale investigations with dimensions of a few tens of meters.

To study the microseismicity of typical rockslides with dimensions of ~100 m to a few kilometers requires a microseismic network with an aperture that is between those used for acoustic emissions and those used for monitoring major active tectonic faults. Similar networks have been used to monitor open pit mines (McCauley, 1975), deep mines (Gibowicz et al., 1991; Trifu and Urbancic, 1996; Iannacchione et al., 2005), fracturing and fluid flow in hydrocarbon reservoirs and hot-dry-rock systems (Jupe et al., 1992; Jones et al., 1995; Rutledge et al., 1998; Talebi et al., 1998; Vécsey et al., 1998; Moriya et al., 2002; Oye and Roth, 2003; Evans et al., 2005a) and volcanoes (Vilardo et al., 1996; De Natale et al.,

1998; Lomax et al., 2001; Pezzo et al., 2004; Presti et al., 2004; Lippitsch et al., 2005). This variety of successful applications suggests that the microseismic method is well suited for investigating deformation processes in unstable slopes.

Publications on the microseismic monitoring of landslides in a broad sense may be divided into three groups: (1) investigations of local seismicity related to slope instabilities (Figure 1.2; Rouse et al., 1991; Gomberg et al., 1995; Scheikl et al., 2000; Eberhardt et al., 2004b; Amitrano et al., 2005; Brückl and Parotidis, 2005; Merrien-Soukatchoff et al., 2005; Roth et al., 2005), (2) detection and classification of large landslide signals recorded on regional seismic networks (Norris, 1994; Weichert et al., 1994; Arattano and Marchi, 2005; Suriñach et al., 2005), and (3) studies of topographic or structural amplification of ground motion that may promote failure (Havenith et al., 2003; Meric et al., 2005).

The goal of the first set of studies was to derive fundamental earthquake parameters: hypocenter coordinates, magnitudes and fault mechanisms of rockslide-related seismicity. The second set of studies was mainly initiated to identify the seismic signatures of landslides in order to remove them from tectonic earthquake catalogues. As by-products of this set of studies, the analyses of rupture mechanisms (Kawakatsu, 1989) and estimates of basal friction angles (Brodsky et al., 2003) or of the released mass (Norris, 1994) have provided bulk estimates of important landslide parameters. The third set of studies evaluated the amplification of ground motion on slopes, which can be an important factor in the triggering of landslides by earthquakes.

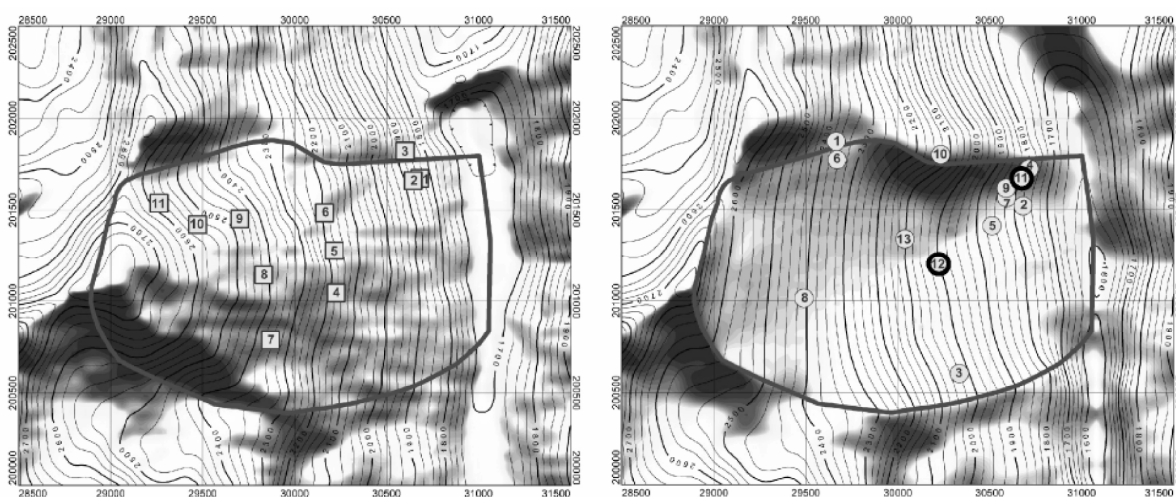


Figure 1.2: Results of seismic monitoring at Hochmais-Atemskopf (Austria; after Brückl and Parotidis, 2005). (a) Location of 12 seismic stations (squares with station number), (b) epicenters of 13 seismic events (circles with event number). Thick lines outline the unstable area.

1.3 THE RANDA ROCKSLIDE PROJECT

In 2000, the *Engineering Geology* and *Applied and Environmental Geophysics* groups of ETH initiated a multidisciplinary research project titled “*Rockslide processes and mechanisms: Progressive development of shear/slide surfaces in rock slopes*”. The project was designed to supply an improved understanding of instability mechanisms leading to natural slope failure. One focus of research involved detailed investigations of structures using geotechnical and geophysical methods employed at the surface and within boreholes. A second focus was concerned with the establishment and operation of a geotechnical/microseismic monitoring network to examine the time-dependent character of displacements, pore pressures and micro-earthquake patterns.

Preliminary investigations at seven potential sites in Switzerland (Willenberg, 2004) resulted in the selection of the Randa rockslide region (Figure 1.3) in Canton Valais (Switzerland) as the research site that optimally met key requirements of the study objectives: (1) no obvious pre-existing sliding plane, (2) topography suitable for drilling and instrumentation, and (3) low ambient seismic noise to facilitate microseismic monitoring.

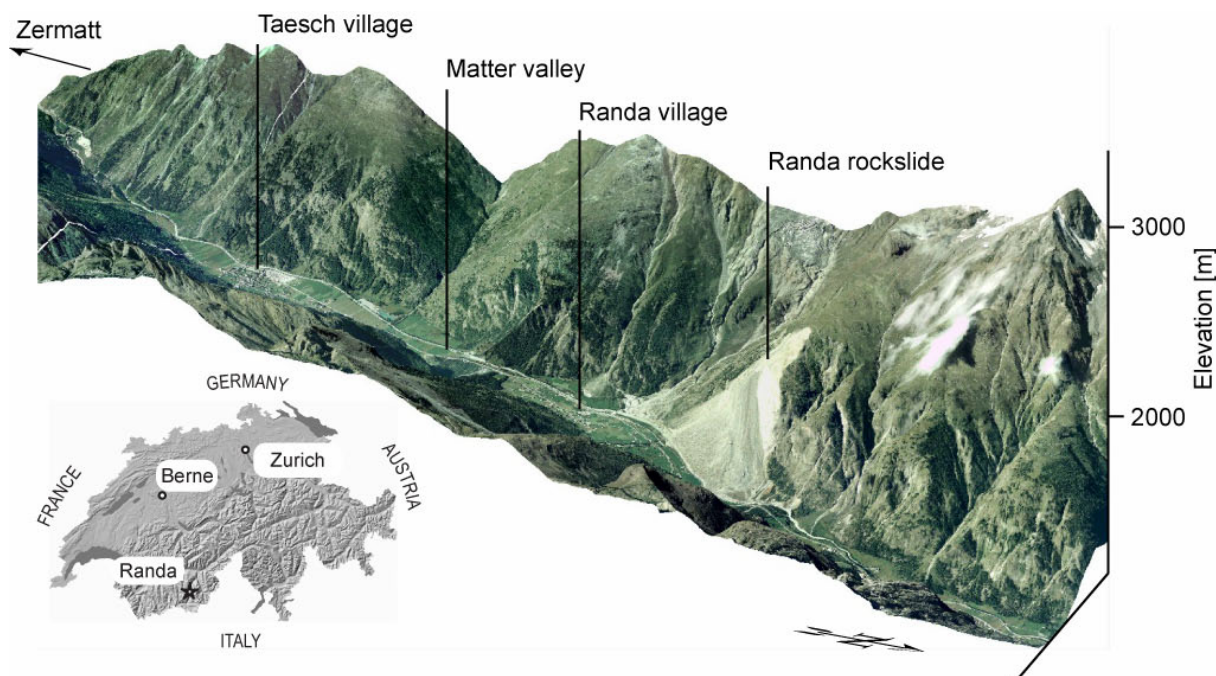


Figure 1.3: Perspective view of the Matter valley showing the Randa rockslide scarp and debris cone. Randa is located in the Southern Swiss Alps. Figure after F. Lemy (personal communication, 2006), reproduced with permission of Swisstopo (BA068028).

1.3.1 1991 Randa rockslides

The Randa study site lies immediately above the scarp of the largest mass movement to have occurred in recent Swiss history (Table 1.2). The two rockslide episodes (April 18 and May 9, 1991) released a total ~ 30 million m^3 of crystalline rock. The released debris obliterated holiday apartments and barns close to the village of Randa and blocked the main transport route connecting the Rhône valley to the major tourist resort of Zermatt (Schindler et al., 1993; Sartori et al., 2003; Figure 1.4). Fortunately, there were no fatalities, but the

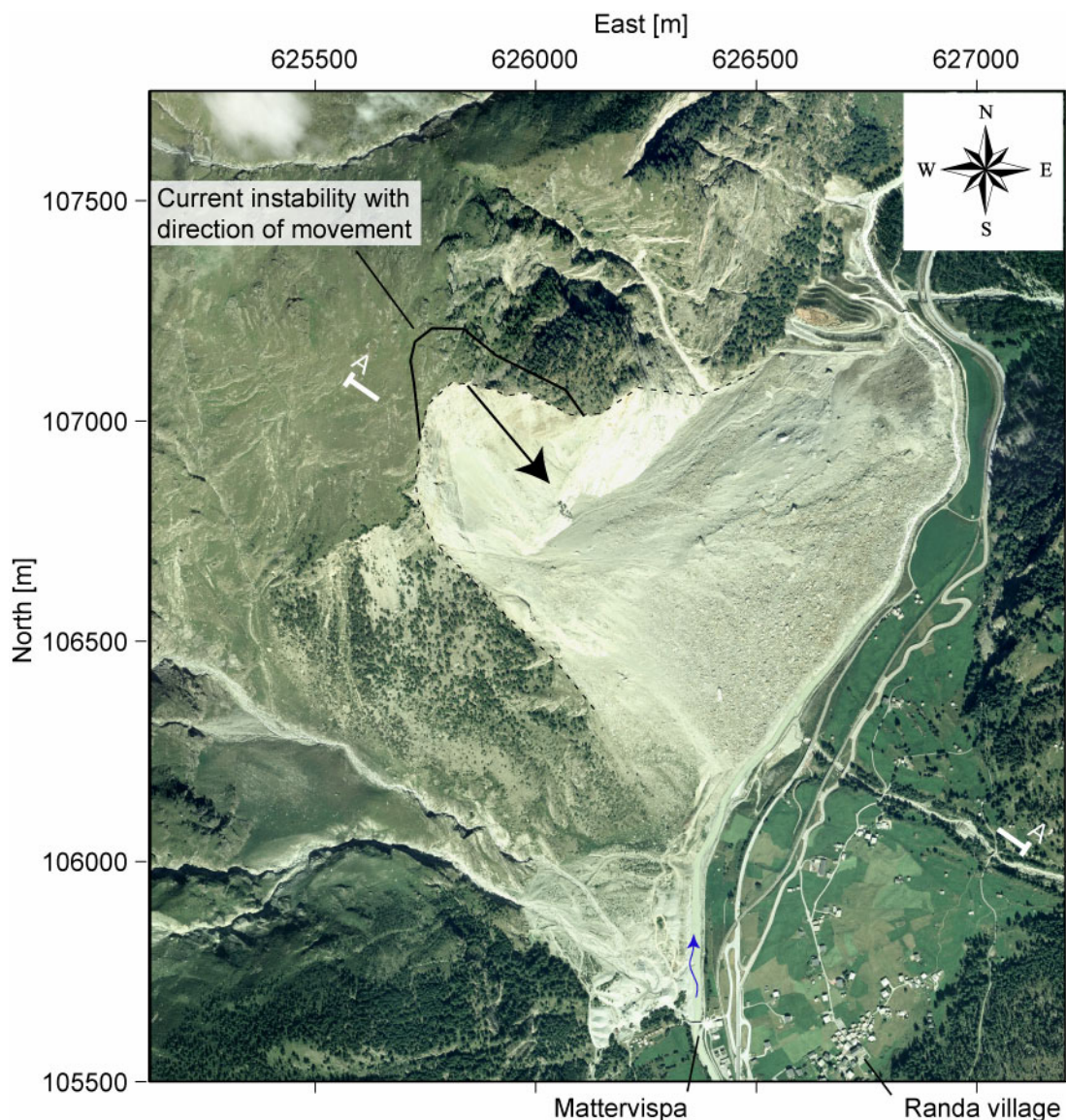


Figure 1.4: Orthophoto showing the scarp and debris cone of the Randa rockslide in the Matter valley. Current instability is outlined by the black line. A-A' locates the cross-section in Figure 1.5. Reproduced with permission of Swisstopo (BA068028).

debris cone dammed the Matternvispa River, causing flooding in upstream regions of the valley. Whereas the first rockslide on April 18 event occurred unexpectedly, a monitoring system installed soon after provided information that allowed the second rockslide on May 9 to be forecast.

Failure at Randa was highly oblique to the rock foliation, which dips southwesterly into the slope (Figure 1.5). It is clear that pre-existing fractures and faults played a significant role in the catastrophic failure. A persistent northeast dipping fault at the foot of the pristine cliff, now covered by debris, has been proposed as the fundamental zone of weakness and basal sliding plane for the first failure episode that occurred dominantly in augengneiss (Figure 1.5; Sartori et al., 2003). After removal of this mass, pre-existing southeast dipping fractures in the paragneiss probably contributed to the development of the second collapse that sequentially released smaller volumes from the upper paragneissic rocks. These latter rockfalls resulted in the moderately dipping, southeast-directed failure plane. Both rockslide episodes lasted for several hours (Schindler et al., 1993; Sartori et al., 2003).

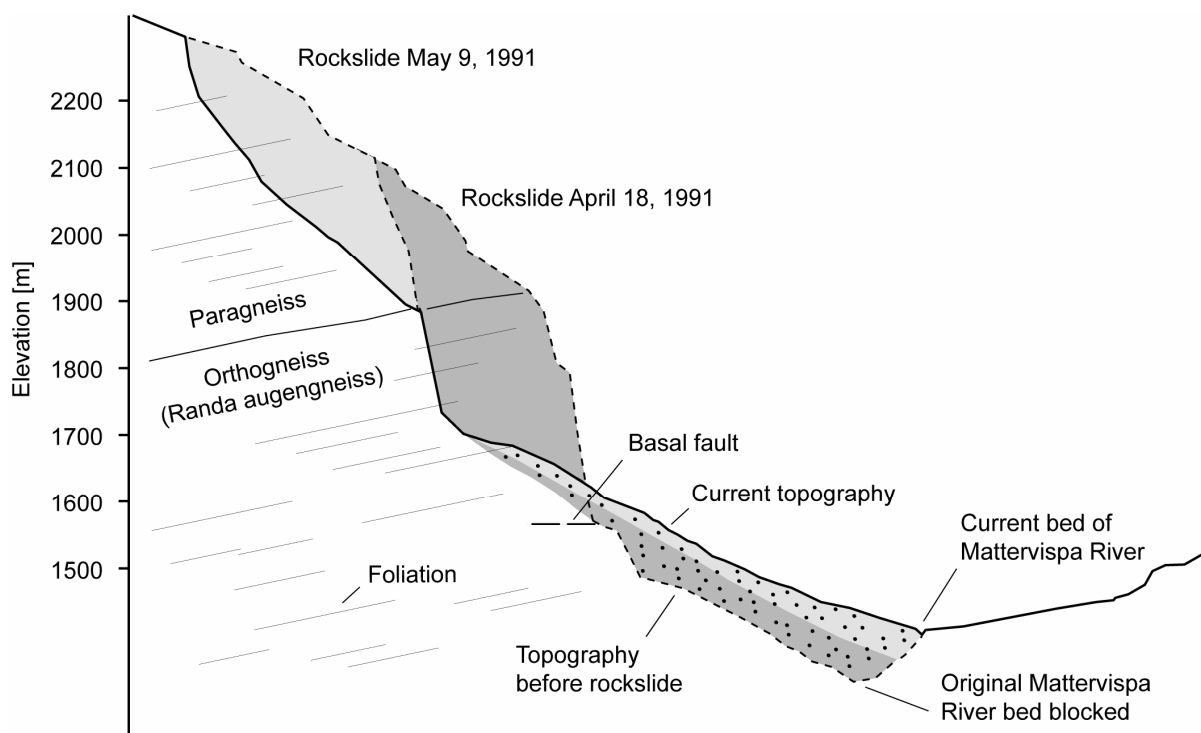


Figure 1.5: Cross-section of the 1991 Randa rockslides (after Schindler, 1993). Sartori (2003) identified the NE dipping basal fault as the initial failure plane of the first slide.

Internal degradation of rock strength over long periods of time likely influenced rock-slope stability at Randa. Progressive degrading mechanisms may have included the promotion of existing fractures and/or the reduction of their shear strength by failure of interlocking asperities (Eberhardt et al., 2004a). These failure mechanisms may have been accelerated by increases in pore pressure and/or ground accelerations associated with nearby large earthquakes (Eberhardt et al., 2004a; Stead et al., 2006).

Eberhardt et al. (2004a) presented a series of back-analysis studies of progressive rock mass destabilization that successfully predicted the general topography at Randa (Figure 1.6). These authors suggested that glacial retreat and associated oversteepening was accompanied by intensive fracturing. They demonstrated that failure planes similar to those of the second 1991 rockslide events evolved when frictional strength was reduced and fracturing of intact rock occurred (Figure 1.6).

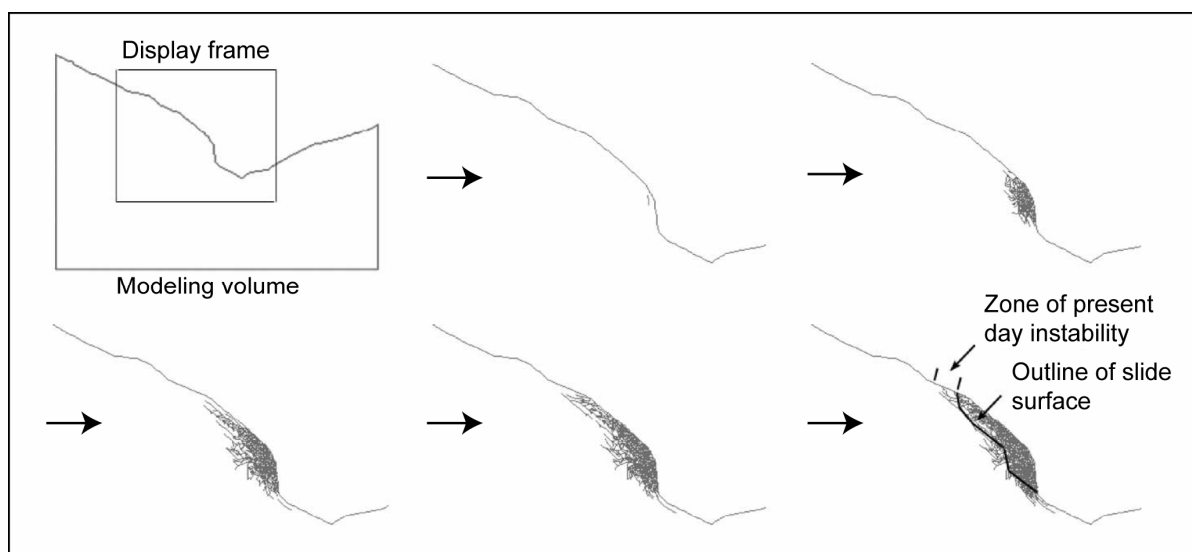


Figure 1.6: Progressive development of the slide surfaces predicted from a hybrid finite-/discrete-element modeling approach (after Eberhardt et al., 2004a).

A direct triggering mechanism has yet to be confidently identified for the 1991 rockslides. Groundwater may have played an important role; water sprays accompanied ejected rock slabs shortly before the April 18 event (Jaboyedoff et al., 2003; Schindler et al., 1991). However, meteorological data suggest that groundwater conditions were normal at the time of the rockslides (Eberhardt et al., 2001).

1.3.2 Current instability

Repeat geodetic surveys after the 1991 rockslides have indicated that 2.7 – 9.2 million m³ of the remaining rock mass continues to move slowly southeastwards (Ischi et al., 1991; Figure 1.4). The depth extent of this rock mass is not well constrained; estimates of the unstable volume are based on the assumption that the upward projection of the second 1991 rockslide failure plane is the lower level of mobility (Sartori et al., 2003; Jaboyedoff et al., 2004). It is this unstable volume that became the focus of the Randa rockslide project.

1.3.3 Geology and discontinuities

Viewed on a broad scale, the area of investigation is located in gneissic rocks that belong to the Penninic Siviez-Mischabel nappe (Bearth, 1964). The core of the Siviez-Mischabel nappe is the Randa-Augengneiss, a Permian porphyritic granite that intruded Palaeozoic rocks of the paragneiss series. Randa Augengneiss outcropping from the valley bottom to approximately 1900 m altitude is overlain by the paragneiss series (Figure 1.5). Field mapping by Willenberg (2004) has led to the recognition of three different gneiss types distinguished by their rock strengths, mineral contents, grain sizes and/or deformation structures: (1) augengneiss and medium-grained feldspar-rich heterogeneous gneiss, (2) chloritic gneiss with feldspar-porphyroblasts and (3) a thin band of chloritic gneiss and schist at 2300 – 2300 m.

Large scale structural models of discontinuities and faults zones at Randa have been presented by Wagner (1991), Schindler et al. (1993), Sartori et al. (2003), and Willenberg (2004). In the latest model of Willenberg (2004), three sets of faults and fracture zones were distinguished: one gently dipping southwesterly, parallel to foliation, and two moderately to steeply northwesterly and easterly dipping sets. Geodetic surveys and crack openings suggested that large scale fracture zones bound the actively sliding rock mass. Major discontinuities parallel to the failure plane of the second 1991 event have not been identified within the currently unstable volume.

1.3.4 Boreholes and borehole experiments

During the summer of 2001, three moderately deep boreholes (SB120, SB50S and SB50N) were drilled through two flat terraces on top of the unstable slope. Borehole SB120 was 120.8 m deep and closest to the scarp. The 52.5- and 51.0-m-deep boreholes SB50S and

SB50N were positioned in rock blocks characterized by successively lower displacement rates. Except for the lowermost 10 m of SB120, all boreholes were dry.

After drilling, the borehole geometries were determined and optical images of the borehole walls were recorded. The single-hole radar, vertical radar profiling (VRP) and crosshole radar data (Chapter 2) were acquired before the boreholes were cased with PVC tubes. The tubing allowed SB50S and SB50N to be temporarily filled with water, thus facilitating the sonic logging.

1.3.5 Monitoring network

The PVC casing provided guide tracks for repeated inclinometer measurements and for the emplacement of monitoring piezometers and 3-component geophones. To record and locate rockslide-related microearthquakes, the three borehole geophones were complemented by nine 3-component geophones located in shallow holes (Chapter 3 and 4). In addition, SB120 was equipped with steel rings that allowed strain along the borehole axis to be determined.

Surface based components of the geotechnical monitoring system included extensometers (continuously monitored crackmeters) and manually monitored benchmark arrays. The surface and borehole geotechnical equipment provided detailed information on local displacements (Willenberg et al., 2004).

1.3.6 Surface geophysics

To characterize the highly fractured region of the unstable slope and adjacent regions, Heincke et al. (2005, 2006a, 2006b) conducted extensive surface 3-D georadar and 3-D tomographic seismic refraction surveys. The surface 3-D georadar data provided vivid images of the shallow- to moderate-dipping fracture zones and faults and evidence for the depth extent of the steep-dipping ones. Information on the distribution of seismic velocities supplied by the tomographic surveys proved critical in my attempt to locate slope-instability-related microearthquakes (Chapter 4).

1.4 THESIS OBJECTIVES

The objectives of my thesis were to:

1. Investigate the internal structure of the unstable slope at Randa using borehole radar techniques.
2. Develop interpretation strategies for integrating geological, geotechnical and geophysical data and construct a comprehensive 3-D model of important discontinuities.
3. Design, deploy and operate a microseismic monitoring system in the remote high alpine Randa area.
4. Process the recorded microseismic data and study microearthquakes associated with rockslide-related processes.

1.5 STRUCTURE OF THE THESIS

The four objectives listed above cover two major themes: structural investigations using borehole radar methods and microseismic monitoring of rockslide processes. In Chapter 2, I present information on the acquisition, processing and interpretation of the borehole radar data. I describe radar velocities and attenuation determined from single-hole, vertical radar profile (VRP) and crosshole data in terms of their ability to detect discontinuities. Special emphasis is placed on the integrated analysis of single-hole radar reflection sections with geotechnical and geological observations. I also demonstrate the use of VRP reflections for imaging steeply dipping fractures. Finally, an integrated structural model of the unstable volume is presented. Chapter 2 has been published in *Journal of Applied Geophysics*.

Acquisition and analysis of rockslide-related microearthquake data was the focus of Chapters 3 and 4. Technical details on the installation and operation of the combined microseismic-geotechnical monitoring system in the high-alpine environment are presented in Chapter 3. A short presentation of a covariance method for optimizing seismic networks is followed by descriptions of our deployment of 3-component geophones in deep and shallow holes. Installation and operation of a high-performance network in a high-alpine environment at reasonable cost is difficult. The experience I gained in running a microseismic network is outlined in this and the following chapter. Of necessity, some

details provided in Chapter 3 are also summarized in the anticipated publication of Chapter 4.

Chapter 4 is dedicated to the data analysis and interpretation of the recorded microearthquake signals. The huge volume of recorded data required the development of automatic algorithms to detect rockslide-related microseismicity. Hypocenters were determined using a probabilistic earthquake location scheme and a comprehensive 3-D velocity model. These results have been submitted for publication in the *Journal of Geophysical Research*.

Finally, Chapter 5 summarizes the results of my thesis and presents some ideas for future research on unstable mountain slopes.

2 Characterization of an unstable rock mass based on borehole logs and diverse borehole radar data

Thomas Spillmann, Hansruedi Maurer, Heike Willenberg, Keith F. Evans, Björn Heincke, and Alan G. Green

Journal of Applied Geophysics (2006)

ABSTRACT

Unstable rocky slopes are major hazards to the growing number of people that live and travel through mountainous regions. To construct effective barriers to falling rock, it is necessary to know the positions, dimensions and shapes of structures along which failure may occur. To investigate an unstable mountain slope distinguished by numerous open fracture zones, we have taken advantage of three moderately deep (51.0-120.8 m) boreholes to acquire geophysical logs and record single-hole radar, vertical radar profiling (VRP) and crosshole radar data. We observed spallation zones, displacements and borehole radar velocity and amplitude anomalies at 16 of the 46 discontinuities identified in the borehole optical televiewer images. The results of the VRP and crosshole experiments were disappointing at our study site; the source of only one VRP reflection was determined and the crosshole velocity and amplitude tomograms were remarkably featureless. In contrast, much useful structural information was provided by the single-hole radar experiments. Radar reflections were recorded from many surface and borehole fracture zones, demonstrating that the strong electrical property contrasts of these features extended some distance into the adjacent rock mass. The single-hole radar data suggested possible connections between 6 surface and 4 borehole fractures and led to the discovery of 5 additional near-surface fracture zones. Of particular importance, they supplied key details on the subsurface geometries and minimum subsurface lengths of 8 of the 10 previously known surface fracture zones and all of the newly discovered ones. The vast majority of surface fracture zones extended at least 40-60 m into the subsurface, demonstrating that their depth and surface dimensions are comparable. **Keywords:** fracture mapping; borehole geophysics; vertical radar profiling (VRP); crosshole radar; single-hole radar.

2.1 INTRODUCTION

Characterizing unstable rock slopes is an increasingly important task in mountainous regions worldwide. Significant expansions of population centres and transport routes in mountain valleys and exceptional climatic events related to global warming are amplifying the risk of catastrophic rock-slope failures (Bader and Kunz, 2000). To prevent loss of life and expensive infrastructure, appropriate mitigation measures in the form of early warning systems and protective barriers need to be implemented. For the construction of effective

barriers, knowledge of the locations, sizes and geometries of brittle discontinuities that are the sources of rock-slope instabilities is required.

Traditional approaches of investigating unstable mountain slopes include geological mapping, remote sensing, analyses of borehole logs and strain measurements at the surface and in boreholes (Cooke and Doornkamp, 1990; Erismann and Abele, 2001; Glade et al., 2005a). Since these approaches only provide limited information on the depth distribution of geological structures, a variety of surface-based geophysical techniques have recently been employed in landslide and rockfall studies (McCann and Forster, 1990; Hack, 2000). Various combinations of ground-penetrating radar (georadar), seismic reflection, seismic refraction, electrical resistivity, self-potential and electromagnetic methods have been used to determine the geometries of failure planes and volumes of unstable rock (Bruno and Marillier, 2000; Cummings, 2000; Havenith et al., 2000; Jongmans et al., 2000; Schmutz et al., 2000; Dussauge-Peisser et al., 2003). In areas of crystalline rock distinguished by ubiquitous fractures and faults, the high-resolution capabilities of surface-based georadar methods have proven to be particularly useful. For example, Grasmueck (1996) and Heincke et al. (2005) have shown how three-dimensional (3-D) georadar mapping is capable of providing high-resolution images of shallow- to moderate-dipping fractures and brittle faults.

Unfortunately, surface-based georadar methods have limited depth penetration in areas covered by fine-grained sediments and they are not well suited for the reflection imaging of steeply dipping features, primarily because of the unfavourable radiation patterns of typical antennas (Engheta et al., 1982). This latter point is a fundamental shortcoming, because it is the steeply dipping fractures and faults that define the instability of many rocky mountain slopes.

To address the issue of probing deeper and mapping steeply dipping brittle discontinuities within unstable rock masses, we have investigated the utility of the single-hole radar reflection, vertical radar profiling (VRP) and crosshole radar techniques at an unstable mountain site in southern Switzerland. Individual and combined interpretations of the different radar data sets were constrained by the results of surface geological mapping and information supplied by geophysical borehole logs.

After a brief introduction to the study site and borehole radar techniques, we describe our borehole logging and radar data acquisition and processing procedures. We then present

individual and combined interpretations of the processed data sets. Although all three types of borehole data furnish new information on subsurface features, the most important details are supplied by the single-hole radar reflection data. When constrained by complementary geological and geophysical information, these data yield high-resolution images of numerous steeply dipping fracture zones¹.

2.2 RANDA STUDY SITE

2.2.1 The 1991 Randa rockslides

The area of interest lies immediately above a scarp created by the largest mass movement of rock in recent Swiss history. During the Spring of 1991, two major rockslides resulted in the release of 30 million m³ of crystalline rock and the formation of a debris cone that obliterated holiday apartments and barns close to the village of Randa (Figure 2.1) and blocked the main transport route connecting the Rhône valley to the main tourist resort of Zermatt (Schindler et al., 1993; Sartori et al., 2003). The debris cone dammed the Matternispa River, causing flooding in upstream regions of the valley.

2.2.2 Continued instability

Various estimates based on geodetic measurements suggest that 2.7-9.2 million m³ of the remaining mountain slope have been moving 0.01-0.02 m/year southeastwards since the 1991 rockslides (Eberhardt et al., 2001; Jaboyedoff et al., 2004; Willenberg, 2004). Movements have been concentrated across major fracture zones with opening rates of 0.001-0.003 m/year (Willenberg, 2004). Many of these brittle discontinuities occur within or close to our study site (Figure 2.2). The continued instability of the mountain slope at Randa is a concern for the local population and responsible authorities.

2.2.3 Topographic relief, rock lithologies and fracture/fault distribution

The 140 x 143 m study site is located above the tree line at elevations of 2310-2400 m (Figure 2.1b). Although the topography is extremely rugged (i.e. >90 m of elevation variation over the site), there are several relatively flat terraces (Figures 2.2 and 2.3a).

¹ Since differential motion has occurred across many of the brittle discontinuities at our study site, they are faults. However, for simplicity we will refer to all brittle discontinuities as fracture zones in this contribution.

Information on the geology in this region is based on rock exposures, geophysical logs recorded in three boreholes and analyses of aerial photographs (Willenberg, 2004). The upper volume of the rock mass is dominated by heterogeneous gneisses with a strong 20-25° west-southwest-dipping foliation and three major fracture/fault systems F1-F3. The F1 system of fracture zones and ductile faults dips at shallow angles to the southwest, parallel to the strong bedrock foliation, whereas the other two systems comprise fracture zones that are mostly steeply dipping. On average, fractures of the F2 system strike between northeast-southwest and northwest-southeast with northwest to northeast dips (Z1 and Z6-Z10 in Figure 2.2b), respectively, whereas those of the F3 system strike approximately north-south with easterly dips (Z2- Z5 in Figure 2.2b). It is the steeply dipping fracture zones, some of which have openings of ten's of centimetres, that mostly influence the instability of the Randa mountain slope (Willenberg, 2004).

Photographs in Figures 2.3b-2.3d provide overviews of three open fracture zones. They range from jagged (Figure 2.3b) to planar (Figure 2.3c) and from closed (Figure 2.3c) to open (Figure 2.3d). At a number of locations, the fracture zones are buried beneath moraine and slope debris (maximum thickness of a few meters) covered by pasture and low-lying vegetation (Figure 2.3a). In these regions, their interpolated or extrapolated positions are based on lineaments identified on aerial photographs. Fracture zones observed in outcrop or interpolated/extrapolated beneath the cover material are referred to as surface fracture zones in this contribution.

2.2.4 Boreholes

In an attempt to improve our understanding of failure mechanisms in massive crystalline rock, the unstable mountain slope at Randa has been subjected to a variety of geological, geotechnical and geophysical investigations (Eberhardt et al., 2001; Willenberg et al., 2004; Willenberg, 2004; Heincke et al., 2005, 2006a, 2006b) Three moderately deep boreholes (SB120, SB50S and SB50N) were drilled through two of the flat terraces (Figure 2.2). Borehole SB120 was 120.8 m deep and vertical until about 40 m depth. Thereafter, it deviated to the east so that the hole bottom lay 18 m to the east of the wellhead. In contrast, the 52.5 and 51.0 m deep boreholes SB50S and SB50N were approximately vertical, with maximum horizontal deviations of ~2 m. In many of the figures and the following text

(unless stated otherwise), depths are given relative to a horizontal datum defined to be the top of borehole SB50N (2360.4 m above sea level).

2.3 BOREHOLE RADAR METHODS

2.3.1 Single-hole radar

To record single-hole full-waveform radar data, a fixed-offset transmitter-receiver antenna pair is pulled slowly up the length of a borehole. Such data supply information on the velocity and attenuation of radar waves in the vicinity of the borehole and on the nature of reflectors distributed about the borehole (Olsson et al., 1992; Wänstedt et al., 2000; Seol et al., 2004). The principle of the single-hole reflection method is similar to that of the surface-based georadar technique, except that reflectors may occur on all sides of the borehole recording line (Figure 2.4). Planar features intersected by a borehole will appear as V-shaped reflections on a single-hole radar section. Because there is a finite separation between the transmitter and receiver antennas, reflections near the intersections of the two arms of the V's will be hyperbolic shaped and no reflections will be recorded at the apices of the V's (i.e. along the axis of the recording system), where the antennas are located on opposite sides of the intersecting features.

Compared to surface-based georadar data, recordings in near-vertical boreholes are well suited for detecting steeply dipping features that are located more than a wavelength from the borehole, but not subhorizontal ones (Wänstedt et al., 2000). Due to the rotational symmetry of non-directional antennas operating in straight boreholes, the georadar data on their own do not provide sufficient information to determine unambiguously the locations of reflectors not intersected by the boreholes. To compensate for this limitation, constraints from other observations are necessary.

2.3.2 Vertical radar profiling (VRP)

Vertical radar profiling (VRP), the electromagnetic wave equivalent of the well known vertical seismic profiling (VSP) technique (Hardage, 1983; Dillon and Thomson, 1984), involves transmitting radar signals from multiple locations along lines at the surface to multiple locations in a borehole, or vice versa (Zhou and Sato, 2000; Tronicke and Knoll, 2005). As for the single-hole radar method, both the transmitted and reflected arrivals provide useful information and there may be ambiguities in reflector locations. The presence of a thick layer of electrically conductive sediments at the surface may preclude the use of

the VRP technique and low amplitude signals will be recorded for certain locations and orientations of the receiver antenna relative to the transmitter antenna (Tronicke and Knoll, 2005).

2.3.3 Crosshole radar

By transmitting radar signals from one borehole to another, radar velocities and attenuation between the two boreholes can be estimated (e.g. Olsson et al., 1992; Wänstedt et al., 2000; Washbourne et al., 2002). For optimum illumination of target structures, the lengths of the boreholes used for a crosshole survey should be substantially greater than the borehole separation. Nevertheless, it is generally difficult to map thin elongated structures that parallel the boreholes (Menke, 1984; Rector III and Washbourne, 1994).

2.4 DATA ACQUISITION

Drilling of boreholes at the Randa study site required a substantial logistical effort. Approximately 30 tons of equipment had to be transported by helicopter to the high mountain slope. Since the holes were percussion drilled, no cores were available. Steel casing was installed in the top 5 m of the three holes, which were dry except for the lower 10 m of SB120.

Table 2.1 provides an overview of parameters used for the geophysical logging and radar surveying; note, that depth information in this table is relative to the top of the respective boreholes. Lithological and structural information were determined from optical televiewer logs (column a in Figures 2.5-2.7) and caliper logs (column f in Figures 2.5-2.7). To derive horizontal displacements across active fracture zones, inclinometer casings grouted into the boreholes after completion of the geophysical measurements were resurveyed twice per year using a 0.61 m long inclinometer probe (column g in Figures 2.5-2.7).

A MALA system with 100 MHz borehole and surface antennas was used to acquire all radar data. Single-hole full-waveform data were recorded in all three holes at 0.1 or 0.2 m increments using transmitter and receiver antennas separated by 2.75 m. Three VRP's were collected along two surface lines. For one VRP, antennas were deployed in SB120 and along a roughly north-south line and for the other VRP's, antennas were deployed in SB50S and SB50N and along a line connecting the two boreholes (Figure 2.2b). The antenna increment was 0.5 m and the surface antenna was oriented perpendicular to the surface lines (Tronicke

and Knoll, 2005). Crosshole radar signals with sufficient signal-to-noise ratios could only be transmitted between SB50S and SB50N. Using an antenna increment of 0.5 m, signals from 93 transmitter positions were registered at 90 receiver positions.

Table 2.1: Acquisition parameters used for borehole logging and georadar measurements at the Randa study site. Depths in this table are relative to the top of the respective boreholes.

	SB120	SB50S	SB50N
Borehole length	120.8 m	52.5 m	51.0 m
<i>Optical televiewer</i>			
Depth range	5.0 - 112.3 m	5.0 - 50.1 m	5.0 - 49.9 m
<i>Four-arm caliper</i>			
Depth range	5.0 - 120.0 m	5.0 - 52.0 m	5.0 - 50.6 m
Increment	0.01 m	0.01 m	0.01 m
<i>Inclinometer</i>			
Midpoint depth range	5.0 - 113.3 m	5.0 - 43.4 m	5.0 - 35.2 m
Increment	0.61 m	0.61 m	0.61 m
<i>Vertical radar profile (VRP)</i>			
Profile azimuth	6°	328°	148°
Surface offset range	5.0 - 28.5 m	0.5 - 30.5 m	0.0 - 24.0 m
Antenna depth range	5.2 - 50.7 m	5.2 - 51.2 m	5.2 - 49.7 m
Antenna increment	0.5 m	0.5 m	0.5 m
<i>Single-hole radar</i>			
Midpoint depth range	5.5 - 118.0 m	5.0 - 50.2	5.4 - 48.8 m
Increment	0.2 m	0.1 m	0.2 m
<i>Crosshole radar</i>			
		transmitter	receiver
Antenna depth range		5.2 - 51.2 m	5.2 - 49.7 m
Increment		0.5 m	0.5 m
<i>Sonic</i>			
Midpoint depth range		5.0 - 38.1 m	5.0 - 32.6 m
Increment		0.05 m	0.05 m

Depths in this table are relative to the top of the respective boreholes.

Shortly after the radar surveys, the boreholes were cased with PVC tubes. This allowed SB50S and SB50N to be filled with water, thus facilitating the sonic logging.

Installation of induction rings on the SB120 casing for vertical extension measurements resulted in a diameter that was too small to allow the sonic sonde to be used along the length of this hole. The SB50S and SB50N sonic logs were acquired using a borehole-compensated tool with a source frequency of 23 kHz and receivers located 0.71 and 1.11m from the source. Full waveforms were recorded every 0.05 m.

2.5 RADAR AND SONIC LOG DATA PROCESSING

2.5.1 Single-hole radar

Based on their traveltimes and numerical modelling, the first detected arrivals in the single-hole radar data represent waves that travel through the rock (the amplitudes of the airwaves travelling along the borehole are too small to be detected). Correlation of these arrivals provide time lags that are converted to velocities representing the volumes of rock within 0.5-1.0 m of the boreholes (column j in Figures 2.5-2.7). We estimate that the correlation process results in traveltime uncertainties of approximately ± 0.5 ns, which translates to a velocity uncertainty of $\pm 2.5\%$ or ± 0.003 m/ns for the Randa data; based on the results of the three types of radar survey, a representative velocity for the Randa rock mass is taken to be 0.120 m/ns. The absolute value of the first arriving pulses, be they negative or positive, provide the corresponding amplitude information (column k in Figures 2.5-2.7).

To enhance the coherency of reflections, a relatively standard processing scheme was applied to the single-hole radar data. After aligning the first arriving pulses to compensate for near-borehole velocity heterogeneities, the data were amplitude scaled (i.e. trace equalisation using a narrow window centred on the first arrivals followed by multiplication of each trace value by t^2 , where t is time), bandpass filtered (30-60 - 200-300 MHz) and FX deconvolved (Figures 2.8a, 2.8d and 2.8g). To aid the interpretation, automatic-gain controlled (150 ns window) versions of the data were phase-shift migrated (Figures 2.8c, 2.8f and 2.8i). Conventional migration is a valid processing step for the nearly vertical boreholes SB50S and SB50N and for the upper vertical part (~40 m) of SB120. It will produce only approximate or erroneous results for the lower curved part.

2.5.2 Vertical radar profiling (VRP)

Georadar velocities in the vicinity of the boreholes were derived from the VRP data. From the SB120, SB50S and SB50N data sets, we were able to pick 2439, 1445 and 1016 first arrival traveltimes with a picking uncertainty of ± 2.0 ns. Inversions of these traveltimes

provided velocity-depth models for the planes containing the boreholes and the surface recording lines (column i in Figures 2.5-2.7).

Processing of the VRP reflection data included amplitude scaling (as for the single-hole radar data), bandpass filtering (30-60 - 150-230 MHz) and median filtering (3 samples, 11 traces) to minimize the effects of the direct arrivals. Examples of the only extensive reflections identified as originating from a common boundary at the Randa study site are outlined by red lines on the SB120 transmitter gathers displayed in Figure 2.9. Numerous other reflections and diffractions in the Randa VRP data were either too limited in extent or observed on too few transmitter and receiver gathers to be located (see below and Appendix 2.9). For the SB120 VRP data, transmitter positions extended to a maximum distance of 28.5 m and receivers were lowered to a maximum depth of 50.5 m relative to the top of the borehole (Table 2.1). From these data, a total of 1608 reflection times (event highlighted in Figure 2.9) could be picked with an average picking uncertainty of ± 5 ns.

Techniques developed for vertical seismic profiling data are intended primarily for mapping shallow- to moderate-dipping sedimentary units (Hardage, 1983; Dillon and Thomson, 1984). Since a preliminary analysis suggested that the identified reflections in Figure 2.9 originated from a steeply dipping planar structure, it was necessary to develop an alternative approach (Figure 2.10 and Appendix 2.9.A). Given sources \mathbf{s}_i ($i = 1 \dots \text{number of source positions}$) along a surface profile and receivers \mathbf{r}_j ($j = 1 \dots \text{number of receiver positions}$) within a borehole, the goal is to estimate the position of planar feature P that is the origin of reflections with observed traveltimes \mathbf{t}_{ij} . The position of P can be represented by a vector \mathbf{p}_n that originates from an arbitrary origin and is perpendicular to P . The parameters defining \mathbf{p}_n can be estimated using a brute force grid search approach, in which a trial vector \mathbf{p}_n^{trial} is systematically varied in an attempt to determine the minimum root-mean square (RMS) difference between the observed reflection times and those predicted by \mathbf{p}_n^{trial} . Using a homogeneous velocity model, the predicted reflection times \mathbf{t}_{ij}^{trial} can be calculated rapidly using the mirror source $\bar{\mathbf{s}}_i$:

$$\mathbf{t}_{ij}^{trial} = \frac{|\bar{\mathbf{s}}_i - \mathbf{r}_j|}{v}, \quad (2.1)$$

where v is the georadar propagation velocity and $|\bar{\mathbf{s}}_i - \mathbf{r}_j|$ is the distance between $\bar{\mathbf{s}}_i$ and \mathbf{r}_j (see Figure 2.10). The results of applying our grid search algorithm to four synthetic reflectors with different orientations are shown in Appendix 2.9.A. Given a suite of reflection traveltimes t_{ij}^{trial} , these tests demonstrate that there are generally two equally plausible solutions for \mathbf{p}_n .

Application of the grid search algorithm to the SB120 VRP data set (Appendix 2.9.B) demonstrates that two planar reflectors with the following parameters can explain the picked reflection traveltimes with RMS differences of 3-4 ns: (1) surface distance to the top of SB120 = 23.6 ± 1.0 m, dip azimuth = $86 \pm 8^\circ$, dip = $82 \pm 4^\circ$, (2) surface distance to the top of SB120 = 22.0 ± 1.0 m, dip azimuth = $284 \pm 8^\circ$, dip = $88 \pm 4^\circ$. The parameters of reflecting plane (1) correspond closely to those of surface fracture zone Z3 (Figure 2.2b): surface distance to the top of SB120 = 22 m, dip azimuth = 93° , dip = 80° . No surface features correlate with the reflecting plane (2). Consequently, our preferred solution is reflecting plane (1).

2.5.3 Crosshole radar

From the 93 x 90 crosshole radar traces acquired from boreholes SB50S and SB50N, we were able to measure the traveltimes and amplitudes of 7066 first-arrival pulses. The average picking uncertainty of the traveltimes was ~ 2 ns. A non-linear tomographic scheme was employed for the inversion of the traveltimes (Musil et al., 2006). It included a finite-difference Eikonal solver for computing traveltimes and wave paths (Podvin and Lecomte, 1991) and a fat-ray method that accounts for the finite bandwidth of the data in calculating the sensitivities (Husen and Kissling, 2001). The zero times of the transmitted signals were refined during the inversion process using the procedure outlined by Maurer (1996).

After 10 iterations of the inversion scheme that was controlled 6% by the damping, 31% by the smoothing and 63% by the data, the velocity tomogram shown in Figure 2.11a was obtained. The RMS difference between the observed traveltimes and those predicted by the final model was 0.7 ns, well below the estimated picking accuracy. Standard ray-based inversion of the amplitude data (Holliger et al., 2001; Musil et al., 2006) was performed using the radiation pattern of an infinitesimal vertical electric dipole and the ray paths obtained from the traveltime inversion. The resultant attenuation tomogram is presented in Figure 2.11b.

2.5.4 Sonic logs

Arrival times of the P-wave onsets were picked manually from the full-waveform sonic data. Uncertainties in the traveltimes differences between the two receivers were roughly 4 μ s, which translated to a velocity uncertainty of approximately $\pm 4\%$ or ± 0.2 km/s for the Randa data. The resulting velocity-depth functions were smoothed using a three-point median filter (column h in Figures 2.6 and 2.7).

2.6 RESULTS AND INTERPRETATION

Considering the limited depth information available from surface observations, the local nature of the borehole logs and the ambiguities associated with the various georadar data sets, an integrated interpretation of all relevant details is necessary to estimate the depth distribution of fracture zones at the Randa study site. Even though fracture zones are observed at a large number of outcrops, substantial portions of these features are buried beneath thin layers of surficial material (Figure 2.3a). As a consequence, our knowledge of the continuity and size of fracture zones shown in Figure 2.2 is incomplete and other major brittle discontinuities may be hidden beneath the surficial cover. After describing the essential characteristics of the borehole logs, crosshole radar tomograms, VRP velocity-depth profiles and single-hole radar reflection sections, we use this information to determine the minimum depth extents of many fracture zones observed at the surface and within the boreholes and reveal the existence of major brittle discontinuities that have not been previously identified.

2.6.1 Borehole logs

Optical televiewer logs supply detailed information on the fractures intersected by the three boreholes. Discontinuities that have thicknesses of ≥ 2 mm and are either open or contain phyllonitic infill are highlighted by red lines in column a of Figures 2.5-2.7. Repeated inclinometer measurements demonstrate that many of these are moving (column g in Figures 2.5-2.7). Nevertheless, except for two or three examples, it is not obvious from the televiewer logs which of these fractures are major features that connect to the surface-mapped fracture zones (Figures 2.2 and 2.3) or are examples of equally important hidden discontinuities. Furthermore, the azimuths and dips of discontinuities inferred from their expressions at the borehole walls may not be representative of their large-scale orientations.

The cross-sectional areas of the boreholes recorded in the caliper logs are significantly larger than those of the drill bits, with a tendency to decrease slightly with depth in SB120 and SB50 (column f in Figures 2.5-2.6). These facets are consequences of the percussive drilling method used. There are also numerous anomalous increases and decreases in hole size, many of which correlate with the fracture zones. Hole enlargements can be explained by spalling of weak material around the discontinuities. Zones of spallation are particularly evident at the active fracture zones A2-A3, A16 and A17-A18 in SB120, S2-8 in SB50S and N1-2 and N7-8 in SB50N. At several locations in all boreholes, the cross-sectional areas are smaller than those of the drill bits. We do not have an explanation for these phenomena.

Our sonic log data are highly variable, with P-wave velocity estimates varying between 3.6 and 5.1 km/s (column h in Figures 2.6-2.7). Intact rock at 30-40 depth in SB50S has an average velocity of ~ 4.7 km/s and that throughout much of SB50N has a slightly lower average velocity of ~ 4.5 km/s. Large deviations from these values occur near most intersected fractures in SB50S, but only near N1 and N2 in SB50N.

The general trends in the single-hole radar velocities are not significant; decreasing velocities in the lower parts of SB120 and SB50S (column j in Figures 2.5-2.6) correlate with the decreasing borehole cross-sectional areas (column f in Figures 2.5-2.6). Notable deviations from the median 0.120 m/ns radar velocity that exceed the estimated inaccuracy of ± 0.003 m/ns are recorded near discontinuities A4-A7 and A16 in SB120, S1-S7 and S10 in SB50S and N1-N2 and N7-N9 in SB50N. Most of these velocity deviations are accompanied by amplitude anomalies (column k in Figures 2.5-2.7).

2.6.2 Crosshole tomogram and VRP velocity-depth models

Radar velocities and attenuations are remarkably uniform in the SB50S-SB50N tomograms of Figure 2.11. It is for this reason that we represent them in terms of only three ranges of values. More than 80% of the velocities lie between 0.118 and 0.122 m/ns and all values are between 0.114 and 0.126 m/ns (i.e. $\pm 5\%$ variation about the median value of 0.120 m/ns). The trends of the VRP velocity-depth models (column i in Figures 2.6 and 2.7) follow closely the velocities along the edges of the tomograms, with small positive velocity anomalies near SB50S at depths of 11-17 m and 30-38 m and near SB50N at 19-20 m.

Attenuations between SB50S and SB50N are mostly between 0.00025 and 0.00035 m^{-1} , with a single noteworthy anomalous zone of 0.00040 m^{-1} near SB50N at 18-21 m depth.

Velocity and attenuation anomalies that intersect SB50N near 20 m depth coincide with spallation zones and displacements at the N1 and N2 discontinuities and associated prominent sonic velocity and single-hole radar velocity and amplitude anomalies. The slight increase in velocity at 11-17 m depth near SB50S occurs close to air-filled fracture zone S1 and the low velocities and coincident high attenuations at 18-19 depth may be explained by the presence of clays and silts in fracture zone S2. There are no explanations from the televiewer log for the small decreases and increases in velocity at other locations near SB50S. There is a hint in the attenuation tomogram that the two shallow dipping discontinuities N1 and S1 are connected. Regardless, N1 is the only shallow dipping fracture zone that can be shown to be laterally extensive on the basis of any radar data.

2.6.3 Single-hole and VRP reflection sections

All three single-hole sections (Figures 2.8a, 2.8d and 2.8g) contain reflections that extend to 500 ns traveltimes, indicating the presence of numerous moderately to steeply dipping features within ~30 m of the boreholes. From these sections, we can only define the inclinations of reflectors relative to the boreholes and the depths to those reflectors cut by the boreholes. To locate all reflectors and determine their azimuths requires additional information.

Given that the lithological contacts and foliations of the gneissic rocks are mostly shallow dipping, it is unlikely that geological variations or rock fabrics are the source of reflections in Figure 2.8. For the same reason, the shallow-dipping F1 fracture zones and ductile faults can also be eliminated from consideration. From the geological information, it is highly likely that the moderately to steeply dipping F2 and F3 fracture zones are the source of strong reflections. Many are open air-filled structures that have large impedance contrasts relative to the adjacent intact rock. Although the openings of some parts of the F2 and F3 discontinuities may be quite narrow relative to the ~1 m dominant wavelength of our 100 MHz georadar signal, georadar surveying at other locations has shown that damage zones around discontinuities in gneissic rock may be sufficiently wide to generate strong reflections (e.g. Grasmueck, 1996).

Our procedure for interpreting the single-hole radar reflections in terms of surface fracture zones F2 and F3 is relatively simple. For a given borehole data set, we begin by

linearly extrapolating the significant radar reflections updip until they intersect the horizontal plane containing the borehole collar. Considering the rotational ambiguity of the acquisition geometry, possible intersecting points for each radar reflection describe a circle centred on the borehole collar. We also linearly project the locations of nearby fracture zones on to the same horizontal plane. If the radius of a radar reflection circle is approximately tangent to the projected trace of a fracture zone and the dips of the two features are comparable, we assume that the reflection originates from the depth extension of that fracture zone.

Our interpretations of the various radar reflection zones are presented in Figures 2.8b, 2.8e and 2.8h. Dips and extrapolated positions of the surface fracture zones at the level of the borehole collars are shown along the tops of these figures. They are plotted to the left or right of the borehole axes according to the reflection zones with which they are correlated. Reflection zones that can be related to borehole or surface discontinuities are marked red in Figures 2.8b, 2.8e and 2.8h (also reproduced in column 1 of Figures 2.5-2.7). Other important reflection zones are marked blue. In Figure 2.12, we display the projected surface locations of all significant radar reflectors together with their dips and minimum lengths.

2.6.4 Fracture zones near SB120

No radar reflections are associated with Z4 and Z5, the two surface fracture zones closest to the collar of SB120 (Figures 2.8a-2.8c and 2.12). Simple linear extrapolation demonstrates that Z4, which is only ~2 m from the collar, and the actively moving borehole fracture A1 are the same discontinuity (note the similarity of their dip azimuths and dips in columns b and c of Figure 2.5). Although the discrete reflection X1 projects upwards to the general vicinity of the borehole collar, its very steep dip and lack of projected intersection with the borehole are not compatible with it being a reflection from the Z4-A1 fracture zone. In Figure 2.12, we place the surface projection of X1 to the east of SB120. This speculative interpretation assumes that X1 is caused by an F3-type fracture zone that parallels the Z4-A1 and Z5 fracture zones.

Surface fracture zone Z3 is the probable source of (i) a broad band of steeply dipping strong reflections that can be traced to at least 50m depth on the single-hole radar section (Figure 2.8a-2.8c) and (ii) the continuous reflection recorded on the VRP data set (Figure 2.9 and Appendix 2.9.B). The dips and locations of these reflections are consistent with surface observations (Figure 2.12). A much thinner band of reflections projects from ~70 m depth to

near the expected position of surface fracture zone Z2. A rare steeply dipping event recorded on surface 3-D georadar data (Figure 2.13; for the location of the cross-section in Figure 2.13 see Figure 2.2b) supports our assertion that Z2 is a radar reflector at this location.

Of the twenty-six fracture zones identified along the length of SB120 in Figure 2.5, only A10, A13, A16 and A26 generate moderate to strong radar reflections. According to Figures 2.8a-2.8c, they dip $53\text{-}67^\circ$ and can be followed over lengths of at least 20-40 m. The $320\text{-}350^\circ$ azimuths indicated by the televiewer logs suggest that they all belong to the F2 fracture system and the repeat inclinometer measurements demonstrate that they are all moving. Only A16 has an associated spallation zone and a significant single-borehole radar velocity anomaly. None of these reflection zones can be traced beyond a sequence of prominent steeply dipping reflections starting at ~ 300 ns traveltime. Nevertheless, it is noteworthy that the A13 and A16 fracture zones and reflections project southwestwards to where Z7 and Z6 are observed at the surface. Furthermore, the orientations of A13 and A16 are similar to those of Z7 and Z6, respectively (see columns b and c in Figure 2.5). If this correlation is correct, then the Z7-A13 and Z6-A16 fracture zones extend ~ 60 and ~ 85 m from their borehole intersections to the surface, respectively.

We cannot correlate any surface feature with the X2 band of radar reflections, despite its proximity to the surface (Figures 2.8a-2.8c). Considering its strength, continuity, length (16 m) and steep dip (75°), we infer that X2 is generated at a fracture zone. Although it is shown as an F3-type fracture zone that parallels the neighbouring A1-Z4 and Z5 fracture zones in Figure 2.12, it could also be an F2-type fracture zone that lies to the north of the borehole.

2.6.5 Fracture zones near SB50S

Surface fracture zones Z4 and Z8 and two linear radar reflections with slightly different dips project to the general vicinity of the fracture zone S2 in borehole SB50S (Figures 2.8d-2.8f). Both surface fracture zones pass to within 5 m of the borehole collar (Figure 2.12). The dips of the surface and borehole fracture zones are similar to those of the radar reflections (columns b, c and d in Figure 2.6) and although the dip azimuths of the fractures differ somewhat, S2 is a complex zone with substantial spalling (column f in Figure 2.6) that could indeed represent the effects of intersecting fractures with different orientations. Our interpretation implies that the Z4-S2 and Z8-S2 fracture zones have minimum subsurface lengths of ~ 40 and ~ 55 m, respectively.

Reflections from the large open surface fracture zone Z9 that bisects borehole SB50S and SB50N (Figure 2.12) are best observed on the migrated section of Figure 2.8f. They can be traced dipping $\sim 70^\circ$ over a length of ~ 20 m. Even though the equally important surface fracture zone Z1 is not the source of near-surface reflections, a near-vertical reflection at 27-38 m depth could originate from its depth extension.

A rather weak radar reflection may be associated with borehole fracture zone S8 (Figure 2.8e), which has a localized spallation zone and is moving. It is noteworthy that there are no clear reflections from the S3-S5, S7, S9 and S10 fracture zones, many of which have caliper, displacement and/or single-hole radar velocity and amplitude anomalies.

The three prominent steeply dipping ($65-85^\circ$) reflection zones X3-X5 (Figure 2.8d-2.8f) do not correlate with mapped surface discontinuities, despite their 40-60 m lengths and proximity to the surface. Considering the geology near SB50S, X3 could originate from a buried fracture zone that either lies to the east of the borehole and parallels Z4 (as shown in Figure 2.12) or lies to the north and parallels Z8. A southeast origin for X4 (i.e. a fracture zone parallel to and southeast of Z1) seems unlikely, because outcrop is extensive at that location. A possible explanation for X4 is provided in the next section. A buried F3-type fracture zone located a few metres to the east of surface fracture zone Z2 could explain the deep-penetrating X5 band of reflections (Figure 2.12).

2.6.6 Fracture zones near SB50N

Four surface fracture zones Z2, Z4, Z9 and Z10 lie within 10-20 m of the SB50N collar. Interference of reflections from these structures creates a complicated reflection pattern between 100 and 300 ns on the SB50N radar sections (Figures 2.8g-2.8h). Fracture zone Z10 is the probable source of the steeply dipping (80°) reflections that can be followed for >50 m from near the surface to the base of the radar section. A broad $\sim 70^\circ$ dipping band of reflections that could originate from Z2 and/or Z9 projects down towards reflections from the region of borehole fracture N7, where large caliper and single-hole velocity and amplitude anomalies are recorded. The dips of the reflection band and the surface and borehole fracture zones are similar, but the dip azimuths of the fracture zones differ (columns b, c and d in Figure 2.7). Surface fracture Z4 correlates well with a rather distinct 70° dipping reflection fabric that cross-cuts the interpreted Z2, Z9 and Z10 reflection zones

over a length of ~14 m, whereas Z8 may be related to some curvilinear events that approach the surface.

Borehole discontinuities N1 and N2 generate substantial caliper, displacement, sonic velocity, radar velocity and radar amplitude anomalies and are the primary active discontinuities intersected by the borehole (columns f-k in Figure 2.7). We have already noted that the shallow-dipping N1 discontinuity is also the source of velocity and attenuation anomalies on the tomograms of Figure 2.11. By comparison, the steeply dipping N2 fracture zone produces strong reflections that dip 80° over a distance of ~25 m on the single-hole radar section of Figures 2.8g-2.8i.

Finally, we note that reflection zones X4 and X6 on the SB50S and SB50N radar sections (Figures 2.8d-2.8i), respectively, could originate from the same fracture zone. Their dips, distances from the boreholes and similarity of reflection character are consistent with a common reflector that coincides with the surface location of Z9. If this interpretation is correct, then Z9 is actually the junction of two distinct fracture zones. The first fracture zone is open at the surface and dips steeply to the northwest (Z9 in Figures 2.8d-2.8i). It is a member of the F2 system of fractures. The second fracture zone, which is equally or more important in terms of the strength and continuity of radar reflections, dips very steeply to the southeast.

2.7 DISCUSSION AND CONCLUSIONS

Of the three georadar methods tested, the VRP and crosshole techniques provided only limited useful information at the Randa study site. Velocities determined from the VRP data had disappointingly low resolutions, and only a single interpretable reflection was observed on the VRP source and receiver gathers (Figure 2.9). The crosshole tomograms provided valuable median radar velocity and attenuation estimates, but they were surprisingly featureless (Figure 2.11). Only three low contrast anomalies could be related to discontinuities that intersected the boreholes. The most significant of these anomalies suggested that the shallow-dipping N1 discontinuity extended >20 m from SB50N. The absence of velocity and/or attenuation anomalies in the region of the steeply dipping surface fracture zone Z9 (and possibly also X4/X6), which crossed the tomographic plane, was likely due to the insensitivity of the crosshole radar method to narrow borehole-parallel structures.

Single-hole radar reflections appear to have been generated at surface fracture zones Z2-Z4 and Z6-Z10 and at borehole fracture zones A10, A13, A16, A26, S2, S8, N2 and N7. Based on our interpretations of the radar data and the fracture zone orientations measured at the surface and within the boreholes, we proposed the following connections: Z2-N7, Z4-S2, Z6-A16, Z7-A13, Z8-S2 and Z9-N7. In addition, simple linear extrapolation demonstrated that surface fracture zone Z4 and nearby borehole fracture zone A1 were the same discontinuity.

We note that the minimum depth dimensions of nearly all fracture zones are large fractions of their mapped lateral dimensions. Consequently, we infer that the majority of important surface fracture zones extend deep into the mountain slope.

Since many borehole fracture zones were not the source of strong borehole geophysical anomalies (Figures 2.5-2.7) and, as such, were likely to be local features, the lack of associated radar reflections was not surprising. However, there were no obvious explanations for the absence of radar reflections from borehole fracture zones A4, A5, A7 and S4-S7, all of which had caliper, displacement, radar velocity and radar amplitude anomalies, and from surface fracture zones Z1 and Z5. In contrast, there was no surface or borehole evidence for the origins of the six prominent reflection bands X1-X6 (Figure 2.8). We suggested that they were generated at five unmapped fracture zones, four of which could be traced to within 5 m of the surface.

A 3-D model that shows the approximate sizes and geometries of many fracture zones observed at the surface, in the boreholes and in the interpreted georadar data is presented in Figure 2.14. In constructing this model, the depth limits estimated from the VRP and single-hole radar data are assumed to apply to the entire lengths of the fracture zones. Except for the newly discovered X4/X6 structure, all fracture zones can be assigned to one of the F1-F3 systems of fractures. If X4 on the SB50S radar section is indeed the same as X6 on the SB50N radar section, then this would be the first example of a slightly southeasterly dipping fracture zone.

Figure 2.14 suggests that the investigated rock volume is divided by major fracture zones into a number of discrete blocks of varying sizes. From our new data, it is not possible to delineate a master fault that could control any future rockslide. However, we have demonstrated that Z2 and Z10, the two furthest investigated fracture zones from the 1991

rock scarp, are major structures that extend at least 50m beneath the surface. Consequently, they likely define the minimum northwesterly extent of potentially unstable rock (Figure 2.2a).

2.8 ACKNOWLEDGEMENTS

We thank Simon Loew and Erik Eberhardt for their cooperation in this interdisciplinary project and appreciate very helpful suggestions provided by Heinrich Horstmeyer. Comments by two journal reviewers are greatly appreciated. The optical televiewer logs and the inclinometer surveys were performed by Terratec GmbH (Germany) and Stump Foratec AG (Switzerland), respectively. We are grateful to Jean Daniel-Rouiller from CREALP (Research Centre on Alpine Environment, Switzerland) for providing the digital terrain model and geodetic survey data, and to the local authorities of Randa for providing logistical support. This project was funded by the Swiss National Science Foundation (Project No. 2000-066877).

2.9 APPENDIX

2.9.A Synthetic examples

To illustrate the benefits and limitations of our grid search technique for locating planar boundaries that are the source of reflections in VRP data, four synthetic examples are presented in Figure 2.A1. A boundary is uniquely defined by a vector $\mathbf{p}_n = [l, \varphi, \theta]$ that is normal to the plane, where l , φ and θ are spherical coordinates relative to an arbitrary origin. The first column of Figure 2.A1 shows the models and numbers of reflections per square metre for the fixed transmitter-receiver geometry identified by the white lines. The second to fourth columns show slices extracted from the volume of root-mean square (RMS) differences between true and predicted reflection traveltimes based on all possible trial planar boundaries. They show RMS differences for varying φ and θ with l fixed to the correct value (second column), varying l and θ with φ fixed to the correct value (third column), and varying l and φ with θ fixed to the correct value (fourth column). The minima of the RMS differences are identified by small white dots. Blank regions represent areas of the RMS slices for which there are no reflection points.

For the vertical plane defined by the normal vector $\mathbf{p}_n = [10, 0, 0]$, all reflection points occur along a vertical strip (Figure 2.A1a). The RMS slices in the top row indicate

that the parameters defining the normal vector are well resolved, with the only potential for a minor trade-off being between l and θ (Figure 2.A1i). There is a similar potential for a minor trade-off between l and θ for a vertical plane that parallels the acquisition plane containing the sources and receivers (Figures 2.A1b and 2.A1j). For this plane, defined by the normal vector $\mathbf{p}_n = [10, 90, 0]$, there are two equivalent solutions at $\varphi = 90$ and 270° (Figures 2.A1f and 2.A1n). With the exception of vertical planes perpendicular to the acquisition plane (e.g. Figure 2.A1a), there always exists at least two solutions, one to the “left” and one to the “right” of the data acquisition plane.

The horizontal plane in Figure 2.A1c mimics a common situation in VSP studies (Hardage, 1983; Dillon and Thomson, 1984). Since the normal vector $\mathbf{p}_n = [10, 0, 90]$ to the plane is vertical, φ is not relevant, but correct values of l and θ are reconstructed accurately (Figure 2.A1k). Finally, the RMS slices in the bottom row are the results for an arbitrary plane defined by the normal vector $\mathbf{p}_n = [10, 46, -14]$. These results, including the trade-offs and ambiguities, are similar to those shown for the vertical planes in the upper two rows.

Information contained in Figure 2.A1 demonstrates that it is possible to retrieve the locations and orientations of most reflecting planes from high quality VRP data. Reasonable estimates of the uncertainties of these parameters can be determined from the isosurface of RMS differences corresponding to the picking accuracy of the reflection times. The left-right ambiguity is best resolved by considering other geological and/or geophysical information.

2.9.B Field examples

The results of applying the grid search algorithm to the reflection traveltimes picked from SB120 VRP data are shown in Figure 2.B1. We use a constant velocity of 0.12 m/ns and set the origin of the coordinate system to the centre of the source-receiver array to provide trial vectors that uniformly sample the volume of interest. To display the minimum RMS values, we choose RMS slices (Figures 2.B1b-d) defined by l , φ and θ values that are equal to our preferred solution (Figures 2.B1a). The two well determined minima in Figures 2.B1b-d correspond to normal vectors $\mathbf{p}_n^{best-1} = [20 \text{ m}, 100^\circ, -8^\circ]$ and $\mathbf{p}_n^{best-2} = [23 \text{ m}, 262^\circ, 2^\circ]$. The RMS differences at both minima are in the 3-4 ns range, well below the estimated 5 ns picking uncertainty of the reflection traveltimes. To determine plausible uncertainties for each parameter, we rescale the RMS colour scale in Figures 2.B1e-g to lie between 0 and 20 ns, such that all values >20 ns are uniformly dark blue. This

figure demonstrates that a 5 ns uncertainty in reflection traveltime picking corresponds approximately to parameter uncertainties of $\Delta l = \pm 2$ m, $\Delta\varphi = \pm 16^\circ$ and $\Delta\theta = \pm 7^\circ$.

The asymmetry of the two solutions in Figure 2.B1 is a result of the borehole curvature. Predicted traveltimes based on these solutions are shown by the blue lines superimposed on the observed data in Figure 2.9. They match well the traveltimes of the identified reflections. The projected surface location of the plane defined by \mathbf{p}_n^{best-1} would be 23.6 ± 1.0 m from SB120 with a $86 \pm 8^\circ$ dip azimuth and $82 \pm 4^\circ$ dip, whereas that defined by \mathbf{p}_n^{best-2} would occur at a distance of 22.0 ± 1.0 m from the borehole with a $284 \pm 8^\circ$ dip azimuth and $88 \pm 4^\circ$ dip.

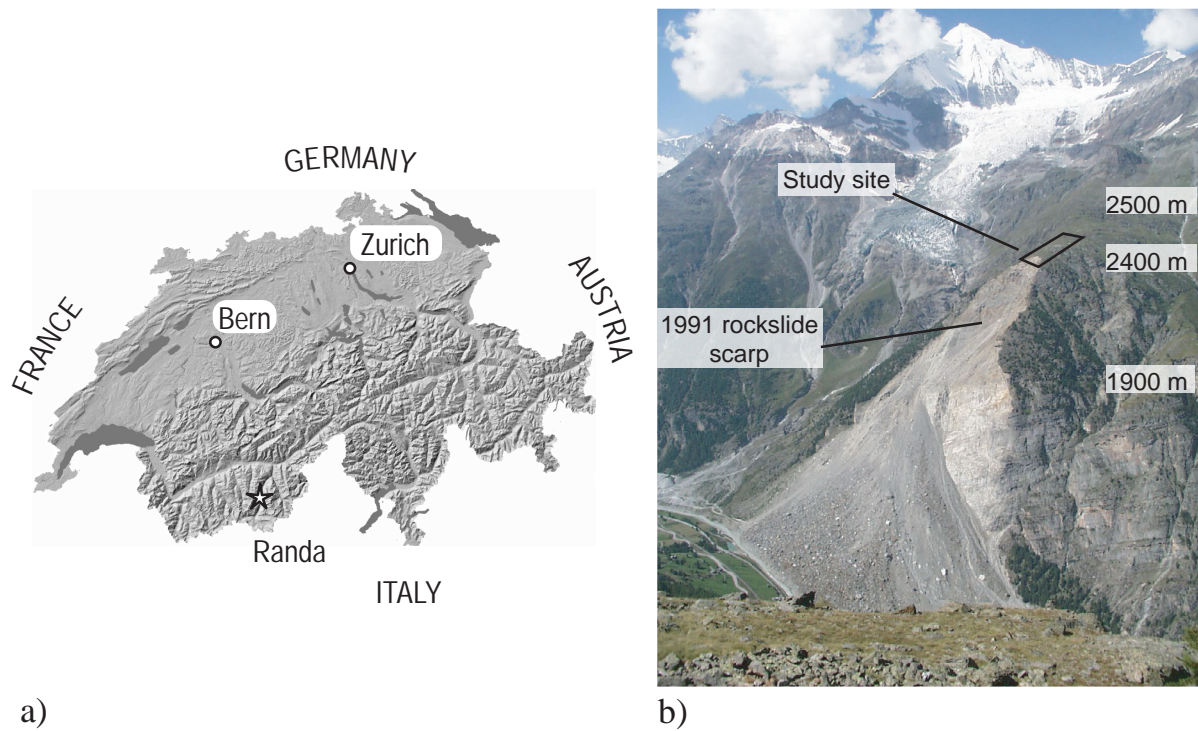


Figure 2.1: (a) Randa rockslide location (star) in the Matter Valley of southern Switzerland. (b) Photograph of the Randa rockslide and study site. (Photo: H. Willenberg)

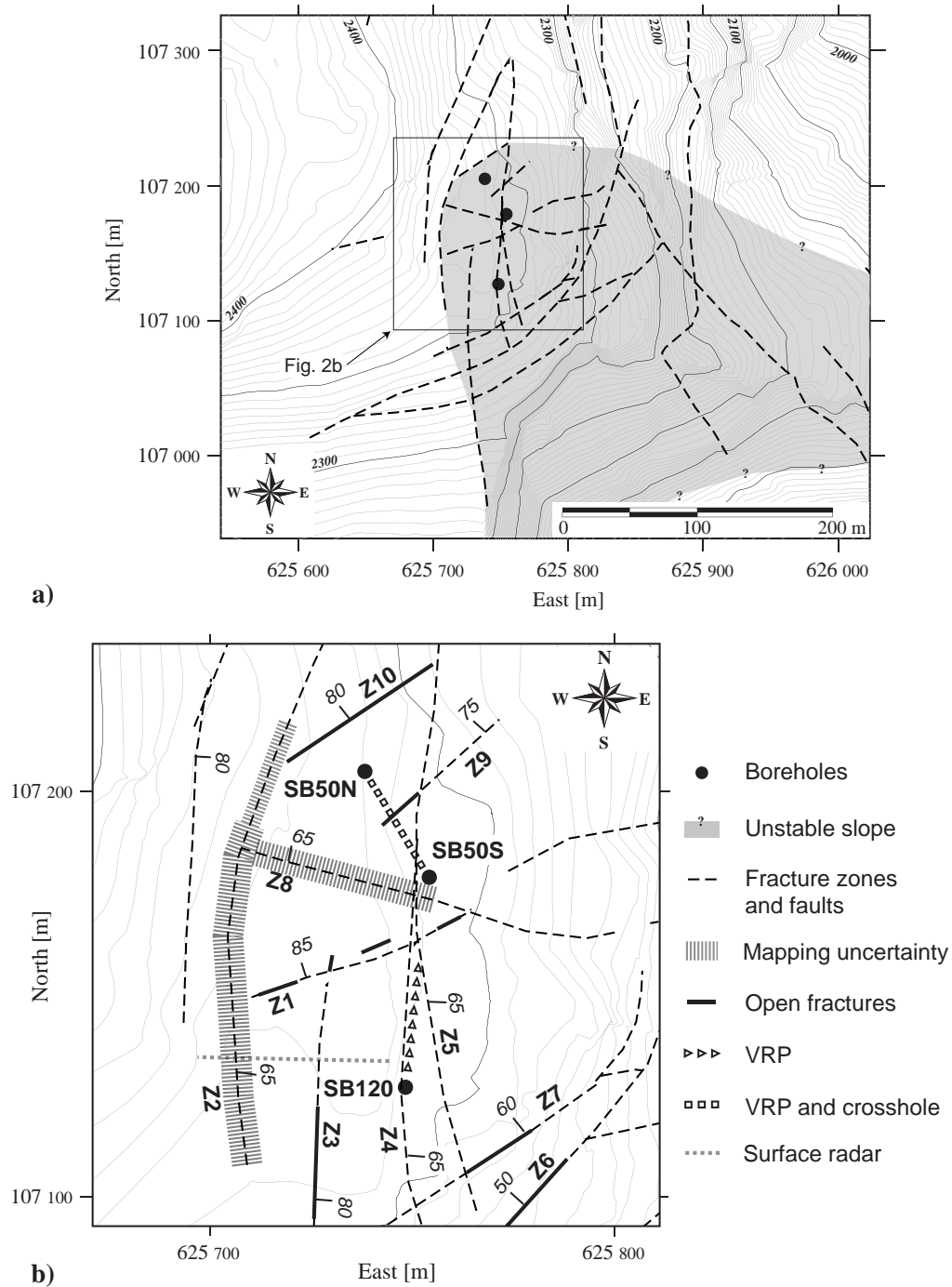


Figure 2

Figure 2.2: (a) Map of Randa study site (black frame in Figure 2.1a) showing the extent of unstable rock based on geodetic measurements, the boreholes and major fracture zones. (b) Enlargement of area surrounding the boreholes identifying the fracture zones and locations of the vertical radar profiles and crosshole radar plane. Hatching outlines zones of dislocation that are broad and/or hidden beneath a thin veneer of surficial material. Thick solid lines delineate open portions of fracture zones. Ticks and numbers identify the surface dip azimuth and dip.

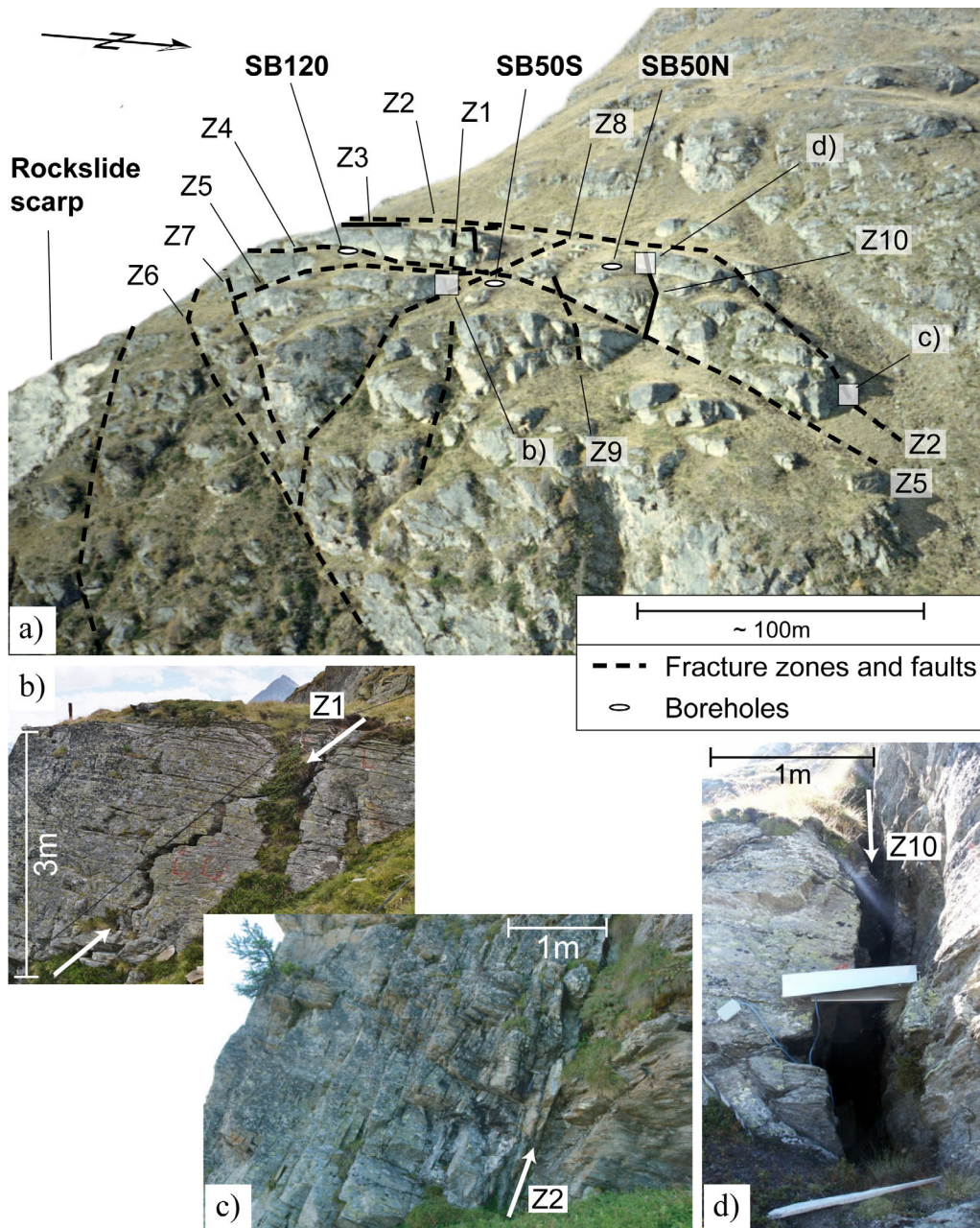


Figure 2.3: (a) Perspective view showing the moraine and slope debris covering part of the study site and the ruggedness of the terrain. Locations of photographs displayed in (b)-(d) are marked by white rectangles. Side views of (b) a jagged portion of open fracture Z1, (c) fracture zone Z2 and (d) open fracture Z10. (Photos: B. Rinderknecht, H. Willenberg and E. Eberhardt)

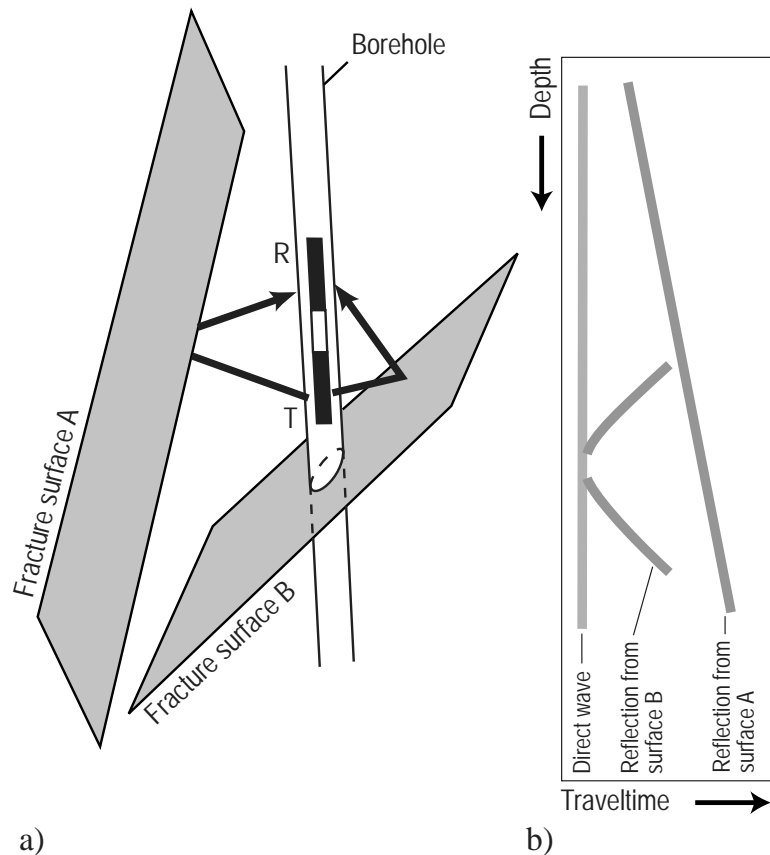
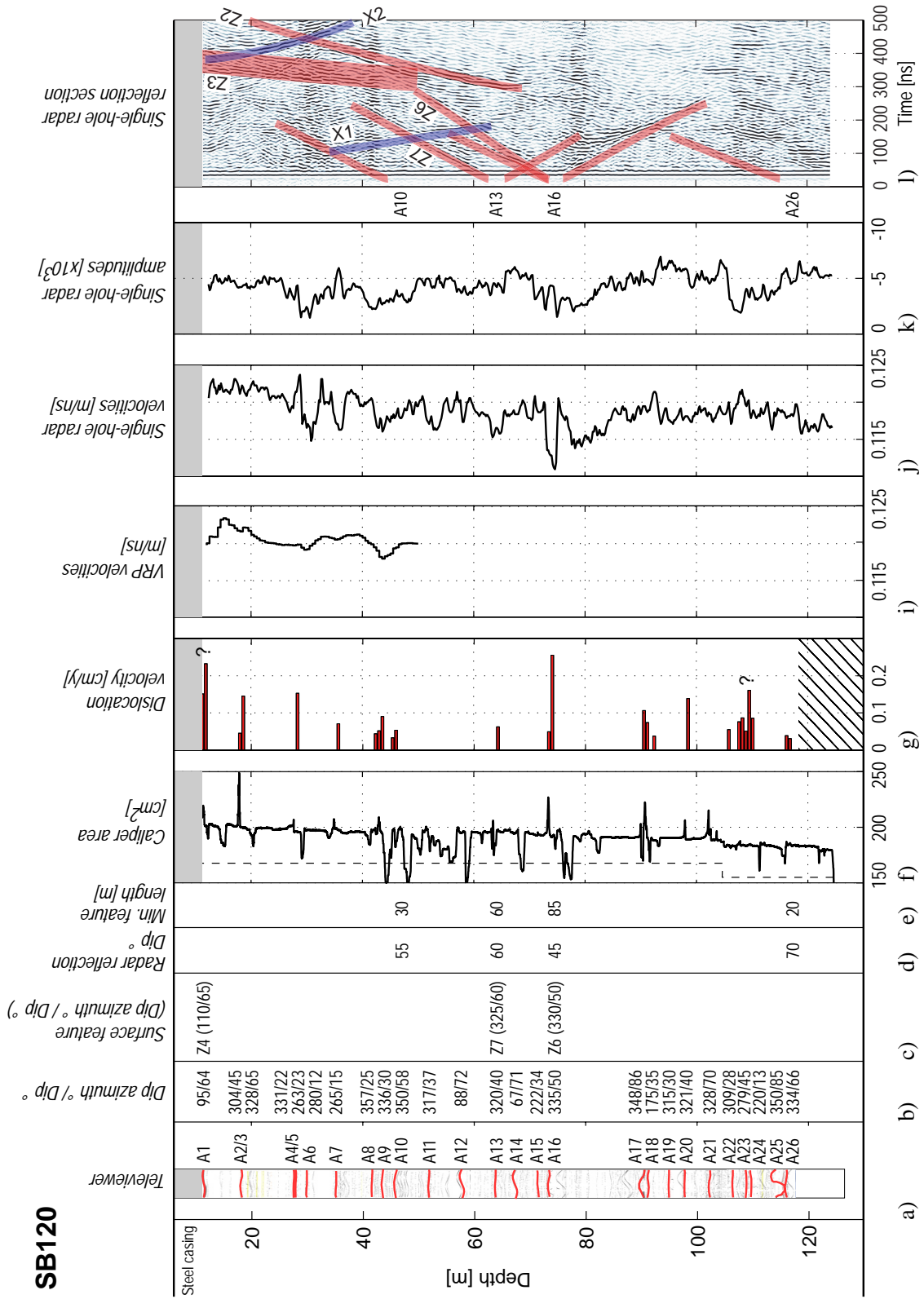


Figure 2.4: (a) Principle of single-hole reflection method and (b) schematic reflection section illustrating typical reflection patterns from intersecting and non-intersecting fractures.

Figure 2.5: Log and other data acquired in borehole SB120 and information on selected surface fracture zones. (a) Televiewer log showing the most important fracture zones (red lines) intersected by the borehole, (b) dip azimuths and dips of these fracture zones, (c) dip azimuths and dips of correlated surface fracture zones, (d) dips of relevant radar reflections, (e) estimated minimum lengths of certain fracture zones, (f) caliper log (dashed line is the nominal area of the drill bit), (g) horizontal displacements/year determined from repeat inclinometer measurements (? indicates uncertain measurements), (i) 1-D velocities determined from VRP measurements, (j) single-hole radar velocities, (k) single-hole radar amplitudes, and (l) single-hole radar section highlighting the most important reflections (see Figure 2.8). The decreasing borehole cross-sectional area identified in column (f) (see also trend of decreasing single-hole radar velocities) is caused by drill-bit abrasion. Borehole elevations and depths are relative to the top of borehole SB50N (2360.4 m above sea level).



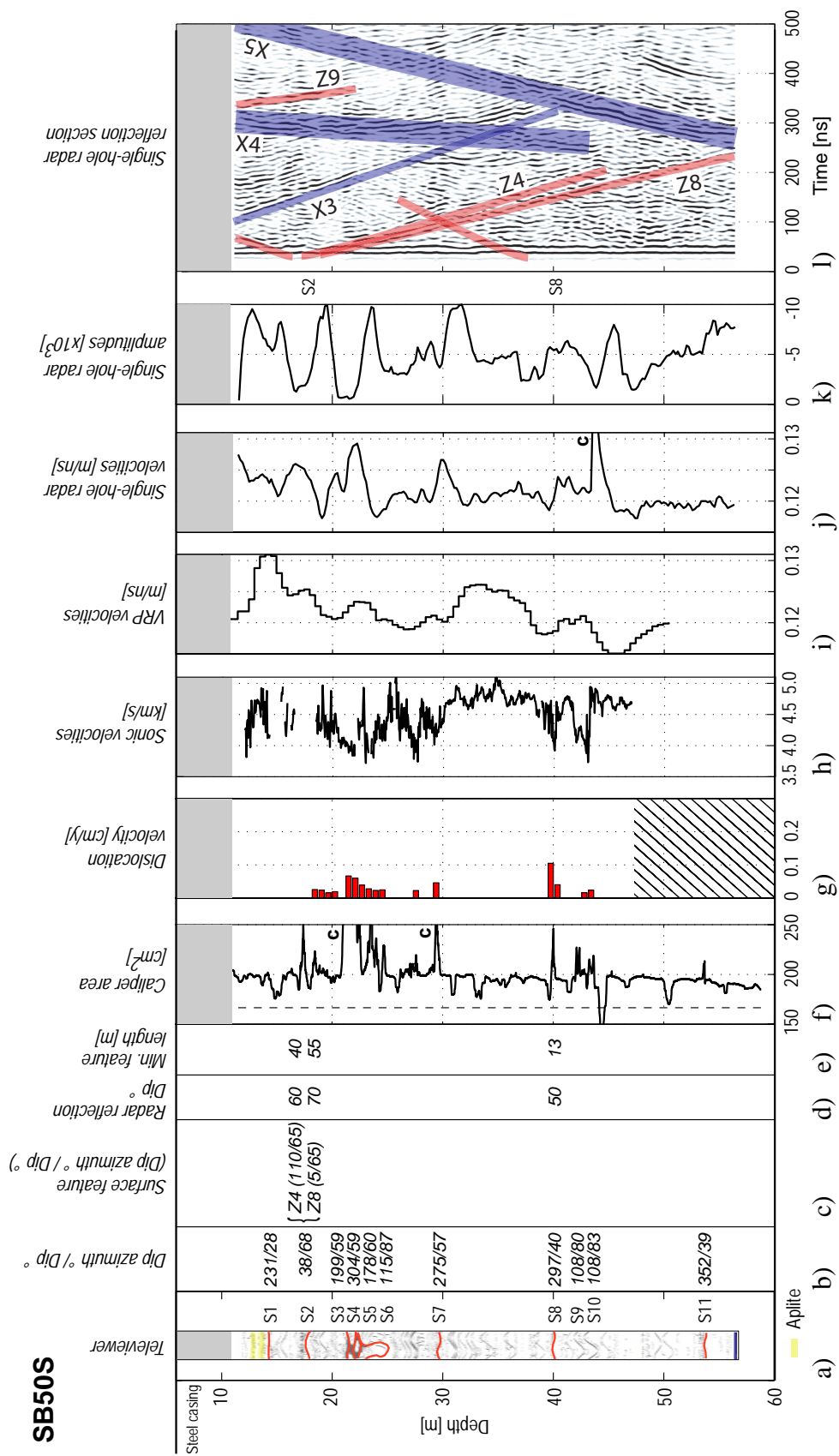


Figure 2.6: As for Figure 2.5, except for borehole SB50S and the addition of the sonic log in column (h). The c's in (f) and (j) identify clipped values.

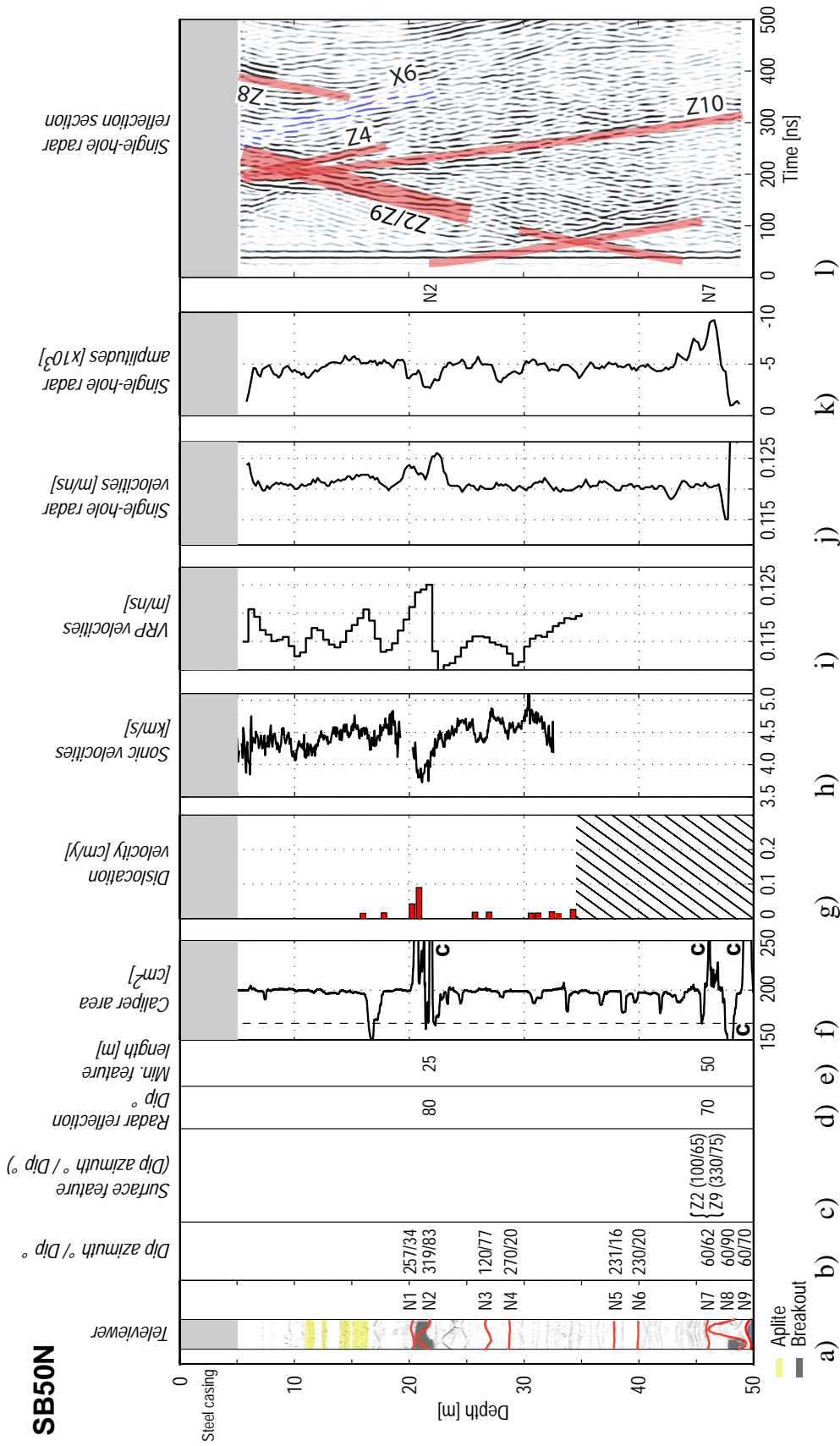


Figure 2.7: As for Figure 2.6, except for borehole SB50N.

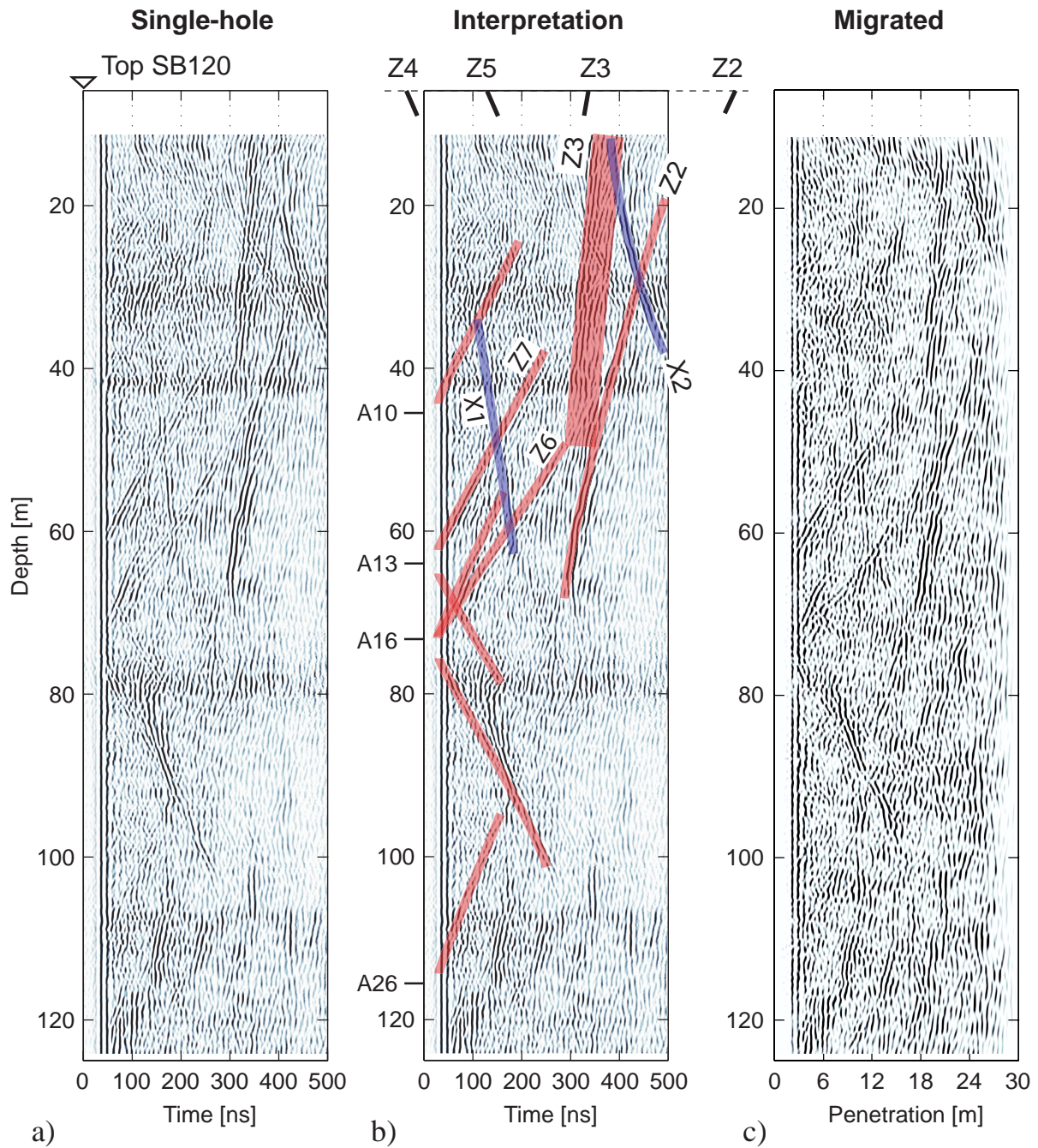


Figure 2.8: Processed single-hole radar sections recorded in boreholes (a) SB120, (d) SB50S and (g) SB50N. Interpretations are superimposed on the same three radar sections in (b), (e) and (h). The A's, S's and N's refer to fracture zones intersected by the respective boreholes (Figures 2.5-2.7), the Z's refer to surface fracture zones (Figures 2.2a and 2.3a), and the X's refer to largely unexplained reflections. Phase-shift migrated radar sections are presented in c), f) and i).

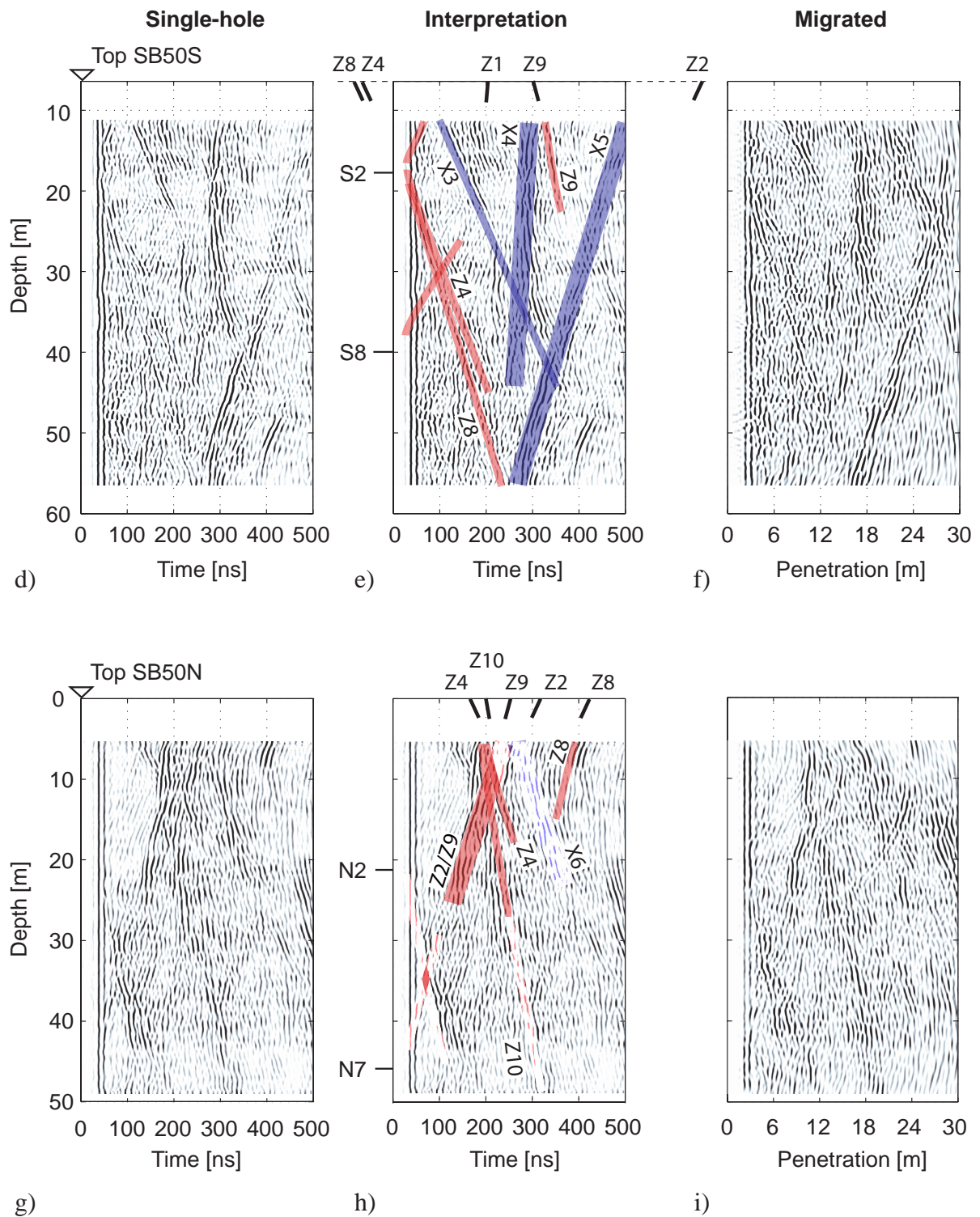


Figure 2.8 (continued)

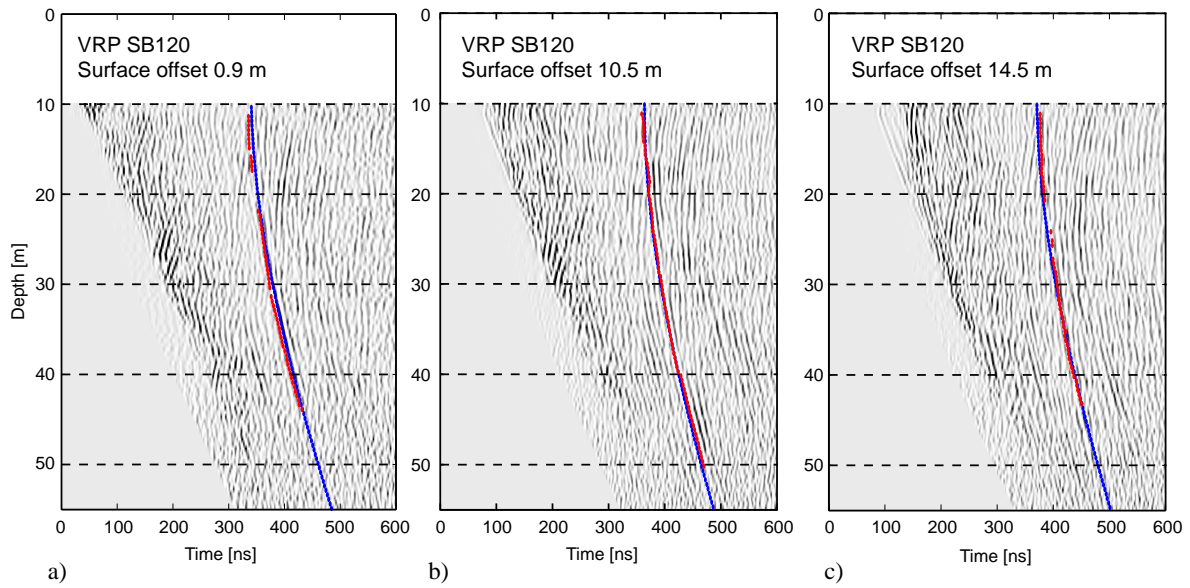


Figure 2.9: (a)-(c): VRP (vertical-radar profile) transmitter gathers for transmitter offsets of 0.9, 10.5 and 14.5 m from borehole SB120 and receivers located between 10.0 m and 57.0 m depth. Red and blue lines are picked reflections and predicted reflections from the best-fit plane shown in Figure 2.B1 of Appendix 2.9.B (in places, the lines coincide), respectively.

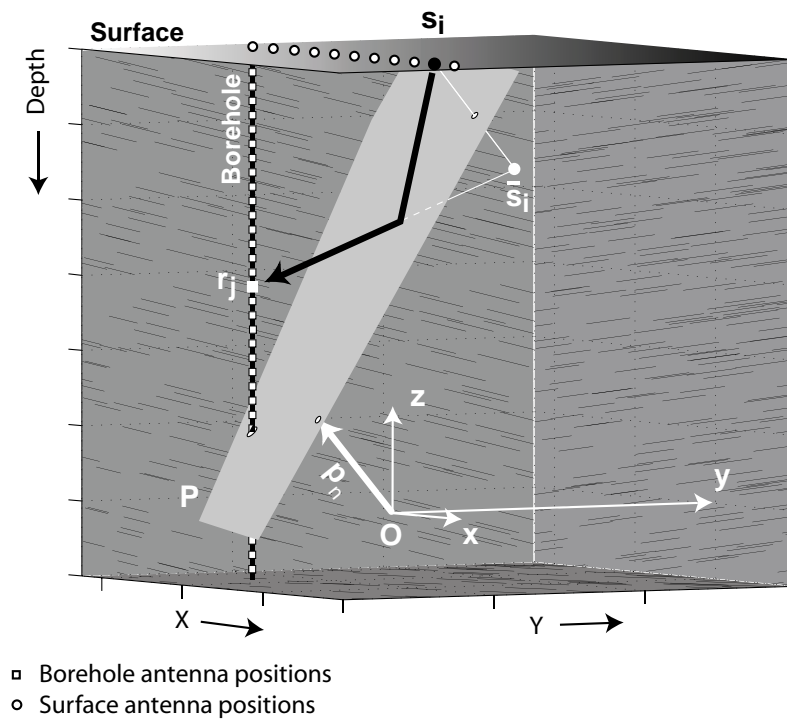


Figure 2.10: Sketch illustrating the geometries of an arbitrary planar reflector P defined by the normal vector \mathbf{p}_n and a typical VRP (vertical-radar profile) ray path. Normal vector \mathbf{p}_n can be described by its Cartesian (x , y and z) or radial (l , φ and θ ; not shown) coordinates. The least-time ray path of energy travelling from the arbitrary surface source \mathbf{s}_i to the arbitrary borehole receiver \mathbf{r}_j via reflector P can be constructed with the help of the mirror source $\bar{\mathbf{s}}_i$. Reflection points illuminated by rays generated at all positions along the surface profile and recorded at all receiver positions down the borehole are outlined by the speckled pattern on P .

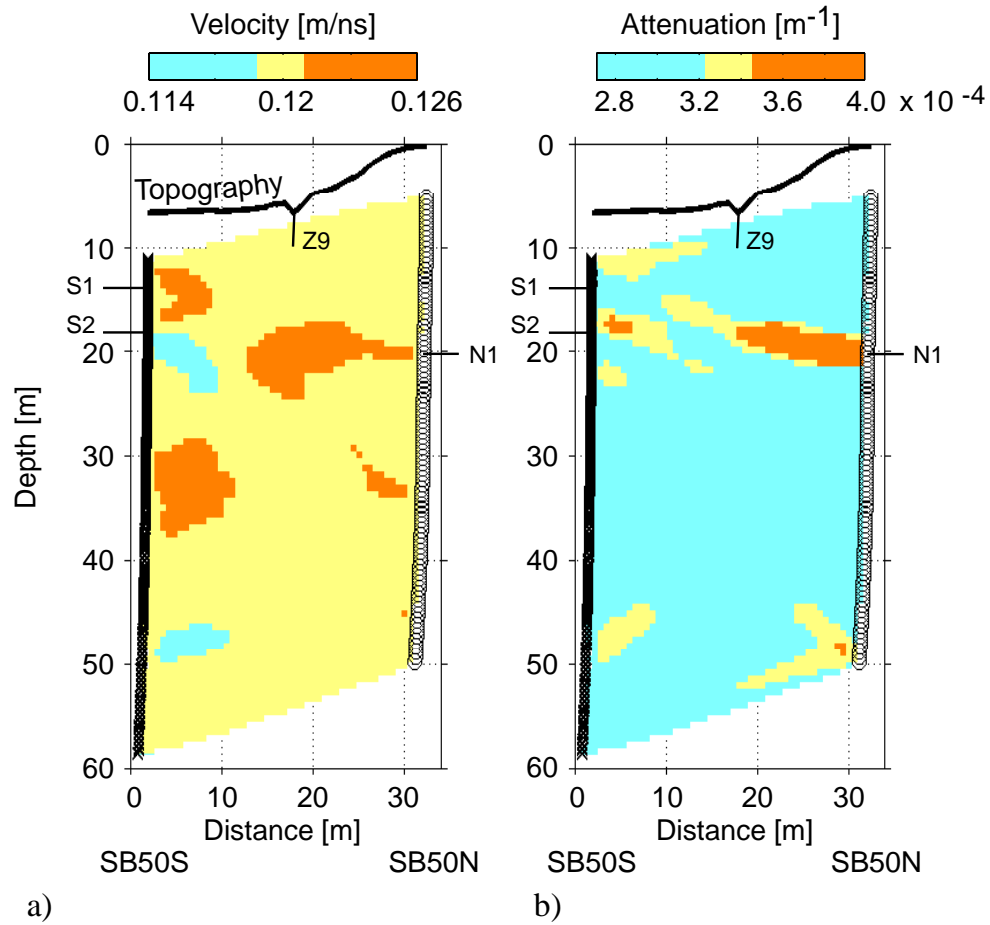


Figure 2.11: (a) Velocity and (b) attenuation tomograms derived from the crosshole georadar data generated in borehole SB50S and recorded in borehole SB50N. S1, S2 and N1 are fracture zones identified in the boreholes.

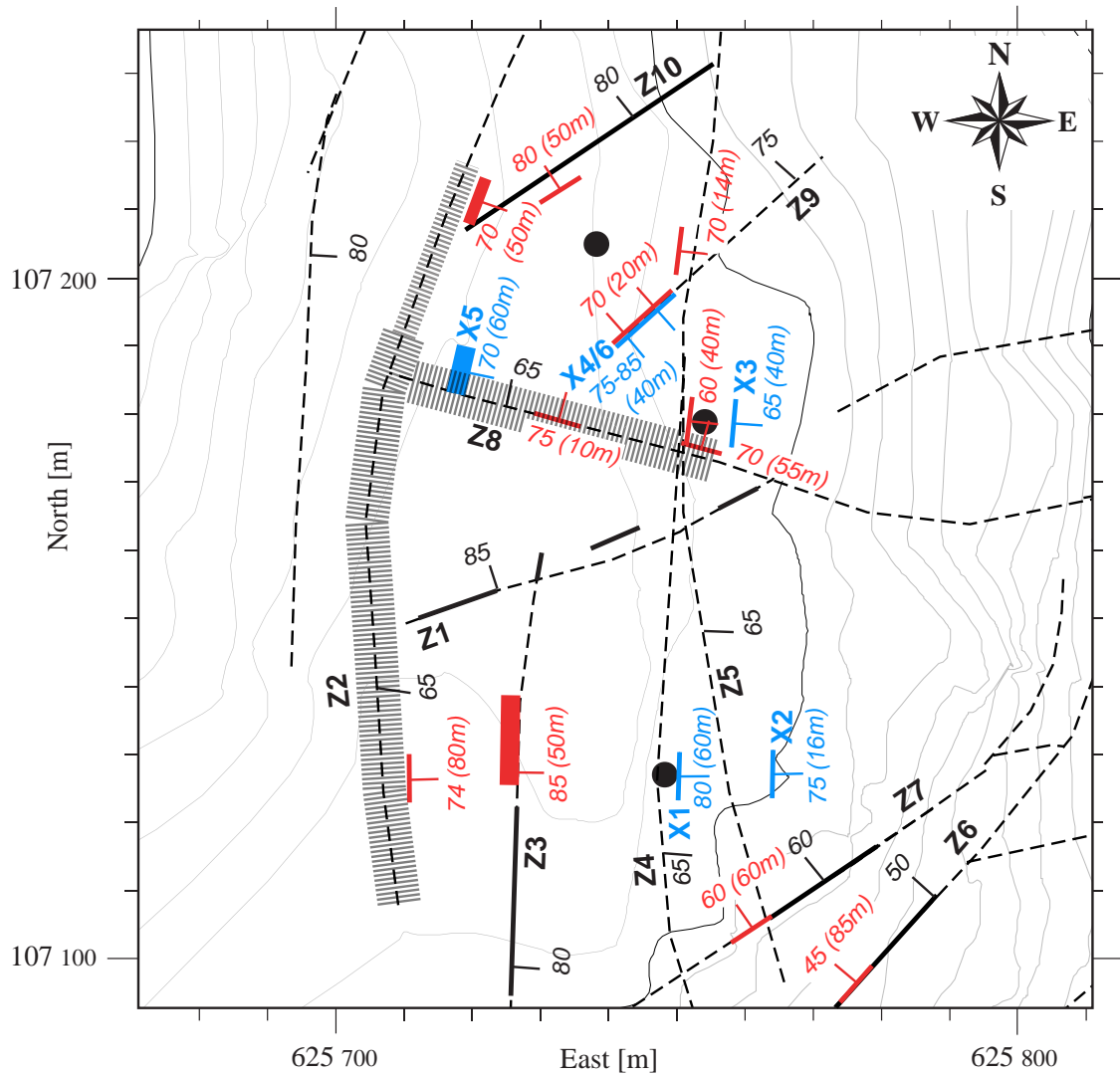


Figure 2.12: Projected surface positions of the most significant radar reflectors (from Figures 2.8 and 2.9) plotted on a simplified version of Figure 2.2b. Thicknesses of the red and blue lines correspond approximately to the reflection zone thicknesses. The surface locations of the X1-X6 reflectors (blue lines) are highly speculative; they have been chosen to be consistent with the orientations of the F2 and F3 systems of fractures

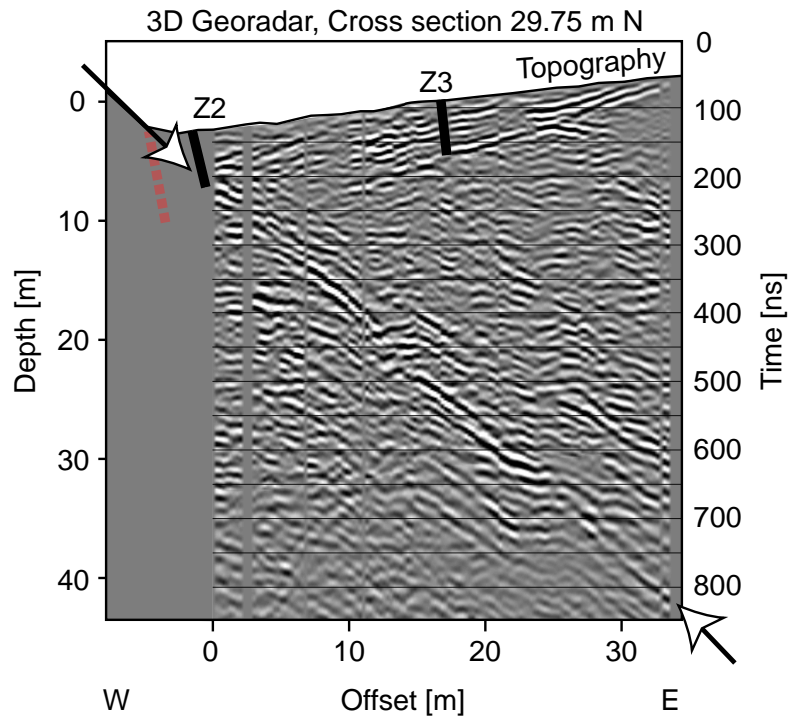


Figure 2.13: Non-migrated cross-section extracted from a 3-D surface georadar data set that samples a large volume of rock between SB120 and the extrapolated location of the Z2 fracture zone (for details on the acquisition and processing of these data see Heincke et al, 2005). The very steep ($>70^\circ$) reflection highlighted by the arrows would approximately migrate to the dashed position shown at the surface. It corresponds closely to the Z2 reflection identified in Figure 2.8b.

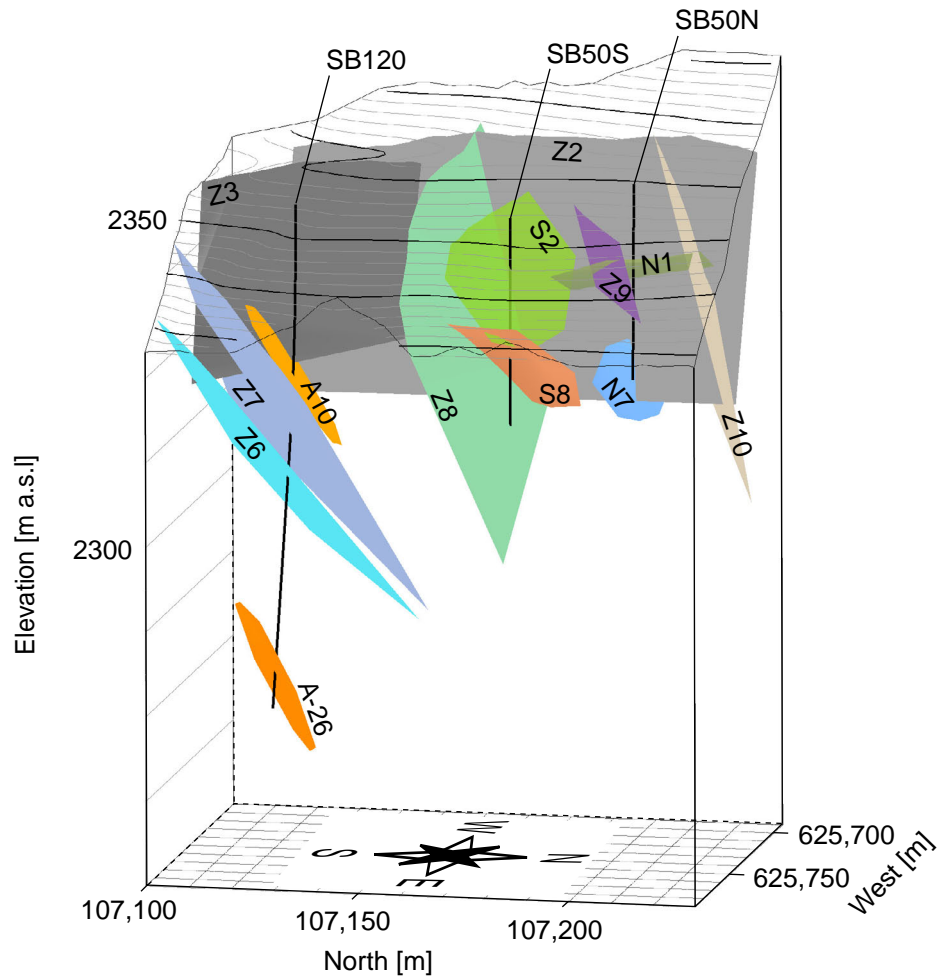


Figure 2.14: Perspective view of major fracture zones identified in the single-hole radar data. The locations of most fracture zones are constrained by surface and borehole observations. Fracture zone Z4 has been omitted, because it would obscure the other fractures when the rock mass is viewed from this direction.

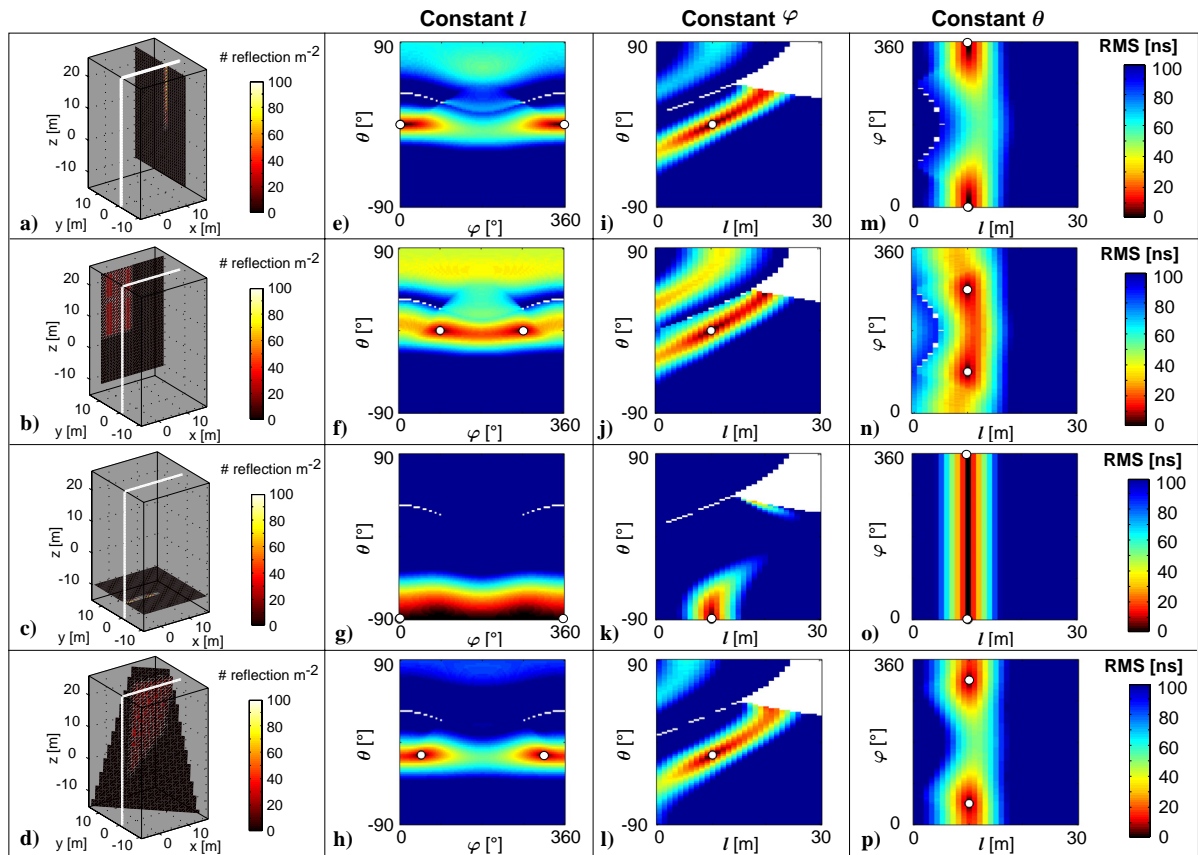


Figure 2.A1: Results of tests on synthetic data. (a)-(d): Position of four planes (black areas) with respect to the source-receiver arrays (white lines). Colours on the planes represent reflection point densities. (e)-(h): RMS slices for constant true normal vector lengths l . (i)-(l): RMS slices for constant true azimuths φ . (m)-(p): RMS slices for constant true dips θ . Correct solutions are represented by the white dots in panels (e) to (p).

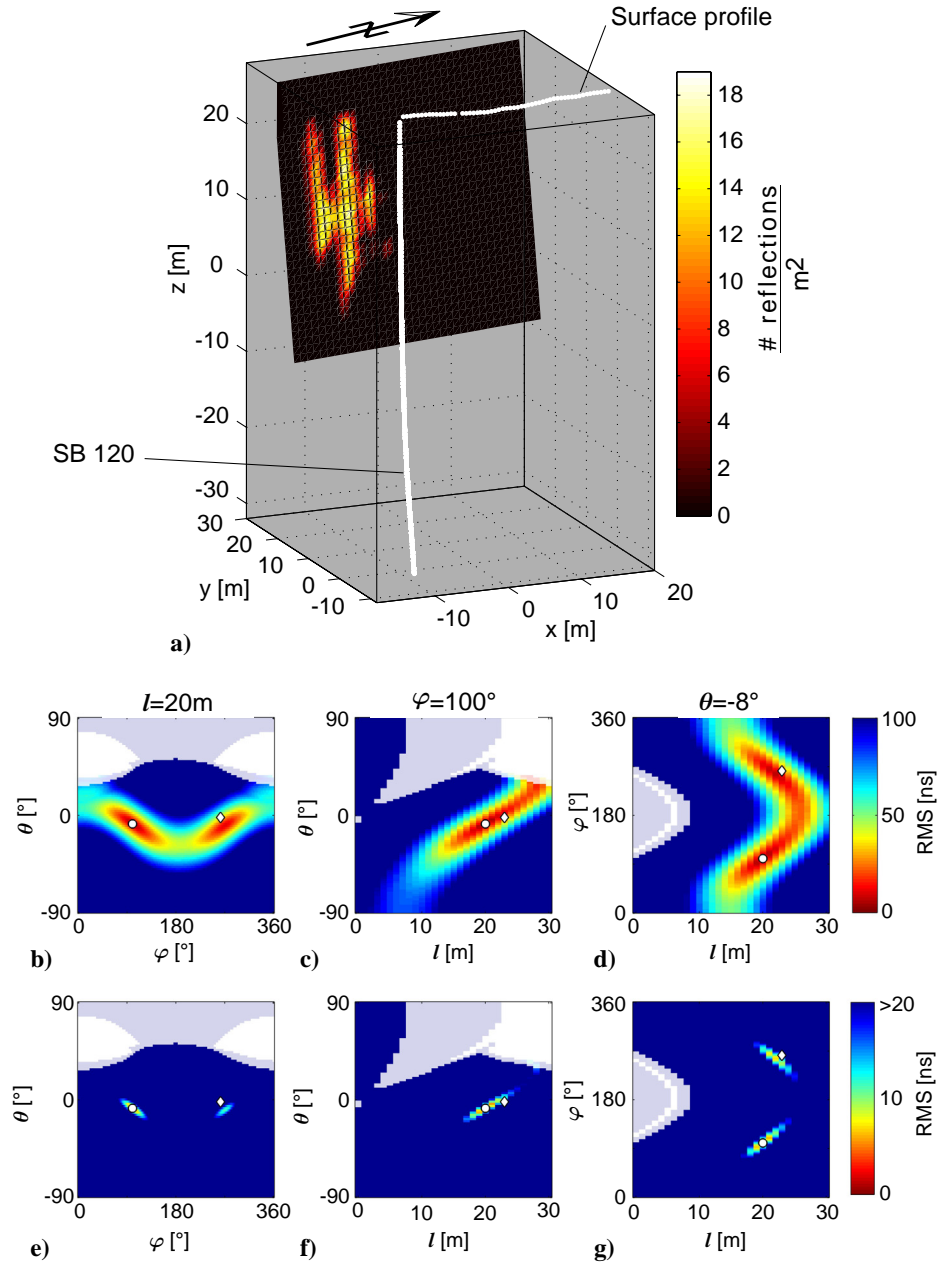


Figure 2.B1: Results of vertical-radar profile (VRP) grid search based on data recorded in borehole SB120. (a) Geometry of sources and receivers (white lines and white dots) and best fitting plane (black area) shown with its reflection point density. (b)-(d): RMS slices for best fitting l , φ and θ ; colour saturation is proportional to the number of data points considered for the RMS calculation (e.g., white delineates areas not sampled and light blue shows regions poorly sampled). The projections of the two symmetric best fitting solutions $\mathbf{p}_n^{\text{best}_1}$ and $\mathbf{p}_n^{\text{best}_2}$ are marked with a white circle and diamond, respectively. (e)-(g): As for (b)-(d), but with limited colour scale (i.e. all values with RMS values >20 are blue).

3 Monitoring network: design, deployment, and operation

3.1 INTRODUCTION

The combined microseismic-geotechnical network was installed across the Randa study site in 2001. Given its hazardous and remote location (Figures 1.3, 1.4, 2.1, and 3.1), many logistical problems had to be resolved. Brief details on the installation and operation of the combined monitoring network, with emphasis on the microseismic components, are provided in the next section. I then discuss some general issues that need to be considered in designing and installing a microseismic network: (i) the network geometry and its earthquake location capabilities, (ii) the type and deployment of sensors, and (iii) a central recording site that allows for interactive data management. Details on the probabilistic earthquake location method and the interpretation of the microseismic activity are provided in Chapter 4.

3.2 RANDA MONITORING NETWORKS

The three moderately deep boreholes SB120, SB50S, and SB50S (the positions of the borehole collars are shown in Figure 2.2a, whereas the locations of the three borehole geophones B1-B3 are depicted in Figure 3.1) were essential components of the combined monitoring system. They were placed northwest of the scarp such that they sampled distinct unstable areas intersected by active surface fractures. Constraints on the borehole locations included accessibility for the drill rig and a maximum distance of ~30 m between the two 50 m-deep boreholes to facilitate crosshole radar surveying (section 2.5.3).

The microseismic network comprised twelve 3-component geophones located across the upper part of the rock slope (Figure 3.1, Table 3.2). Three geophones (B1-B3 in Figure 3.1) were established near the bottoms of the boreholes, and nine were deployed in shallow holes (S1-S9 in Figure 3.1). Table 3.1 summarizes the main specifications of all components that were installed at the Randa study site. Coordinates of the twelve geophones are listed in Table 3.2.

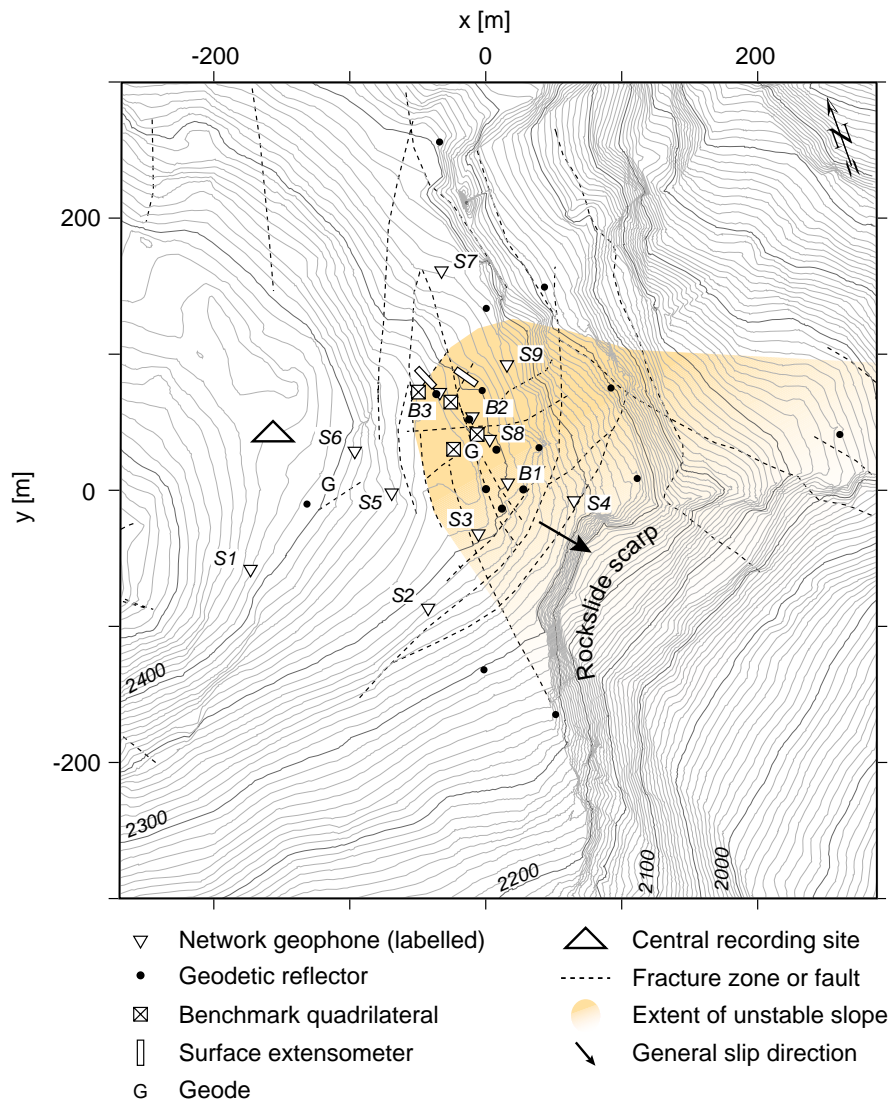


Figure 3.1: Locations of the diverse elements of the monitoring network above the Randa rockslide.

3.3 MICROSEISMIC NETWORK DESIGN

Two general rules need to be considered in designing a microseismic network. To obtain a reliable epicenter, the maximum azimuthal gap between geophones should be $<180^\circ$ and to obtain a reliable focal depth, the distance from the epicenter to the nearest geophone should be less than the focal depth (e.g., Lee and Stewart, 1981). Accordingly, an optimal network should consist of evenly distributed geophones centered on the area of interest, and the sensor spacing should be set to the minimum expected hypocenter depths.

Table 3.1: Monitoring instruments and specifications.

<i>Instrument</i>	<i>Number of instruments</i>	<i>Type</i>	<i>Sampling period</i>	<i>Purpose</i>
Microseismic network				
Moderately deep geophones	3	OYO Geospace GS-20D 3-component, $f_n=28$ Hz	Event-triggered (0.0625-0.125 ms)	Microseismic activity
Shallow geophones	9	OYO Geospace GS-11D 3-component, $f_n=8$ Hz	Event-triggered (0.0625-0.125 ms)	Microseismic activity
Geotechnical network at surface				
Geodetic survey	7	Optical reflectors	1-2 times/year	Surface displacements
Extensometers	2	Vibrating-wire	6 min	Continuous monitoring of surface fracture opening
Benchmark quadrilaterals	4	Beam-compass	2-3 times/year	Magnitude and direction of surface fracture opening
Benchmarks	26	Tape measure	1-2 times/year	Surface fracture opening
Geotechnical network in boreholes				
Inclinometer tubes	One per borehole	Servo-accelerometers	1-2 times/year	Horizontal displacements
In-place inclinometers	2 in SB120	Vibrating-wire	6 minutes	Dynamics of horizontal displacements across fractures
Extensometer	SB120	Induction-coil transducer	1-2 times/year	Vertical displacements

Table 3.2: Coordinates of the microseismic array.

<i>Geophone</i>	<i>East [m]</i>	<i>North [m]</i>	<i>Elevation [m]</i>
S1	625'565.5	107'130.4	2'410.7
S2	625'678.3	107'057.5	2'339.1
S3	625'732.7	107'096.6	2'353.5
S4	625'806.7	107'096.4	2'307.7
B1	625'765.3	107'125.1	2'242.6
S5	625'682.6	107'147.9	2'376.7
S6	625'666.5	107'185.7	2'397.0
S7	625'772.3	107'288.8	2'327.9
B3	625'740.1	107'205.1	2'317.8
S8	625'763.6	107'159.7	2'353.9
B2	625'756.5	107'179.8	2'310.8
S9	625'795.1	107'206.5	2'328.5

Optimization schemes for determining network geometry have been studied by Uhrhammer (1980), Hardt and Scherbaum (1994), Steinberg et al. (1995) and Curtis et al. (2004). In practice, an optimum network is rarely achieved. Many factors may influence the final installation of a small-scale network, including hazardous and logistically difficult operating conditions and/or insufficient number of geophones.

A well-known problem with seismic networks, which may be addressed by optimization schemes, concerns the trade-offs between the different hypocentral parameters

and origin times during the location procedure. In particular, hypocenter depth and origin time often show strong dependencies. This effect can be reduced by having geophones located at various depths. As a consequence, the >100 m topographic relief of the Randa microseismic network and the geophones placed near the bottom of the boreholes were major advantages for the location of microearthquakes in the upper ~100 m of the subsurface.

A resolution test of the 12-station microseismic network is provided in Appendix C. Here, additional material on the design of microseismic networks is presented. I describe important details on the methodology, followed by two resolution tests based on the assumption that P-wave arrival times are available at (1) the shallow geophones and (2) the full network at Randa. A third test includes hypothetical S-wave arrivals at the moderately deep borehole sensors.

To estimate network resolution, I calculate the model resolution matrix for the linearized earthquake location problem in a homogeneous full-space model (Lee and Stewart, 1981; Menke, 1989). The damped least squares solution to the linear version of the problem is:

$$\mathbf{m}^{est} = \mathbf{G}^{-g} \mathbf{d}^{obs}, \quad (3.1)$$

where \mathbf{m}^{est} are the best estimates of the hypocentral parameters \mathbf{x}_0 and origin time t_0 , \mathbf{G}^{-g} is the generalized inverse, and \mathbf{d}^{obs} are the observed arrival times at station \mathbf{x}_i . The generalized inverse is given by:

$$\mathbf{G}^{-g} = (\mathbf{G}^T \mathbf{G} + \lambda^2 \mathbf{I})^{-1} \mathbf{G}^T, \quad (3.2)$$

where

$$G_i = \begin{pmatrix} \frac{\partial T_i}{\partial x_0} & \frac{\partial T_i}{\partial y_0} & \frac{\partial T_i}{\partial z_0} & 1 \end{pmatrix},$$

λ^2 is the damping parameter, \mathbf{I} is the identity matrix, and \mathbf{G} is the matrix of partial derivatives of travel time T_i (from the source to station i) with respect to the source coordinates. The resolution matrix is then:

$$\mathbf{R} = \mathbf{G}^{-g} \mathbf{G}. \quad (3.3)$$

Since \mathbf{R} directly relates the true parameters to the estimated model parameters by:

$$\mathbf{m}^{est} = \mathbf{R} \mathbf{m}^{true}, \quad (3.4)$$

it indicates if sufficient data exists to yield a unique estimate of the model parameters. In an ideal situation, $\mathbf{R} = \mathbf{I}$ and the estimated parameters equal the true ones. To test my network

configurations, I measure the deviation from the unit matrix using the *Dirichlet spread* (Menke, 1989, p.68):

$$\text{Dirichlet spread}(\mathbf{R}) = \sum_{i=1}^4 \sum_{j=1}^4 [R_{ij} - I_{ij}]^2. \quad (3.5)$$

To determine the distribution of the Dirichlet spread, equations (3.2), (3.3), and (3.5) are evaluated for a 3-D grid of simulated point sources based on the topography and microseismic network at Randa. The grid extends ± 300 m north-north-east and ± 300 m west-north-west of the SB120 collar (Figure 3.1) and from 2080 to 2460 m elevation. In total, 19220 grid points uniformly spaced at 20 m are included in the model. The damping constant is fixed to $\lambda^2 = 0.1$ for all tests.

A Dirichlet spread of 0 indicates independent resolution of all hypocentral parameters and origin times, whereas large values are diagnostic of trade-offs and unreliable hypocenter estimates. Absolute spread values are unimportant, because their magnitudes are largely controlled by the damping parameters. They do not directly indicate errors in the estimated parameters. Accordingly, only relative changes within the test volume or between different test configurations for the same volume are relevant.

Figure 3.2 shows the locations of the shallow geophones S1-S9 and the corresponding Dirichlet spread along three slices through the event grid. A minimum Dirichlet spread value of 0.0127 is obtained in the central part of the network, with values increasing (i.e. resolution decreasing) laterally and with depth. This nine-geophone network would only reliably locate shallow earthquakes that occurred within the network boundaries.

By including the geophones in the moderately deep boreholes, the minimum Dirichlet spread value is reduced to 0.0035 and the depth extent of low Dirichlet spread values increases (Figure 3.3). This enhances resolution in an essential part of the unstable slope close to geophone B1 (Figure 3.3b and c), where the opening fractures and faults are observed (Chapter 2; Willenberg, 2004; Heincke et al. 2005; 2006a; 2006b). It is in this region that significant earthquakes may eventually occur.

Dirichlet spread values for the situation in which S-wave arrivals at the three moderately deep geophones are also included in the earthquake location procedure. The minimum Dirichlet spread value is now only 0.0012, which indicates nearly perfect hypocentral parameters and origin times in the vicinity of the array center. High-quality

hypocenter and origin time estimates are also observed over large regions well outside the microseismic network.

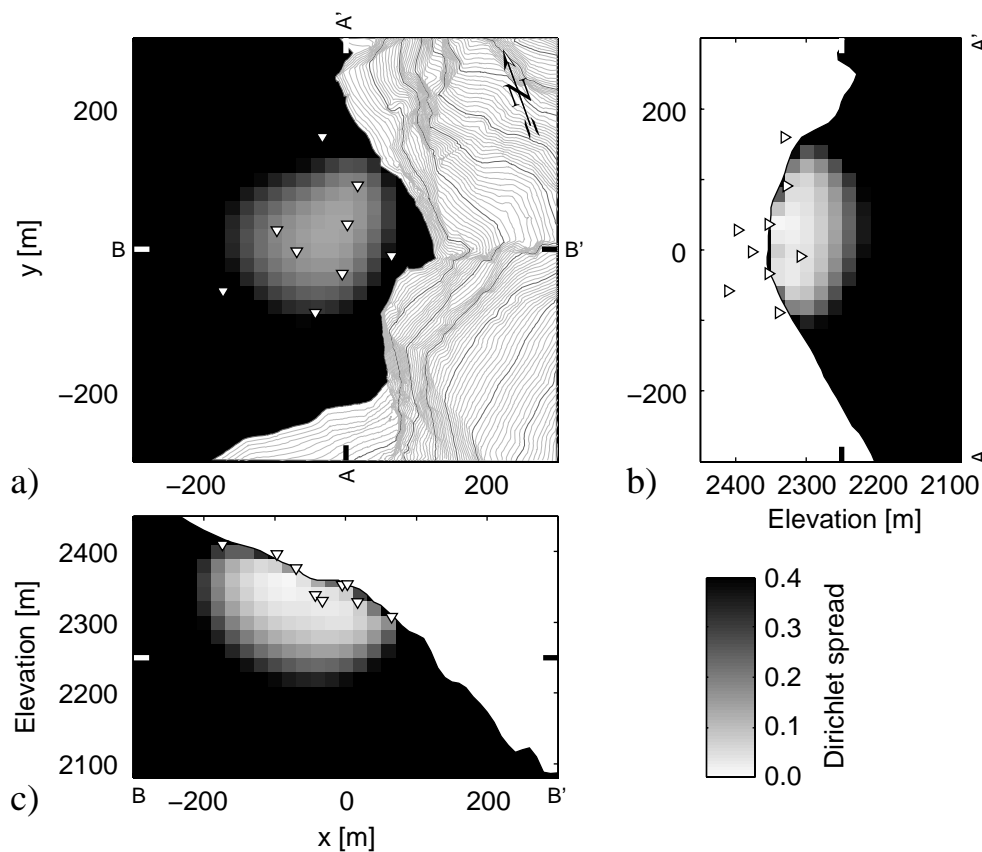


Figure 3.2: Distribution of shallow network geophones (triangles) and corresponding Dirichlet spread (resolution) of the hypocenter parameters and origin times: (a) horizontal plan section at 2250 m elevation, (b) vertical cross-section A-A', and (c) vertical cross-section B-B'. Only P-arrivals are considered, resolution values above topography are blanked.

These simple resolution tests demonstrate the importance of the borehole geophones in determining reliable hypocenter parameters and origin times. They show that the Randa microseismic network is well designed for locating microearthquakes that may originate at the many fracture zones and faults near the boreholes.

The tests described above do not consider the very important effects of arrival time uncertainties and the reliability of the seismic velocity model on the hypocenter-parameter and origin-time estimates. These issues are discussed in Chapter 4.

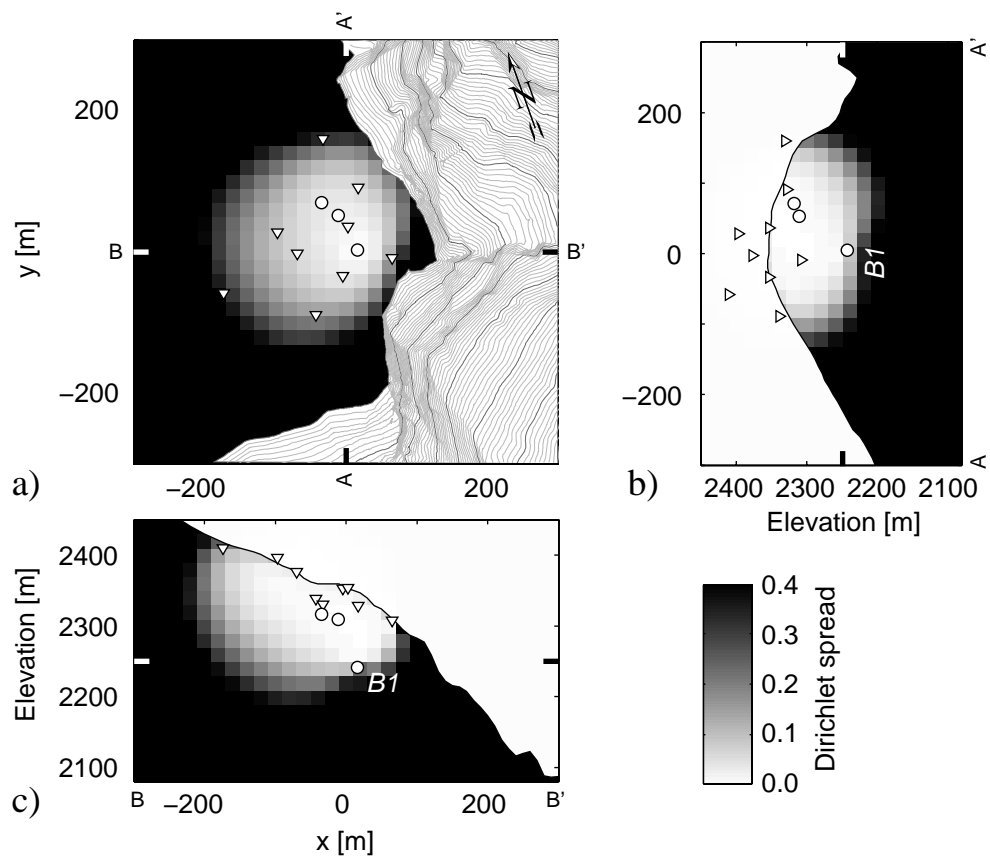


Figure 3.3: As for Figure 3.2, but including the geophones in the moderately deep boreholes (circles).

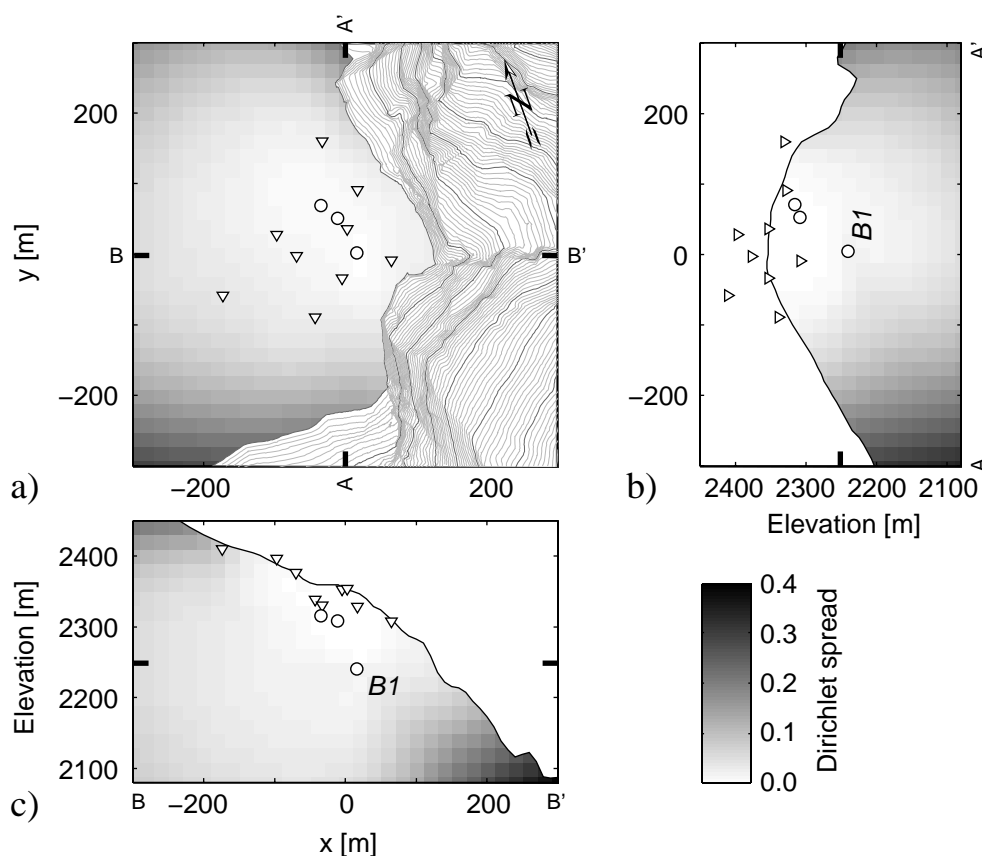


Figure 3.4: As for Figure 3.3, but including *S*-arrivals at the deep borehole geophones (circles).

3.4 TECHNICAL SETUP OF THE RANDA MICROSEISMIC NETWORK

3.4.1 Geophones

The type and placement of the seismic sensors are key elements of any seismic monitoring system. The expected ranges of seismic signal amplitude and frequency, which depend on the magnitudes of the seismic sources and their distances from the sensors, determine the type of sensor. Events in deep mines, for example, commonly have moment magnitudes m between -4 and 5, which translates to frequencies ranging from <1 Hz up to several kHz (Mendecki, 1997). In such environments, it may be necessary to install geophones to cover the low to medium frequencies and accelerometers to cover the medium to high frequencies. For networks installed at or near the Earth's surface, frequencies are typically well below 1 kHz.

Good quality geophones are characterized by nearly linear responses above their natural frequencies, but attenuate energy at lower frequencies. Generally, broadband instruments are best suited for near-surface networks. Unfortunately, such sensors are very

expensive and need accurate horizontal placement. Tilting a broadband geophone may attenuate its response or introduce spurious frequencies (Oh, 1996). The effect is most serious for sensors with low natural frequencies. However, the use of geophones with high natural frequencies may result in more distant events (characterized by low corner frequencies) not being rewarded.

A reasonable compromise between cost, sensitivity, and ease of installation was provided by 8 Hz geophones installed in the 0.3 – 4.6 m deep holes that were inclined within $\pm 5^\circ$ of vertical (Figures 3.5 and 3.6). To facilitate eventual removal of the 3-component geophones from the shallow holes, they were fixed to the bedrock via a thin bed of grout. Coupling was enhanced by filling the gap around the geophone casing with sand. Geophones were then protected from rain, wind, and snowfall by improvised housings (Figure 3.5).

Deviations of the borehole trajectories from vertical (especially for borehole SB120) required us to install tilt-tolerable geophones with natural frequencies of 28 Hz in the moderately deep boreholes (Figure 3.6b). They were placed just above the piezometer sections. By using prepared inclinometer casing modules that hold either a piezometer or a geophone (Figure 3.7a), all required data cables could be collected together in the gap between the casing and the borehole wall (Figure 3.7b). After lowering the casing into the

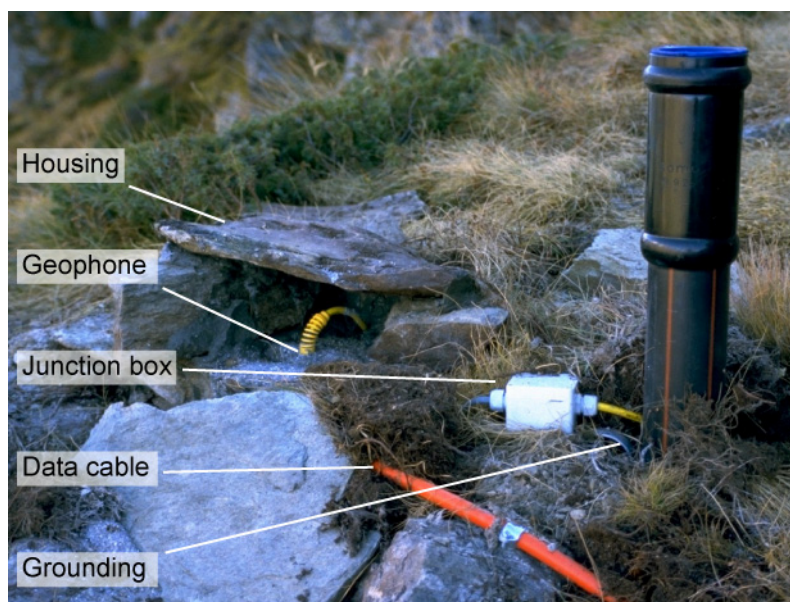


Figure 3.5: Placement of near-surface geophone S9 in a shallow hole. A second ~5 m-deep hole was used to install a grounding plate for cable shielding.

borehole, the gap around it was grouted to achieve good coupling of the sensors to the surrounding rock. Geotextile prevented the grout from being absorbed by fractures intersecting the borehole (Willenberg et al., 2002). The casing was left open for repeat inclinometer surveys.

3.4.2 Geophone orientation

Accurate information on the orientations of the three sensors of each geophone was important for the polarization analyses of incoming seismic waves. The shallow sensors H1, H2, and V formed a right-hand coordinate system (x , y , and z in Figure 3.6a). They were oriented such that an impact from the north or east or from above would cause an initial positive signal. Consequently, a compressional P-wave from a moderately deep hypocenter north or east of a 3-component geophone would result in positive first-arrival onsets on the horizontal sensors, but a negative onset on the vertical sensor.

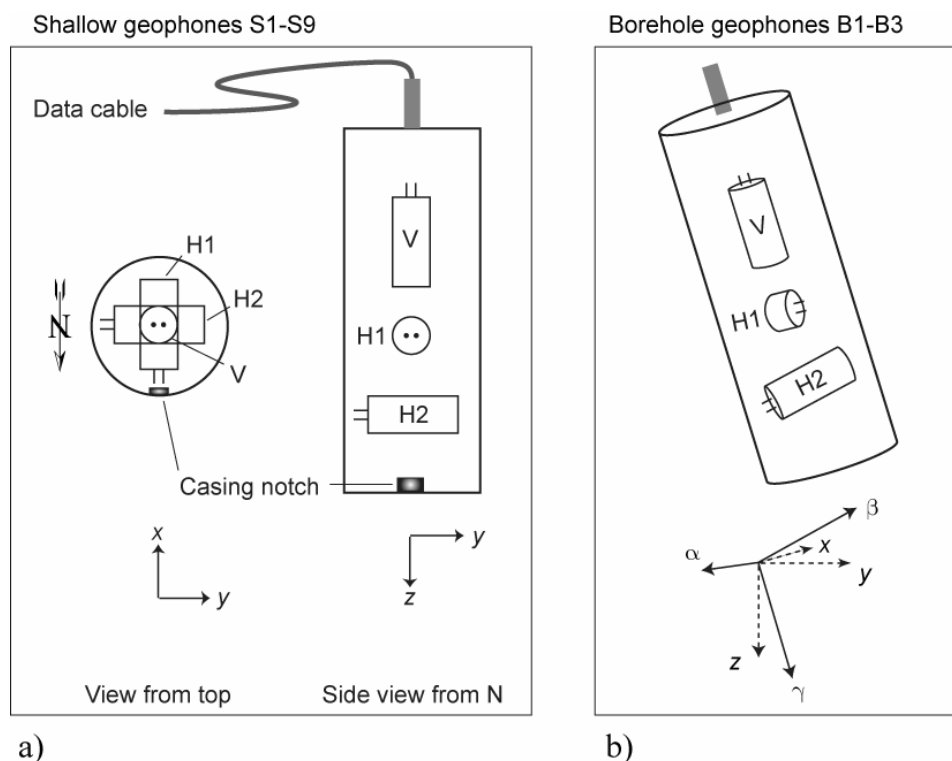


Figure 3.6: Sketches of borehole geophones with three perpendicular sensors (H1, H2, V). (a) Shallow 8 Hz sensors define a right-hand coordinate system (x , y , z) with x pointing south and z pointing down. (b) Tilted 28 Hz sensor coordinate system (α , β , γ) in geographic reference system (x , y , z).

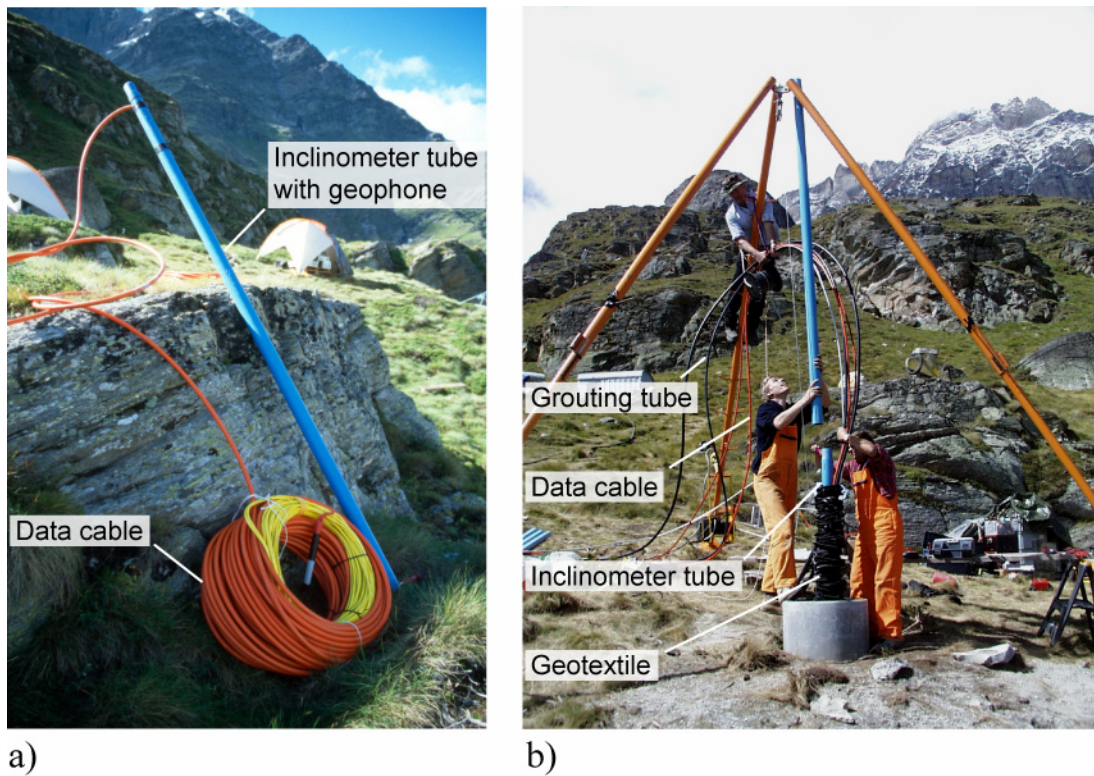


Figure 3.7: (a) Incliner tube with pre-installed geophone and data cable. (b) Installing geophone B2 in borehole SB50S.

For the obliquely oriented borehole geophones B1-B3, I defined a coordinate system with axes (α, β, γ) that paralleled the axes of the respective sensors (Figure 3.6b). The orientations of these sensors relative to the (x, y, z) coordinate system of the shallow geophones could then be constructed from the borehole trajectory and inclinometer measurements. Borehole azimuth ϕ and dip θ defined the orientation of the z -component sensors. The sub-horizontal components α and β were oriented parallel to the guide tracks of the inclinometer tubes, the directions of which were measured at the surface. Small corrections to these orientations were required to compensate for torsional twists that the tubing suffered while being lowered down the boreholes. We used a spiral probe to measure these twists. Application of the following equations allowed the data in the (α, β, γ) coordinate system to be transformed to data in the (x, y, z) system:

$$\begin{bmatrix} x \\ y \\ z \end{bmatrix} = \mathbf{A} \begin{bmatrix} \alpha \\ \beta \\ \gamma \end{bmatrix}, \quad (3.6)$$

where \mathbf{A} is the rotation matrix defined by the Eulerian angles: dip direction ϕ , dip θ , and azimuth ψ .

3.4.3 Geode seismographs

The twelve 3-component geophones were connected to two 24-channel *Geode* seismographs (*Geometrics Inc.*) that operated in a self-trigger mode. These systems included 24-channel acquisition boards with 24-bit A/D converters, allowing sampling frequencies of up to 50 kHz. The locations of the two seismographs were designed to keep the analog cables to the geophones as short as possible (Figure 3.1).

Since a total ~ 1.5 km of cables were deployed across the Randa study site, it was necessary to protect the electrical systems against excess-voltages. Our installations include shielded cables and surge protection (Figure 3.5 and Figure 3.8a, respectively).

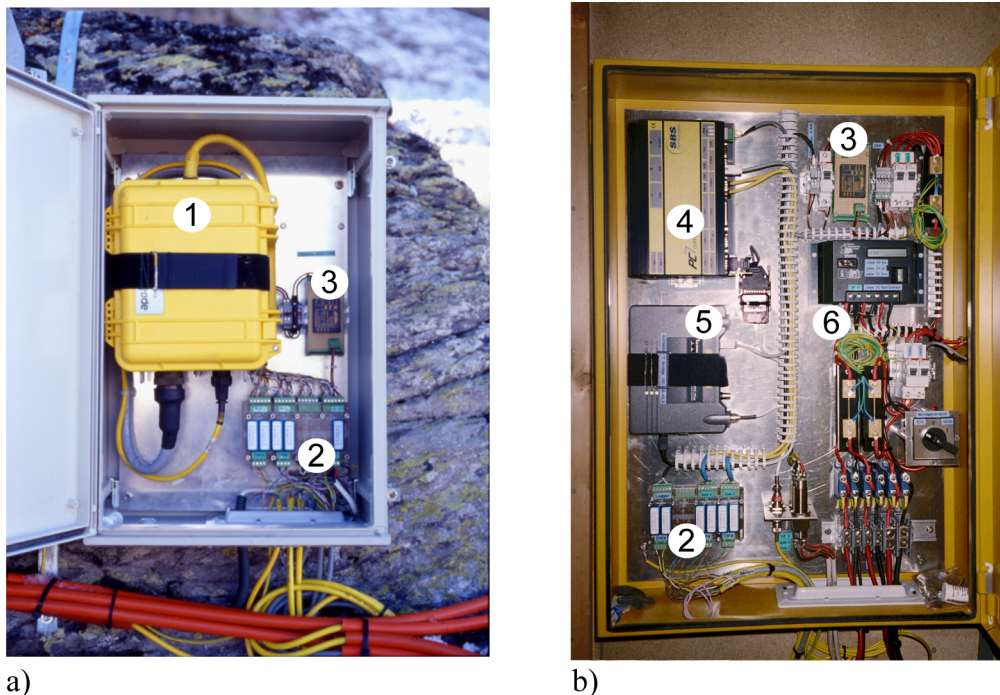


Figure 3.8: Details on the installation of the Randa in situ monitoring network. (a) Geode seismograph (1), lightning protected data cables (2), and DC/DC converter (3). (b) Installation at the central recording site with industrial PC (4), wireless Ethernet bridge (5), and controller of power production unit (6). Photographs: B. Rinderknecht.

3.4.4 Central recording site

The central recording site supplied the power necessary to run the system and acquisition software, temporarily stored the data, and provided an accurate clock for timing the measurements. Event triggered data packages were transferred from the Geodes via Ethernet to an industrial PC at the central recording site (Figure 3.1). The PC was designed to operate in the harsh weather conditions of the high alpine environment. Critical hardware components were selected to function at low temperatures down to -40°C . The hardware included a Celeron processor, a solid-state hard disk that stored the operating system, and a standard 20 GB hard disk for temporary data storage. Figure 3.8b displays some components of the installation at the central site.

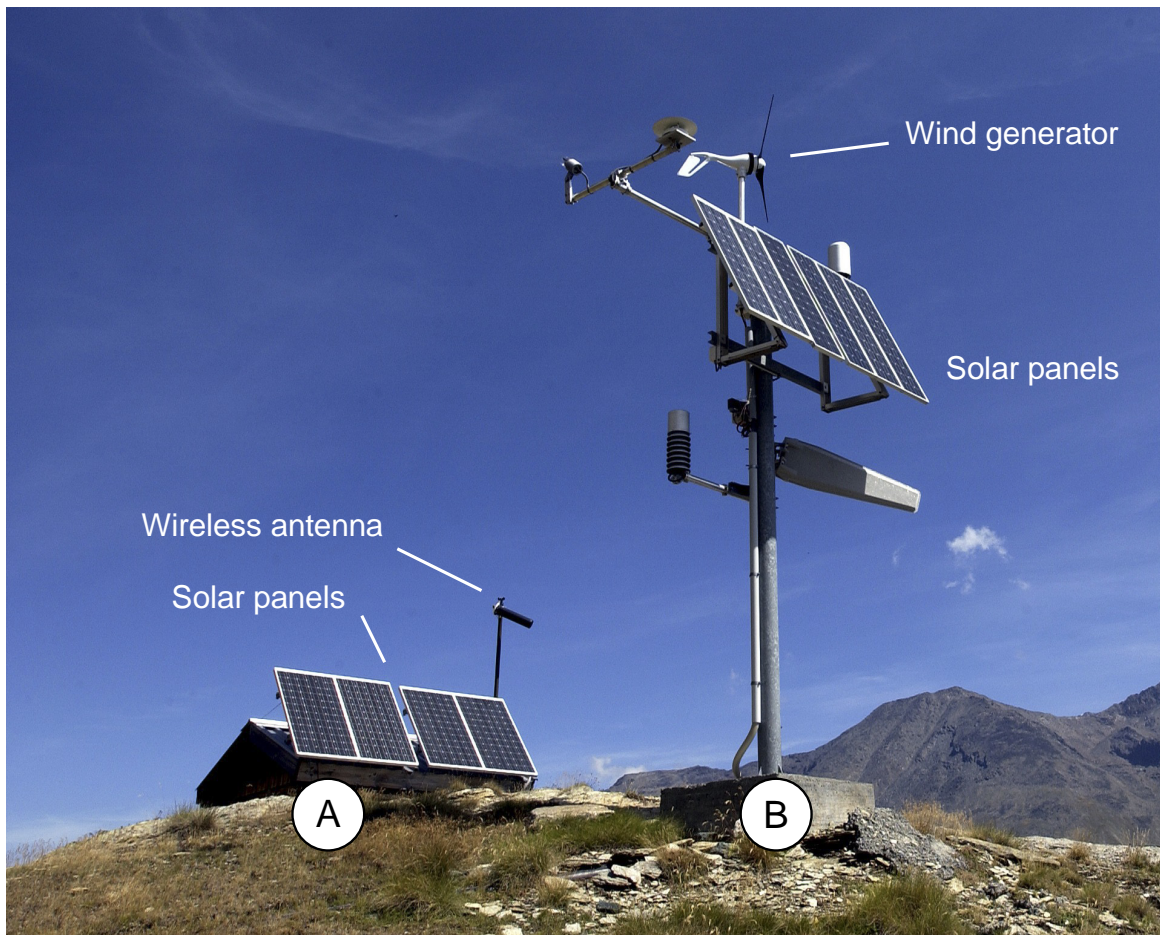


Figure 3.9: Small hut (A) and climatic station (B) at the central recording site (Figure 3.1). 4 m^2 solar panels and a wind generator provided the on-site power, and wireless Ethernet allowed remote access.

Electrical power for the entire monitoring system was generated by solar panels and a wind generator (Figure 3.9). During the absence of sufficient sun radiation and/or wind, battery packs (24V/600 Ah) ensured autonomy for approximately 10 days. The batteries were recharged during subsequent sunny/windy periods.

3.5 MODES OF OPERATION AND DATA HANDLING

Data flow from the seismic (and geotechnical) sensors distributed across the Randa study site was primarily uni-directional: from the sensors via a variety of equipment to the analyst. Several tasks (e.g., function tests, parameter setting, system maintenance) required bi-directional communication between the analyst and the acquisition system. Some of these tasks were fully automatic, whereas others required interactive input or a trigger to start up.

Many of these tasks required reliable communication between the network components. Communication technology and data handling are discussed in the next section. A brief overview of the automatic procedures for managing the accumulated data and maintaining functionality of the network follows.

3.5.1 Network communication

The setup and basic functions of the entire microseismic-geotechnical monitoring system are shown in Figure 3.10. Data were transferred on a regular basis from the on-site field PC via an approximately 2 km long wireless Ethernet connection to a desktop PC located in a building of the Randa local authorities in the valley. To control the system and transfer small amounts of data, the desktop PC was accessed by telephone from ETH Zurich. The large volumes of seismic data were dumped to digital audio tape (DAT's) and sent by mail on a regular basis to Zurich.

Data from the piezometers, inclinometers, and surface extensometers were digitized and automatically collected by a data logger and transferred via a RS-232 interface to the central recording site. The relatively small amount of data produced by these instruments was downloaded via the telephone link.

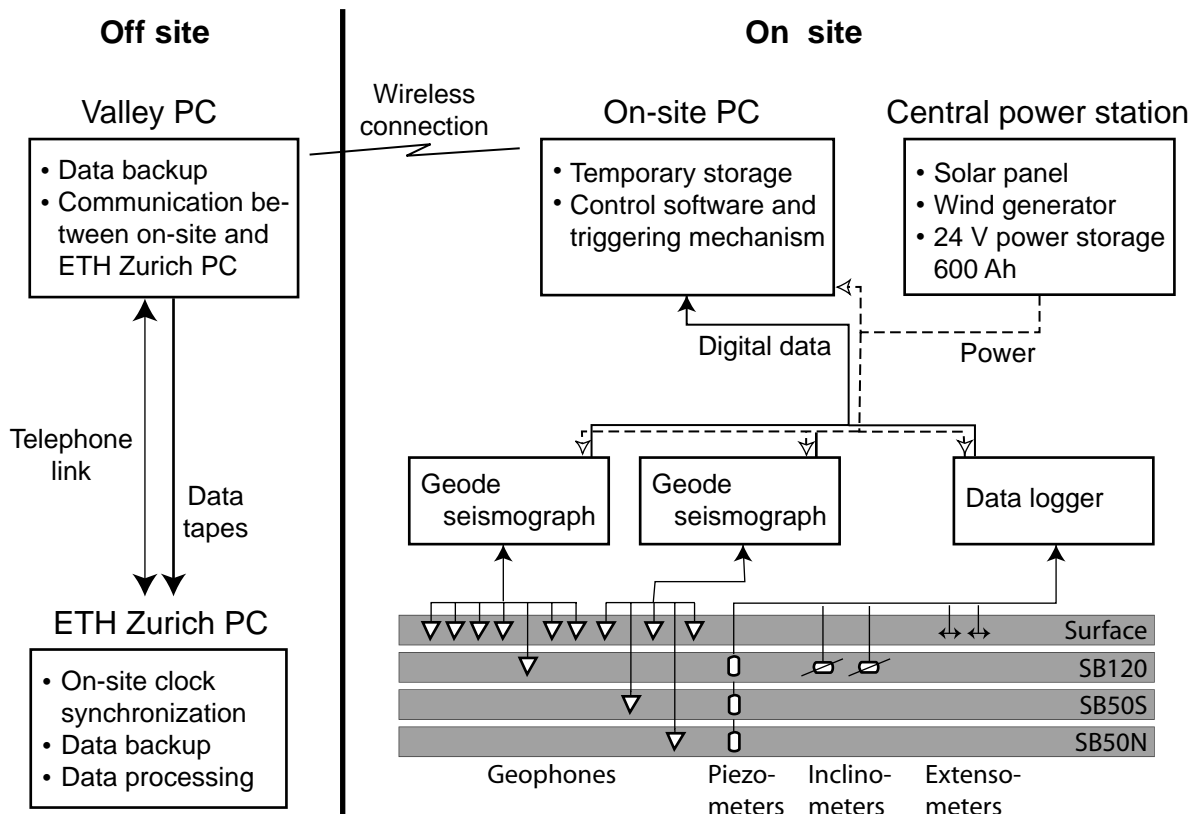


Figure 3.10: Sketch of the monitoring system. Data flow from the diverse sensors to ETH offices is shown by black arrows. Dashed lines indicate the flow of electrical power.

3.5.2 Automatic and interactive network control

Well-determined timing is a critical element of any seismic network. The system clock of the on-site field PC was updated on a daily basis from ETH.

From 2004 onwards, occasional power fluctuations locked the *Geodes* in an inoperative state. To prevent long down-times, we installed an automatic error detector that initiated a complete system restart on activation. This happened several times a day.

Interactive remote access to the on-site field PC allowed me to check and update trigger parameters, perform error diagnosis, and inspect the data. Access to the desktop PC in the valley enabled me to initiate the dumping of the data to tapes. Exchange and mailing of the tapes was kindly provided by the local Randa authorities.

3.5.3 Seismic event triggering

The *Geode* seismographs were run by the commercial software package MGOS V7.15 provided by the manufacturer *Geometrics Inc.* Included in this software was a self trigger option for detecting events. The detection algorithm calculated the average signal

energy in short- and long-time windows (so-called STA's and LTA's) and then computed STA/LTA ratios (Lee and Stewart, 1981). Once the STA/LTA ratio exceeded a certain threshold on one or more specified channels, a file containing data from all geophones was created. Details on the various trigger settings at the Randa network are given in Table 3.3.

Table 3.3: Sampling and trigger parameters for the Randa microseismic network.

Date	Sampling rate [Hz]	Record length [s]	Trigger geophone	LTA [ms]	STA [ms]	ratio
2002-01-01	16'000	4.0	S3, S9	500	30	10
2002-04-27	8'000	8.0	S3, S4, S9	500	40	40
2003-04-01	8'000	8.0	S3, S4, S9, B2	500	40	40
2003-08-01	8'000	8.0	S3, S4, S9, B2	500	50	40
2003-10-01	4'000	16.0	S3, S4, S9, B2	500	50	40

The microseismic monitoring network was in service from January 1, 2002 until July 31, 2004. During this time, 66,409 events that required ~1 Terabyte disk space were recorded. For some periods, the seismic network triggered nearly every minute, resulting in a peak recording rate of ~850 events per day. Early analysis of about 9000 records demonstrated that the majority of the acquired data consisted of noise, so called *transients*. The processing required to separate the triggered events into various categories is explained in section 4.12. Here, I describe my manual arrival-time picking scheme. These times are used in the non-linear probabilistic technique used to locate the microearthquakes within the unstable Randa mountain slope (see Chapter 4).

3.6 ESTIMATING ARRIVAL TIMES

Arrival times required to locate microearthquakes within the unstable slope at Randa were manually picked. I wrote a MATLAB graphical user interface (PickGui) to analyze data windows that contained the first-arriving wave-trains (B in Figure 3.11). Picking of the onsets at each geophone was then performed on a second screen (Figure 3.12) that showed the three-component data in combination with the total signal amplitude

$$A_k = \sqrt{x_k^2 + y_k^2 + z_k^2}, \quad (3.7)$$

where x_k , y_k , and z_k are the digital seismic waveforms recorded at the individual sensors. The picked arrival-times were used to derive very preliminary locations using a standard linearized approach and a homogeneous full-space model. To identify gross picking errors,

predicted arrivals based on these locations were displayed with each suite of recordings (Figure 3.11).

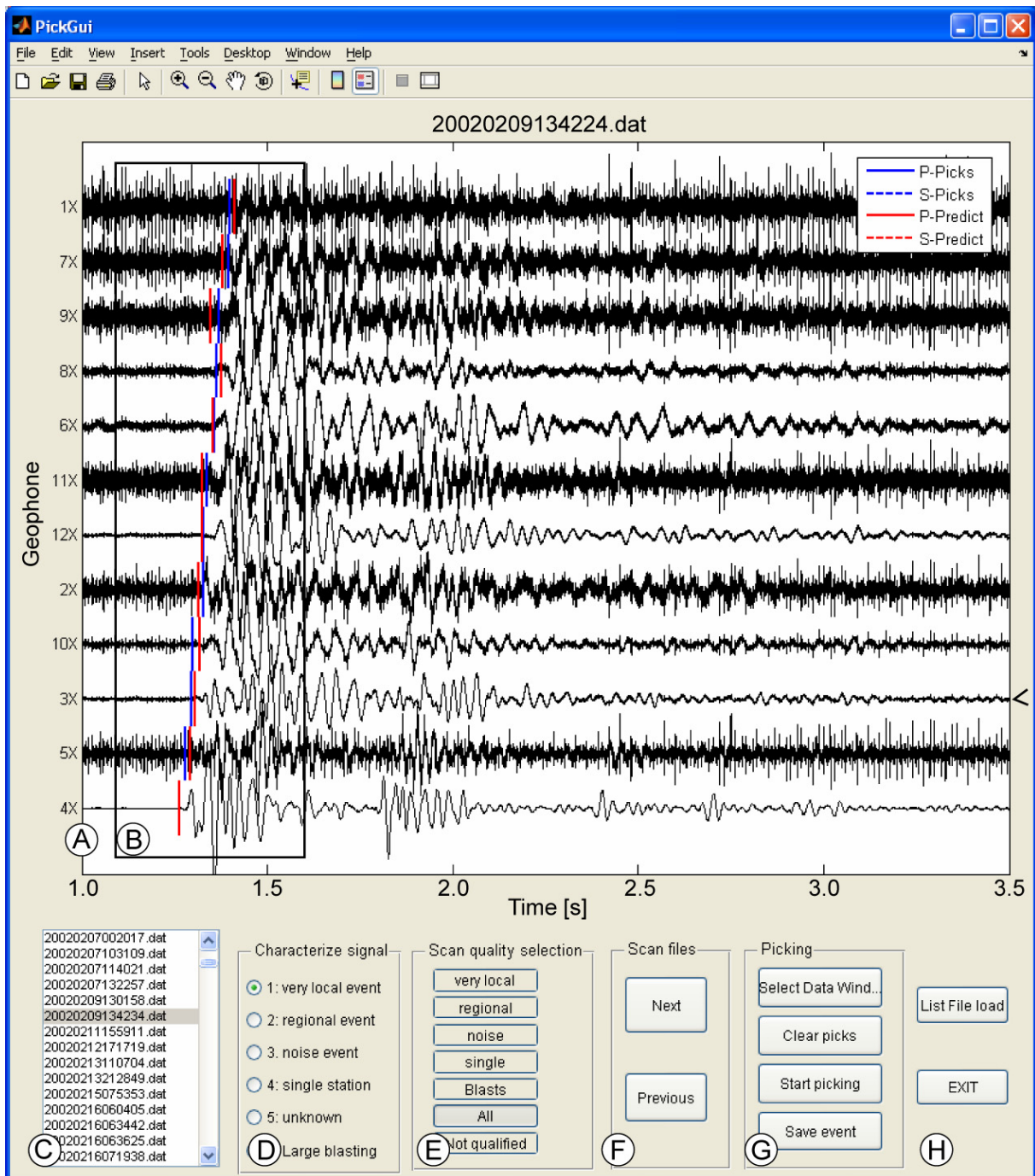


Figure 3.11: PickGui tool showing (A) single component data with (B) data selection window, (C) list of accessible files, (D) buttons to re-classify events, (E) buttons to specify file browser classification, (F) file browser buttons, (G) picking commands, and (H) data load and exit commands. Blue and red solid bars show picked and predicted P-onsets. Small arrow to the right denotes the active trace in the PickWindow (Figure 3.12).

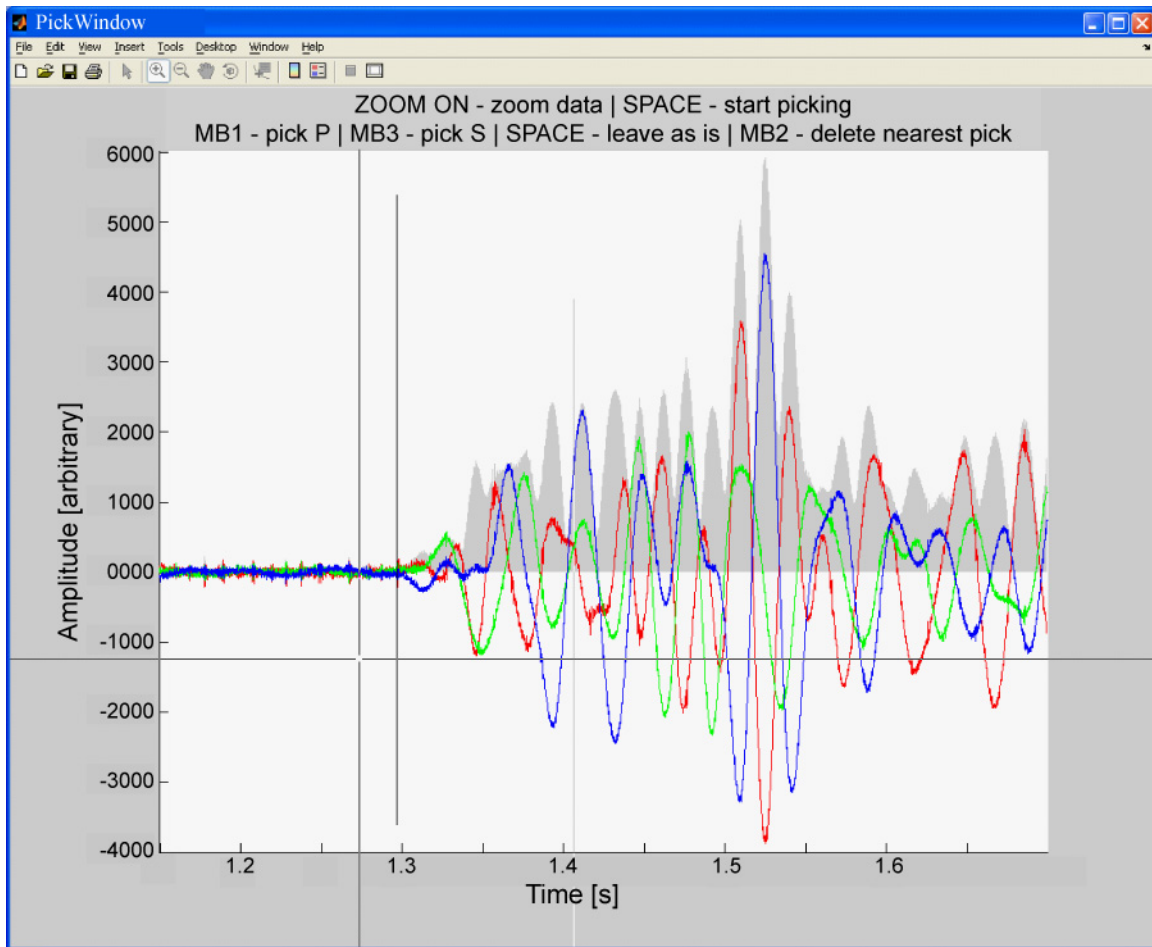


Figure 3.12: Pick window showing three component data (green, blue, and red for x_k , y_k , and z_k) and the total signal amplitude A_k (gray). Vertical black line indicates picked P-onset, black crosshair is picking cursor.

4 Microseismic investigation of an unstable mountain slope in the Swiss Alps

Thomas Spillmann, Hansruedi Maurer, Alan G. Green, Björn Heincke, Heike Willenberg, and Stephan Husen

submitted to Journal of Geophysical Research

Abstract

Risks associated with unstable rocky slopes are growing as a result of climate change and rapid expansions of human habitats and critical infrastructure in mountainous regions. To improve our understanding of mountain slope instability, we developed a microseismic monitoring system that operates autonomously in remote areas afflicted by harsh weather. Our microseismic system comprising twelve 3-component geophones was deployed across ~60,000 m² of rugged crystalline terrain above a huge recent rockfall in the Swiss Alps. During its 31-month lifetime, signals from 223 microearthquakes with -2 to 0 moment magnitudes were recorded. Determining the hypocenters was challenging for several reasons: (i) highly heterogeneous P-wave velocities that varied abruptly from < 1.5 km/s to > 3.8 km/s, (ii) inaccurate or shortage of first-break picks for some microearthquakes, (iii) no reliable S-wave picks, and (iv) numerous microearthquakes just outside the network boundaries. These issues were addressed by linking a 3-D P-wave velocity model of the mountain slope determined from tomographic refraction data with a non-linear probabilistic location technique that provided hypocenter parameters as probability density functions containing all plausible solutions and complete uncertainty information. Recordings from geophones at different altitudes and in boreholes constrained microearthquake depth estimates. Most microearthquakes were found to be concentrated within 50-100 m of the surface in two zones, one that followed the recent rockslide scarp and one that spanned the volume of highest fracture zone/fault density. These two active zones delineated a mass of rock that according to geodetic measurements has moved towards the scarp at 1-2 cm/year.

4.1 INTRODUCTION

Risks associated with sudden mountain-slope failures are escalating as a result of increases in exceptional climatic events and accelerated melting of alpine permafrost due to global warming and rapidly expanding population centers, lifelines, and other critical infrastructure within mountain valleys (Schuster, 1996; Bader and Kunz, 2000; Glade et al., 2005a; Geertsema et al., 2006). To mitigate the effects of mountain-slope failures, robust protective barriers and early warning systems need to be constructed in the most vulnerable regions. Such installations require reliable information on the locations and key characteristics of unstable rock masses.

Conventional strategies for identifying unstable mountain slopes and estimating the volumes, lithologies, and physical properties of susceptible rocks have involved geomorphological and geological mapping and geotechnical investigations (Brunsdon and Prior, 1984; Turner and Schuster, 1996; Glade et al., 2005a). Relatively recently, various remote sensing techniques have allowed large mountainous areas to be rapidly examined (Mantovani et al., 1996; Hervás et al., 2003; Metternicht et al., 2005) and diverse geophysical methods have been used to investigate unstable and adjoining stable rock at depth (McCann and Forster, 1990; Hack, 2000). As examples, geoelectrical, electromagnetic, seismic refraction, and surface wave surveys have supplied valuable information on the spatial variations of electrical resistivity and seismic velocity (Bruno and Marillier, 2000; Cummings, 2000; Havenith et al., 2000; Jongmans et al., 2000; Mauritsch et al., 2000; Schmutz et al., 2000; Dussauge-Peisser et al., 2003; Meric et al., 2005; Brückl and Brückl, 2006; Godio et al., 2006; Heincke et al., 2006a) and high-resolution seismic reflection and ground-penetrating radar (georadar or GPR) studies have yielded vivid subsurface images of active fractures and faults (Bruno and Marillier, 2000; Dussauge-Peisser et al., 2003; Heincke et al., 2005, 2006b; Spillmann et al., 2006).

Most of the above mentioned approaches only provide information on the static characteristics of the ground. Yet, detailed knowledge on the kinematic and dynamic conditions of mountain slopes is essential for understanding and predicting catastrophic rockslide failures (Erismann and Abele, 2001; Kilburn and Petley, 2003; Eberhardt et al., 2004a; Stead et al., 2006; van Westen et al., 2006). To tackle this issue, traditional methods for determining movements in unstable regions (i.e., geodetic networks and point strain measurements; Dunncliff, 1988; Jaboyedoff et al., 2004) are being complemented by modern GPS, interferometric synthetic aperture radar, and airborne laser altimetry techniques (Gili et al., 2000; Tarchi et al., 2003; Antonello et al., 2004; Hilley et al., 2004; Catani et al., 2005; Metternicht et al., 2005; Bulmer et al., 2006; Burgmann et al., 2006; Glenn et al., 2006; Marcato et al., 2006), all of which are capable of supplying high-resolution displacement data over large areas.

In addition to these purely kinematic techniques, studies of microseismic activity have the potential to provide information crucial for improving our understanding of mountain slope instabilities. Microseismic monitoring can be used to track the movements of

various types of material. It is a well established method in studies of volcanoes (Vilardo et al., 1996; De Natale et al., 1998; Lomax et al., 2001; Pezzo et al., 2004; Presti et al., 2004; Lippitsch et al., 2005), fracturing and fluid flow in hydrocarbon reservoirs and hot-dry-rock systems (Jupe et al., 1992; Jones et al., 1995; Rutledge et al., 1998; Vécsey et al., 1998; Moriya et al., 2002; Oye and Roth, 2003; Evans et al., 2005a), mining-induced earthquakes (Gibowicz et al., 1991; Trifu and Urbancic, 1996; Iannacchione et al., 2005), and major tectonic faulting (Malin et al., 1989; Ito et al., 2002; Schorlemmer and Wiemer, 2005). It is starting to play an increasingly important role in investigations of unstable hill and mountain slopes (Rouse et al., 1991; Gomberg et al., 1995; Scheikl et al., 2000; Eberhardt et al., 2004b; Amitrano et al., 2005; Brückl and Parotidis, 2005; Merrien-Soukatchoff et al., 2005; Roth et al., 2005).

As part of a multidisciplinary effort to understand the physical processes that lead to mountain slope instability and failure (Eberhardt et al., 2001, 2004a, 2004b; Willenberg et al., 2002, 2003; Willenberg, 2004; Heincke et al., 2005, 2006a, 2006b; Green et al., 2006; Spillmann et al., 2006), we have been monitoring microseismic activity across a well-studied mountain slope that lies directly above a scarp generated by the largest rockslide in recent Swiss history. Many of the following issues confronted during our pilot microseismic study are likely to influence microseismic investigations of other collapsing mountainous terrains:

- Dangerously steep slopes (Figures 4.1b and 4.1c) limited the emplacement of seismic sensors, such that the aperture of the microseismic network was less than optimal.
- The inevitable harsh weather conditions and remoteness of the high mountain made it difficult to maintain continuous operation of the network during its 31-month lifetime.
- The recorded data were plagued with noise transients, some of which were undoubtedly caused by spherics (due to near and distant lightning storms) and other electrical disturbances associated with the resistive environment of the high mountain and the long recording cables.
- P-wave seismic velocities of the crystalline rocks varied abruptly from very low values of <1.5 km/s to more normal values of >3.8 km/s, such that locating the microearthquakes in the extremely heterogeneous environment was a major challenge.

- Strong scattering and absorption resulted in most seismograms having rather emergent P-phases and generally complex codas with only poorly identifiable S-phases.

After briefly introducing the study site and results of related geological and geophysical investigations, we describe the essential details of our microseismic monitoring system. We then focus on the detection and location of microearthquakes within the unstable rock mass, emphasizing the importance of our independently determined 3-D tomographic velocity model and the probabilistic approach we employ for estimating the hypocenter parameters. We conclude with an integrated interpretation of the resultant microseismicity pattern, displacement rates defined by point strain estimates, and major fracture zones/faults.

4.2 RANDA STUDY SITE

4.2.1 The 1991 Randa rockslides

As a result of two major rockslides during the Spring of 1991, approximately 30 million m³ of crystalline rock plunged into the Matter Valley from a high mountain slope overlooking the village of Randa in southwest Switzerland (Figure 4.1; Schindler et al., 1993; Sartori et al., 2003). The dislocation of the rock created a ~700 m high scarp on the side of the mountain and a huge debris cone that obliterated holiday apartments and barns, blocked the only land route to the major tourist resort of Zermatt, and dammed the Matternvispa River, causing flooding in upstream areas of the valley.

4.2.2 Geology and fracture/fault systems

Our knowledge of the geology of the mountain slope is based on extensive rock outcrops (Figures 4.1b and 4.1c), analyses of aerial photographs, and interpretations of televiewer and geophysical logs recorded in three moderately deep boreholes (SB120, SB50S, and SB50N with lengths of 120.8, 52.2, and 51.0 m, respectively; Figure 4.1c). The upper part of the slope is dominated by heterogeneous gneisses with a strong 20-25° west-southwest-dipping foliation and three major fracture zone/fault systems (Willenberg, 2004). One system parallels the bedrock foliation. Fracture zones/faults of this system can be traced on surface-based 3-D georadar data from their exposures at the surface to 10-20 m depth (Heincke et al., 2005, 2006b). The other two systems are steeply dipping, with strikes ranging from northeast-southwest to northwest-southeast (Figure 4.2a). Borehole georadar reflection data and semblance-migrated versions of the surface-based georadar data allow

many steeply dipping fracture zones/faults to be mapped to depths as great as 75 m (Heincke et al., 2006b; Spillmann et al., 2006). The instability of the mountain slope appears to be strongly influenced by the steeply dipping fracture zones/faults, some of which have openings of tens of centimeters and are actively moving (Willenberg, 2004; Spillmann et al., 2006).

4.3 RANDA MONITORING SYSTEMS

4.3.1 Geodetic-geotechnical-meteorological monitoring systems

Shortly after the 1991 rockslides, a monitoring system comprising geodetic reflectors, surface extensometers, and meteorological stations was installed on the mountain slope (Jaboyedoff et al., 2004). The distances of the geodetic reflectors to various stable points have since been monitored using an electronic distance meter and the relative positions of selected reflectors have been determined via triangulation. At the beginning of our project, an independent geotechnical monitoring system was established. It included borehole extensometers, inclinometers, and piezometers and additional surface extensometers (Willenberg, 2004; Spillmann et al., 2006). Some of these new instruments supplied data on a semi-continuous basis to the ETH data processing laboratory via links to the microseismic system (Figure 4.3; see next section), whereas others provided data only when accessed by on-site personnel.

The geodetic observations and surface displacement measurements suggest that 2.7-9.2 million m³ of the rock mass is moving southwestward towards the scarp at 1-2 cm/year (see solid arrows in Figures 4.2a and 4.2b; Eberhardt et al., 2001; Jaboyedoff et al., 2004; Willenberg, 2004). Displacements at the surface are greatest near the scarp, decreasing to zero at distances >150 m from the scarp edge, whereas those in the boreholes appear to be concentrated at the intersections of major discontinuities. Most significantly, movements have been detected near the base of borehole SB120, suggesting that instabilities extend to > 120 m depth (Figures 4.1c and 4.2b; Willenberg, 2004).

4.3.2 Microseismic monitoring system

Our microseismic network was deployed across topographically rugged terrain above the rockslide scarp at elevations of 2285-2450 m (Figures 4.1c and 4.2). It included nine 3-component 8 Hz geophones (S1-S9) in 0.3-4.6 m deep holes and three 3-component 28 Hz geophones (B1-B3) at depths of 113.5, 42.7, and 43.2 m in boreholes SB120, SB50S, and

SB50N, respectively. Positions of the outermost network geophones S2, S4, and S7 were limited by the dangerously steep slopes at greater distances (Figure 4.1c). The maximum north-south and east-west apertures of the network (i.e., the distances between the furthest geophones) were both ~250 m.

The microseismic data acquisition system and the ETH geotechnical equipment were designed to operate under harsh weather conditions in an isolated high-mountain environment. Analog cables connected the geophones to two Geode 24-bit multichannel seismographs and the geotechnical sensors to A/D converters and a data logger. Solar panels and a wind generator were the principal sources of energy for all instruments. When there was neither sun nor wind, large battery packs ensured autonomous operation of the instruments for approximately 10 days. The battery packs were recharged during subsequent sunny/windy periods.

An on-site field PC controlled the entire data acquisition system and temporarily stored large volumes of triggered microseismic data. To detect microearthquakes, we employed a standard trigger algorithm based on short-time averages (STA) and long-time averages (LTA) of the incoming signals. For example, by setting the lengths of the STA and LTA windows to 40 and 500 ms, respectively, a single station was considered to have triggered when $STA/LTA \geq 40$. A single trigger resulted in the recording of 8 s of data from all twelve 3-component geophones. The data were sampled at a rate of 8000 Hz.

All data were transferred to a desktop PC in the valley below to be temporarily stored and written to tapes that were regularly shipped to the ETH data processing laboratory. A land telephone link enabled us to access the desktop PC in the valley and through a radio connection between the desktop and on-site field PC's we were able to control the data acquisition system. During its 31 month deployment, the microseismic system was fully operational 81% of the time. For a three-month period in 2002, the operational parameters of the system were reconfigured to allow the network to become an important component of the 3-D tomographic seismic refraction survey (Heincke et al., 2006a).

4.4 INITIAL PROCESSING OF THE RANDA MICROSEISMIC DATA

A total of 66,409 triggered events were recorded between January 1, 2002 and July 31, 2004, corresponding to approximately 1 Terabyte of data. A selection of the various types of event is presented in Figure 4.4. To identify efficiently recordings generated by

microearthquakes in the vicinity of the unstable mountain slope, we first designed and implemented a semi-automatic two-step pattern recognition procedure (Appendix 4.12). Those events recognized by this procedure as possible microearthquakes were then analyzed manually. Application of this combined scheme led to the identification of (i) 55,563 noise transients generated by electrical disturbances, (ii) 10,432 recordings that contained either noise, low coherency events, generally weak signals, or emergent signals probably originating from distant earthquakes and explosions, (iii) 206 regional earthquakes (such events often occur in the western Swiss Alps; Maurer and Kradolfer, 1996), and (iv) 223 mountain slope events comprising 129 sequences of multiple microearthquakes and 94 single microearthquakes. The microearthquake recordings were characterized by moderately high-frequencies (mostly less than < 200 Hz) and short durations.

Unfortunately, the overall data quality of the mountain slope microearthquake recordings was not high. Only about ten tremors generated seismograms with signal-to-noise ratios as high as the single event shown in Figure 4.4. Nevertheless, we could pick 2,118 first-arrival P-wave times for the 223 single and multiple microearthquakes (first-arrival times were only picked for the most prominent event in any sequence). A minimum of 5 first-arrival P-wave times was available for all 223 microearthquakes.

Although polarization analyses demonstrated the presence of S-wave energy in many seismograms, it was extremely difficult to determine S-wave onset times with sufficient accuracy to be useful for microearthquake location purposes. Furthermore, coherent S-wave arrivals were not observed on any microearthquake seismic section (i.e., plots of the recorded data arranged according to their first-arrival times). There were a variety of possible explanations for this. As a consequence of the moderate frequency content of all microearthquake recordings, the first P-wave pulse or its coda interfered with the first S-wave arrivals at all geophones close to the events. Moreover, the very strong velocity contrasts of the mountain slope rocks (see next section) undoubtedly resulted in the generation of P-to-S converted waves, which again would have interfered with the pure S-waves; because of strong velocity heterogeneity, the effects would have been different at different azimuths relative to the microearthquakes. Finally, the moderate frequency content of the recordings at short distances suggests that anelastic attenuation was generally high, such that S-wave energy would have suffered significant absorption .

4.5 3-D SEISMIC MODEL

An accurate velocity model is required for reliably locating earthquakes in highly heterogeneous media (Lomax et al., 2000; Lomax et al., 2001; Husen et al., 2003; Husen and Smith, 2004; Presti et al., 2004). It is especially important for earthquakes located near or outside the boundaries of microseismic networks and/or for traveltimes data sets lacking reliable S-wave information. To obtain the necessary detailed velocity information, we benefited from a comprehensive 3-D tomographic seismic refraction survey across a large region of the mountain slope (Heincke et al., 2006a).

Our 3-D seismic refraction survey comprised five profiles parallel to the general downslope direction, three profiles perpendicular to it, 33 source locations slightly offset from the profiles and the twelve 3-component geophones of the microseismic network (Figure 4.2a). Source and geophone spacings along the 126-324 m long profiles were 4 and 2 m, respectively. Small explosive charges of 5 - 50 g² detonated in 0.5-0.7 m deep holes provided the sources of seismic energy. Shots along the profiles were recorded by geophones along the respective profiles and by the entire microseismic network, whereas shots at the offset source locations were recorded on geophones along all profiles and, again, by the entire network.

From the >99,000 recorded traces we were able to pick 52,600 first arrivals with an accuracy of better than ~5 ms. A 3-D tomographic inversion of these traveltimes revealed a highly heterogeneous rock mass dominated by a broad northeast-southwest trending zone of remarkably low seismic velocities (Figure 4.5a; Heincke et al., 2006a). Velocities of < 1.5 km/s occurred over a 200 x 100 m area extending to ~25 m depth and velocities of 1.5-2.7 km/s could be traced to various depths across a large segment of the mountain slope. Continuous tracts of rock with velocities >3.8 km/s were only found in the northwest part of the site. Blocks of relatively high velocity material were detected within the mostly low velocity regions and vice versa. Heincke et al. (2006a) suggested that the low velocities

² We used only small charges to avoid damaging the sensitive high alpine environment and possibly increasing mountain slope instability.

resulted from the presence of numerous dry cracks, fractures, and faults at a wide variety of length scales.

To account for the possibility that some microearthquakes occurred exterior to the microseismic network boundaries, it was necessary for us to define velocities beyond the limits of the 3-D velocity model. For this purpose, we derived from the 3-D velocity model an average 1-D velocity model that followed the topography and then expanded the volume of investigation to include a much larger portion of the mountain slope. The 1-D velocity model was then employed as the initial input model for a new 3-D tomographic inversion. Well-constrained velocities within the new model, which matched those of the original 3-D model, graded relatively smoothly to values defined by the input 1-D velocity model (Figure 4.5b). We emphasize the limited accuracy of velocities not explicitly determined from the 3-D tomographic survey data.

4.6 DETERMINING EARTHQUAKE LOCATIONS

It is clear that we need an earthquake location scheme that accounts for strong 3-D velocity heterogeneity. This scheme should also provide realistic estimates of location uncertainty in the presence of a variety of factors that cause the computational process to be ill conditioned. These factors include the relatively large reading inaccuracies (~ 5 ms) of many first-arrival P-waves, a paucity of first-arrival P-wave times for some events, the lack of reliable S-wave information, and the occurrence of a large number of tremors just outside of the microseismic network boundaries.

Traditional methods for locating earthquakes involve iteratively solving linearized approximations to the equations that connect hypocenter parameters and origin times to the observed traveltimes and velocity structure of the Earth (Lee and Stewart, 1981). Estimates of hypocenter parameter uncertainty, usually assumed to be normally (Gaussian) distributed, are provided by error ellipsoids defined by the diagonal elements of the model covariance matrix (Menke, 1989). Although traditional methods work well in many circumstances, recent work based on synthetic and field examples and 1- and 3-D velocity models highlight their shortcomings when the inversion process is ill conditioned (Lomax et al., 2000; Husen et al., 2003; Presti et al., 2004; Lippitsch et al., 2005). Under such conditions, the estimated locations may be far from the true ones and the estimated uncertainties may be highly inaccurate; the error ellipsoids may not even encompass the true event positions. Most

importantly, the locations of earthquakes that appear to be well determined may transpire to be very poorly constrained when more exact techniques are employed (e.g., see Lippitsch et al., 2005).

As expected, traditional earthquake location methods provided flawed information at the Randa study site. Accordingly, to estimate the distribution of hypocenter parameters we have used the comprehensive nested-grid search version of Lomax et al.'s (2000) implementation of Tarantola and Valette's (1982) non-linear probabilistic location technique. This technique has previously been used to locate earthquakes in topographically rugged and highly heterogeneous volcanic terrains (Vilardo et al., 1996; De Natale et al., 1998; Lomax et al., 2001; Presti et al., 2004; Husen and Smith, 2004; Lippitsch et al., 2005).

As for the traditional methods, the input data to the non-linear probabilistic location technique include the arrival times and geometry of the microseismic network, and a reliable representation of the Earth's velocity structure is needed. In addition, the probabilistic technique requires the uncertainties in the arrival times and theoretical traveltimes to be defined by probability density functions (PDF's). By using Gaussian distribution functions to represent these input PDF's, the output hypocenter PDF's can be analytically derived (Tarantola and Valette, 1982).

It is relatively straightforward to incorporate arbitrarily complicated velocity models in the probabilistic location technique (Lomax et al., 2000; Presti et al., 2004). To minimize computational effort, the traveltimes of seismic waves from the network geophones to all grid points are calculated and stored in the form of look-up tables. Considering that these calculations are usually only required once for a microseismic network, very accurate forward routines can be employed. For example, a 3-D version of Podvin and Lecomte's (1991) finite-difference eikonal solver provides accurate direct-, diffracted-, and head-wave traveltimes in Lomax et al.'s (2000) scheme. For the probabilistic location of earthquakes, it is only necessary to access the look-up traveltime tables on a frequent basis.

A hypocenter PDF provided by the non-linear probabilistic location technique encompasses all likely solutions (i.e., it is a complete probabilistic solution) and includes comprehensive information on the effects of (i) uncertainties in the arrival times and theoretical traveltimes, (ii) any incompatibility of arrival time picks, and (iii) the spatial relationships between the network geophones and the earthquake locations. Although

uncertainties in the arrival times and theoretical traveltimes are usually defined as Gaussian, the non-linear relationships involved in the location process result in the solution uncertainties being non Gaussian (i.e., non ellipsoidal). Indeed, the hypocenter PDF's may be highly irregular (Lomax et al., 2000, 2001; Husen et al., 2003; Husen and Smith, 2004; Lippitsch et al., 2005; Lomax, 2005).

In most earthquake studies, uncertainty can be readily estimated for each arrival time pick, but uncertainties in the theoretical traveltimes (i.e., inaccuracies in the velocity model) are generally poorly known. This is an important limitation in many investigations, because errors in the velocity model may result in systematically biased locations, especially near and outside the boundaries of microseismic networks (Lomax et al., 2000).

For the location of all events in our study, uncertainties are defined by a Gaussian distribution function that represents the ~5 ms reading accuracy of many first arrivals and a Gaussian distribution function that represents a 0.2 ms inaccuracy in the theoretical traveltimes. Although our extended 3-D model is generally well constrained throughout much of the investigation volume, it certainly does not include all small scale velocity heterogeneities that influence the P-wave arrival times. To compensate partly for this shortcoming, we compute and apply station corrections that minimize errors in locating a number of calibration shots (see section 4.7.2). Furthermore, we demonstrate the sensitivity of our microearthquake locations to variations in the theoretical travel times by comparing hypocenters obtained using our 3-D model with those obtained using a constant velocity model.

We display a hypocenter in three forms: (i) a PDF scatter cloud in which the densities of dots are proportional to the probabilities³ or (ii) PDF volumes shown in planar sections by a color scale representation, and (iii) a maximum-likelihood location. Scrutiny of the PDF scatter cloud or volume allows us to estimate the level and type of uncertainty. As examples, tightly grouped dots in the PDF scatter cloud (i.e., a small PDF volume) are evidence for a well-resolved hypocenter, whereas broadly scattered dots in all directions (i.e., a large PDF volume) indicate a poorly constrained one. A tight grouping of dots in the x-y plane and a

³ Each hypocenter PDF is represented by 1000 dots and the volume integral of all probabilities of a PDF is normalized to a value of 1.

broad scatter in the z direction (i.e., a narrow elongated PDF volume) are diagnostic of an event that has a well-resolved epicenter but a poorly constrained depth. Although there may be multiple acceptable solutions, we choose the maximum-likelihood (or minimum misfit) point of the hypocenter PDF as the optimum location.

4.7 PERFORMANCE OF THE RANDA MICROSEISMIC NETWORK

4.7.1 Effect of network size and geometry on the hypocenter estimation process

The size and geometry of the Randa microseismic network was controlled by (i) the position of the steep rockslide scarp and generally rugged topography (Figures 4.1 and 4.2), (ii) our wish to have the geophones located or within the bedrock, (iii) a limit on the number of 3-component geophones available for the 31-month duration of the project, (iii) the need for the geophones to be reasonably close to the two Geode seismographs and power sources (Figure 4.3) to minimize cable lengths and, thus, the effects of atmospheric and ground-based electrical disturbances. To determine the influence of the network's size and geometry on the hypocenter estimation process, we performed a simple synthetic experiment in which the effects of velocity heterogeneity and uncertainties in arrival time picks were explicitly excluded. We created a model that simulated the 3-D topography of the unstable mountain slope, the true locations of the microseismic network of geophones, and 16 earthquakes situated at different depths within two planes (Figure 4.6). Constant P-wave velocities above and below ground level were set to 0.3 and 2.5 km/s, respectively. Noise-free arrival times were determined for P-waves traveling from the simulated earthquakes to all network geophones. We then used the non-linear probabilistic location technique to determine the hypocenter PDF's and maximum-likelihood locations displayed in Figure 4.6. For this case and the calibration exercise described in the next section, we allowed the grid-search program to seek solutions above the ground to the limit of the model space. In contrast, to locate the microearthquakes we excluded the region exterior to the rock mass from the search process.

Although the maximum-likelihood locations coincide with the true hypocenters throughout the mountain slope (Figure 4.6), the varying shapes and sizes of the hypocenter PDF scatter clouds highlight the very different confidence levels assigned to each location estimate. Within the network boundaries, the scatter clouds are generally symmetric with diameters mostly less than 30 m in planes parallel to the mountain slope (Figure 4.6a) and

somewhat elongated in planes perpendicular to it (Figure 4.6b). Elongation increases with hypocenter depth. Nevertheless, because geophones are located in moderately deep boreholes and distributed over a wide range of elevations, the well-known ambiguity in earthquake depth estimate is relatively minor in the top ~50 m of our study site. Outside of the network boundaries, the dimensions of the scatter clouds and resultant uncertainties in earthquake locations increase significantly. Since we allowed the search space to extend above the ground, earthquakes close to the surface and mountain edge are better determined than indicated by the sparse nature of their scatter clouds.

4.7.2 Calibration of the network using small test shots: station corrections

To enhance the accuracy of our hypocenter parameter estimates, we have calibrated the microseismic network using a number of small test shots detonated at various locations across the study site. These shots were not included in the derivation of the 3-D velocity model. Traveltimes from twelve of the test shots grouped together in five small areas (SG1 - SG5 in Figures 4.7- 4.9) were sufficiently well determined (~5 ms reading accuracy) to be useful in the calibration procedure. Two of the shot groups were positioned within the network (SG2 and SG4 in Figure 4.7), two were located along network boundaries (SG1 and SG3), and one was situated northwest of the network (SG5)

We began by computing for each calibration shot the root-mean-square (RMS) difference between the observed traveltimes and predicted traveltimes based on the true shot location and six different velocity models: the extended 3-D velocity model of Figure 4.5b and five homogeneous models with velocities between 2.0 and 5.0 km/s. The RMS differences varied from 6-40 ms, with nine of the twelve differences below 10 ms based on the 3-D velocity model and three based on the 2.5 km/s constant velocity model (Figure 4.8a). To improve the traveltime predictions, we averaged the traveltime differences at each geophone to produce a suite of azimuthally invariant station corrections⁴ for each velocity model. These corrections partly accounted for velocity model inadequacies close to the geophones. Application of the station corrections yielded substantially reduced RMS differences of 3-20 ms (Figure 4.8b), with the lowest values (3-8 ms) for all calibration shots

⁴ The geographic distribution of successful calibration shots was insufficient for the computation of azimuthally dependent station corrections.

based on the 3-D velocity model (Figure 4.8b). The average of the RMS differences for the extended 3-D-velocity-model calculations was ~ 5 ms, practically the same as the reading accuracy of many calibration-shot and microearthquake recordings. We have applied station corrections to all recorded data sets before subjecting them to the non-linear probabilistic location technique.

Using the six velocity models, we determined the hypocenter PDF's and maximum-likelihood locations of the twelve calibration shots. As demonstrated by Figure 4.9, the absolute misfits of the maximum-likelihood locations were highly variable. The lowest misfits were mostly based on the 3-D velocity model, with the epicenters mislocated by 1-40 m (most mislocations were ≤ 21 m), and the depth estimates incorrect by 0-18 m (most depth errors were ≤ 8 m). The 2.0-3.0 km/s constant velocity models produced plausible hypocenter PDF's and maximum-likelihood locations for some calibration shots, but not for others. For example, Figures 4.7a and 4.7b show that several of the calibration shots occurred along the boundaries or completely outside of the PDF scatter clouds based on the constant 2.5 km/s model. By comparison, all calibration shots are enclosed by the respective hypocenter PDF scatter clouds based on the 3-D velocity model (the single shot of the SG2 group occurred along the boundary of its PDF scatter cloud; Figures 4.7c and 4.7d). It is noteworthy that the hypocenter uncertainties are uniformly higher for the 3-D velocity model than for the constant 2.5 km/s model. As for the synthetic examples of Figure 4.6, the PDF scatter clouds in Figure 4.7 are markedly more compact for events inside the microseismic network than for those outside.

4.8 MICROEARTHQUAKE LOCATIONS AND MAGNITUDES

Despite the clear superiority of the extended 3-D velocity model, for comparison purposes we have estimated the hypocenter PDF's and maximum-likelihood locations of all microearthquakes using both the 3-D and constant 2.5 km/s velocity models. We begin by describing probabilistic hypocenter parameters for two very different sets of recordings, one for a microearthquake clearly within the network (Figure 4.10a) and one for a microearthquake that was likely outside (Figure 4.10c), and then present the location results for the entire microearthquake data set.

4.8.1 Two single microearthquakes

The hypocenter PDF's and maximum-likelihood locations for microearthquake-A recordings (Figure 4.10a) are practically identical for computations based on the two velocity models (compare Figures 4.11a and 4.11c with Figures 4.11e and 4.11g). This event occurred directly above borehole geophone B2 (triangles showing the geophone position in Figures 4.11a and 4.11e are covered by the stars depicting the maximum-likelihood locations). The high amplitude signals rich in high frequencies received by the 3-component geophone B2 and the much lower amplitude signals largely devoid of high frequency energy received by all other 3-component geophones (Figure 4.10a)⁵ are in accord with the derived maximum-likelihood locations and associated small PDF volumes.

In contrast to microearthquake A, the hypocenter PDF's and maximum-likelihood locations for microearthquake-B recordings (Figure 4.10c) are very different for the two velocity models (compare Figures 4.11b and 4.11d with Figures 4.11f and 4.11h). Yet, the RMS differences between the observed and predicted arrival times are very similar for the two maximum-likelihood locations (i.e., 9.3 and 10.3 ms). Which of these two very different solutions should we accept: one with a relatively small PDF volume (i.e., seemingly well-resolved) and a maximum-likelihood location that positions the event within the network very close to geophone S4 (Figures 4.11b and 4.11d) or one with a large PDF volume (i.e., poorly constrained) and a maximum-likelihood location that places the event southeast of the network near the rockslide scarp (Figures 4.11f and 4.11h) ?

There are two lines of evidence that support the second solution of a poorly constrained location exterior to the network. First, the recordings at geophone S4 do not contain the high frequencies expected of a nearby microearthquake (Figures 4.10c and 4.10d). Indeed, recordings at all geophones have similar low-frequency coda with comparably flat spectra in the narrow 5-50 Hz frequency band; amplitudes are more than two orders of magnitude lower for frequencies > 100 Hz than for frequencies < 50 Hz. Second, S-wave energy appears to arrive 0.04-0.08 s after the first breaks detected on five of the 3-component recordings displayed in Figure 4.10c. This assertion is supported by the results of

⁵ High amplitudes in the spectra of the B2 traces extend from 5-200 Hz, whereas those in the spectra of the S6 and other recordings are limited to 5-100 Hz (Figure 10b).

the polarization analyses presented in Figure 4.12, in which the dominant particle-motion directions are plotted as a function of arrival time for the five identified recordings⁶. For a relatively distant event more than 100 m below the network (e.g., as shown in Figures 4.11f and 4.11h), the rays and P-wave particle motions should be steeply dipping at the geophones and the S-wave particle motions shallowly dipping. The opposite would be true for an event at the same depth level and close to the network (e.g., as shown in Figures 4.11e and 4.11g). Particle motion directions are $>70^\circ$ for at least the first 0.04 s of the identified recordings (Figure 4.12). They change to shallow dipping at later times, compatible with the arrival of S-wave energy (near the second row of ticks in Figure 4.10c). Between 3.45 and 3.50 s, the particle motions of these recordings are practically horizontal. (Figure 4.12). The observed particle motion directions and the poorly resolved > 0.04 s time gaps between the first P- and S-wave arrivals are consistent with the solution shown in Figures 4.11f and 4.11h, but not with that shown in Figures 4.11b and 4.11d.

4.8.2 Analysis of all microearthquakes

The maximum likelihood epicenters of all microearthquakes obtained for the two velocity models are displayed in Figures 4.13a and 4.13b. There are similarities and notable inconsistencies between the two epicenter patterns. Both show roughly half the events within the microseismic network and half outside and both include concentrations of shallow (i.e., <30 m deep) events near to and beneath the rockslide scarp; a cluster of ~ 70 microearthquakes can be followed below a broad zone of the exposed scarp to well inside the network. Microearthquake A (Figures 4.10 and 4.11) is one of only a small number of well-resolved events that have practically identical maximum-likelihood locations based on the two velocity models. The well-resolved events are mostly situated within the network very close to one or more geophones. Maximum-likelihood locations of other events differ for the two suites of solutions. One consequence of these differences is the much tighter grouping of epicenters in Figure 4.13a than in Figure 4.13b. Based on our analyses of the calibration-test-shot and microearthquake-B recordings, we conclude that the tightly clustered appearance of epicenters in Figure 4.13a is an artifact.

⁶ The dominant particle motion directions were computed from the 3-component recordings using the covariance technique introduced by Flinn (1965).

Comparisons of the epicenter patterns in Figures 4.13a and 4.13b highlight uncertainties associated with inadequacies of the velocity models, but they take no account of the considerable uncertainties caused by arrival time inaccuracies and the less-than-optimal spatial relationships between the network geophones and many microearthquakes. Furthermore, the characteristics of each individual microearthquake are much less important in seismicity pattern analyses than the accumulative characteristics of many such events. For example, a single low magnitude tremor is unlikely to influence greatly the stability of the mountain slope, but many tremors along a limited number of structures could eventually be linked to catastrophic collapse. To address these points, we analyze the sum of hypocenter PDF's computed for all microearthquakes rather than the individual PDF's. Figures 4.13c-4.13f display slices and cross-sections through the two resultant cumulative hypocenter PDF's (one for each velocity model). Within some favorable parts of the network, a cumulative hypocenter PDF may delineate active faults, whereas in others it may only provide sufficient information to distinguish between zones of seismic activity and inactivity (Presti et al., 2004).

As for the epicenter patterns of Figures 4.13a and 4.13b, the cumulative hypocenter PDF's in Figures 4.13c-4.13f reveal general correlations and significant discrepancies between the results provided by the two velocity models. High PDF values in the vicinity of the rockslide scarp and beneath the eastern half of the network are common to the two solutions, but the detailed PDF patterns differ markedly. In addition, the seemingly prominent microseismogenic zone that extends through the cross-section of Figure 4.13e is not observed in Figure 4.13f.

The contrasting hypocenter PDF patterns displayed for the two velocity models in Figures 4.7, 4.11, and 4.13 have demonstrated the importance of incorporating reliable velocity information in the microearthquake location process. For the computation of microearthquake magnitudes and interpretation of microseismicity at the Randa study site, we employ the cumulative hypocenter PDF and maximum-likelihood locations based on our extended 3-D velocity model.

4.8.3 Magnitudes

We computed moment magnitude estimates m for microearthquakes recorded by the Randa microseismic network using the following formulas introduced by Hanks and Kanamori (1979):

$$m = \frac{2}{3} \log M_0 - 6.1, \quad (4.1)$$

where

$$M_0 = \frac{4\pi\rho v_p^3 R \Omega_0}{U}, \quad (4.2)$$

M_0 is the seismic moment, density $\rho = 2.7 \text{ g/m}^3$, P-wave velocity $v_p = 2.500 \text{ km/s}$, R is the hypocentral distance, Ω_0 is the long period amplitude determined from the displacement spectra, and $U=0.52$ is a general correction for the mean radiation pattern (Aki and Richards, 1980).

Application of equations (1) and (2) using hypocentral distances based on the maximum-likelihood locations yielded estimates of m for all microearthquake recordings. Average moment magnitudes and standard deviations were then determined from the 5-12 estimates of m for each event. The resultant average moment magnitudes were mostly in the -2.0 to -0.5 range with an average standard deviation of ± 0.2 (Figure 4.14).

4.9 INTERPRETATION

Our interpretation of microseismicity at the Randa study site is based on detailed analyses of the cumulative hypocenter PDF from different viewing angles (e.g., Figure 4.15) and comparisons of the PDF pattern with diverse geological, geodetic, geotechnical and other geophysical data (Figure 4.16; Eberhardt et al., 2001, 2004a, 2004b; Willenberg et al., 2002, 2003; Willenberg, 2004; Heincke et al., 2005, 2006a, 2006b; Green et al., 2006; Spillmann et al., 2006). Various perspective views of the cumulative hypocenter PDF and slices and cross-sections through it prove to be particularly useful. In the map and two perspective views of Figure 4.15, volumes in which the cumulative PDF values are uniformly $> 3.2 \cdot 10^{-5}$ are opaque and those in which the PDF values are uniformly $< 3.2 \cdot 10^{-5}$ are transparent. Such diagrams represent well our knowledge of microseismic activity at the site. They provide a robust means of identifying and mapping microseismogenic and aseismic zones.

Figure 4.16a brings together information on the topography, fracture zones/faults, geodetically determined movements of the unstable mountain slope, and the minimum lateral extent of the anomalously low-velocity crystalline rocks, whereas Figures 4.16b and 16c show the fracture zones/faults projected on to the PDF slice and cross-section of Figures 4.13d and 4.13f. The orange dashed line in Figure 4.16a delineates the boundary of the

mobile section of the mountain slope, with the highest rates of displacement occurring south of the blue line (Jaboyedoff et al., 2004). The displacements are concentrated across major fracture zones/faults with opening rates of 0.001-0.003 m/year (Willenberg, 2004).

In the following, we describe the principal characteristics of the microseismogenic and aseismic features A to G and review information relevant to defining the boundaries of the unstable section of the mountain slope.

4.9.1 Microseismogenic zones (A, B, D, E, and G)

The highest levels of microseismic activity are observed within microseismogenic zone A near and beneath the rockslide scarp (Figures 4.15 and 4.16). This large zone of enhanced cumulative hypocenter PDF values is approximately 200 m long, 30-100 m wide, and 20-60 m thick. High PDF values extend to the outer limits of the rock mass, such that the southeastern boundary of zone A coincides with the scarp face. Since zone A is mostly outside the microseismic network and the well-resolved part of the extended 3-D velocity model, its internal features and outer boundaries are poorly constrained. Consequently, the microseismicity may not be as widely distributed as suggested by the cumulative hypocenter PDF. Nevertheless, it is significant that a major fracture zone/fault extends the length of zone A (Figures 4.16b and 4.16c; see also the linear feature adjacent to geophone S4 in Figure 4.1c) and that the highest mountain-slope displacement rate (2 cm/year) is recorded within its boundaries (blue cross in Figure 4.16a). Microearthquakes likely occur along the major fracture zone/fault and on the numerous smaller discontinuities that cause this segment of mountain slope to be highly fractured and craggy (Figure 4.1c). Considering the paucity of geodetic reflectors in this area, it is possible that most rocks within zone A are moving relatively rapidly southeastwards.

Microseismogenic zone B is defined by a number of small to moderately large volumes of high PDF values that occur within the region most affected by major fracture zones/faults (Figures 4.15 and 4.16). Although the hypocenters are situated within the boundaries of the network and well-resolved part of the extended 3-D velocity model and are, therefore, relatively well determined, the location uncertainties and the dense distribution of major discontinuities in this region preclude us from confidently assigning individual microearthquakes to specific fracture zones/faults. However, the close proximity of enhanced PDF values to the fracture zones/faults (Figures 4.16b and 4.16c) suggests that the latter are microseismically active. High PDF values along the eastern part of the northern

boundary of zone B do not coincide with any known major discontinuity. We note that zone B is characterized by very low seismic velocities that are generally diagnostic of low quality rock (compare Figures 4.16a and 4.16b; Heincke et al., 2006a).

The scattered volumes of enhanced PDF values that comprise microseismogenic zones D and E are situated near or beyond the boundaries of the microseismic network. As a result, their geometries and locations are poorly constrained. Moreover, they are remote from any mapped fracture zones/faults. Microseismogenic zone D appears to extend from a small terrace above the focus of contemporary surface displacements to approximately 50 m depth. Microearthquakes in zones D and E are evidence for low levels of instability far from the rockslide scarp.

Microseismogenic zone G (only shown on Figure 4.15c) seems to be situated close to the base of our velocity model, approximately 200 m below the surface. We judge this to be a minimum depth estimate; minor microseismicity may extend deeper in the mountain.

4.9.2 Aseismic zones (C and F)

The largely aseismic zone C separates microseismogenic zones A and B from microseismogenic zones D and E. Considering that a large portion of this zone lies within the boundaries of the microseismic network and well-resolved part of the extended 3-D velocity model, the very low cumulative hypocenter PDF values are judged to be reliable. Seismic quiescence may be a consequence of aseismic creep or negligible movements. The lack of major fracture zones, faults, and lineaments throughout this zone is consistent with the latter explanation, but the very low velocity rocks enclosed by zone C (compare Figures 4.16a and 4.16b) must surely be the result of relatively recent movements.

Aseismic zone F immediately below seismic zones A and B was unexpected. It encompassed the lower part of borehole SB120, along which there were many significant fractures and recently measured displacements (Willenberg, 2004; Spillmann et al., 2006). Clearly, these displacements either occurred aseismically or they only generated very small events not detected by a sufficient number of network geophones. A detailed analysis of geophone-B1 (located near the base of SB120) recordings was not helpful in distinguishing between these two possibilities, primarily because the data were contaminated with high levels of noise (see Figures 4.10a and 4.10c). The source of this noise is unknown.

4.9.3 Extent of the unstable slope

There is a general correspondence between the geodetically determined boundaries of mobile rock and the near-surface borders of microseismogenic zones A and B (Figure 4.16b), and borehole georadar reflection data demonstrate that fracture zones/faults along the northern and western boundaries of mobile rock (Figure 4.16b) are important structures that extend at least 50-75 m beneath the surface (Spillmann et al., 2006). Furthermore, horizontally travelling seismic waves are abruptly truncated at the western boundary (see the seismic section in Figure 5b of Heincke et al., 2006a). In summary, information supplied by the geodetic, georadar, seismic refraction and microseismic investigations is consistent with the lateral extent of mobile rock delineated in Figures 4.16a and 4.16b. Moreover, the measured displacements near the base of borehole SB120, the deep-penetrating nature of the fracture zones/faults, and the thicknesses of the microseismogenic zones (Figures 4.15 and 16c) are compatible with the mobile rock mass having a minimum depth extent of 50-120 m.

Results of the 3-D tomographic seismic refraction survey indicate the presence of low quality rock beneath a considerable part of the Randa test site (Heincke et al., 2006a). The section of mountain slope that eventually collapses may well include the large volume of low velocity crystalline rock that continues >100 m to the west of the mobile rock mass.

4.9.4 Microseismicity and the presence of water

Water under high pressure probably played a role in triggering the 1991 rockslides (Schindler et al., 1993; Sartori et al., 2003). Accordingly, it is reasonable to ask if water is currently influencing the microseismicity at the Randa test site. Two observations suggest that this is not happening. The top >40 m of all three moderately deep boreholes are usually dry, and we see no convincing correlation between increased microseismicity and high precipitation rates, unusual accumulations of snow, or periods of rapid snow melting (Figure 4.17).

4.10 DISCUSSION AND CONCLUSIONS

We have completed a pilot microseismicity study of the unstable mountain slope immediately above the huge Randa rockslide scarp in the Swiss Alps. Our microseismic network of twelve 3-component geophones placed in shallow and moderately deep holes was distributed across ~60,000 m² of rugged terrain. Over a period of 31 months, the network recorded signals from 66,409 events, of which only ~0.3% originated from mountain-slope

microearthquakes. The majority of microearthquakes had magnitudes in the -2.0 to -0.5 range.

In an earlier phase of our studies, the P-wave velocities of the mountain-slope crystalline rocks were discovered to be extremely heterogeneous (Heincke et al., 2006a). Inversion of a comprehensive 3-D tomographic seismic refraction data set had revealed the presence of voluminous highly fractured and faulted rocks with very low velocities (< 1.5 km/s) juxtaposed against rocks with more normal velocities (> 3.8 km/s). To determine reliable hypocenter parameters, it was essential to include the effects of these large velocity variations in the earthquake location process. In a first step towards this goal, we derived an extended 3-D velocity model from the tomographic seismic refraction data set.

In addition to incorporating detailed 3-D velocity information in the hypocenter estimation procedure, it was necessary for us to account for relatively large inaccuracies and/or a shortage of first-arrival picks for some microearthquakes, no reliable S-wave picks, and the occurrence of numerous microearthquakes outside the microseismic network. Accordingly, traditional approaches (Lee and Stewart, 1981) were judged to be unsuitable for locating earthquakes at the Randa study site. By comparison, Lomax et al.'s (2000) realization of Tarantola and Vallete's (1982) non-linear probabilistic location technique allowed us to address all of the critical issues in an efficient and satisfactory manner.

A number of well-located shots provided us with information to calibrate the microseismic network. The non-linear probabilistic location code was then used to compute hypocenter-parameter estimates from the station-corrected first-arrival times. For each microearthquake, we obtained a probability density function that included all plausible hypocenter parameter solutions and complete information on the uncertainties of each parameter. We presented the microseismicity pattern in two formats: (i) a cumulative hypocenter PDF comprising the sum of all individual hypocenter PDF's and (ii) the distribution of maximum likelihood locations.

By combining the results of our microseismicity study with information supplied by earlier geological, geodetic, geotechnical, and geophysical investigations, we can summarize the key physical characteristics of the Randa study site as follows:

- Extensive regions of the mountain slope are highly fractured and faulted. As a

consequence, seismic velocities are extremely heterogeneous and attenuation of the seismic energy is substantial, especially for the high frequency components; the frequency content of most seismic recordings is limited to 5-100 Hz.

- Microseismicity is concentrated in two main zones, one that follows the rockslide scarp and one that coincides with the highest density of fracture zones/faults.
- Most microearthquakes occur within 50-100 m of the surface. Considering the generally high attenuation of the seismic energy, it is possible that we do not record or recognize arrivals from deeper events.
- The shallow boundaries of the two principal microseismogenic zones correspond closely to the boundaries of slow-moving rock defined by geodetic observations. Major fracture zones/faults along these boundaries can be traced to 50-75 m depth on borehole georadar reflection sections. At least one of the boundary fracture zones/faults is a partial barrier to horizontally traveling seismic waves.
- A large portion of the slow-moving crystalline rock mass and adjacent region to the west are distinguished by exceptionally low seismic velocities. These low velocities are diagnostic of low quality rock. It is possible that the entire block of low quality rock will be involved in the eventual next phase of mountain-slope collapse.
- There are no obvious seasonal variations of microseismicity.

To improve further our understanding of instability processes at the Randa study site, we need to identify the specific fracture zones/faults that are microseismically active and determine microearthquake fault plane mechanisms. These goals can only be achieved by increasing the density of geophones near the potentially seismogenic structures, while at the same time enlarging the network aperture with geophones on the rockslide scarp. The improved geophone density would provide additional recordings rich in the higher frequencies necessary for more accurate first-arrival time determinations and waveform analyses. Although placing geophones on the rockslide scarp would require the assistance of qualified mountaineers and may be dangerous, information supplied by these sensors would improve enormously the location accuracy of most microearthquakes.

Many of the problems and challenges we faced at the Randa study site⁷ are likely to be characteristic of other microseismic investigations of unstable mountain slopes. In particular, unusually low seismic velocities have already been detected in mountain-slope crystalline rocks of the Tien Shan Range (Havenith et al., 2002), French Alps (Meric et al., 2005), and Norwegian Fjords (L.H. Blikra, personal communication, 2005). Our sensitivity tests demonstrate the importance of the velocity model in the earthquake location process; an inaccurate velocity model may result in highly erroneous hypocenter parameters, especially for events near or beyond the microseismic network boundaries.

4.11 ACKNOWLEDGEMENTS

We thank Christoph Bärlocher and Beat Rinderknecht for their considerable technical assistance in establishing and operating the microseismic network, numerous people for field assistance, Anthony Lomax for providing the NonLinLoc software package and valuable discussion, Heinrich Horstmeyer for assistance and advise on the ETH data processing system, Nicholas Deichmann, Simon Loew, Keith Evans, and Erik Eberhardt for their cooperation in this interdisciplinary project, Jean Daniel-Rouiller and colleagues from CREALP (Research Centre on Alpine Environment, Switzerland) for supplying the digital terrain model and geodetic survey data, and the local authorities of Randa for providing logistical support. This project was funded by the Swiss National Science Foundation.

⁷ Hazardous and logistically difficult operating conditions, limited aperture of the microseismic network, not enough geophones, strong sources of electrical noise, highly heterogeneous seismic velocities, and high levels of seismic-wave attenuation.

4.12 APPENDIX

SEMI-AUTOMATIC SEISMIC EVENT CLASSIFICATION

A major effort was required to classify the 66,409 events recorded by the Randa microseismic system. Based on a manual analysis of roughly 9,000 event files, we designed and implemented a semi-automatic two-step procedure that allowed the entire data set to be classified in an efficient manner (steps I and II in Figure 4.A1). We then studied manually the <7 % of event files that potentially contained events of interest (Step III in Figure 4.A1).

4.12.A Step I: identification of impulsive transients

It was obvious early in our analysis that the vast majority of recorded events were transients. Although they appeared to be relatively uniform spike-like features on standard plots (Figures 4.4 and 4.B2a), they were seen to have quite complicated waveforms that varied somewhat from channel to channel in expanded time plots (Figure 4.B1b). We considered their very short durations and near simultaneous occurrence on all channels to be diagnostic of electrical noise. They were probably caused by lightning (i.e., spherics) and other electrical disturbances associated with the resistive environment of the high mountain and the long recording cables. The strongest signals were recorded on channels connected to the longest cables and essentially the same effects were observed on another seismic instrument (MARS 88) used for testing.

Since the effects of the transients could not be easily eliminated in the field, they were identified and discarded during processing. From M 3-component recordings of an event, where M equals 12 the number of stations at Randa, the 3-component recordings from the station with the highest signal levels were defined to be the master traces. After dividing all traces into N sections of 500 ms length, with 50% overlap between adjacent sections, unbiased covariance functions between the master trace sections and all other trace sections were computed. This process yielded two matrices: $S(i, j)$ and $L(i, j)$, where S contained the maxima of the unbiased covariance functions, L contained the lags of the maxima, and ($i = 1 \dots N, j = 1 \dots 3(M-1)$). In the next step, the semi-automatic procedure determined i and j at the maximum value of S [$S(i_{max}, j_{max}) = \max(S)$] and the median value of the i_{max} row of L [$\tau = \text{median}(L(i_{max}, j))$]. For seismic events and uncorrelated noise, τ was relatively large, whereas for transients it was very small (Figure 4.B1b). A threshold of $\tau \leq 2$ ms was found

to be appropriate for identifying the vast majority of transients generated by electrical noise. An event file containing both a transient and a seismic signal was discarded if the amplitude of the transient was substantially larger than that of the seismic signal. Application of this algorithm yielded 55,563 noise transients (i.e., ~84% of all events; Figure 4.A1). Results of applying this algorithm to the subset of 9000 events suggest that less than 2% of the seismic events would have been erroneously classified as transients.

4.12.B Step II: sonogram pattern recognition scheme

Once most of the transients were removed, it was necessary to distinguish between files that contained potentially interesting seismic events and those that only contained noise or signals with low coherency. To meet this objective, we employed a modified version of Joswig's (1995) sonogram (spectrogram or running spectra) pattern recognition scheme, in which the time variation of a recording's frequency content was used as a discriminant. The results of applying this procedure to typical 3-component recordings of a rock-slope microearthquake and noise are presented in Figure 4.C1. To compute the sonograms presented in Figures 4.C1c and 4.C1d, we:

- divided each trace of a 3-component recording (Figures 4.C1a and 4.C1b) into 100-ms-long sections with 50% overlap between adjacent sections;
- tapered the ends of each section using a cosine function and computed the energy spectrum;
- summed the spectra of the respective three components and took the logarithm (basis 2) of the sum;
- plotted the running \log_2 spectra on a time-versus-frequency graph using a gray-scale representation for the intensity levels.

To highlight better the signal due to the seismic event, it was necessary to define a model for the background noise. Following Joswig (1995), we assumed that noise in the frequency domain could be adequately defined by a log-normal distribution, which translated to a Gaussian distribution in \log_2 space. We then only accepted values of the sonogram that exceeded an amplitude threshold based on the noise model (Figures 4.C1e and 4.C1f; see equations (3) to (7) in Joswig, 1995). Although the human eye could distinguish seismic signal from background noise in the modified sonograms of Figures 4.C1e and 4.C1f, some extra processing was required for it to be identified as meaningful signal using a computer-

based approach. This was achieved by setting to 0 all intensity values ≤ 3 in the modified sonograms, setting to 1 all intensity values > 3 , and then applying an image morphology process that flattened and preserved essential shape characteristics while removing protuberances and noise (Pratt, 2001; Heincke et al., 2006b). The final binary patterns are shown in Figures A3g and A3h.

Since we were primarily interested in microearthquakes that could be located, the final step of our semi-automatic scheme involved identifying events that were recorded on multiple channels. Tests on the subset of 9000 events demonstrated that this could be achieved by demanding that at least 10 of the 12 binary patterns significantly overlapped. Indeed, all 12 binary patterns overlapped for microearthquakes that generated recordings with moderately high signal-to-noise ratios. After applying this process, 6,471 files containing noise and low coherency events were discarded (Figure 4.A1).

4.12.C Step III: manual classification

A manual inspection of the remaining 4,375 event files was the final step in our classification procedure. Based mainly on their frequency contents and coda lengths, we identified 223 single microearthquakes and sequences of multiple microearthquakes that were probably generated within the unstable mountain slope and 206 small regional earthquakes (Figure 4.A1). The remaining 3961 files contained relatively low frequency, low amplitude emergent signals that were probably generated by distant earthquakes and explosions and low quality signals from which we could not determine event locations.

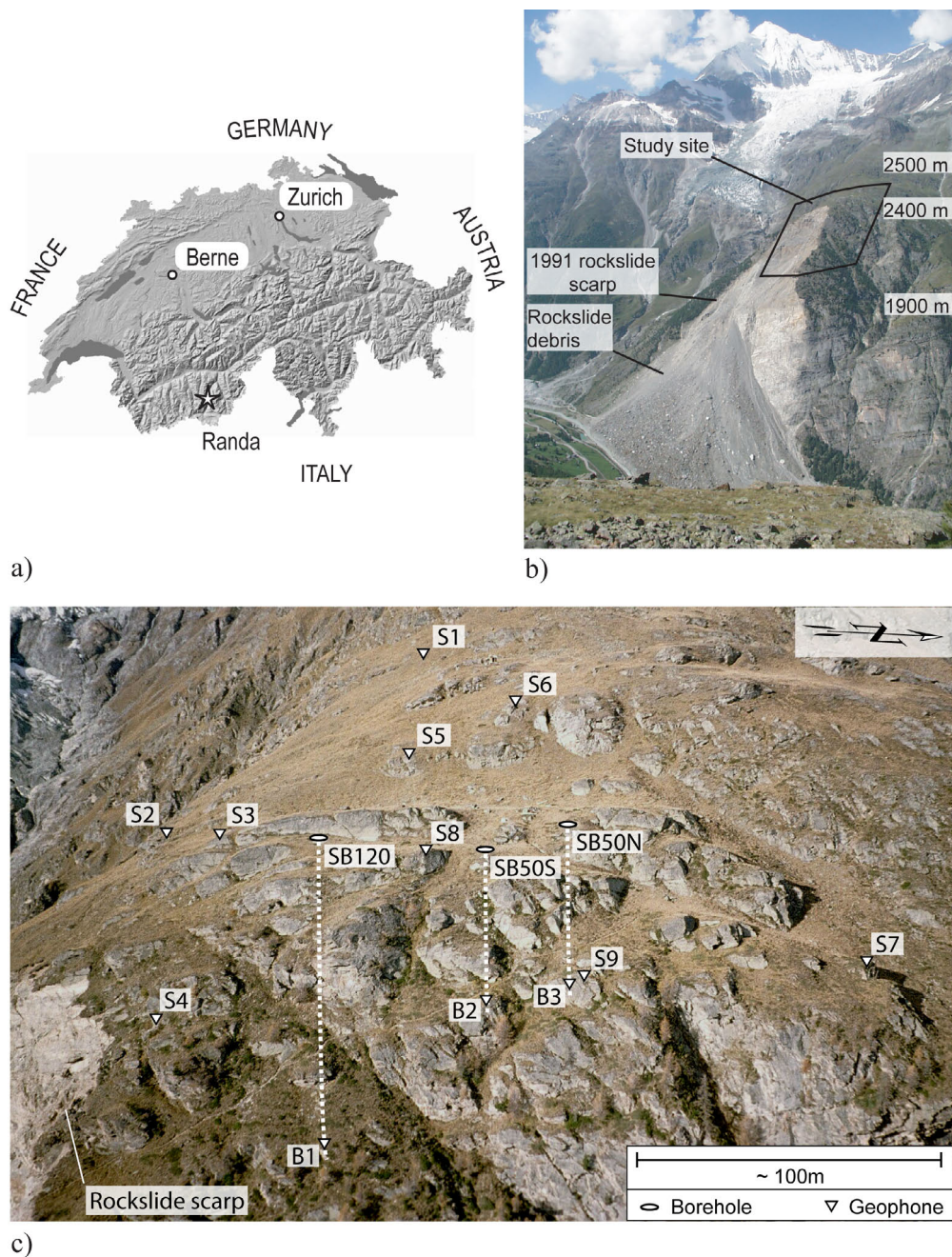


Figure 4.1: (a) Star shows the location of the Randa study site in the Matter Valley of southern Switzerland. (b) Photograph of the Randa rockslide and study site. (c) Photograph highlighting the rugged nature of the terrain on which the microseismic network was deployed. SB120, SB50S and SB50N: boreholes, with dotted lines showing schematically their lengths within the crystalline rock. S1-S9: near-surface geophones. B1-B3: borehole geophones. Photographs by Heike Willenberg and Beat Rinderknecht.

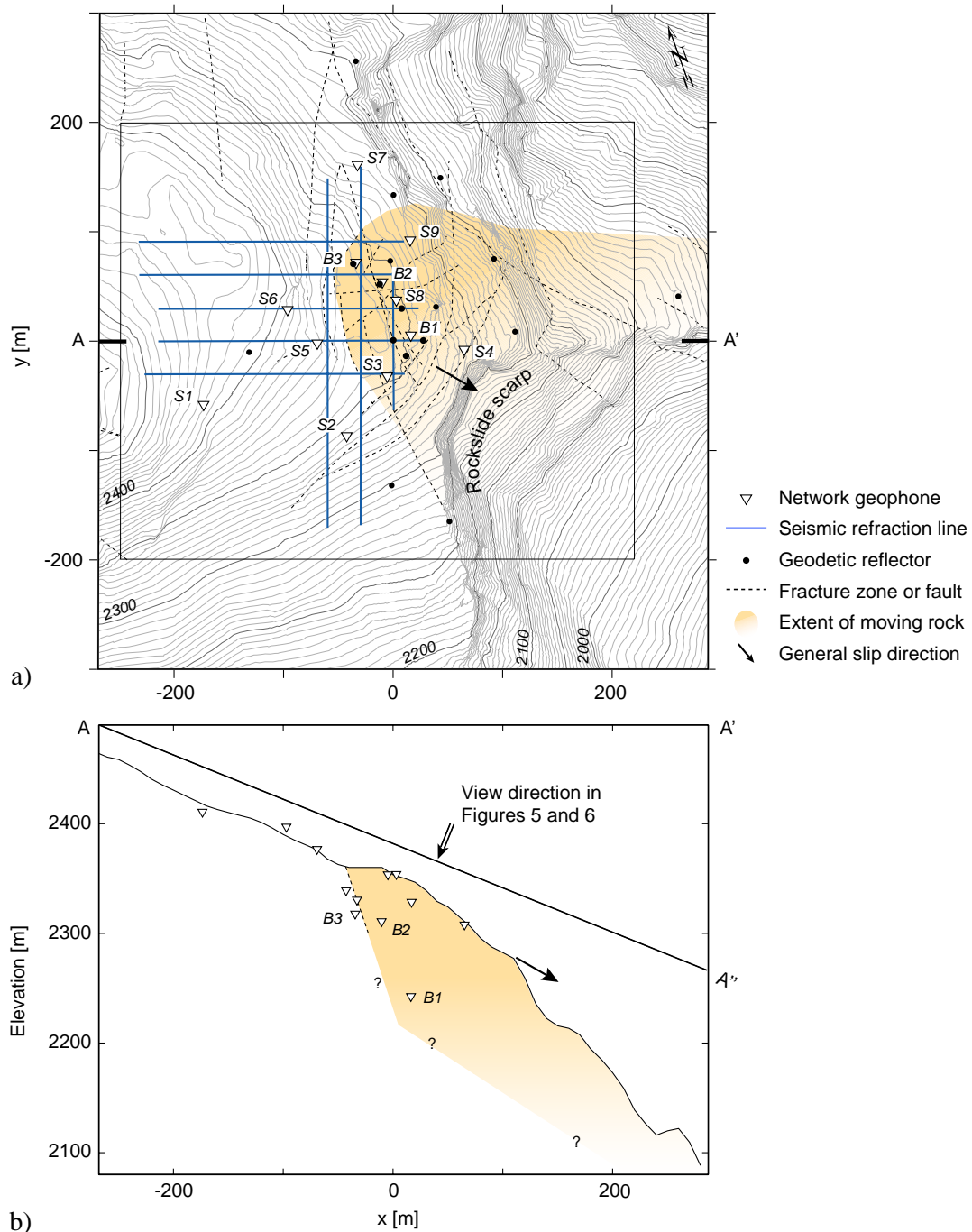


Figure 4.2: (a) Map outlining the locations of the network geophones (S1-S9; B1-B3), 3-D refraction seismic lines, geodetic reflectors, fracture zones and faults (mostly steep dipping), and estimated extent of mobile rock based on geodetic and geotechnical information. Geophones B1, B2 and B3 are near the bottoms of boreholes SB120, SB50S, and SB50N, respectively (see Figure 4.1c). The inner rectangle delineates the boundaries of maps presented in Figures 4.11-4.14. (b) Locations of the network geophones are projected on to cross-section A-A'. The line A-A'' is a side view of the plane represented in Figures 4.6a, 4.7a, and 4.7c.

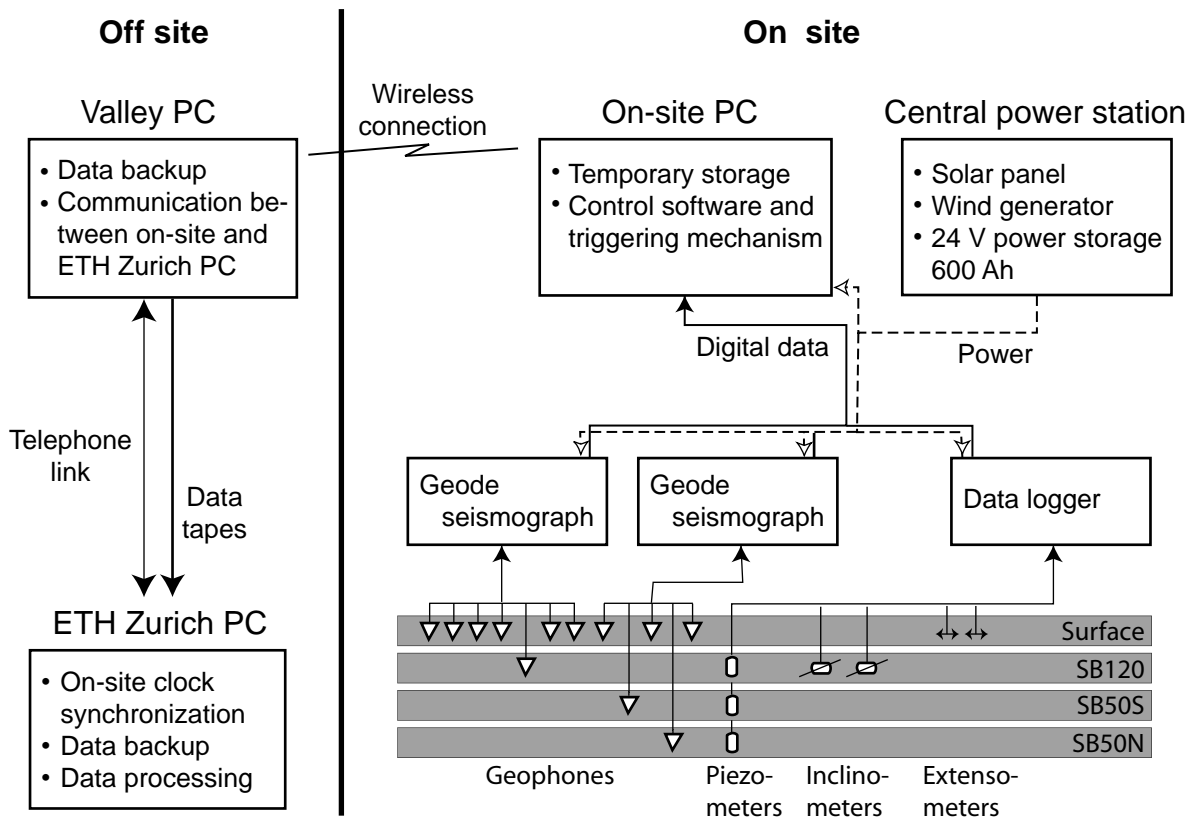


Figure 4.3: Sketch of the ETH microseismic and geotechnical monitoring systems.

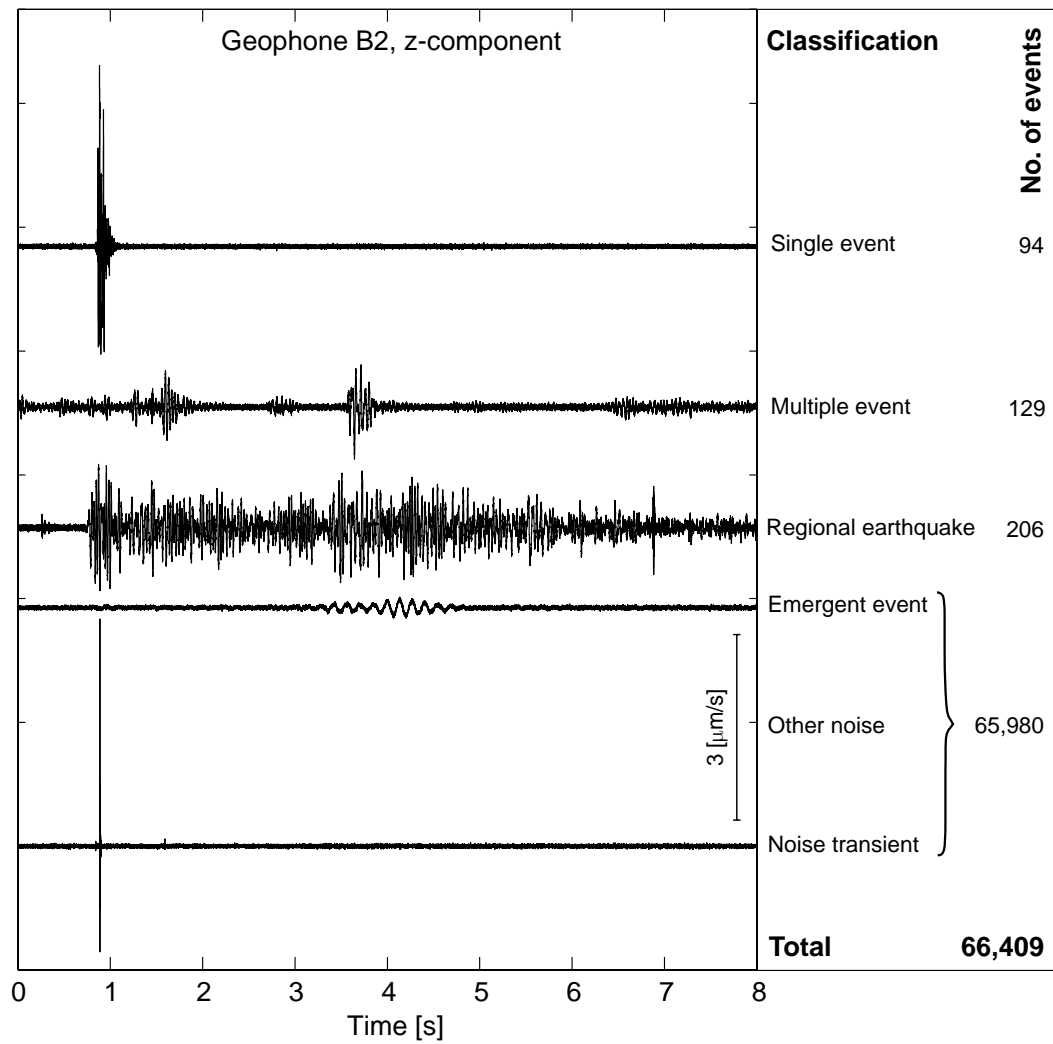


Figure 4.4: Examples of seismograms recorded at the Randa study site plotted using a common amplitude scale. Most single and sequences of multiple events are likely related to rockslide activity. The emergent events probably originate from distant earthquakes. Numerous regional earthquakes occur in the western Swiss Alps.

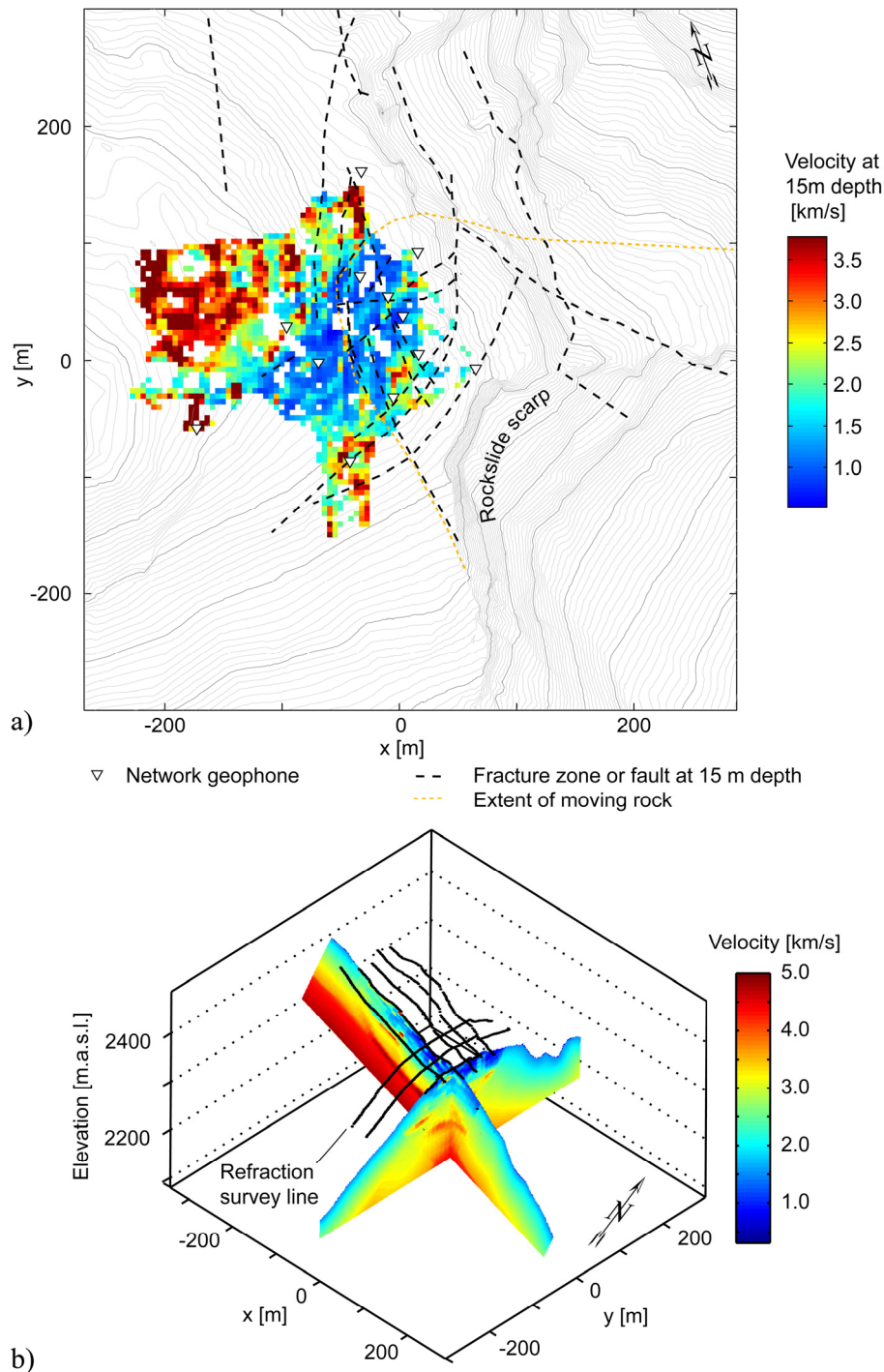


Figure 4.5: (a) P-wave velocities extracted from Heincke et al.'s (2006a) tomographic model at 15 m depth below the surface (velocities >3.8 km/s are plotted with the same reddish brown color). Also displayed are fracture zones and faults projected to 15 m depth and the estimated extent of mobile rock based on geodetic and geotechnical information. Map boundaries are as for Figure 4.2a. (b) Two cross-sections through the expanded 3-D velocity model shown in perspective view. Closely spaced dots (almost lines) identify geophones deployed for the tomographic survey.

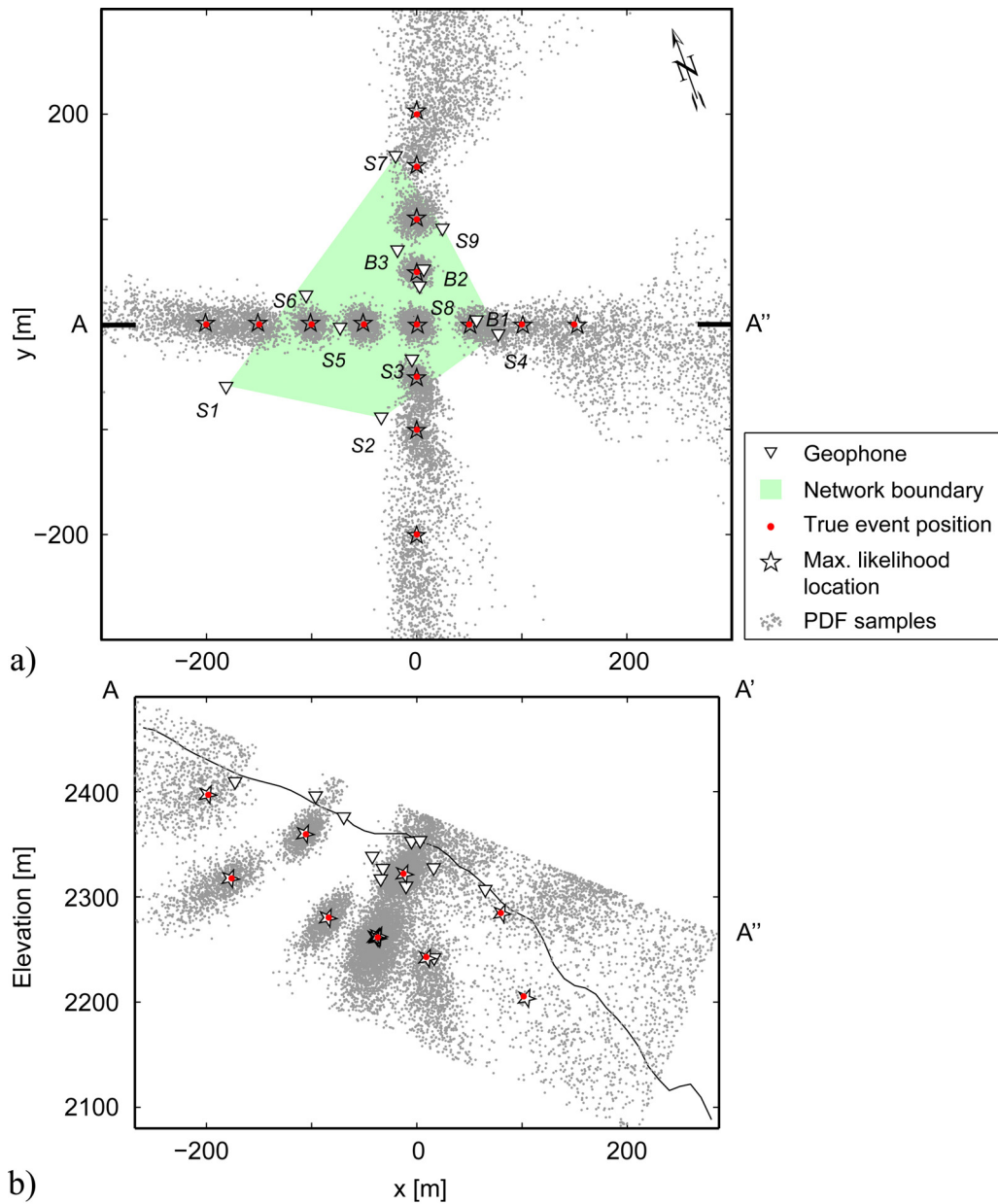


Figure 4.6: Estimating the resolution of the microseismic network for a sequence of events along two planes within a homogeneous velocity model (velocity = 2.5 km/s). Both diagrams show projections of all network geophones, true event locations, complete PDF scatter clouds, and maximum-likelihood locations. (a) Map boundaries are the same as for Figure 4.2a, but the viewing direction is approximately perpendicular to the dipping surface (see Figure 4.2b). Note the near-perfect correspondence between the true and maximum-likelihood event locations. (b) Various details are projected on to cross-section A-A'.

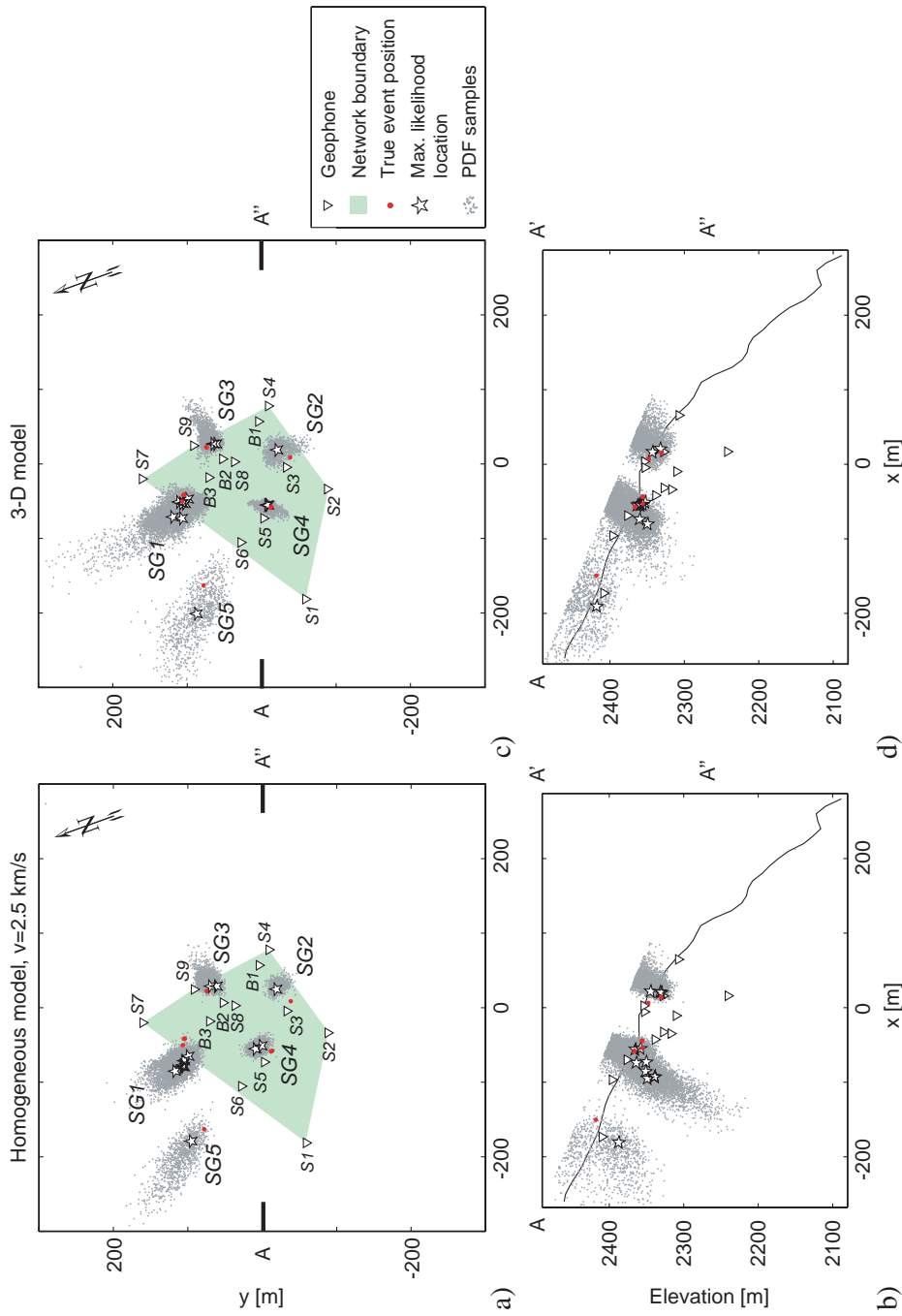


Figure 4.7: Calibration of the microseismic network using 5 groups of shots SG1-SG5. All diagrams show projections of all network geophones, complete PDF scatter clouds, and maximum-likelihood locations. (a)-(b) Results based on a homogeneous model with velocity = 2.5 km/s. (c)-(d) Results based on our extended 3-D velocity model. Map boundaries of (a) and (c) are the same as for Figure 4.2a, but the viewing directions are approximately perpendicular to the dipping surface (see Figure 4.2b). (b) and (d) Various details are projected on to cross-section A-A". Several of the shots are very close together, such that only 6 of the 12 can be distinguished in the figures.

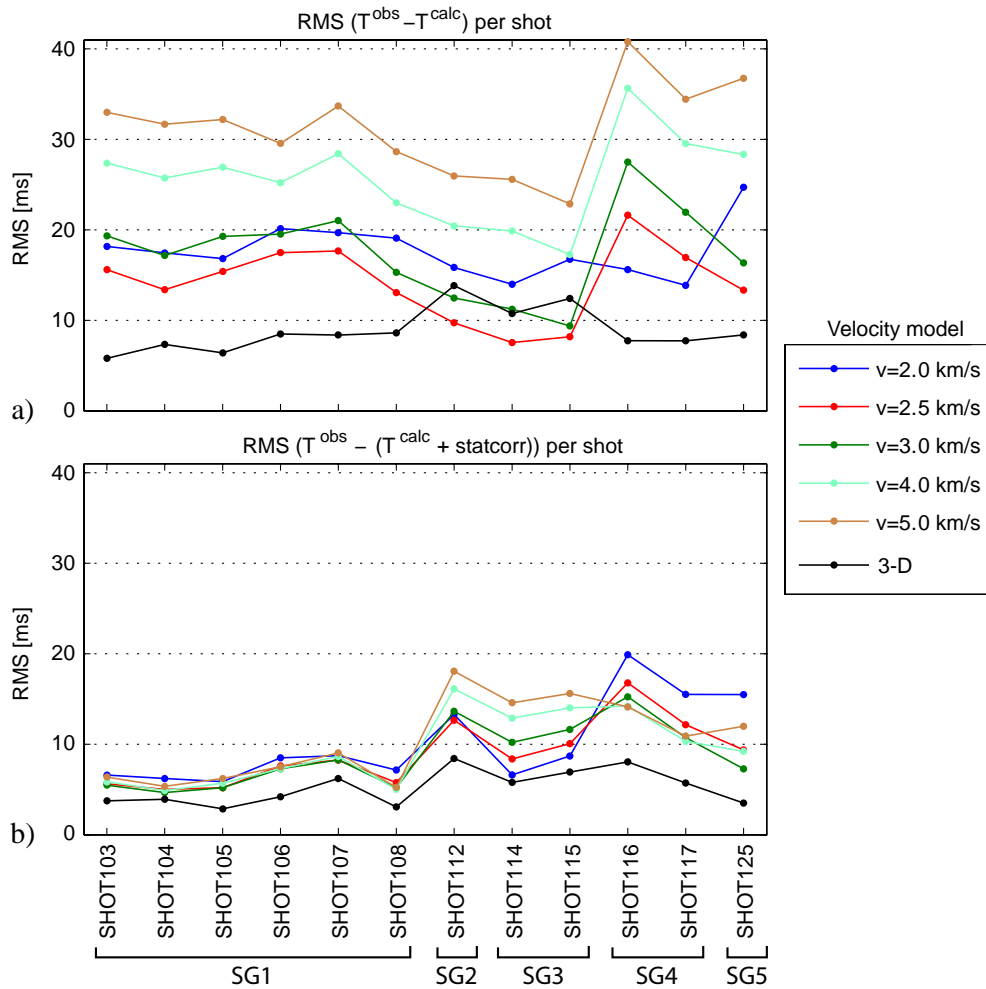


Figure 4.8: (a) Root-mean square (RMS) differences between the observed traveltimes (T^{obs}) of the calibration test shots and computed traveltimes (T^{calc}) based on our extended 3-D model and a variety of homogeneous models. True shot positions were used for these computations. (b) As for (a), but after application of station corrections ($statcorr$). Shots are collected into five groups SG1-SG5 (see Figure 4.7).

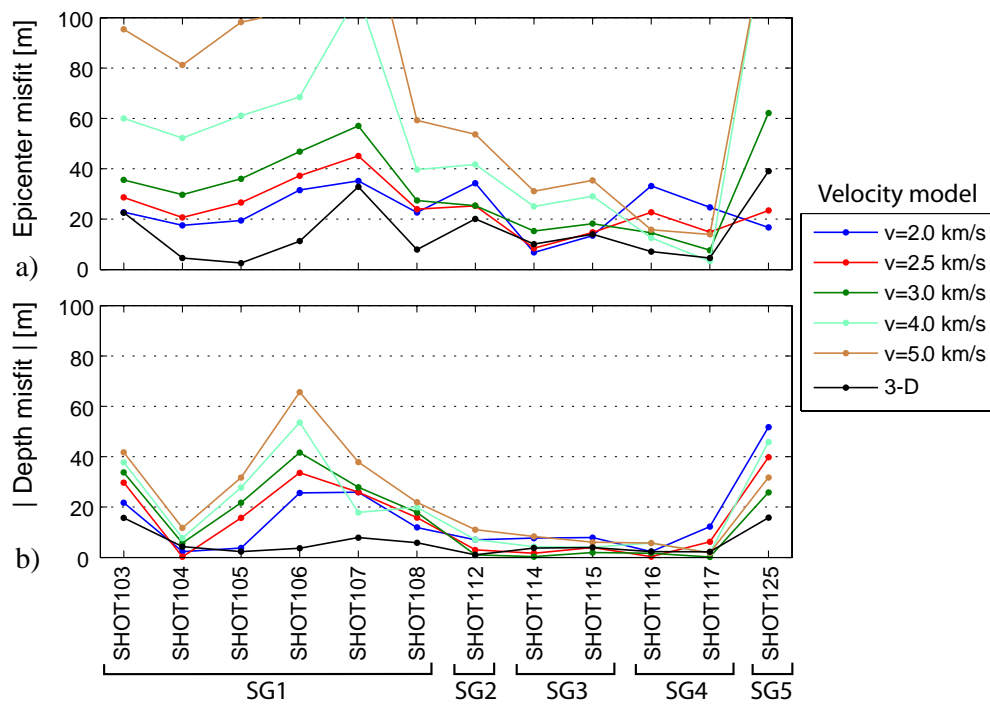


Figure 4.9: Accuracies of test-shot maximum-likelihood locations based on our extended 3-D model and a variety of homogeneous models. (a) Absolute values of misfits between true and estimated epicenter locations. (b) Absolute values of misfits between true and estimated depths.

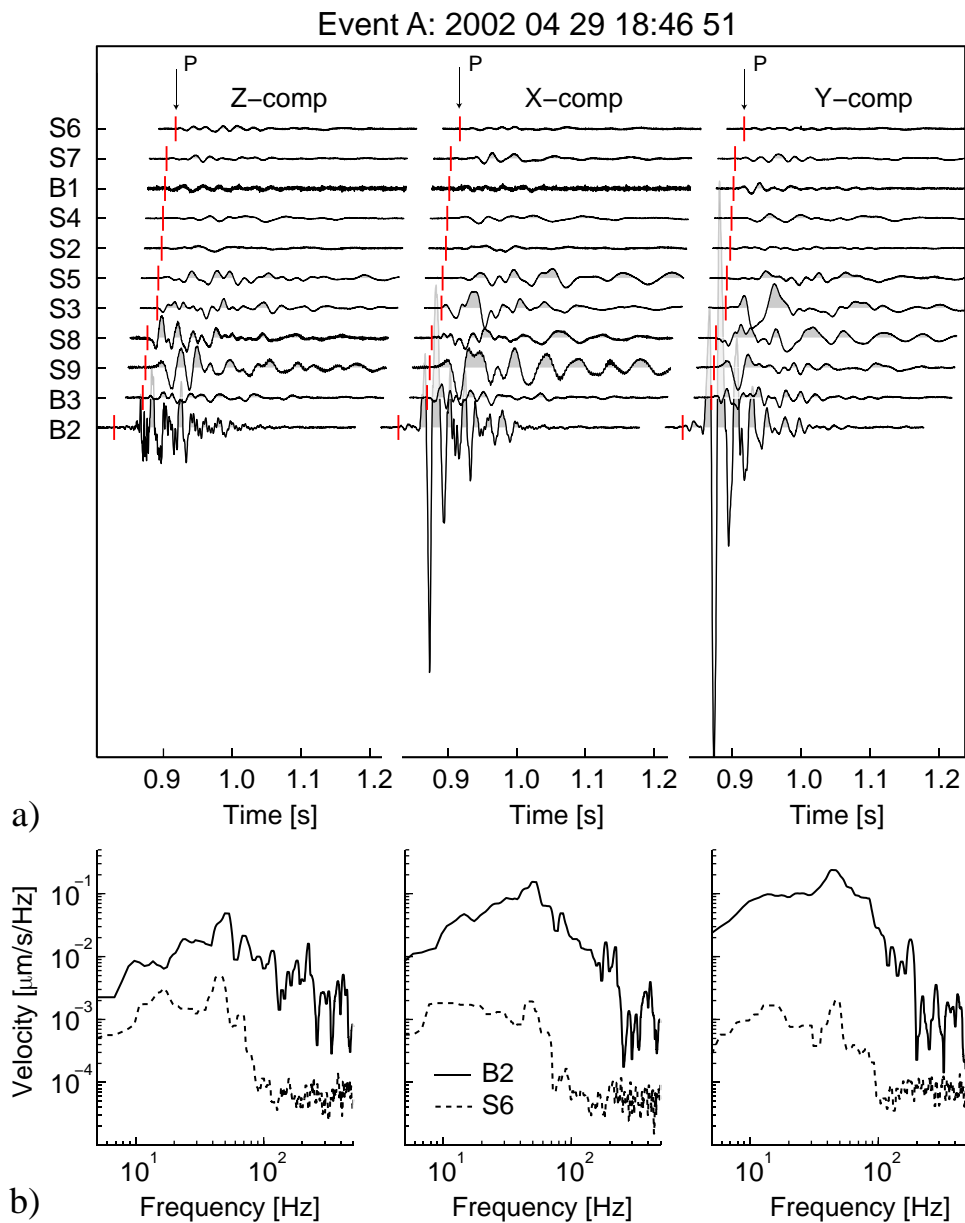


Figure 4.10: (a) and (c) Suites of 3-component seismograms for two microearthquakes. (b) and (d) Spectra for selected seismograms. To enable direct comparisons to be made, a matching filter has been used to transform the 28-Hz-geophone recordings of stations B1-B3 to effective 8-Hz geophone recordings. Traces are sorted according to first-arrival times. Event date and time is indicated above each suite of seismograms. The "P" ticks delineate picks of first arriving P-waves, whereas the "S?" ticks show the approximate arrivals of S-wave energy.

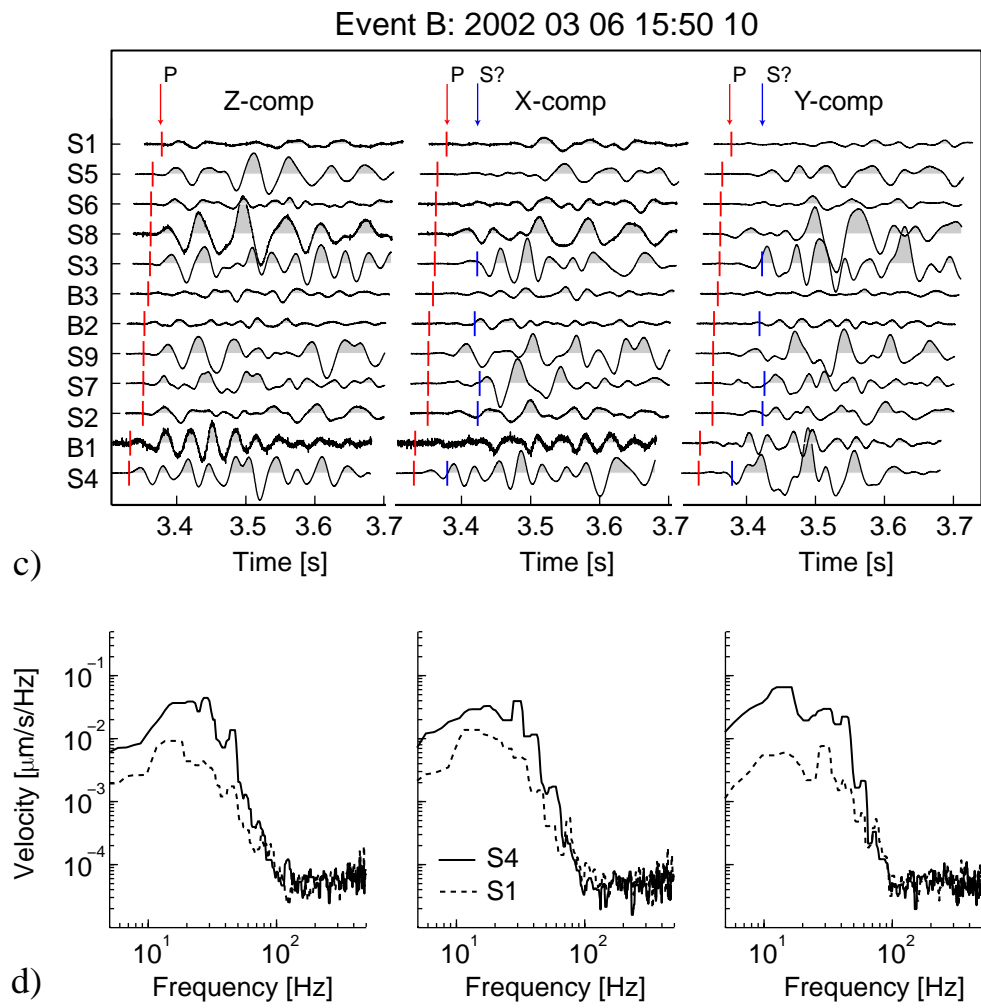


Figure 10 (continued)

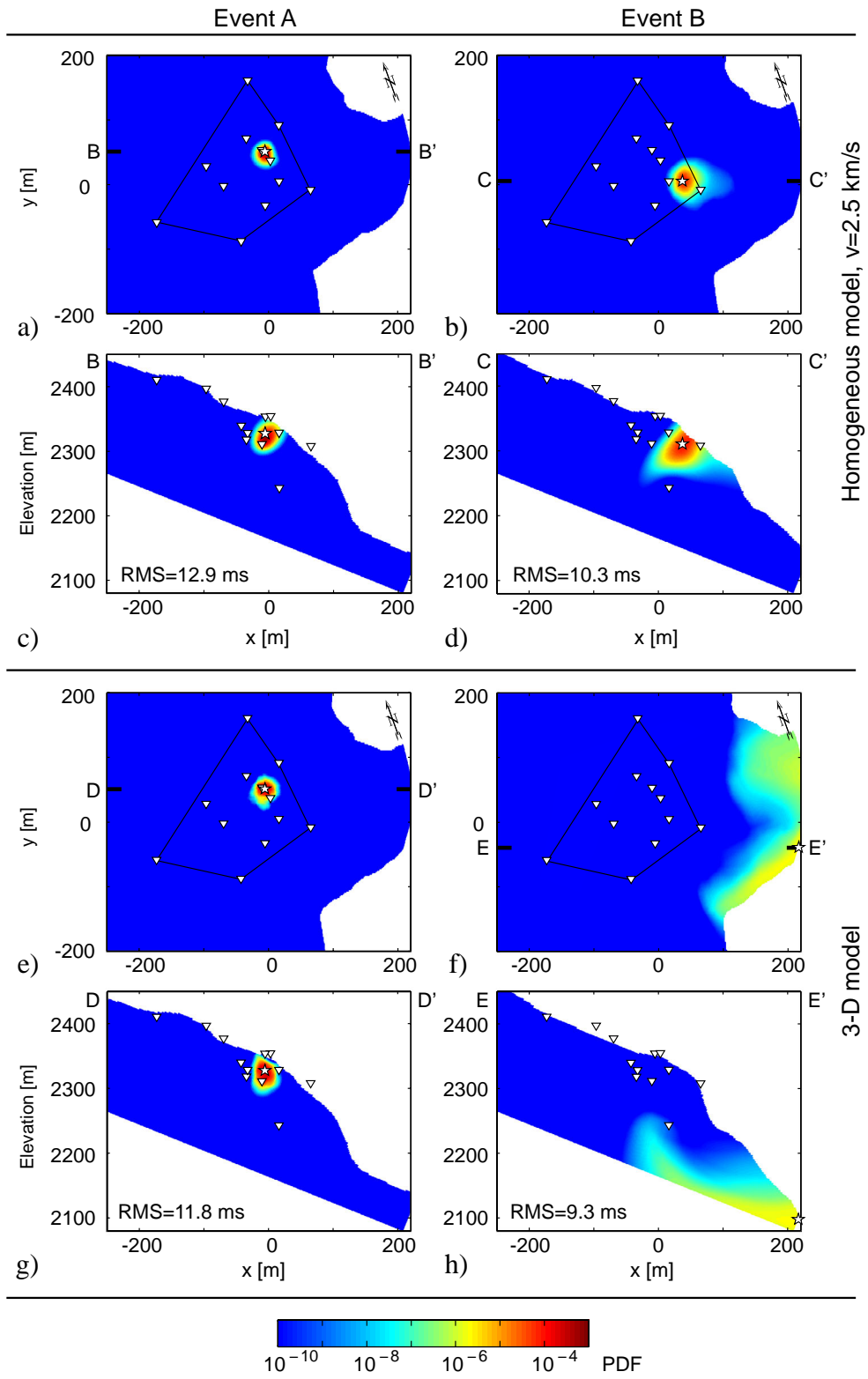


Figure 4.11: PDF volumes and maximum-likelihood locations (stars) of microearthquakes represented by the seismograms of Figure 4.10. Triangles - geophones. Lines connecting geophones delineate the outer limits of the microseismic network. (a)-(d) Results based on a homogeneous model with velocity = 2.5 km/s. (e)-(h) Results based on our extended 3-D velocity model. (a), (b), (e) and (f) Undulating sections through the PDF volumes at constant depths below the surface. The depths are defined by the respective maximum-likelihood locations of the microearthquakes. Map boundaries are as for the inner rectangle of Figure 4.2a. (c), (d), (g), and (h) Cross-sections through the PDF volumes and maximum-likelihood locations with projected locations of geophones. RMS differences between the observed and predicted arrival times based on the maximum-likelihood locations are similar for the two velocity models.

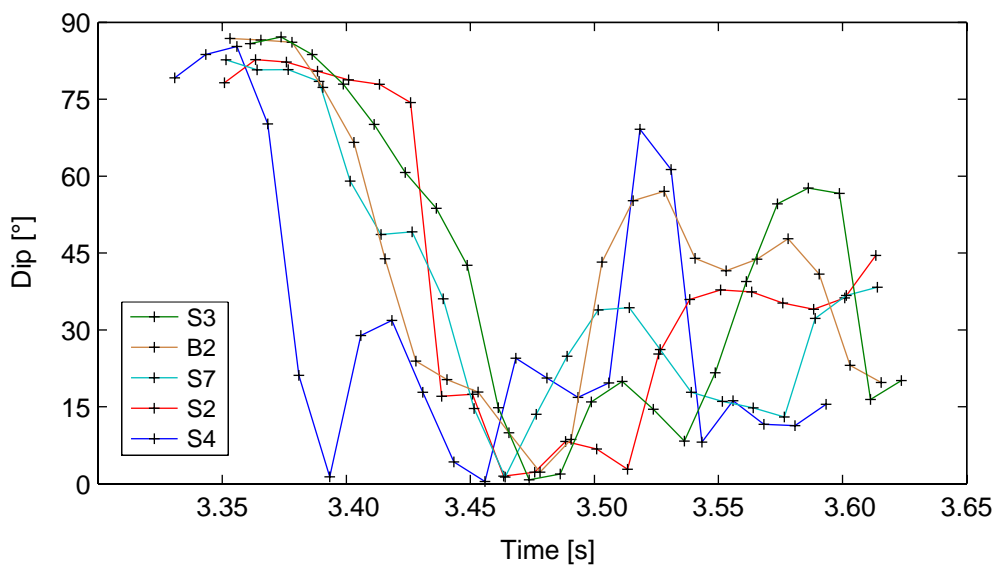


Figure 4.12: Results of selected polarization analyses of event B seismograms of Figure 4.10c showing the dominant angle of particle motion relative to the horizontal. For vertical incident rays, pure P- and S-waves have 90° and 0° dips, respectively.

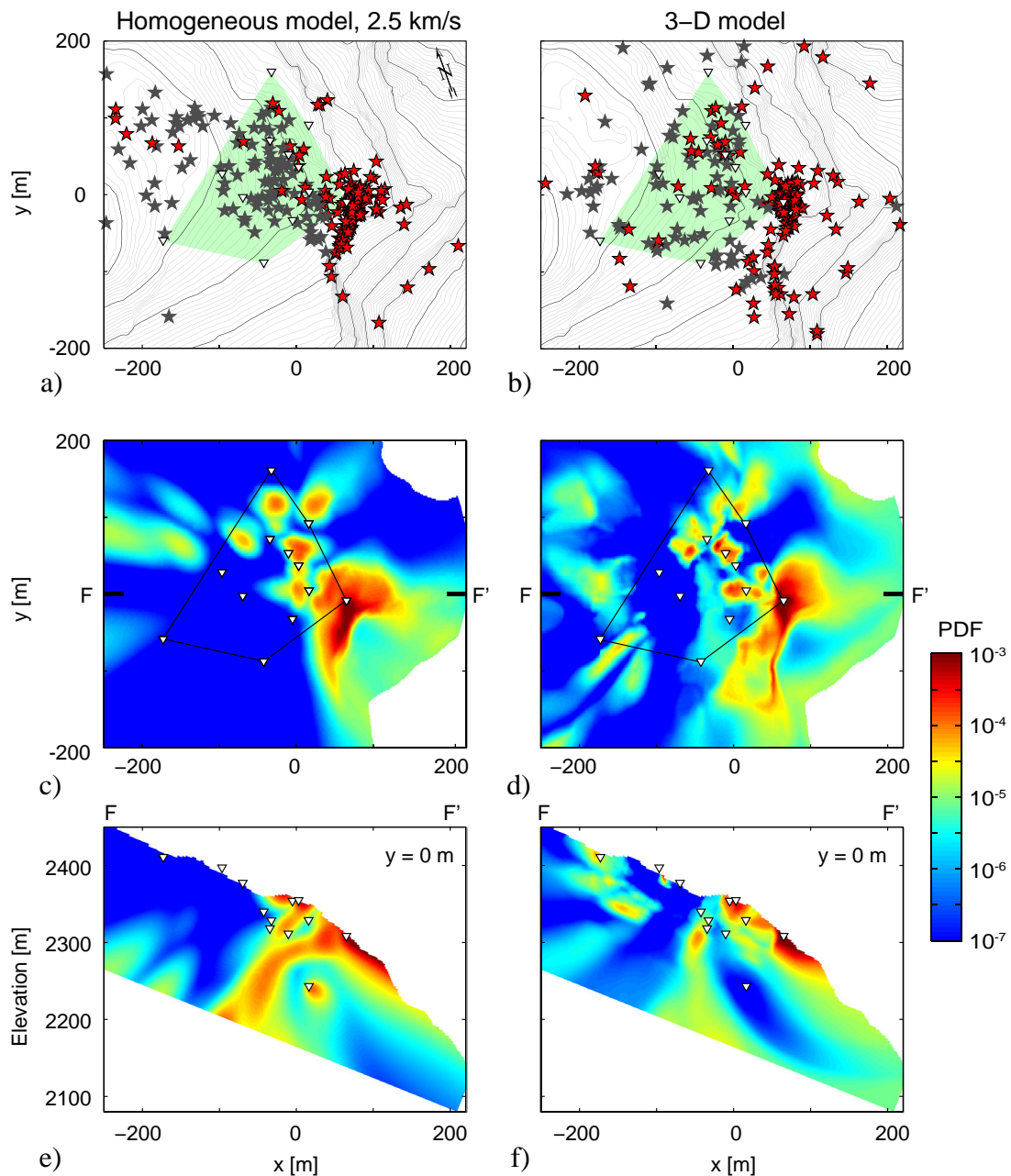


Figure 4.13: (a) and (b) Maximum-likelihood epicenters of all located microearthquakes. Triangles - geophones; red stars - shallow microearthquakes (depths ≤ 30 m below surface); gray stars - relatively deep microearthquakes (depths > 30 m below surface). Light green shading delineates the extent of the microseismic network. (c) and (d) Undulating sections through the cumulative hypocenter PDF volumes at a constant 15 m depth below the surface. Lines connecting the geophones delineate the outer limits of the microseismic network. Map boundaries are as for the inner rectangle of Figure 4.2a. (e) and (f) Cross-sections F-F' with projected locations of geophones. (a), (c) and (e) Results for a homogeneous model with velocity = 2.5 km/s. (b), (d) and (e) Results for our extended 3-D velocity model.

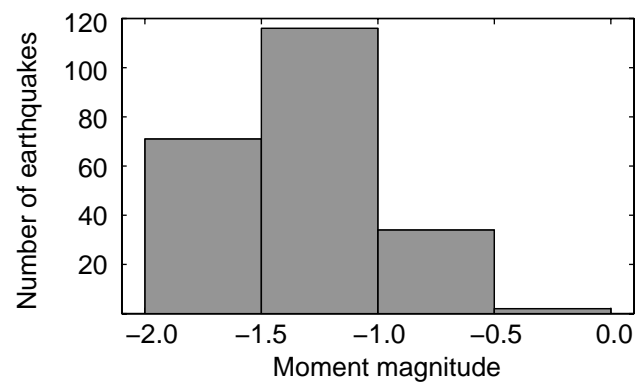


Figure 4.14: Histogram plot of Randa microearthquake moment magnitude estimates.

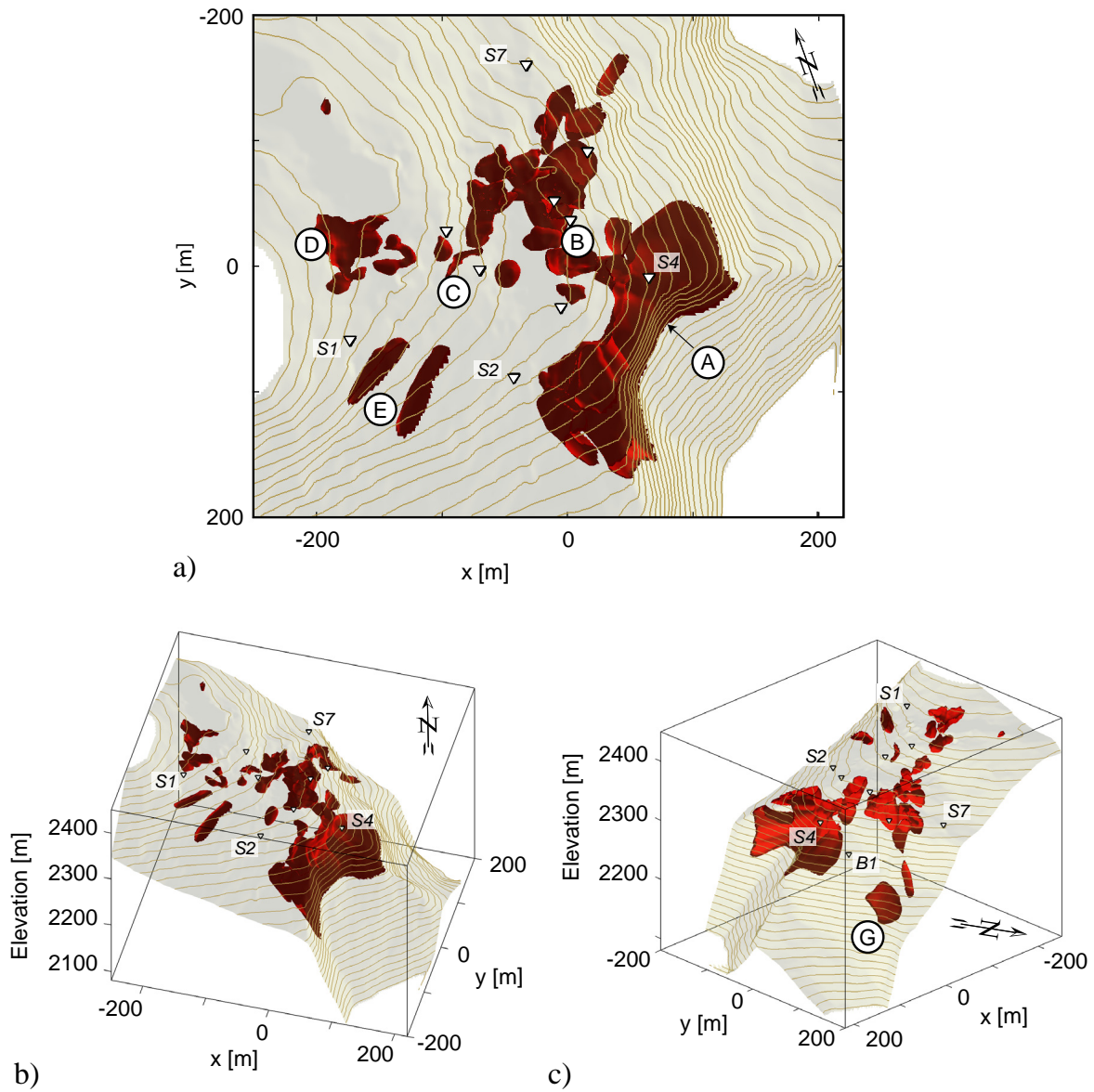


Figure 4.15: Map and two perspective views of microseismogenic and aseismic zones. The opaque volumes have uniform cumulative hypocenter PDF values $> 3.2 \cdot 10^{-5}$, whereas the transparent regions have uniform values $< 3.2 \cdot 10^{-5}$. Shaded surface and contours represent topography. Letters A-E and G identify features discussed in the text.

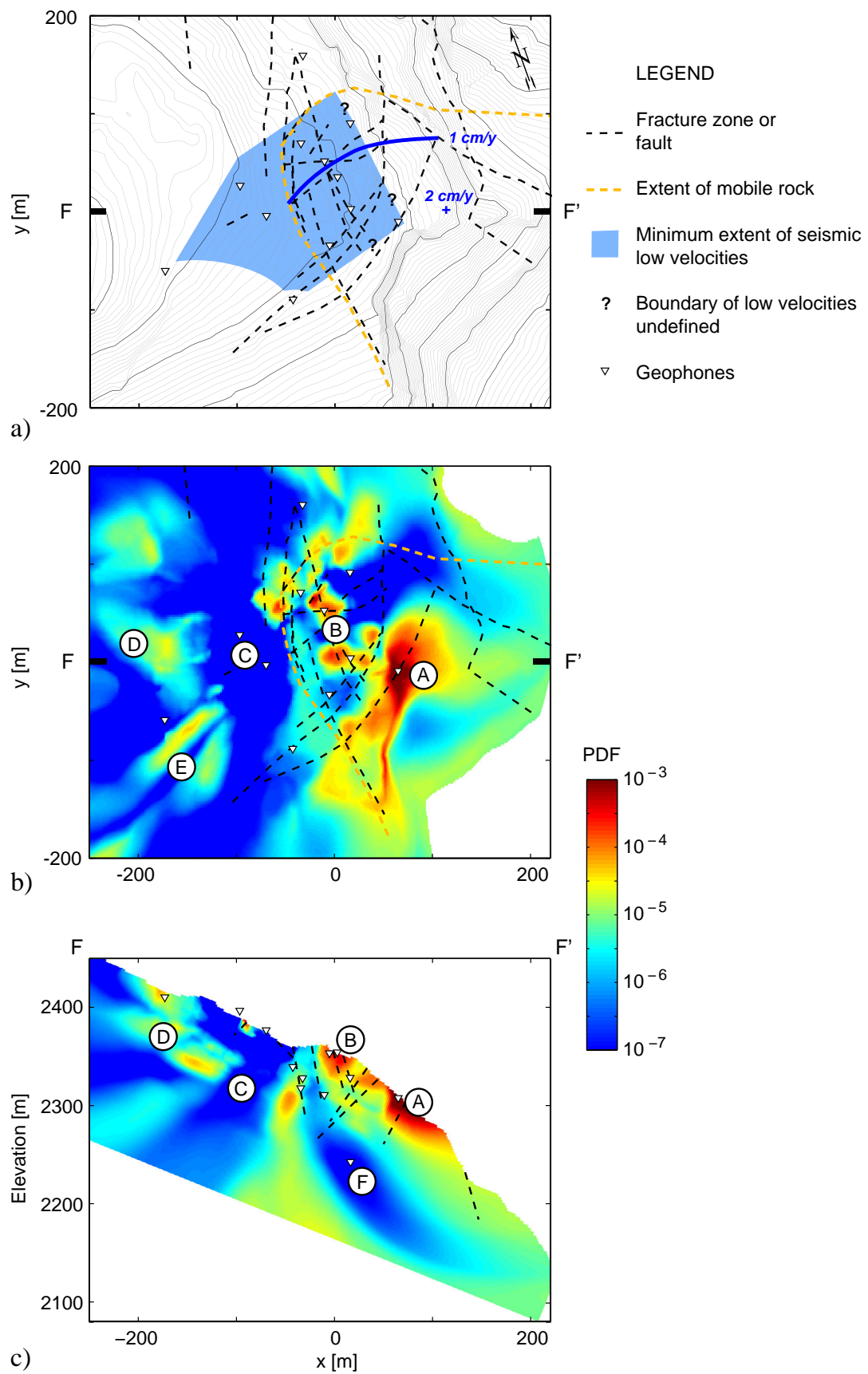


Figure 4.16: (a) Map showing topography, traces of fracture zones and faults projected to 15 m depth below the surface, minimum extent of unusually low P-wave velocities based on refraction tomography, and estimated extent of mobile rock. The rock slope south of the dark blue line is moving southwestwards at ≥ 1 cm/year. The point marked by the blue plus sign is moving at 2 cm/year (after Jaboyedoff et al., 2004). (b) and (c) Undulating section and cross-section through the summed PDF volume (reproduced from Figures 4.13d and 4.13f) showing fracture zones and faults projected to 15 m depth. Letters A-F identify features discussed in the text.

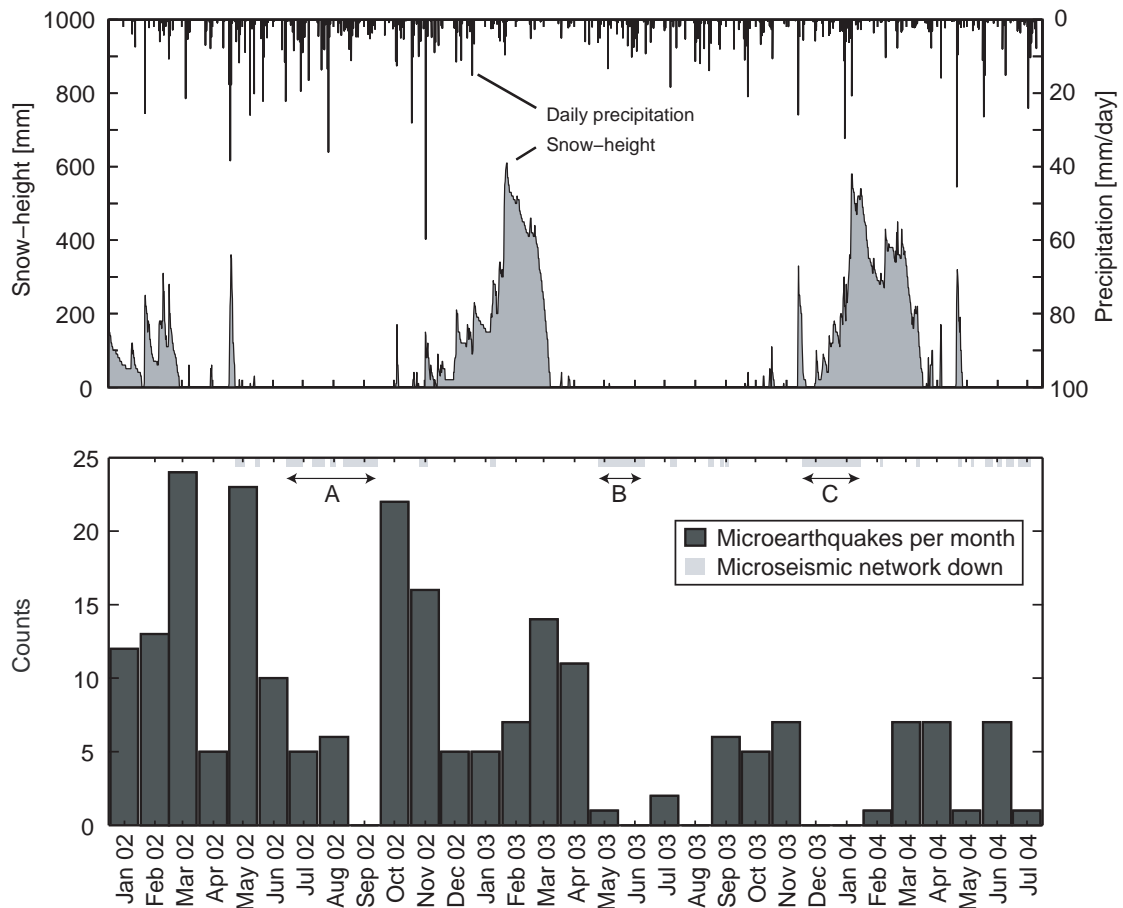


Figure 4.17: Temporal variations of microseismicity, precipitation, and snow accumulation and melting. During three extensive periods, the microseismic network was either being used for other purposes (A - tomographic seismic refraction survey) or was not operating (B - problems with the on-site field PC; C - problems with the on-site field PC and valley PC).

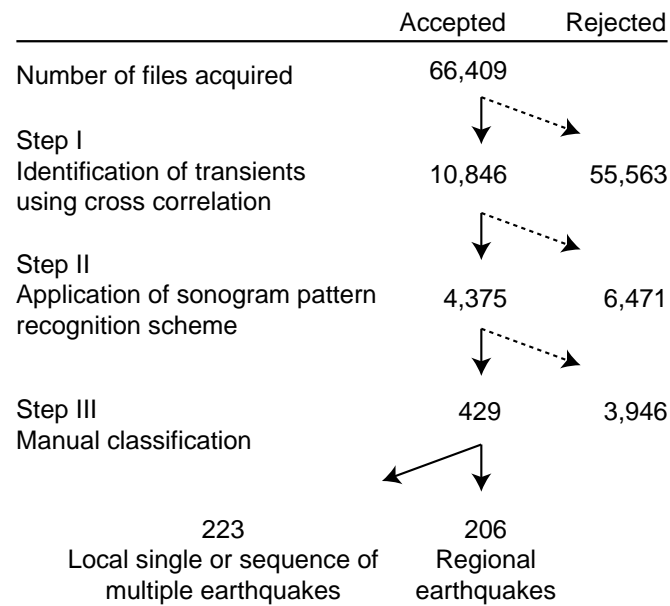


Figure 4.A1: Simple flow chart showing how the various filtering steps result in the recognition of 223 local single and sequences of multiple microearthquakes and 206 regional earthquakes.

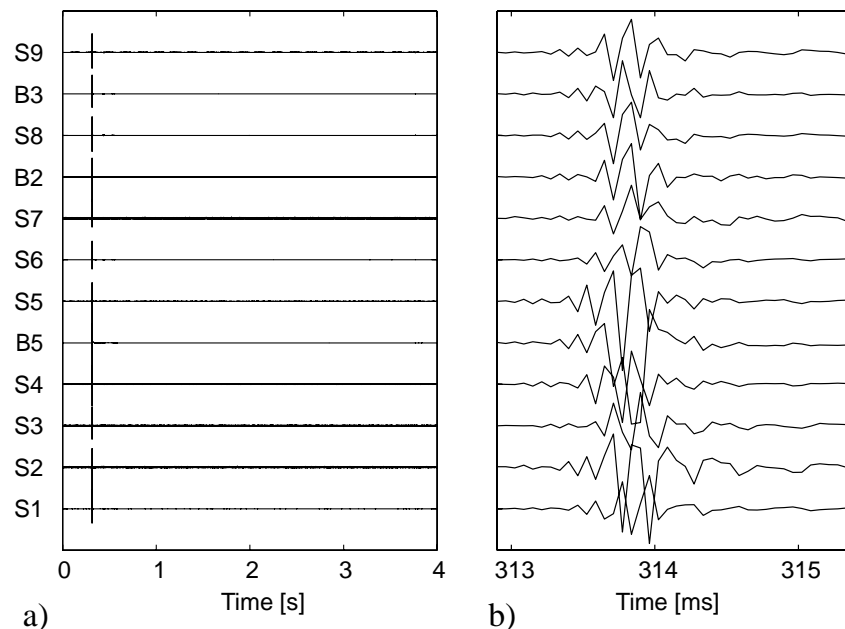


Figure 4.B1: Vertical-component seismograms showing the nearly simultaneous occurrence of a transient on all traces. (a) Time scale as for Figure 4.4. (b) Expanded time scale (note, that these seismograms were recorded using a sampling rate of 0.0625 ms). Traces have been normalized to make the maximum positive amplitude on all traces equal.

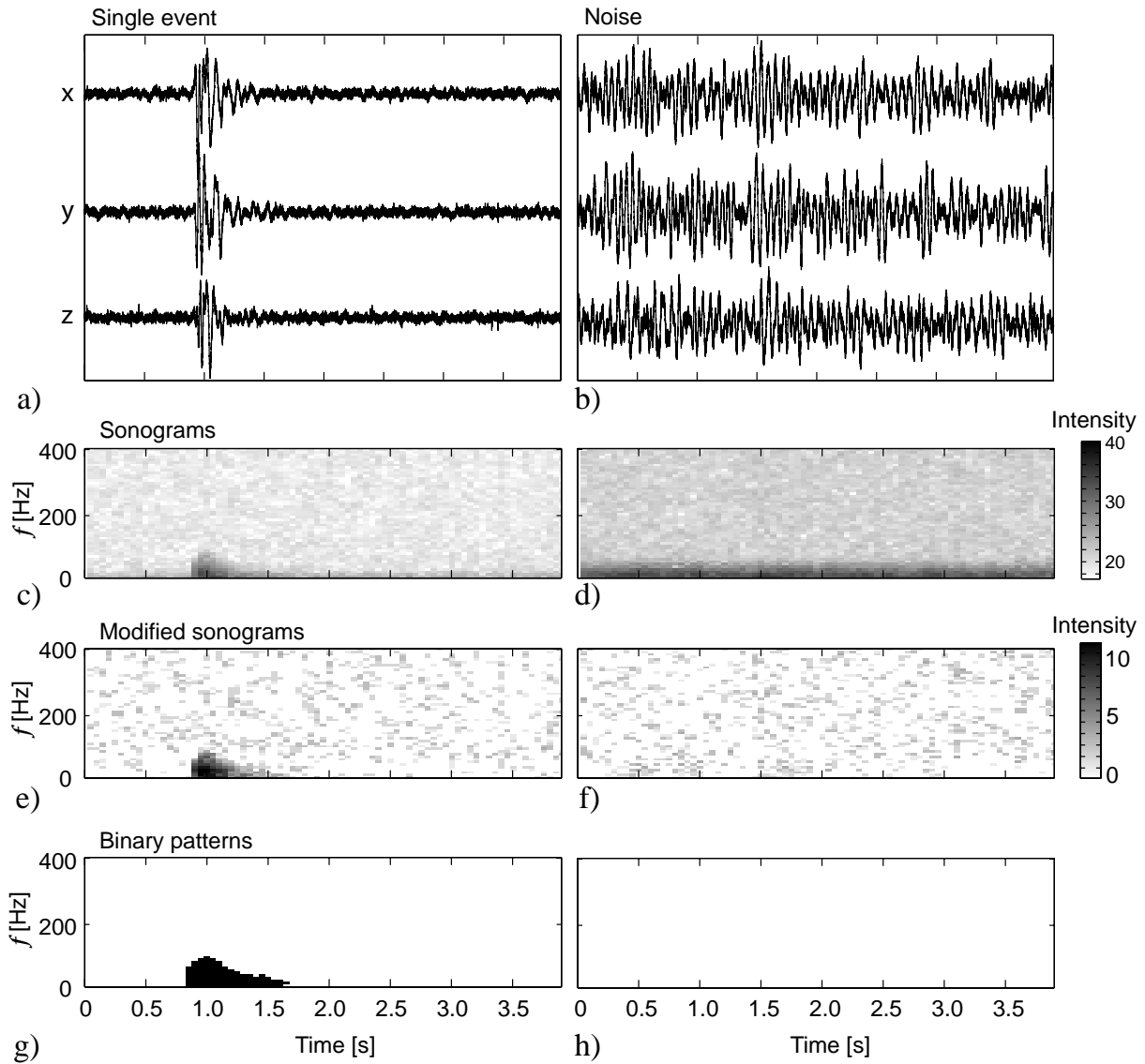


Figure 4.C1: Example of the sonogram (spectrograms or running spectra) processing scheme applied to 3-component seismograms of a typical microearthquake (left column of diagrams) and noise (right column of diagrams). (a) and (b) Seismograms. (c) and (d) Sonogram stacks. (e) and (f) Sonogram stacks after noise reduction. (g) and (h) Binary patterns derived from the sonograms. Note the absence of signal in (h) for the noise recording in (b). See text for details.

5 Conclusions and outlook

Reliable stability analyses of rockslides require detailed knowledge of the important structures and the kinematics and dynamics of the unstable slopes. Geophysics offers a variety of surface and borehole methods for investigating such structures and processes at depth.

In this thesis, I presented results from borehole radar surveying and microseismic monitoring experiments performed on the unstable mountain slope above the scarp of the huge 1991 Randa rockslides, where three moderately deep boreholes (51.0-120.8 m) have been drilled. The borehole radar and microseismic studies addressed two fundamental problems of unstable rock slopes: (1) the location of weakness zones within the rock mass and (2) the characterization of the mechanisms and processes involved in the slope instability. In the following sections, the major findings presented in Chapter 2-4 will be summarized.

5.1 BOREHOLE RADAR

Traditional geophysical approaches of investigating unstable mountain slopes have limited depth penetration and they are not well suited for imaging the steeply dipping features that usually outline the unstable volumes. In Chapter 2, I demonstrated the utility of geophysical borehole logs in combination with single-hole radar reflection, vertical radar profiling (VRP), and crosshole radar techniques for mapping and characterizing moderately to steeply dipping brittle discontinuities. The results can be summarized as follows:

- Many single-hole radar reflections appear to have been generated at fracture zones observed at the surface and within the boreholes. The combined interpretation of the single-hole radar reflections and fracture-zone locations and orientations measured at the surface and within the boreholes revealed a connection between the radar reflections and six surface and four borehole fracture zones. Six additional borehole radar reflections likely originated at previously unmapped fracture zones.

- Velocities determined from the VRP data had disappointingly low resolutions. Only a single interpretable VRP reflection could be identified, which was associated with the prominent steeply dipping surface fracture zone Z3 (Figure 2.12).
- The crosshole tomograms provided median radar velocity and attenuation estimates, but otherwise they were surprisingly featureless. Velocity values, for example, varied by only $\pm 5\%$ about the median value of 0.120 m/ns. Three low-contrast anomalies in the tomograms could be related to discontinuities that intersected the boreholes. A prominent steep-dipping surface fracture zone (Z9 on Figure 2.11), which crossed the tomographic plane at a steep angle, was not detected. This was likely due to the insensitivity of the crosshole method to narrow borehole-parallel features.

5.2 MICROSEISMIC NETWORK AND MONITORING

Chapter 3 provided detailed information on our approach to designing, deploying, and operating the microseismic network at the Randa study site, which was operated in combination with a geotechnical monitoring network. The microseismic network consisted of twelve 3-component geophones installed beneath the rugged alpine terrain. Tests to determine the theoretical resolution of the microseismic network demonstrated the importance of information provided by the borehole geophones.

The design and deployment of the network involved tackling numerous challenging technical problems associated with operating on a hazardous and remote mountain slope. Important details included lightning protection and power generation at the central recording site. Although installation and operating costs were relatively low, the monitoring system was able to acquire and administer large volumes of data in an efficient and mostly unsupervised manner.

During the operating time of the microseismic monitoring network from January 2002 to July 2004, 223 microearthquakes with moment magnitudes between -2.0 and 0.0 were detected (see Chapter 4). The distribution of microearthquake hypocenters and magnitudes suggested that they were related to instability processes within the mountain-slope. The frequency content of the microseismic recordings was mostly limited to 5-100 Hz, demonstrating that attenuation of the seismic energy within the fractured and faulted rock mass was substantial. To determine reliable hypocenter parameters, it was essential to incorporate comprehensive information on the 3-D distribution of seismic velocities in the

hypocenter estimation process. Such a 3-D velocity model was derived from an existing tomographic seismic refraction data set (Heincke et al., 2006a). Analysis of twelve calibration shots proved that the epicenters and depths of events within and close to the network boundaries were mostly determined to better than 21 m. Outside the network and at greater depths, the uncertainties were considerably larger. The following microseismicity patterns at the Randa study site were established:

- The microseismic activity was concentrated in two main zones: one that followed the rockslide scarp and one that coincided with the highest density of fracture zones/faults. These two zones were bound by the geodetically determined limits of mobile rock. Most microearthquakes occurred at shallow depths within 50-100 m of the surface.
- Microseismic activity was also observed near and beyond the western boundary of the microseismic network. The geometries and locations of these zones were poorly constrained. Minor microseismicity near the base of the location model was evidence for activity deeper in the mountain.
- Two zones were noticeably aseismic: one ~50-100 m wide zone lay to the west of the zones of concentrated microseismic activity and one was found below the activity.

5.3 INTEGRATED STRUCTURAL MODEL

Based on an integrated interpretation of all relevant surface and borehole data sets, I derived a 3-D structural model that outlined the sizes and geometries of fracture zones observed at the Randa study site. Based on this model, I suggested that the investigated rock volume was divided by major fracture zones into a number of discrete blocks.

The borehole methods provided important constraints on the dip angles and minimum depth extents of the fracture zones and faults. Given their lateral dimensions at the surface, the majority of these structures may extend even deeper into the mountain slope than observed in the radar data.

Two important steeply dipping fracture zones and faults observed at the surface and in the borehole radar data were also imaged in the surface georadar data and in the tomographic seismic refraction model. The Z2 and Z3 fracture zones/faults (Figure 2.12) were associated with (1) mapped surface lineaments (Willenberg, 2004), (2) borehole radar

reflections (Chapter 2), (3) surface georadar reflections and strong diffractions (Figures 5 and 8 of Heincke et al., 2006b), and (4) broad zones of low seismic velocity (C and D in Figure 7 of Heincke et al., 2006a).

The microseismicity study provided insights into the displacement characteristics of a large volume of the mountain slope. However, correlation of the microseismic activity with the results of other geophysical and geotechnical investigations was difficult, primarily because of the different sensitivities of each method. Nevertheless, the shallow boundaries of the principal microseismogenic zones generally aligned with the rockslide scarp and with fracture zones and faults mapped at the surface and/or observed in surface and borehole radar sections. Geodetic observations demonstrated that this volume was actively moving.

In summary, information supplied by the georadar, microseismic, seismic refraction and geodetic investigations was generally consistent. Together, the various data sets show the extent of mobile rock mass northwest of the 1991 rockslide scarp to be defined by the Z2-Z3 and Z10 fracture zones/faults. Unfortunately, it was not possible to delineate a master fault at depth that could control future rockslides. The thickness of the microseismogenic zones and displacement data from within the boreholes were compatible with the mobile rock mass having a depth extent of 50-120 m.

5.4 SUGGESTIONS FOR FURTHER INVESTIGATIONS AT RANDA

5.4.1 Unresolved depth extent of instability

A major issue for further investigation at the Randa study site is the unresolved detailed depth extent of the mobile rock mass. Additional deeper boreholes and extensions to existing ones would allow significant new deep data to be acquired. Sufficiently deep boreholes would open-up the possibility of placing accelerometers below the lower boundary of mobile rock mass, where seismic attenuation is perhaps less severe. This would provide the possibility to record and analyze any high-frequency microseismic events occurring at the base of the moving mass.

The heavily fractured and dissected nature of the rock mass suggests that a zone more complex than a discrete plane may form the base of current instability. To address this question, studies on a larger scale may be required. The application of remote sensing methods to the steep scarp of the 1991 rockslide would provide detailed structural and/or displacement maps that might allow the lower boundary of instability (as expressed on the

scarp face) to be identified. Such a study was launched in September 2005 with initial measurements of ground-based synthetic aperture radar (SAR) data. This technique compares quantitatively the phase information between initial and repeat radar images of the same area (Figure 5.1; Antonello et al., 2003; Tarchi et al., 2003). The resulting deformation maps at Randa should provide estimates with an accuracy of better than 1 mm over the entire 1991 failure surface with a spatial resolution of a ~ 5 m.

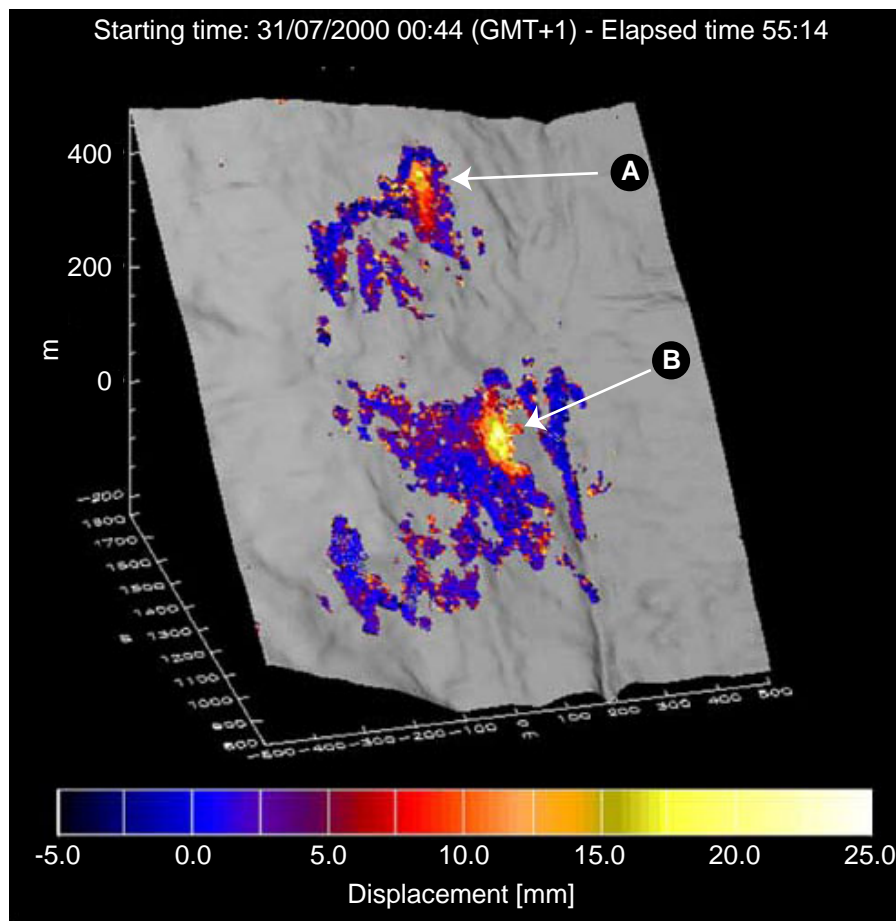


Figure 5.1. Ground-based DInSAR interferogram showing two distinct displacement patterns (A) and (B) on the Ruinon rockslide (Italy). Maximum displacements of 25 mm (B) were observed over a period of 55 h 14 min (after Tarchi et al., 2003).

An improved understanding of processes affecting the base of the unstable rock mass would be expected from investigations using information provided by an expanded microseismic monitoring network. The expanded network should increase geophone density to constrain better microearthquake locations and enable fault plane mechanisms to be determined. Furthermore, enlarging the network aperture, if possible by fixing geophones

onto the rockslide scarp, would enhance the detection of deeper events. However, the very heterogeneous seismic velocity field and strong attenuation will continue to pose challenges for microseismic investigations of the unstable slope. A larger microseismic network at the Randa study site would require additional tomographic refraction seismic surveys to determine seismic velocities throughout a larger region of the rock mass.

5.4.2 Reduce inaccuracies of the microseismic technique

At present, microearthquakes at the Randa site have not been related to individual fracture/fault zones. Using relative relocating techniques for clustered events in microseismic zones A and B may improve further the hypocenter accuracies. Applications of the double-difference algorithm have produced sharper images of earthquakes occurring along major tectonic faults (e.g. Hayward fault - Waldhauser and Ellsworth, 2000; Calveras fault - Schaff et al., 2002; North Apennine Belt - Chiaraluce et al., 2003). After relocation, microearthquakes at Randa may be found to cluster close to fracture zones and faults.

Additional improvements to the hypocentral parameter estimates may be expected from a joint determination of hypocentral parameters and velocities. Microearthquakes in zone A, which occurred close to the rockslide scarp beside the network boundary where velocities were nearly unresolved by the existing 3-D velocity model, could benefit from relocation. The value of this method has been demonstrated in local earthquake tomography studies in Switzerland (Husen et al., 2003), California (Thurber, 1983; Eberhart-Phillips and Michael, 1993), and Japan (Shibutani and Katao, 2005).

5.5 SUGGESTIONS FOR METHODOLOGICAL IMPROVEMENTS

5.5.1 Borehole and surface radar

Unfortunately, because of the rotational symmetry of single-hole radar data, additional information is required to locate unambiguously the imaged reflectors. I derived the missing information from fracture orientations measured at the surface and in boreholes. This approach is not always applicable, such that alternatives need to be explored.

One approach is to use directional borehole antennas that allow the azimuth of the reflected signal to be estimated (Seol et al., 2004). A drawback of this approach is the generally lower signal-to-noise ratios of directional data compared to regular borehole radar data.

Another approach is to consider the polarization of the reflected electromagnetic waves. Using a cross-polarized antenna configuration in VRP (Tronicke and Knoll, 2005) minimizes the mirror symmetry of steeply dipping reflections. VRP reflections from opposite sides of the acquisition plane would show reversed polarizations, when the reflection properties of the causative fracture are comparable. Complementary information on shallow dipping structures would be obtained by using co-polarized configurations (Zhou and Sato, 2000; Tronicke and Knoll, 2005). In general, co-polarized data show stronger amplitudes than cross-polarized data. To benefit fully from VRP, multi-component data that includes both configurations should be acquired.

A novel and challenging use of GPR to map steeply dipping discontinuities was presented by Jeannin et al. (2006). These authors acquired two GPR profiles in which the georadar antennas were positioned directly on the surface of a limestone cliff (Figure 5.2a). This configuration proved very sensitive to the two sets of steep-dipping discontinuities observed on the cliff and on the plateau (Figures 5.2a and b). After arranging the acquired GPR data in a 3-D perspective form (Figure 5.2c), minimum extensions and orientations of the imaged fractures could be derived. On the basis of these data, Jeannin et al. (2006) could delineate potentially unstable rock. Application of this technique to the steep scarp of the 1991 Randa rockslide would provide additional information on the discontinuity network.

5.5.2 Research on transients

A major effort was required to characterize and classify the enormous number of transients (Chapter 4) recorded by the Randa microseismic network. Although it is still unclear what caused the transients at Randa, similar features have been recorded elsewhere (S. Mertl, S. Husen, personal communications, 2006). It would be wise to conduct in-depth research on the origin(s) of these transients. As result, filters may be then constructed to remove the noise before contaminating the recordings of seismic/seismological interest.

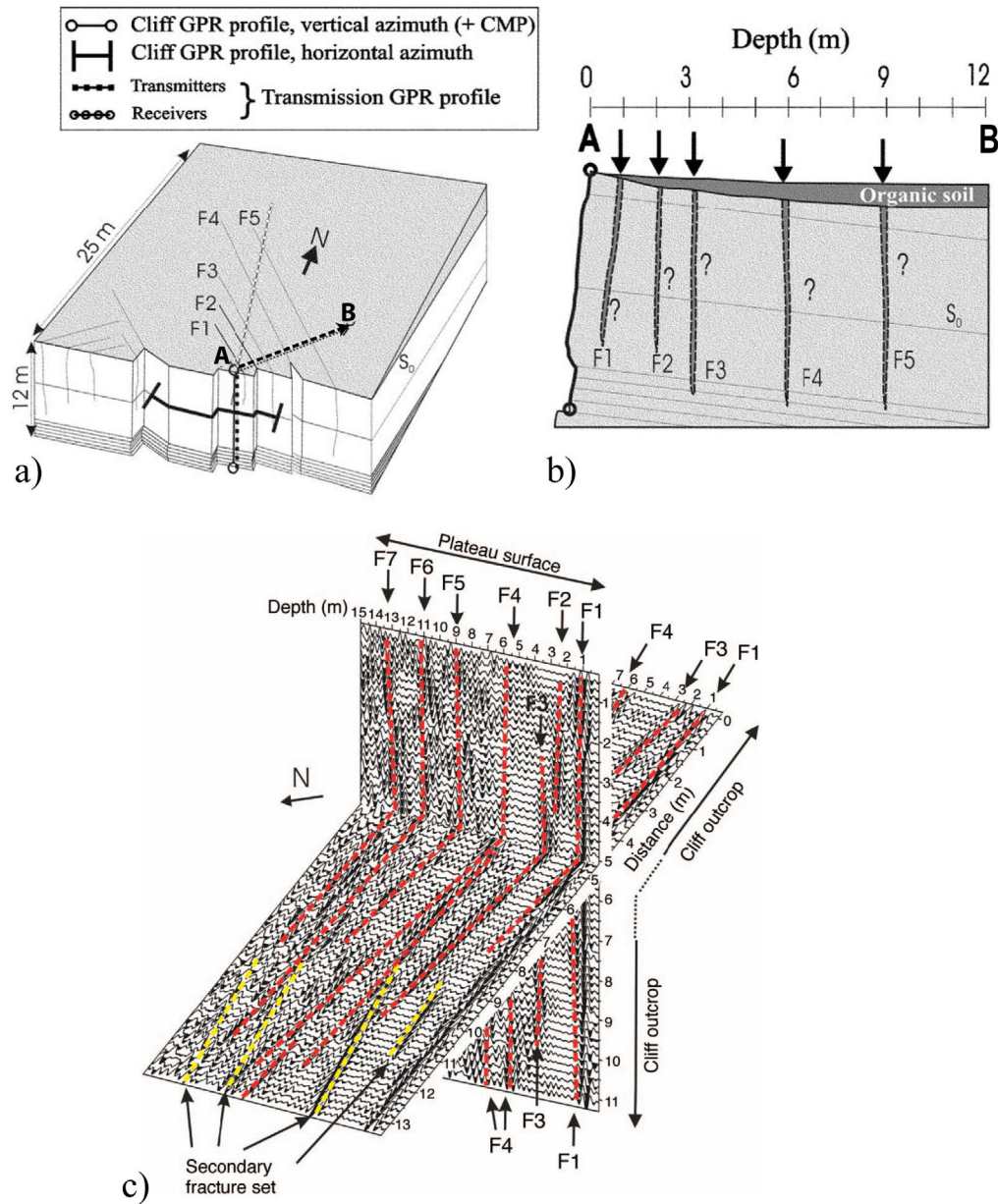


Figure 5.2: (a) Schematic representation of the limestone cliff, the main fractures (F1 to F5), and a hypothetical survey line A-B of the chartreuse test site. (b) Hypothetical cross-section A-B. (c) A vertical and a horizontal georadar profile showing (red) the orientation and dip of the main fractures and (yellow) secondary fractures (after Jeannin et al., 2006).

5.5.3 Microseismic monitoring

Methodological improvements of the microseismic monitoring technique on unstable slopes may include:

- Broader band geophones capable of faithfully recording signal-frequencies as low as ~1 Hz. Even though high-frequency microearthquakes are the primary objective, regional earthquake information is useful for network calibration, velocity estimates, and determining earthquake scaling relationships. A broader band network would record the full spectral bandwidth of very local and regional earthquakes (with hypocentral-network distances of <1 km and <40 km, respectively).
- Develop more effective and economic ways of designing microseismic monitoring networks. A possible approach would be to combine nested networks of different sensors (Figure 5.3). Evans et al. (2005b) combine a relatively sparse strong-motion network of high-quality sensors (Class A) with denser networks of lower-quality sensors (Classes B and C). This approach of regularly spaced networks would have to for use on unstable slopes. I suggest employing a relatively sparse network of high-quality broader band geophones to record 3-component waveforms. This initial network would be augmented by numerous cheaper single-component sensors (geophones or accelerometers) to enhance spatial resolution. Network design could provide flexible interfaces for adaptively augmenting or reducing sensor density during the network deployment. Interesting results would be obtained from vertical strings of borehole sensors near located active discontinuities or across the lower boundary of the moving mass. They would provide a unique opportunity to obtain fault plane solutions or moment tensors of instability-related microearthquakes.

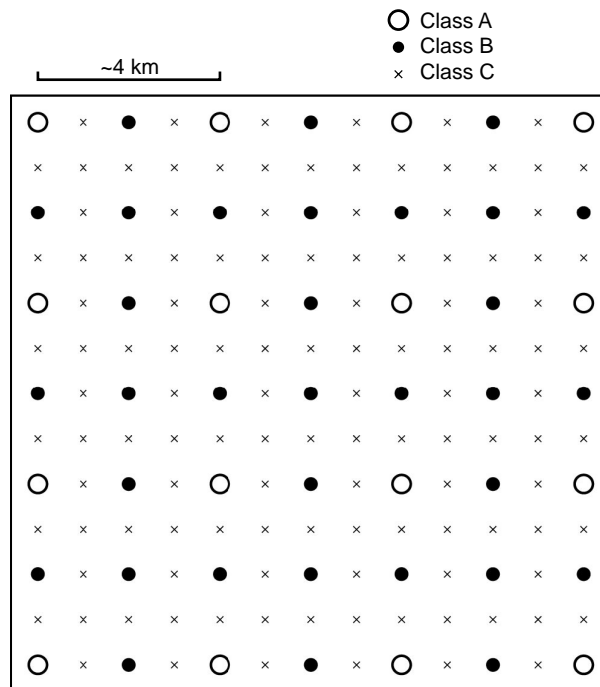


Figure 5.3: Sketch of nested array with three grades of sensors (A, B, and C from highest to lowest quality) to obtain both amplitude and spatial resolution economically (example for a strong motion network, after Evans et al., 2005b).

Appendix A

Polarization for two selected rockslide-related microearthquakes

A.1 THE COVARIANCE METHOD

Analyses of particle motions were important in the interpretation of the two microseismic events A and B in Chapter 4. In general, 3-component recordings are required to decompose the acquired data into their principal components. This decomposition, which provides information about the size, shape, and orientation of the dominant particle motions, is useful for identifying or separating the P-, S-, and the surface waves in a seismogram. The P- and S-waves are both linearly polarized, with the P- and S-wave particle motions parallel and perpendicular to the propagation direction, respectively.

The covariance matrix method provides the means to analyze particle motions of 3-component seismograms (Flinn, 1965). Applications based on this method have been developed to detect various phases (Montalbetti and Kanasewich, 1970; Vidale, 1986; Klumpen and Joswig, 1993; Oye and Roth, 2003).

The general idea of this method is to analyze the covariance matrix

$$\mathbf{C} = \begin{bmatrix} c_{xx} & c_{xy} & c_{xz} \\ c_{yx} & c_{yy} & c_{yz} \\ c_{zx} & c_{zy} & c_{zz} \end{bmatrix}, \quad (\text{A.1})$$

where, for example,
$$c_{xy} = \frac{1}{N-1} \sum_{k=1}^N (x_k - \langle \mathbf{x} \rangle)(y_k - \langle \mathbf{y} \rangle) \quad (\text{A.2})$$

is the covariance for two discrete seismograms $\mathbf{x} = x_k$ and $\mathbf{y} = y_k$ of length N , and $\langle \cdot \rangle$ is the arithmetic mean. If the polarization of the signal is linear, \mathbf{C} has just one non-zero eigenvalue λ_1 , and $\lambda_2 = \lambda_3 = 0$. The first eigenvector \mathbf{v}_1 is the direction of the dominant particle motion. If there are two non-zero eigenvalues, the polarization is elliptic (e.g., as for Rayleigh waves).

For real data, zero eigenvalues will rarely occur. Instead, linear polarization is usually indicated by λ_1 being considerably larger than λ_2 and λ_3 . Typically, the polarization vectors and ray directions of P-waves from moderately deep earthquakes are nearly vertical, and the polarization vectors of S-waves dip at shallow angles.

I computed the orientations of the first eigenvectors by analyzing data contained in sliding cosine-tapered windows. A window length of 0.080 s contained roughly one wavelength of a recorded signal. A polarization analysis began by determining particle motions with a window centered on the first-break of the initial P-wave arrival. The window was then shifted by time increments of 0.012 s and the process repeated. The following results illustrate polarization analyses for two suites of microearthquake recordings (A and B in Chapter 4).

A.2 RESULTS

Figure A.1 highlights the windows of the 3-component seismograms of local event A and more distant event B (see Figure 4.10) that are dominated by P-wave energy. Particle motions for the selected windows are shown in Figure A.2. Clearly, event A (Figures A.2a and b) occurred very close to geophone B2, which recorded by far the strongest amplitudes.

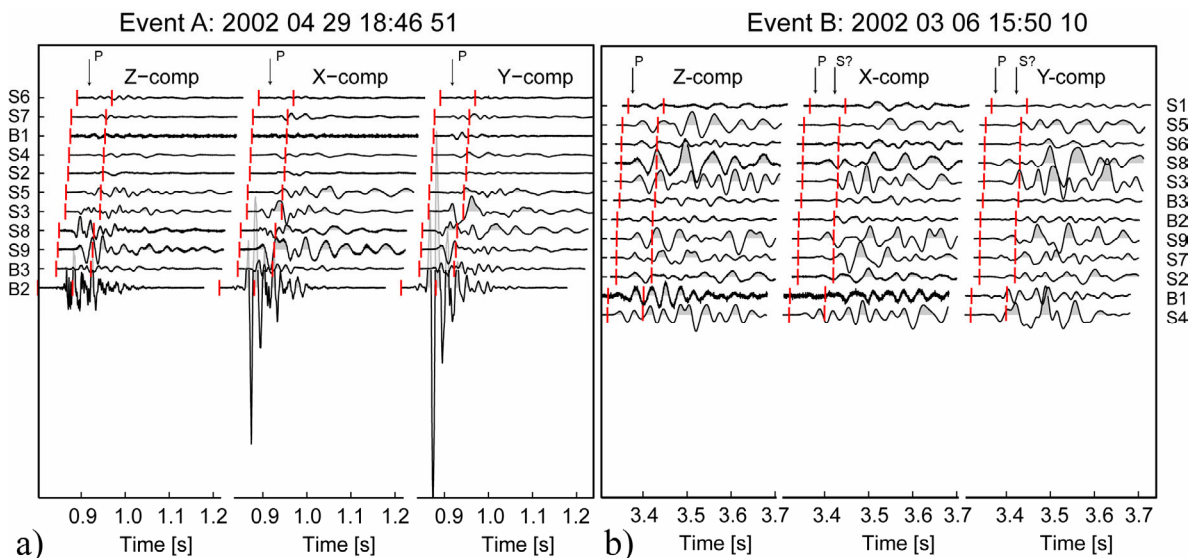


Figure A.1: Microseismic events with typical polarization windows (between red lines). (a) Local event A, and (b) distant event (B). Geophones are identified to the left and right of the respective traces.

The hodogram characteristics vary from nearly linear to elliptical, with the dominant particle-motion directions varying significantly between recordings. In contrast, very coherent hodograms for event B (Figures A.2c and d) were obtained. Dominant particle motions were mostly vertical, as expected from a moderately deep event outside the network boundaries.

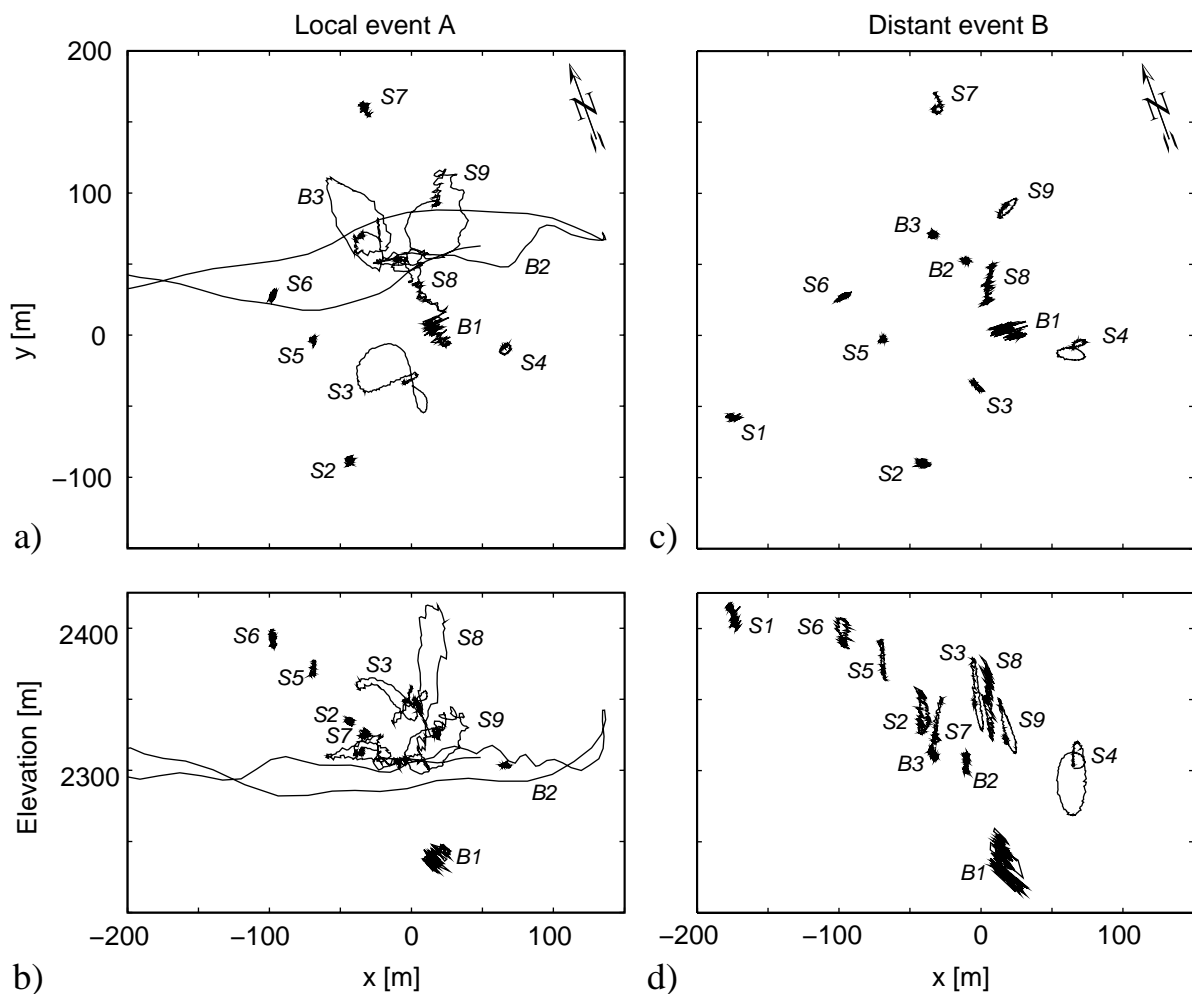


Figure A.2: Particle motions projected on to (a and c) horizontal and (b and d) vertical planes. Initial values of each hodogram correspond to the location of the respective geophone (labeled). (a and b) Event A is located close to geophone B2. (c and d) Event B is probably located >300 m east of the network (Figures 4.11f and h). Data were uniformly scaled.

These results are consistent with Figure A.3, in which the dominant particle-motion angles are plotted as functions of arrival time. For local event A (Figures A.3a and b),

particle motions dip at various angles, such that individual P- and S-waves cannot be identified. For event B, the initial P-wave particle motions have angles $>70^\circ$ for at least the first 0.04 s (close geophones in Figure A.3c) or 0.1 s (far geophones in Figure A.3d). They generally change to shallow dipping angles at later times.

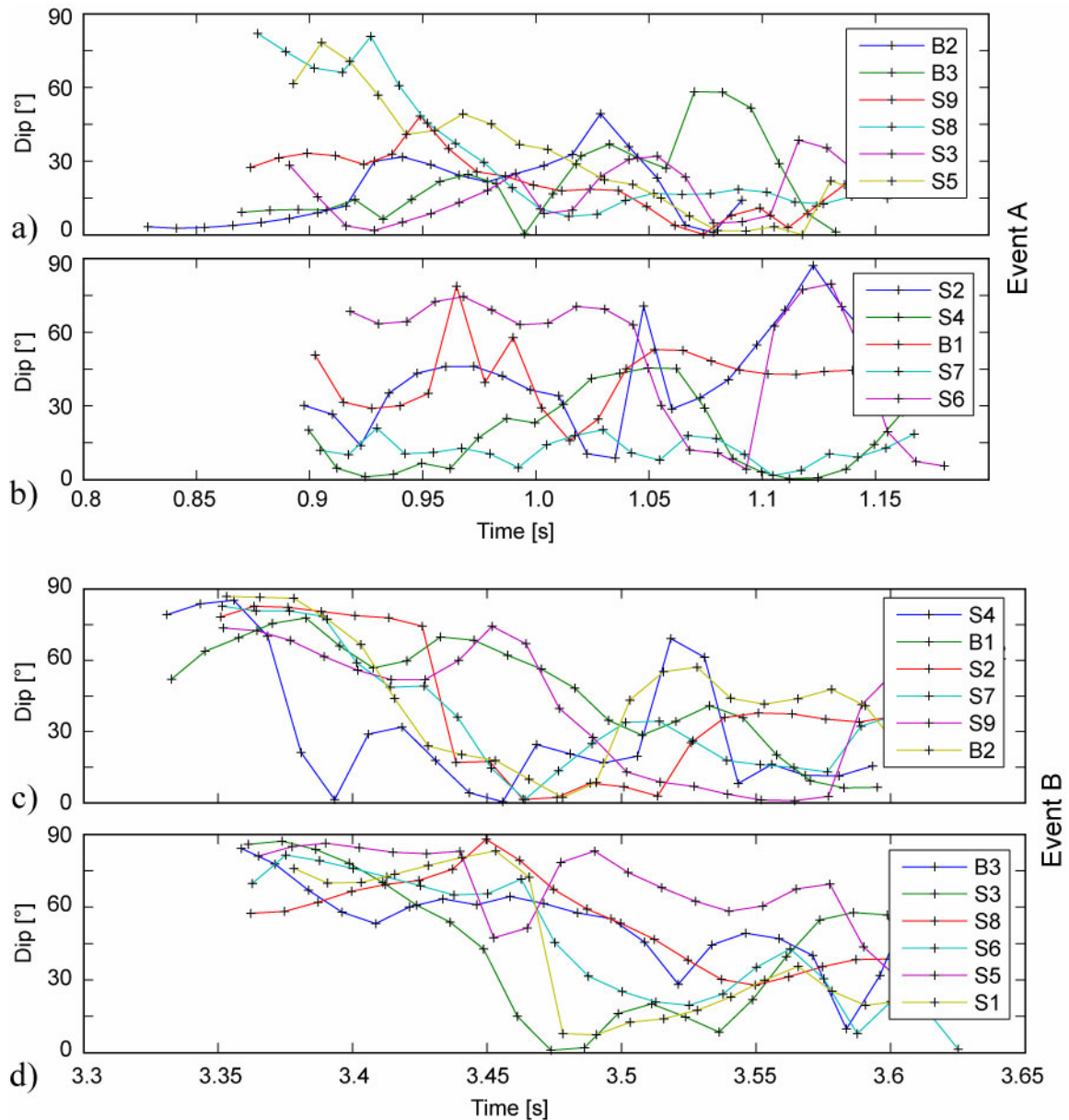


Figure A.3: Polarization results for local (a and b) event A and (c and d) distant event B showing the dominant angle of particle motion relative to the horizontal. For clarity, angles are displayed for geophones (a and c) close and (b and d) far from the respective hypocenters.

Appendix B

Magnitudes for rockslide-related microearthquakes

B.1 INTRODUCTION

Initially, I tried to obtain microearthquake magnitudes using the following general magnitude relationship (e.g. Lee and Stewart, 1981)

$$M = a \log(A/T) + b \log(D) + c, \quad (\text{B.1})$$

where A is the maximum ground displacement amplitude, T is the signal period, D is epicentral distance, and a , b , and c are parameters to be derived. I attempted to obtain a , b , and c by fitting data for events that were recorded on the Randa network and by the Swiss Seismological Service. Although 76 regional earthquakes had been recorded on both networks, the approach failed. It was not possible to derive reliably the attenuation parameter b .

B.2 MOMENT MAGNITUDES

I was successful in computing moment magnitude estimates m for microearthquakes recorded by the Randa microseismic network using the following formulas introduced by Hanks and Kanamori (1979):

$$m = \frac{2}{3} \log M_0 - 6.1, \quad (\text{B.2})$$

where

$$M_0 = \frac{4\pi\rho v_p^3 R \Omega_0}{U}, \quad (\text{B.3})$$

M_0 is the seismic moment, R is the hypocentral distance, Ω_0 is the long-period amplitude determined from the displacement spectra, $U=0.52$ is a general correction for the mean radiation pattern (Aki and Richards, 1980), and I set density $\rho = 2.7 \text{ g/cm}^3$, and P-wave velocity $v_p = 2.5 \text{ km/s}$.

The long period amplitude Ω_0 was obtained using a standard spectral analysis technique. Brune (1970) and Madariaga(1976) proposed a general model for fitting the displacement spectra of both P- and S-waves:

$$\Omega(f) = \frac{\Omega_0 \exp(-\pi ft / Q)}{[1 + (f / f_c)^n]^{1/\gamma}}, \quad (\text{B.4})$$

where f is frequency, f_c is the corner frequency, t is the traveltime, Q is the quality factor, n is the high-frequency fall off rate, and γ is a constant. I closely followed Abercrombie (1995) in fitting this model to the seismograms observed at the Randa network. As reliable separation between P- and S-waves was not possible, I analyzed data selections only containing P-waves. The necessary steps were:

- (1) correct the seismograms for the geophone response,
- (2) select and extract data windows and rotate the data into principal components,
- (3) compute the Fourier spectra and integrate (from velocity to displacement), and
- (4) obtain Ω_0 by fitting Equation (B.4) to the displacement spectra.

Steps (1) – (4) were evaluated for every picked arrival time. Details on important parameters are given in Table B.1.

Table B.1: Parameters used to fit displacement spectra.

<i>Parameter</i>	<i>Value</i>
Window taper	Cosine (Tukey window)
Window length	0.15 s
Time preceding pick	0.03 s
Analysis bandwidth	3 - 390 Hz
t	0.1 s
n	1
γ	2

A Nelder-Mead simplex algorithm available in MATLAB was used to determine iteratively the best fitting parameters for the model (Equation B.4).

B.3 RESULTS

Figure B.1a shows displacement spectra for microseismic event A. Since this event occurred close to geophone B2, displacements recorded at this geophone are ~10 times larger than on others. Corner frequencies of ~20 – 50 Hz are observed. The fitting algorithm provided good estimates of Ω_0 , thus allowing the seismic moment M_0 and magnitude m to be

reliably estimated (Figure B.1b). Poor results were obtained for f_c and Q for some events, but were not used in the calculations.

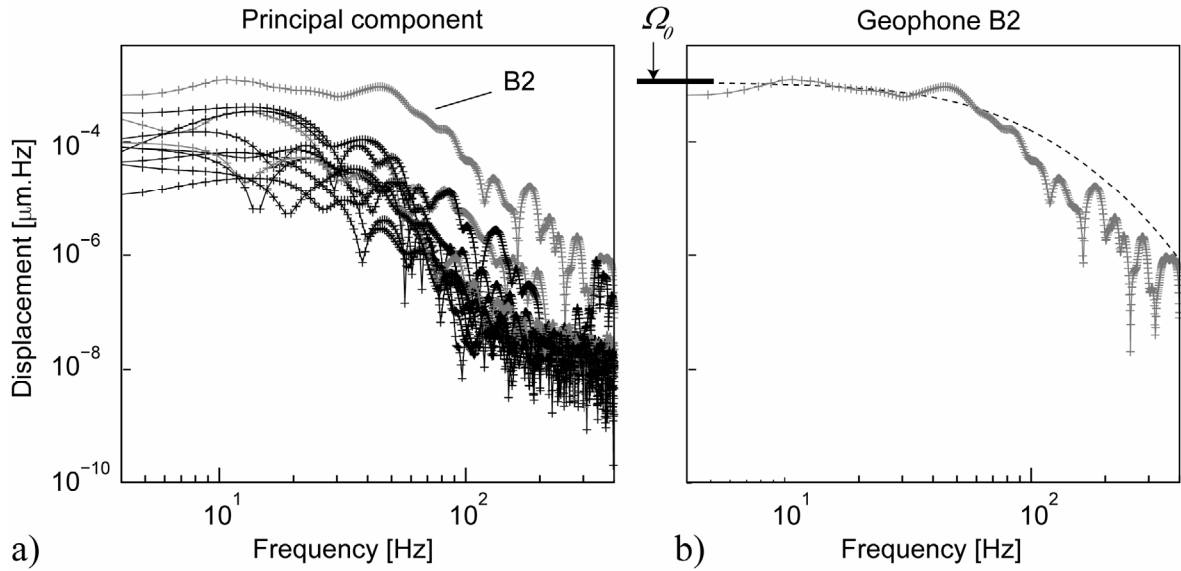


Figure B.1: (a) Displacement spectra of the principal components for event A. (b) Spectrum for geophone B2, spectral model (dotted), and long period amplitude Ω_0 .

A mean magnitude and standard deviation for each microearthquake was finally computed from the magnitude estimates determined from each recording. Table B.2 summarizes hypocentral coordinates, mean moment magnitudes, and standard deviations for all 223 microearthquakes detected at the Randa network.

Table B.2: Hypocentral coordinates, magnitudes, and magnitude standard deviation for Randa microearthquakes.

Line	Event	X [m]	Y [m]	Z [m]	m	std	Line	Event	X [m]	Y [m]	Z [m]	m	std
1	20020109145936	625800.86	107089.83	2317.60	-1.5	0.2	41	20020307165030	625741.66	107040.96	2257.95	-1.3	0.2
2	20020109150033	625799.50	107086.06	2317.60	-1.6	0.2	42	20020307185920	625943.05	107040.91	2086.45	-0.8	0.3
3	20020111155346	625802.40	107061.65	2270.03	-1.6	0.2	43	20020308085459	625737.36	107038.25	2319.61	-1.8	0.3
4	20020114162947	625812.77	107072.80	2284.86	-1.6	0.2	44	20020309204818	625717.66	107009.20	2159.20	-1.6	0.2
5	20020121054734	625829.42	107113.57	2294.88	-1.7	0.2	45	20020310064912	625817.20	107086.09	2300.09	-1.6	0.2
6	20020121153412	625756.23	107084.60	2282.09	-1.4	0.2	46	20020318091255	625766.27	107019.37	2258.58	-1.2	0.2
7	20020122225031	625620.15	107022.95	2198.16	-1.2	0.2	47	20020319150410	625789.89	106919.52	2119.49	-0.5	0.3
8	20020125141342	625938.31	107053.23	2171.90	-1.2	0.2	48	20020319220958	625792.08	107054.73	2283.79	-1.5	0.2
9	20020125140547	625798.80	107086.32	2315.75	-1.7	0.2	49	20020320093705	625763.07	106984.40	2226.98	-1.3	0.2
10	20020127052227	625827.14	107099.52	2295.99	-1.5	0.2	50	20020409021906	625985.09	107095.94	2138.37	-1.1	0.2
11	20020127185143	625780.56	107103.49	2333.66	-1.1	0.2	51	20020409070625	625724.65	107072.56	2165.19	-1.1	0.1
12	20020128040115	625759.56	106994.15	2253.38	-1.5	0.3	52	20020423141554	625847.04	107268.75	2238.18	-1.4	0.2
13	20020203075812	625775.64	107175.38	2347.50	-1.9	0.2	53	20020428070131	625745.33	107041.76	2319.21	-1.7	0.2
14	20020207114021	625818.19	107092.11	2302.69	-1.6	0.3	54	20020429184651	625760.60	107176.53	2327.49	-1.4	0.2
15	20020209134234	625803.56	107097.36	2317.60	-1.3	0.2	55	20020501191910	625701.45	107121.27	2262.63	-1.9	0.2
16	20020212171719	625719.63	107053.11	2164.44	-1.1	0.2	56	20020501233910	625800.86	107089.83	2317.60	-1.5	0.2
17	20020213110704	625699.37	107139.01	2216.23	-1.3	0.1	57	20020502091637	625777.62	106974.92	2172.70	-1.3	0.1
18	20020213212849	625822.78	107084.09	2293.39	-1.5	0.2	58	20020502213134	625804.11	107073.79	2301.23	-1.9	0.2
19	20020217040043	625779.18	107067.86	2322.85	-1.5	0.2	59	20020502222730	625777.02	107185.51	2160.69	-1.2	0.1
20	20020217093633	625740.34	107113.68	2311.52	-1.8	0.1	60	20020503011934	625732.69	107059.05	2237.94	-1.5	0.1
21	20020217123313	625805.64	107096.61	2312.40	-1.8	0.2	61	20020503021800	625809.10	107097.49	2309.04	-1.2	0.3
22	20020222121314	625803.56	107097.36	2317.60	-1.2	0.2	62	20020505043609	625606.94	107199.82	2371.85	-1.5	0.2
23	20020223100533	625801.53	107091.71	2317.60	-1.4	0.2	63	20020506125527	625799.50	107086.06	2317.60	-1.5	0.2
24	20020223113730	625858.85	107039.26	2206.68	-1.2	0.1	64	20020507103153	625813.27	107098.12	2307.55	-1.5	0.3
25	20020226234453	625820.36	107116.83	2303.09	-1.6	0.1	65	20020508000812	625762.65	106993.05	2234.79	-0.7	0.2
26	20020304105621	625800.91	107083.44	2312.40	-1.5	0.2	66	20020508104355	625644.08	107095.11	2198.90	-1.1	0.2
27	20020304120553	625824.52	107083.46	2292.64	-1.5	0.2	67	20020520011804	625658.68	107172.75	2344.16	-1.5	0.2
28	20020304133207	625788.95	107098.35	2325.45	-1.3	0.2	68	20020523181100	625730.56	107138.44	2171.93	-1.3	0.1
29	20020304144642	625835.02	107109.44	2290.03	-1.5	0.1	69	20020523181141	625448.13	106999.71	2329.42	-1.1	0.2
30	20020304164130	625779.75	107190.91	2162.55	-1.4	0.1	70	20020523201550	625658.88	107100.42	2271.66	-1.6	0.2
31	20020305065432	625811.66	107117.82	2308.69	-1.5	0.2	71	20020524013244	625764.81	107041.15	2311.72	-1.9	0.2
32	20020305184035	625704.89	107139.16	2309.06	-1.8	0.2	72	20020524035843	625746.16	107132.84	2346.43	-1.9	0.3
33	20020305212452	625757.14	106992.90	2254.12	-1.2	0.3	73	20020524094745	625809.78	107099.38	2309.04	-1.4	0.3
34	20020306071846	625805.51	107069.03	2287.11	-0.9	0.2	74	20020525163319	625730.93	106862.06	2211.72	-1.3	0.1
35	20020306104233	625682.58	107091.92	2248.54	-1.5	0.2	75	20020525192447	625840.34	107130.90	2284.47	-1.5	0.2
36	20020306155010	625939.17	107016.80	2097.57	-0.9	0.2	76	20020525230236	625706.20	106904.94	2246.39	-1.4	0.1
37	20020307100431	625804.47	107069.41	2289.71	-1.1	0.2	77	20020527094146	625740.25	107024.46	2305.84	-1.5	0.2
38	20020307120140	625881.95	107096.84	2223.01	-1.1	0.2	78	20020604065339	625751.15	107124.67	2354.20	-1.3	0.3
39	20020307113312	625746.23	107013.82	2179.16	-1.3	0.2	79	20020605163559	625775.77	107007.46	2141.18	-0.9	0.2
40	20020307121630	625698.43	107060.73	2199.43	-1.4	0.2	80	20020607192311	625695.68	107299.71	2265.46	-1.3	0.2

81	20020609133331	625805.28	107098.87	2315.00	-1.2	0.3	126	20021106082952	625785.34	107095.40	2276.81	-1.3	0.2
82	20020618090745	625711.66	107183.47	2293.12	-1.4	0.1	127	20021106085635	625826.47	107097.64	2295.99	-1.2	0.2
83	20020618230546	625862.35	107118.75	2265.81	-1.5	0.2	128	20021109115352	625808.40	107097.75	2307.19	-1.4	0.2
84	20020621140923	625723.52	107251.47	2205.14	-0.9	0.1	129	20021121192517	625759.67	107181.11	2166.69	-0.8	0.1
85	20020623031743	625815.60	107316.16	2258.77	-1.3	0.2	130	20021123134017	625807.02	107098.24	2314.25	-1.6	0.4
86	20020624074729	625789.86	107221.28	2160.69	-0.8	0.1	131	20021124120406	625574.77	107192.24	2303.23	-1.1	0.2
87	20020626152526	625749.48	107191.15	2171.93	-0.9	0.0	132	20021126171046	625740.69	107175.18	2196.83	-1.2	0.1
88	20020716160105	625769.60	107050.05	2315.43	-0.9	0.2	133	20021127131009	625734.73	107139.07	2170.43	-0.8	0.1
89	20020718065246	625678.22	107354.85	2221.38	-0.9	0.1	134	20021127160841	625817.52	107090.22	2302.69	-1.2	0.2
90	20020718084424	625782.09	107232.57	2165.19	-1.0	0.1	135	20021128092250	625820.50	107104.03	2303.44	-1.5	0.3
91	20020718182409	625776.12	107204.96	2163.69	-1.0	0.1	136	20021130034145	625804.56	107094.88	2295.31	-1.2	0.2
92	20020722094700	625724.83	107144.75	2356.17	-1.3	0.2	137	20021204133358	625802.88	107095.48	2317.60	-1.1	0.1
93	20020810094310	625851.90	106982.26	2126.04	-1.0	0.1	138	20021220115447	625807.98	107106.40	2315.00	-1.4	0.3
94	20020810112930	625826.95	107303.59	2172.93	-1.3	0.3	139	20021220170926	625821.74	107084.46	2295.99	-0.9	0.2
95	20020810152452	625800.86	107089.83	2317.60	-1.2	0.3	140	20021221084040	625922.46	107282.05	2135.82	-0.8	0.3
96	20020820190511	625589.88	107214.44	2421.31	-1.3	0.2	141	20021223160432	625805.39	107088.20	2313.50	-0.4	0.3
97	20020822213321	625611.08	107313.08	2420.25	-1.4	0.1	142	20030111022645	625749.32	107133.83	2358.31	-1.7	0.1
98	20020824193406	625623.89	107272.36	2366.68	-1.2	0.2	143	20030115123850	625806.20	107109.16	2313.90	-1.4	0.2
99	20021001192400	625784.48	107340.08	2299.75	-1.7	0.1	144	20030115170317	625711.20	107194.26	2186.92	-1.2	0.1
100	20021009071650	625696.38	107227.21	2343.73	-1.5	0.4	145	20030118113651	625803.56	107097.36	2317.60	-1.4	0.2
101	20021009072536	625707.04	107236.13	2334.42	-1.6	0.3	146	20030120100558	625799.78	107090.22	2309.44	-1.6	0.3
102	20021009073810	625700.23	107223.70	2339.63	-1.6	0.2	147	20030216172147	625802.05	107068.15	2290.46	-1.1	0.2
103	20021009082311	625756.53	107192.87	2309.70	-1.7	0.2	148	20030220145427	625752.41	107177.34	2168.94	-0.9	0.1
104	20021009082600	625753.09	107219.60	2306.03	-1.8	0.2	149	20030221040700	625852.08	107105.44	2274.37	-1.2	0.2
105	20021009083011	625751.40	107194.71	2344.26	-1.7	0.1	150	20030221110223	625802.88	107095.48	2317.60	-1.3	0.2
106	20021009083403	625734.99	107189.97	2315.34	-1.8	0.1	151	20030223111940	625800.67	107100.52	2297.56	-1.3	0.2
107	20021009100027	625762.22	107195.07	2353.14	-1.6	0.2	152	20030224135725	625805.93	107126.26	2288.29	-1.4	0.1
108	20021009132155	625724.59	107193.71	2341.37	-1.4	0.2	153	20030225072523	625593.37	107213.19	2419.82	-1.2	0.1
109	20021010151336	625685.02	107161.16	2377.86	-1.5	0.3	154	20030301172400	625691.35	107462.76	2231.12	-0.6	0.1
110	20021016182945	625572.46	107173.95	2387.90	-1.2	0.3	155	20030302124921	625824.89	107115.20	2298.99	-1.1	0.2
111	20021016184859	625799.50	107086.06	2317.60	-1.6	0.2	156	20030302143158	625899.34	107062.97	2211.78	-1.2	0.2
112	20021017220538	625763.90	107011.72	2254.12	-1.2	0.3	157	20030306043445	625694.19	107092.00	2179.42	-1.0	0.2
113	20021019072438	625734.11	107016.04	2207.80	-1.4	0.2	158	20030307010002	625714.09	107044.48	2249.50	-1.1	0.2
114	20021019233423	625826.61	107116.71	2296.38	-1.7	0.2	159	20030307162828	625775.12	107107.57	2280.20	-1.0	0.2
115	20021023210048	625632.09	107097.29	2372.02	-1.2	0.2	160	20030310165731	625832.88	107114.46	2291.53	-0.8	0.2
116	20021025152043	625664.80	107108.92	2192.91	-1.1	0.2	161	20030311185818	625710.46	107009.66	2302.21	-1.3	0.3
117	20021025154926	625800.91	107083.44	2312.40	-1.3	0.2	162	20030311214413	625804.52	107105.51	2318.35	-1.6	0.2
118	20021025172646	625807.72	107095.87	2307.19	-1.5	0.5	163	20030324170905	625805.95	107100.75	2315.00	-0.7	0.2
119	20021025171613	625802.88	107095.48	2317.60	-1.5	0.2	164	20030325030452	625669.11	107092.50	2286.10	-1.7	0.2
120	20021029080237	625805.51	107066.91	2278.19	-1.4	0.1	165	20030325183005	625751.40	107141.58	2164.44	-1.1	0.2
121	20021102123632	625777.88	107308.45	2198.72	-1.3	0.1	166	20030329205402	625815.97	107105.65	2307.55	-1.4	0.3
122	20021102122951	625725.66	106985.08	2288.76	-0.2	0.4	167	20030330185731	625767.99	107020.88	2255.98	-1.3	0.2
123	20021103134427	625791.24	106923.28	2119.49	-1.1	0.1	168	20030402185709	625763.90	107011.72	2254.12	-0.6	0.3
124	20021103161707	625802.26	107087.20	2312.40	-1.5	0.2	169	20030403084126	625807.98	107106.40	2315.00	-1.6	0.2
125	20021106055750	625564.85	107197.93	2376.81	-1.1	0.2	170	20030405134754	625557.37	107143.24	2357.09	-1.1	0.2

171	20030414210000	625801.01	107068.52	2293.07	-1.5	0.2	198	20031129113506	625827.34	107080.32	2291.14	-0.8	0.2
172	20030419002820	625760.21	106998.17	2251.52	-1.4	0.2	199	20031130124731	625794.78	107106.89	2326.56	-1.2	0.1
173	20030424122405	625581.64	107098.40	2387.04	-0.7	0.1	200	20040202185957	625821.65	107092.99	2299.34	-1.3	0.2
174	20030426031441	625756.86	106986.62	2253.38	-1.2	0.2	201	20040314140248	625805.28	107098.87	2315.00	-1.3	0.3
175	20030426203311	625801.36	107062.02	2272.63	-1.2	0.2	202	20040314144547	625900.39	107277.22	2184.54	-1.2	0.1
176	20030429031849	625658.13	107447.06	2241.61	-0.9	0.1	203	20040317124408	625754.27	107166.05	2166.69	-1.1	0.1
177	20030430200116	625799.50	107086.06	2317.60	-0.9	0.2	204	20040317144732	625816.62	107109.67	2305.69	-1.0	0.2
178	20030430214908	625720.40	107044.34	2264.33	-1.3	0.2	205	20040318112800	625797.93	107231.13	2320.75	-1.2	0.2
179	20030502231805	625736.43	107155.46	2320.86	-1.4	0.2	206	20040318115957	625702.16	107059.39	2273.32	-1.1	0.2
180	20030704015943	625765.10	107240.79	2321.61	-1.5	0.3	207	20040319015722	625765.02	107219.57	2333.84	-0.8	0.4
181	20030706024125	625633.59	107483.50	2314.15	-1.0	0.1	208	20040417060607	625696.73	107048.58	2280.38	-1.3	0.2
182	20030906114140	625755.77	107180.39	2355.74	-1.3	0.2	209	20040417101045	625662.72	107141.54	2198.16	-1.0	0.3
183	20030908072539	625853.86	107060.18	2241.63	-0.6	0.3	210	20040417150517	625726.34	107014.58	2169.57	-1.0	0.2
184	20030909051342	625809.32	107061.29	2254.41	-0.9	0.2	211	20040418184115	625918.51	107255.84	2116.49	-0.7	0.1
185	20030927003558	625693.42	107298.40	2207.89	-1.0	0.2	212	20040419033235	625802.29	106970.31	2143.28	-1.3	0.2
186	20030930002809	625746.35	107207.15	2332.77	-1.9	0.2	213	20040419141243	625802.65	107082.81	2311.65	-1.5	0.2
187	20030930130624	625766.38	107131.95	2351.56	-1.6	0.2	214	20040423040427	625798.95	107062.89	2282.30	-0.9	0.2
188	20031008120112	625764.68	106956.19	2200.95	-0.9	0.2	215	20040505155333	625818.64	107081.32	2296.74	-0.9	0.2
189	20031014013736	625815.94	107107.79	2305.69	-1.4	0.2	216	20040601183159	625697.09	107139.83	2268.98	-1.1	0.2
190	20031017122538	625716.57	107198.71	2355.89	-1.2	0.2	217	20040601193435	625809.10	107097.49	2309.04	-1.2	0.3
191	20031021095904	625879.08	107106.37	2229.72	-1.2	0.2	218	20040602032501	625809.10	107097.49	2309.04	-1.0	0.4
192	20031028203918	625807.72	107095.87	2307.19	-1.5	0.4	219	20040602042702	625802.88	107095.48	2317.60	-1.5	0.2
193	20031101112635	625720.87	107214.17	2336.95	-1.2	0.1	220	20040602070739	625796.89	107059.38	2280.44	-1.0	0.2
194	20031104230447	625799.68	107137.00	2328.80	-1.7	0.2	221	20040602073413	625856.37	106987.02	2127.15	-0.8	0.1
195	20031105013818	625723.54	107310.96	2198.16	-0.9	0.1	222	20040602165214	625816.22	107114.06	2306.44	-0.8	0.2
196	20031105084928	625820.30	107089.22	2299.34	-1.5	0.3	223	20040724155143	625821.97	107248.00	2277.24	-1.1	0.2
197	20031117131619	625798.80	107086.32	2315.75	-1.3	0.2							

Appendix C

Multidisciplinary monitoring of progressive failure processes in brittle rock slopes – concepts and system design

Heike Willenberg, **Thomas Spillmann**, Erik Eberhardt, Keith Evans, Simon Loew, and Hansruedi Maurer

Proceedings of the 1st European Conference on Landslides, Prague, 2002

Abstract

The evolutionary failure processes leading to large-scale mass movements in massive crystalline rock slopes are the subjects of a multidisciplinary research project in the Swiss Alps. Focus is directed towards detecting and analysing rockslide processes that involve the progressive development of a failure surface as opposed to sliding along a pre-existing one. In order to monitor the underlying mechanisms of progressive failure, several new and conventional instrumentation systems were combined with an existing *in situ* monitoring program at an active rockslide site in the Valais (Switzerland). Design of the instrumentation network is based on site investigations and preliminary geomechanical models of the acting rockslide processes with respect to the rate of displacements, position and orientation of geological features that delineate the unstable rockmass. The network set-up considers additional findings from borehole logging and testing. Parameters that will be measured include microseismicity, fracture patterns and the temporal and spatial evolution of 3-D displacement fields and fluid pressures.

C.1 INTRODUCTION

The understanding of rock slope instabilities is becoming increasingly important as a consequence of population growth and increased land use and transportation demands in mountainous regions. In order to optimize early warning systems, knowledge about the specific geological conditions of each landslide site is necessary. However, attention must also be paid to the processes leading to rock slope failures as these are known to lead to observable signs of destabilization before the actual failure (e.g. Keusen, 1997). In this sense, rock stability investigations should focus on the establishment of a valid geological model and the cause-effect relationships/mechanisms driving instability.

The progressive nature of slope failures has long been identified in the field of soil mechanics with respect to clay slopes. The initial concept of progressive failure describes failure starting at one point of a potential sliding surface and spreading outwards from it, driven largely by redistribution of shear stresses (Bishop, 1967). The term "progressive" refers to the time-dependent nature of structural changes within the slope mass that act to reduce the factor of safety with time (Terzaghi, 1950). Within the framework of this study, the term is used to describe the development of a failure surface in space as well as in time.

The adoption of a more mechanistic-based methodology contrasts general trends in rock slope analysis, which tend to focus on pre-defined persistent failure planes formed by bedding, foliation or faults. Yet for massive crystalline rock slopes, the assumption of pre-existing persistent failure planes formed along discontinuities is a simplification, and the link between external triggers, like meteorological events, and the actual slope failure is not clearly established (Sandersen et al., 1996).

In June 2000, a large multidisciplinary study was initiated in Switzerland with the aim to better understand the processes and mechanisms involved in brittle rock slope failure. Both field-based mapping studies and *in situ* measurements were directed towards identifying these processes. In summer 2001, this led to the construction of a unique *in situ* laboratory on an unstable rock slope – integrating instrumentation systems designed to measure temporal and 3-D spatial relationships between fracture systems, displacements, pore pressures and microseismicity. This paper presents the steps taken to conceptualise, design and implement this system.

C.2 CONCEPTUALIZATION

Two principal processes of progressive rock mass destabilization are considered in this study: brittle fracture of intact rock bridges between non-persistent discontinuities and frictional sliding with asperity interlocking (i.e. stick slip). To identify and discriminate between these different processes, several forms of surface and subsurface information are required.

First, it is essential to properly investigate the 3-D geological structure of the monitored rock mass. Important geometrical parameters include discontinuity orientation, spacing, persistence and connectivity, and the location of discrete surface features (Einstein et al. 1983). This information can be attained through a combination of geological mapping, detailed discontinuity mapping, both at surface and in boreholes, and active geophysical testing. New developments in 3-D seismics, 3-D georadar, crosshole tomography and borehole to surface testing methods show promising trends with respect to improving the quality of geological models based on surface mapping data (e.g. Schepers et al. 2001).

More specific problems related to identifying and characterizing progressive failure processes can be addressed through the combined monitoring of mass movement kinematics, pore pressures and microseismic activity. Each of these physical quantities must be captured in terms of their 3-D spatial distribution and time (i.e. 4-D) to provide sufficient data quality for a mechanism-directed analysis.

The kinematics of a sliding rock mass generally manifests itself in terms of surface displacements and subsurface deformation. Surface displacements are commonly derived through geodetic measurements. Of great value are surveys providing information on displacement rates and directions. Continuous monitoring of surface displacements is less common, although new developments in GPS techniques are answering this need. In terms of monitoring subsurface deformation fields, several borehole-based methods are available to provide information that is continuous in time as well as continuous along the borehole axis (Kovari, 1990). For example, the 3-D deformation field around a borehole can be measured using a combined inclinometer-extensometer system (e.g. Solexperts' TRIVEC or Interfels' INCREX systems). However, these measurements are only taken periodically and must be supplemented by multipoint in-place inclinometers to provide continuous real-time monitoring. As such, continuous monitoring is restricted to multiple zones of interest where

deformations are expected or previously measured using conventional inclinometer probe surveys.

Another key to monitoring progressive rock slope destabilization is to focus on the localized failure mechanisms underlying the development of fracture systems. Microseismic monitoring provides a key tool in this respect. Precise mapping of micro-earthquake swarms can resolve the geometry and extent of the developing structure (Fehler et al., 2001), whilst fault plane solutions of the microseisms themselves obtained through moment tensor inversion provides insight as to its microstructure by defining the local orientation of the failure plane and the nature of slip on it (Nolen-Hoeksema and Ruff, 2001). Such techniques have been successfully applied in mining (Mendecki 1997), hydraulic fracture mapping (Phillips et al., 1998), and large-scale tectonic investigations (Maurer et al., 1997). Building on these developments, it is believed that microseismic monitoring will provide a key means to image rockslide dynamics. Furthermore, it is important to recognize that these techniques must be applied at depth, i.e. through the deployment of subsurface geophones, in order to provide sufficient data quality.

The final key component to monitoring progressive rockslide processes is pore water pressures. In a fractured rock mass, water pressures act to drive fracture propagation (e.g. sub-critical fracture propagation), and during periods of significant increases, acts as an important triggering factor. To identify the influence of fracture water pressures on rock slope destabilization, piezometric conditions at depth must be recorded continuously. Temporal variations in measured water pressures can also provide additional information with respect to identifying active fracture processes, sliding mechanisms and/or dilatancy effects (e.g. Scholz, 1990).

By integrating these different systems into one monitoring network design, it is believed that the key elements required to meet the objectives of this study (focussing on the progressive development of brittle rock slope sliding surfaces) can be measured and analysed.

C.3 SITE SELECTION AND INVESTIGATION

C.3.1 Study site Randa

Based on the preliminary investigation of several sites across the Swiss Alps (Eberhardt et al. 2001), an active rockslide site was selected near the village of Randa

(Canton Valais, Switzerland) in the Matter Valley (Figure C.1a). This site was chosen based on the identification of several indicators suggesting that the destabilizing mechanisms relate to progressive brittle fracture processes. These included the massive crystalline nature of the rock mass, the absence of highly persistent discontinuities dipping out of the slope along which a pre-existing slide plane may be inferred, the presence of open fractures, relatively small displacement rates and observations relating to an earlier massive rockslide at the site (the 1991 Randa rockslide). An additional consideration with respect to the microseismic component of the planned instrumentation network was the relatively low background noise level (e.g. that arising from heavy vehicle traffic).

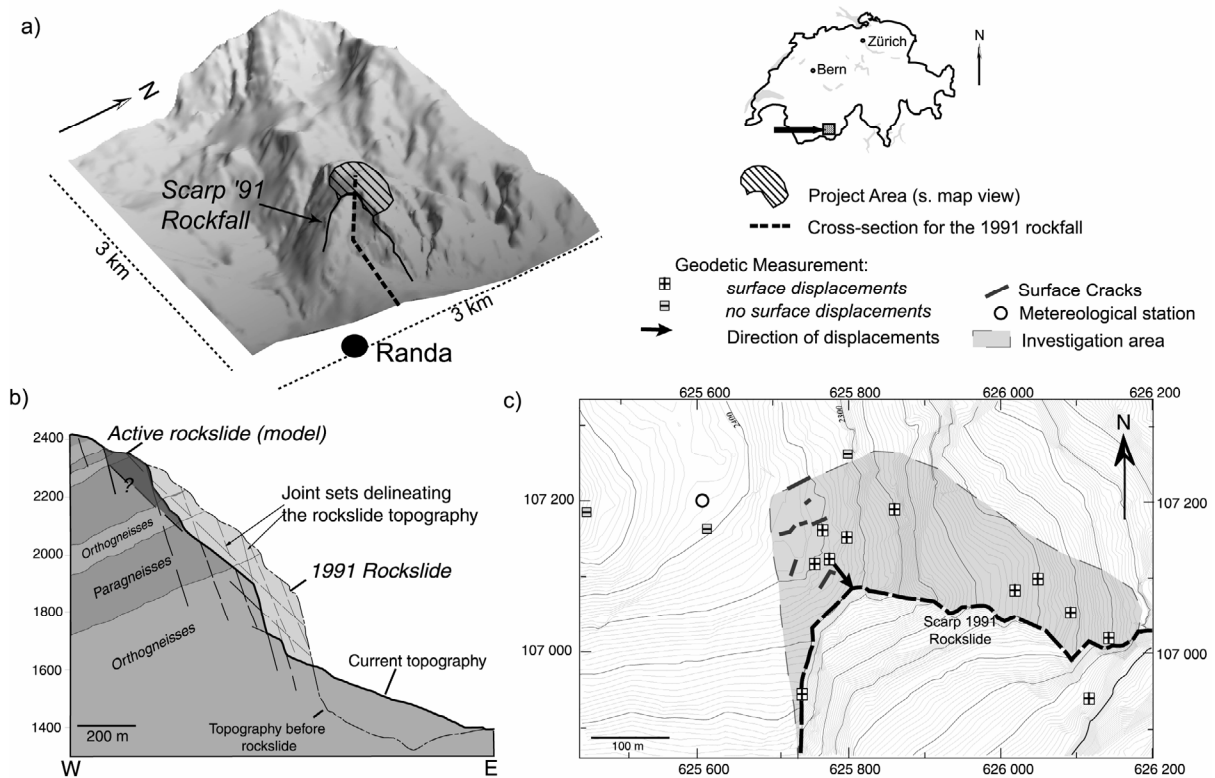


Figure C.1: a) Location and digital elevation model of project area (DEM provided by CREALP); b) cross-section showing 1991 rockslide (after Wagner 1991); c) existing early warning system and distribution of surface cracks.

The research area covers a 500 x 500 m area between elevations of 1800 and 2650 m above sea level. The area belongs to the Penninic Siviez-Mischabel nappe. Its lithology comprises polymeta-morphic gneisses, schists and amphibolites (paragneisses) and metamorphosed Permian granite intrusions (orthogneiss, Randa Augengneiss); the meta-

morphosed Permian-Triassic sedimentary cover is not included in the project area. In terms of surface topography, the lower boundary of the research area is defined by the back scarp of an earlier rockslide, which occurred as two main slide events in April and May 1991 with an estimated total volume of 30 million m³ (Schindler et al. 1993).

By reviewing the general geological situation and initial analysis of the 1991 slide, much can be inferred with respect to the present-day instability, especially with regards to the progressive nature of the failure mechanisms. As foliation is dipping into the slope, the most important discontinuities contributing to slope instability were identified by Wagner (1991) as persistent cross-cutting joint sets along which sliding was believed to have occurred (Figure C.1b). These persistent joints can be observed in the scarp of the earlier slide but are more limited in persistence when encountered in surface outcrops. In terms of triggering factors for the 1991 rockslide, analysis of climatic and regional seismic data showed no clear indications of a triggering event (Schindler et al. 1993). Permafrost distribution models of the Matter Valley by Gruber and Hoelzle (2001) likewise show that permafrost is not to be expected today. Instead, Eberhardt et al. (2001) suggest time-dependent mechanisms relating to strength degradation (e.g. through weathering, brittle fracturing, etc.) and progressive failure as causing the failure.

C.3.1 Existing data

Collected data used in the site selection process was supplemented by an existing early warning system established following the 1991 rockslide. This system includes periodical geodetic surveying, automatic crack-extensometer measurements, manual crack measurements and a climate station (Figure C.1c). The system is restricted to surface observations; nevertheless it supplies valuable information on the distribution of movements at surface. Three-dimensional surface displacement vectors have been established periodically since 1995 for a network of geodetic reflectors, and indicate annual displacement rates of up to 1.5 cm/year. The direction of movement is to the southeast, perpendicular to open surface tension cracks (as shown in Figure C.1c).

C.4 INSTRUMENTATION NETWORK DESIGN

C.4.1 Geological model – working hypothesis

For the instrumentation network design a preliminary geological model was developed and used. The model was based on the spatial distribution of surface

displacements, the location of open cracks and the analysis of discontinuity orientations and persistence. The distribution of surface displacement rates was interpreted as involving the movement of three large blocks, or zones, each separated from the other by open cracks. Maximum displacement rates were seen to occur along the block closest to the rockslide scarp and decrease with distance away from the scarp. This analysis was used to define the area for which the monitoring network would be concentrated (high-lighted in Figure C.1c). To plan the borehole drilling depths, assumptions on potential shear-/sliding zone depths were made. These assumptions were based on steeply dipping fractures that cut and define the unstable blocks at surface, and at depth, by several extended discontinuities outcropping in the rockslide scarp (consistent with measured surface displacement vectors). The lowest of these daylighting discontinuities can be observed in the paragneisses and was extrapolated under the study area as a persistent plane (Figure C.1b). Recognizing that a more likely stepped-path surface would run even higher, a margin of safety was thus provided in selecting the borehole drilling depths. As such, a maximum drilling depth of 120 m was determined.

C.4.2 Geotechnical instrumentation

Three deep boreholes were drilled with depths varying between 50 and 120 m. The locations of these boreholes (Figure C.2 a) were constrained in part by the results of the

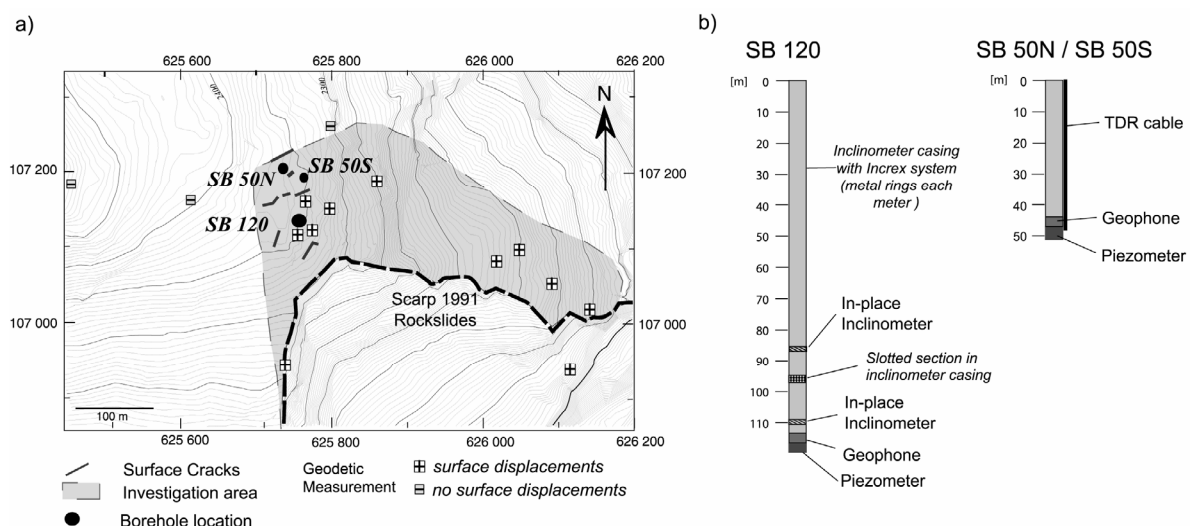


Figure C.2: a) Location of boreholes (SB120 – 120 m depth; SB50S & SB50N - 50 m depth); b) installation design for geotechnical and seismological borehole instrumentation.

geological model developed, as well as by drilling logistics, surface topography and geomorphology and spatial requirements for active crosshole seismic and radar experiments. Borehole SB120 (i.e. 120 m deep) was located in the area where the greatest surface displacements were recorded.

Its length corresponds to the assumed maximum depth of instability. Boreholes SB50N and SB50S (i.e. 50 m deep) were located within 30 m of each other to permit active crosshole testing and to provide close spatial measurements of deformation, pore pressure and microseismic activity contrasts between two blocks separated by a steep fracture cutting down into the moving rock mass. Instrumentation of the boreholes, as derived through the system conceptualization, included elements measuring sub-surface deformations in combination with pore pressures and micro-seismicity. Active testing, including geophysical borehole logging, hydrogeological testing and optical televiewer logging, provided information for locating interesting intervals along which to position continuous deformation measuring devices. Bore-holes were cased with 71 mm diameter PVC inclinometer casing, lined with metal INCREX rings spaced at 1 m intervals. As such, the 3-D subsurface displacement-measuring component of the instrumentation network involves the combined use of biaxial vibrating wire in-place inclinometers for continuous monitoring, but which can be removed for periodic inclinometer-/extensometer-probe measurements (i.e. INCREX) along the entire borehole length. In addition, piezometers, triaxial geophones and co-axial cable for time domain reflectometry (TDR) measurements were installed (Figure C.2b). Specifications for these instruments are provided in Table C.1.

Table C.1: specifications of instruments installed in borehole SB120.

Instrument	<i>In-Place Inclinometer</i>	<i>Inclinometer Probe</i>	<i>Extensometer Probe</i>	<i>Geophone</i>	<i>Piezometer</i>
Type	vibrating wire	servo-accelerometers	induction coil (INCRES)	3-component ($f_n = 28$ Hz)	vibrating wire (690 kPa)
Accuracy	± 0.2 mm/m	± 0.07 - 0.1 mm/m	± 0.02 mm/m		± 3.5 kPa
Measurement Depth	2 intervals of 2 m (at 90 & 115m); biaxial	continuous along borehole axis; biaxial	continuous along borehole axis at 1m intervals	1 instrument at 114 m depth; triaxial	1 instrument at 120 m depth
Sampling Period	continuous	periodical	periodical	event triggered	continuous

Installation was completed by modularizing the different instrumentation components (e.g. piezometers, geophones) in 3 m sections of inclinometer casing.

By pre-installing these devices within the casing, it was possible to position and pack off the piezometer modules along zones showing significant fracture permeability as determined from borehole televiewer data. Furthermore, it was possible to position the geophones with a known orientation with respect to north. An additional upper piezometer module, involving a slotted section of casing, was also inserted and packed off around an upper fracture zone near 100 m depth (as shown in Figure C.2b). This was inserted as a backup to the lower automatic piezometer system and to provide the possibility of periodic measurements along a second major fracture zone intersected by the borehole.

Following installation of the instrumentation modules and inclinometer casing, boreholes and borehole packers were cemented.

C.4.3 Microseismic network

Prior to the installation of the borehole geophones described above, a small test array using 5 standard surface-mounted seismographs was installed for an observation period of approximately 8 months. Data obtained from this network were expected to provide information about: (i) the existence of microseismic activity, (ii) the characteristics of seismic waveforms and (iii) approximate event locations. Analysis of the data recorded provided evidence for seismic activity, with measured signals showing very high frequencies close to the Nyquist frequency (250 Hz) of the seismographs. Most likely, significant portions of energy were released at even higher frequencies. This prevented the detection and recording of events by 4 or more stations, which would have allowed the events to be located.

An important conclusion from the experiences gained through the preliminary test array was that a high-frequency recording system was essential. As such, two Geode seismographs from Geometrics Inc. were chosen for integration into the Randa *in situ* monitoring network. These state-of-the-art systems include 24 channel acquisition boards (i.e. for eight 3-component geophones) with 24 bit A/D converters, allowing sampling frequencies of up to 50 kHz. Since high frequency signals are most affected by near-surface heterogeneities, the geophones were deployed in boreholes – e.g. one near the bottom of each of the three boreholes, as previously described (Figure C.2b).

To complement this network of deep boreholes, a larger network of shallow boreholes (5 m deep) was drilled at suitable locations for the installation of additional geophones. The spatial distribution of these sites was chosen, such that the recordings would allow the hypocentral parameters (hypocenter coordinates and origin time) and other source characteristics (orientation of the fault plane, source-time function, etc.) to be constrained reliably. A well-known problem with standard seismic networks, which are generally planar in nature (i.e. geophone locations positioned along a flat surface), concerns trade-offs between different hypocentral parameters during the location procedure (e.g. Lee & Stewart 1981). In particular, hypocenter depth and origin time often show strong dependencies. When the seismic network is not planar, but exhibits a 3-D distribution, this effect can be reduced. This was partially achieved by placing geophones at the bottom of the 3 deep boreholes. Additional vertical aperture could be achieved by considering the pronounced topography of the investigation area. Based on these constraints, it was believed that 9 additional shallow borehole geophone sites were required.

Before the geophones were installed, a resolution analysis was performed to test the suitability of the network distribution. This involved the simulation of a dense 3-D grid of seismic events, extending over the investigation area and depths of interest. For each generated event, synthetic arrival times were calculated using a homogeneous full space velocity model. It was assumed that geophones positioned in the shallow boreholes would be limited to recording only the first arrival P-waves, whereas both P- and S-waves could be identified at the bottom of the 3 deep boreholes.

As a measure of resolution a Dirichlet spread was chosen to approximate the sensitivity and degree of trade-off between the different hypocentral parameters (Menke 1989). Figure C.3a shows the location of the shallow geophone boreholes and the corresponding Dirichlet spread along a horizontal slice through the source grid at 2200 m elevation. This is within the depth range, where the seismic activity is expected to occur. In this figure, a Dirichlet spread of 0 indicates independent resolution of all hypocentral parameters, whereas large values are diagnostic for pronounced trade-offs and thus unreliable hypocenter estimates. The absolute spread values are unimportant since their magnitudes are largely controlled by the damping parameters of the corresponding inversion problem. Only the relative changes between the centre of the array, where the location accuracy is expected to be good, and the border areas are relevant.

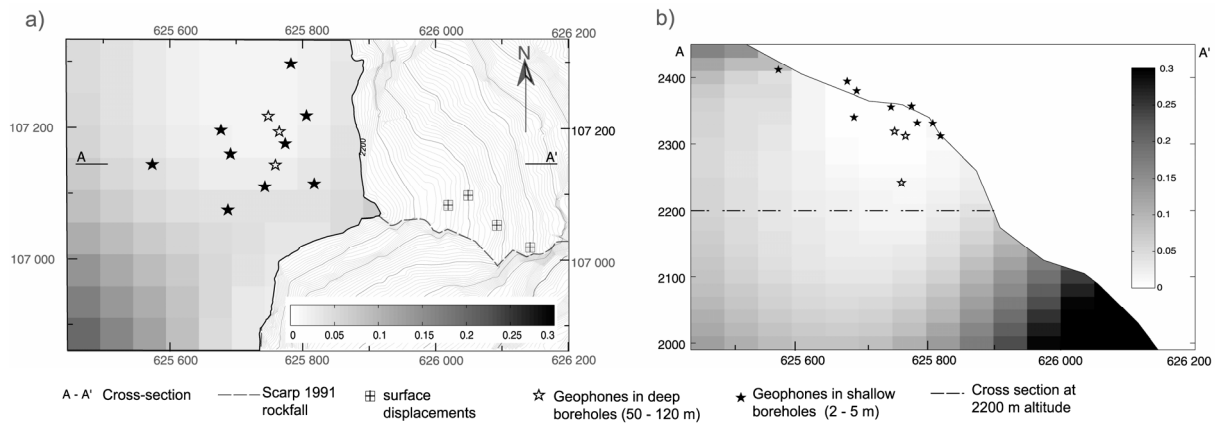


Figure C.3: Seismic network geophone distribution and corresponding Dirichlet spreads for: a) horizontal plan section along 2200 m elevation; b) vertical cross-section A-A'. Values near zero (i.e. bright areas) indicate zones of optimal resolution.

Accordingly, Figure C.3a shows that the Dirichlet spread exhibits only minor variations, and the location accuracy should be uniformly high for the depth range targeted. Similarly, the Dirichlet spread variation along the rock slope cross-section is quite uniform (Figure C.3b). Only towards the northeastern end of the cross-section are significant increases observed. Therefore, if necessary, additional geophones could be installed to increase the performance of the network, if in future significant seismic activity is found to originate from this area.

C.4.2 Communication and data management

Seismic activity recorded by the twelve 3-component geophones (as described above, 3 in deep boreholes, 9 in shallow boreholes), will be monitored using two 24-channel seismographs. The system has been designed so that several hundred seismic events, with data files of 12 Mbytes each, can be recorded and stored every day. Retrieval of this vast amount of data has been accommodated by linking the on-site storage computer to a central recording location in the Matter valley through a wireless Ethernet connection (Figure C.4). This concept allows off-site storage and easy accessibility to the seismic data files. Furthermore, it also allows for recording parameters to be adjusted remotely, thus reducing the amounts of data transferred for analysis.

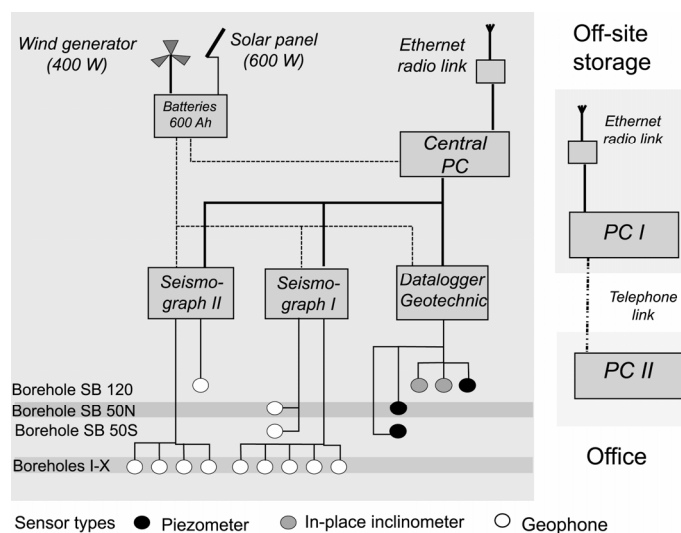


Figure C.4: Schematic diagram of data acquisition system.

A parallel system was similarly used to automatically record borehole piezometer and in-place inclinometer measurements. These instruments are triggered every 6 minutes, with the corresponding measurement values being stored on-site on a Campbell Scientific CR-10X data logger. Through a dial-up connection, the measurement values can be directly accessed and downloaded from the data logger using a local network connection. Solar panels combined with a wind generator supply the necessary power on site.

C.5 CONCLUSIONS

To measure processes relating to the progressive development of failure planes in massive rock slopes, an *in situ* multidisciplinary laboratory was constructed in the Swiss Alps. This first of its kind network integrates a variety of instrumentation systems designed to measure temporal and 3-D spatial relationships between fracture systems, displacements, pore pressures and microseismicity. The network design is based on theoretical concepts concerning progressive strength degradation and progressive brittle failure, and experiences gained through preliminary investigations.

Data recorded by this network will be analyzed and combined within the framework of a multidisciplinary study that will include geological mapping, deterministic and stochastic discontinuity analysis, 3-D surface georadar and seismics, crosshole tomography and numerical modelling.

It is believed that the unique design of the instrumentation system and the multidisciplinary nature of the study, will help to significantly advance current understanding of rock slope failure processes, from the early stages of development through to catastrophic failure.

C.6 ACKNOWLEDGEMENTS

Funding for this project was provided through a grant from the Swiss National Science Foundation (Project Nr. 2100-059283.99/1). Additional support was provided by the Swiss Air Force and the Centre de recherche sur l'environnement alpin (CREALP). The authors wish to thank Stump Messtechnik, Injectobohr/SIF, B. Rinderknecht, C. Bärlocher, B. Heincke, R. Siedler and F. Gönner for their contributions to the work performed.

Appendix D

The Randa Rockslide Laboratory: Establishing brittle and ductile instability mechanisms using numerical modelling and microseismicity

Erik Eberhardt, **Thomas Spillmann**, Hansruedi Maurer, Heike Willenberg, Simon Loew, and Doug Stead

Proceedings of 9th International Symposium of Landslides, Rio de Janeiro, 2004

Abstract

The underlying complexity associated with unstable massive rock slopes has generally restricted the investigation of such slopes to phenomenological studies that are largely descriptive and qualitative. Continued rockslide problems experienced throughout mountainous regions of the world, however, demonstrate the need for a deeper understanding of the physical processes and mechanisms leading to catastrophic failure. This paper focuses on the role brittle fracture and plastic deformation processes play in the development of catastrophic failures in massive, crystalline rock slopes. The work presented is based on the 1991 Randa rockslide in southern Switzerland and combines several conceptual and numerical models developed with respect to tensile and shear mechanisms that drive progressive rock slope failure. The paper also presents preliminary microseismic monitoring results recorded through the Randa Rockslide Laboratory, a unique multidisciplinary alpine facility focusing on ongoing movements at Randa. Such data are expected to provide valuable constraints for specialized hybrid finite-/discrete-element modelling designed to explicitly model rock slope deformation, damage initiation and fracture propagation.

D.1 INTRODUCTION

Ever increasingly, experts are called upon to analyse and predict - assessing risk, rock mass response, potential modes of failure and possible preventive/remedial measures. The ability to do so, however, is limited by the descriptive and qualitative nature of most analyses, which tend to provide only minimal insights into the underlying processes and mechanisms driving instability and failure. The degree to which prediction is achievable is also contentious, with many seeing it as being limited to the assessment of a stability state (i.e. factor of safety) or the probability that a certain slope may fail. The ability to predict with respect to time, what society asks from us, seems distant as we try to contend with the large number of unknowns and complexity involved in the subsurface geology and hydrogeology.

To move in this direction and improve our ability to predict, both in terms of probability and time, more sophisticated tools are required to better assess the subsurface mechanisms contributing towards catastrophic rock slope failure. Limit equilibrium analysis and other phenomenological approaches only provide a snapshot of the force- and/or moment-balance conditions at the instant of failure, and as such provide a simplified answer as to why the slope failed, but not within the context of time or its progressive development from a stable to unstable state.

This paper focuses on the application of new advanced numerical tools aimed at better understanding the mechanistic role brittle and ductile processes play in the progressive development and evolution of catastrophic failure in massive, crystalline rock slopes. The work presented utilizes initial hypotheses based on numerical modelling of the 1991 Randa rockslide in southern Switzerland to develop conceptual models with respect to the underlying tensile and shear mechanisms that helped to promote failure. These models exploit hybrid techniques that combine finite- and discrete-element solutions, allowing for the explicit modelling of rock slope deformation and fracture initiation/propagation.

Yet it must be recognized that such modelling techniques have advanced beyond our capabilities to confidently constrain the necessary input (Stead et al. 2001). The second part of this paper touches on the collection of microseismic data from a unique field facility – the Randa Rockslide Laboratory, and its potential role in providing spatial and temporal constraints through event counting, frequency content analysis, source location and source

mechanisms. Problems associated with attenuation, which negatively affect the quality of microseismic data, are also discussed.

D.2 BRITTLE FRACTURE PROCESSES IN MASSIVE ROCK SLOPES

A key kinematic requirement for rock slope failure is the existence of a fully interconnected discontinuity system bounding the moving mass. Three-dimensionally, this can be accommodated by intersecting bedding plane/foliation parallel fractures, faults, tectonic joint systems, unloading joints, tension cracks, erosional scarps, etc. In some cases, the failure surface can be seen to coincide with extensive geologic features such as bedding planes (e.g. 1806 Goldau rockslide, Switzerland; 1905 Frank slide, Canada), but even then such features may only explain the existence of a basal shear surface but not the lateral release scarps. In other cases, for example the 1991 Randa rockslide in Switzerland, the structural nature of the failure surface is even more complex with few signs of fully persistent discontinuities other than those limited to small outcrops relative to the total failure surface area. In either case, the likelihood of a completely developed failure surface existing for any substantial period of geologic time is unlikely, since prior to failure, many of these rock slopes have remained relatively stable for thousands of years with few major external changes occurring with respect to their kinematic state. The last major external change most rock slopes in an alpine environment would have experienced would have been the over-steepening of their slopes during glaciation and loss of confinement during ice-free periods.

Strength degradation over time and progressive failure (i.e. the progressive development of the failure surface) can be used to explain the temporal nature of massive rock slope failures (Eberhardt et al. 2004a). Several authors have pointed to the presence of intact rock bridges as providing cohesive strength components along a potential failure surface (e.g. Jennings 1970; Einstein et al. 1983), while others have also examined the role of internal rock mass shearing and yield (Mencl 1966; Martin & Kaiser 1984). Figure D.1 illustrates these rock slope failure controls viewed in terms of shear plane development, and strength degradation manifested through internal deformation, dilation and damage mechanisms. Underlying many of these controls are time-dependent processes such as material creep, brittle fracture propagation, stress corrosion, fatigue and weathering.

In terms of brittle fracture propagation, several authors have examined the application of fracture mechanics' principles to model the destruction of intact rock bridges leading to catastrophic rock slope failure (e.g. Scavia 1995; Kemeny 2003). Kemeny (2003) notes that these unbroken segments along the sliding surface provide a cohesive element both in shear and in tension that may deteriorate in time depending on the applied stresses.

In the field, Fleming & Johnson (1989) observed the evolution of large-scale fractures over successive field campaigns with respect to the progressive development of lateral release scarps bounding an unstable slope. Thus, the importance of incorporating brittle fracture processes (both the initiation of fractures and the propagation of pre-existing fractures), can be stressed as being paramount to better assessing the stability state for a given rock slope and more realistically simulating its failure mechanism.

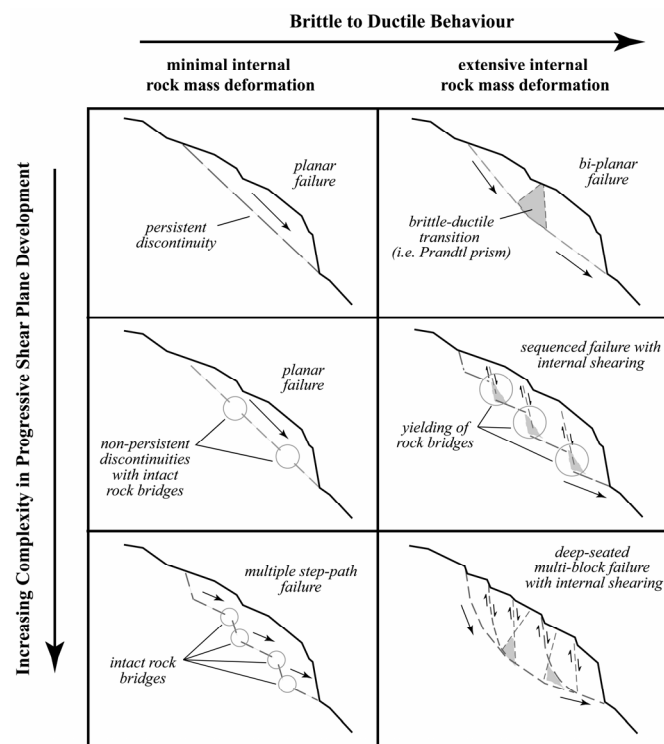


Figure D.1: Massive rock slope failure mechanisms as controlled by progressive shear plane development and/or internal rock mass deformation and shear (after Eberhardt et al. 2002).

D.3 NUMERICAL MODELLING OF BRITTLE AND DUCTILE MECHANISMS

D.3.1 The Randa Rockslide Laboratory

The “Randa Rockslide Laboratory” in the southern Swiss Alps was conceived and constructed as a high alpine *in situ* laboratory utilising state of the art instrumentation systems to study mechanisms controlling progressive failure and pre-failure rock mass deformations in massive crystalline rock slopes (Eberhardt et al. 2001). The resulting facility represents a first of its kind installation integrating instrumentation systems designed to measure temporal and 3-D spatial relationships between fracture systems, displacements, pore pressures and microseismicity (Willenberg et al. 2002). The test site itself is located on a moving mass (with an approximate volume of 10 million m³), but which is presumably in an uncritical state characterized by low deformation rates (max. 1-2 cm per year).

Advanced numerical models are also used in conjunction with the instrumentation data to provide key insights into the interplay between brittle and ductile mechanisms driving the development of the failure surface (i.e. progressive failure) and accommodating internal displacements within the slide mass through rock deformation, strength degradation and internal shearing (Eberhardt et al. 2004a). To help further constrain these models, the site benefits from its close proximity to the scarp the 1991 Randa rockslide, for which back-analyses can be performed. The back scarp of the 1991 failure forms the face of the present day instability.

The 1991 Randa rockslide involved the failure of 30 million m³ of massive crystalline rock in two separate episodes (Figure D.2). Structurally, the foliation dips favourably into the slope. As such, Schindler et al. (1993) suggested that failure occurred along extensive shallow dipping joints parallel to the surface. These joints can be observed along parts of the sliding surface but are limited in persistence when encountered in surface outcrops (Willenberg et al. 2002). Schindler et al. (1993) also proposed a series of steep sub-vertical faults as dividing the slide mass into smaller units. A comprehensive description of the unstable rock mass above the 1991 scarp is given in Willenberg et al. (2004; see these proceedings).



Figure D.2: Cross-section of 1991 Randa rockslide (modified after Schindler et al. 1993).

D.4 NUMERICAL FORMULATION AND MODEL SETUP

The application of numerical modelling to slope stability investigations is generally approached either from the perspective of a continuum (e.g. finite-element) or a discontinuum (e.g. discrete-element). However, as discussed in the previous section, the actual complexity involved in most massive rock slope failures involves both the behaviour of the continuum (e.g. intact rock yield) and the discontinuum (e.g. shearing along pre-existing discontinuities), and most importantly, the transformation of the rock mass from a continuum to a discontinuum (e.g. the generation of new fractures). To treat these problems, new developments in hybrid finite-/discrete-element codes have been forwarded which allow for the explicit modelling of brittle fracture initiation and propagation by means of adaptive remeshing routines (Munjiza et al. 1995).

For the purposes of this study, the commercial hybrid finite-/discrete-element code ELFEN (Rockfield 2001) was used. A Mohr-Coulomb based constitutive model with a Rankine Tensile cutoff was adopted, through which the extensional inelastic strain accrued during compression can be coupled to the tensile strength degradation in the dilation direction (permitting the explicit modelling of discrete fracturing under compressive stresses). Stacey et al. (2003) argue that extensional strain is an important factor in slope stability that has not been fully appreciated.

These techniques were applied to a 2-D cross section based on the pre-1991 Randa rockslide surface topography (Figure D.2). Based on this geometry, modelling was directed towards simulating the progressive development of the 1991 failure surface from that of an initial continuum. The role of pre-existing discontinuities was not included. A Mohr-Coulomb constitutive yield model with a Rankine tension cutoff was used to model deformation and fracture initiation. The basic material properties used were based on those for a fractured crystalline rock mass: Young's modulus = 30 GPa, Poisson's ratio = 0.33, unit weight = 26 kN/m³, cohesion = 1 MPa, internal friction = 30° and tensile strength = 0.1 MPa. A strain energy release rate of 200 N/m was assumed.

D.5 EXTENSIONAL STRAIN AND BRITTLE FRACTURE

Stacey et al. (2003) note that although the advent of numerical modelling has led to more studies in which rock slope stresses are considered, little if any consideration has been given to the occurrence of strains. When considering the free boundary or unsupported face of a steep slope, down-slope strains can be expected. Such strains would be extensional in nature, with extension strain being defined as the minimum principle strain, ϵ_3 . Figure D.3

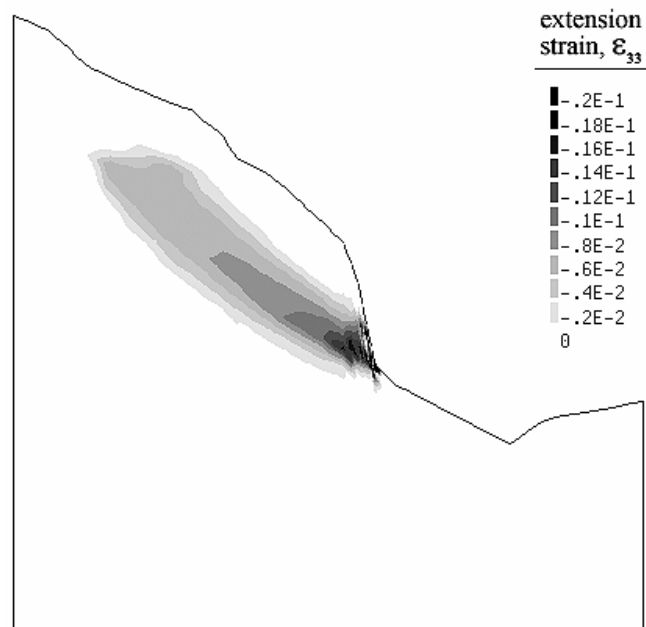


Figure D.3: Extension strain, ϵ_3 , calculated for the pre-failure geometry of the 1991 Randa rockslide.

shows the extensional plastic strains for the 1991 Randa rockslide based on a finite-element continuum analysis with a Mohr-Coulomb yield model, but without the hybrid discrete-element coupling enabling fracture initiation (using the material properties previously listed). The model shows that large extensional strains develop along a path that roughly coincides with the 1991 Randa rockslide failure surface (as shown in Figure D.2). The strains reproduced in this model are well in excess of those reported by Stacey (1981) as being the critical levels for brittle fracture initiation and propagation.

Figure D.4 shows the same model run (i.e. same geometry and material properties), but where brittle fracturing was permitted through the hybrid finite-/discrete-element solution. Again, the model reproduces the dimensions of the failed mass very well, both with respect to the outline of the first Randa slide event (Figure D.4b) and the final outline of the slide surface (Figure D.4d). In doing so, the influence of the shear constitutive fracture model can be fully appreciated; the extensional strains and elasto-plastic yielding induced through the down-slope movements of the continuum result in fracture initiation and

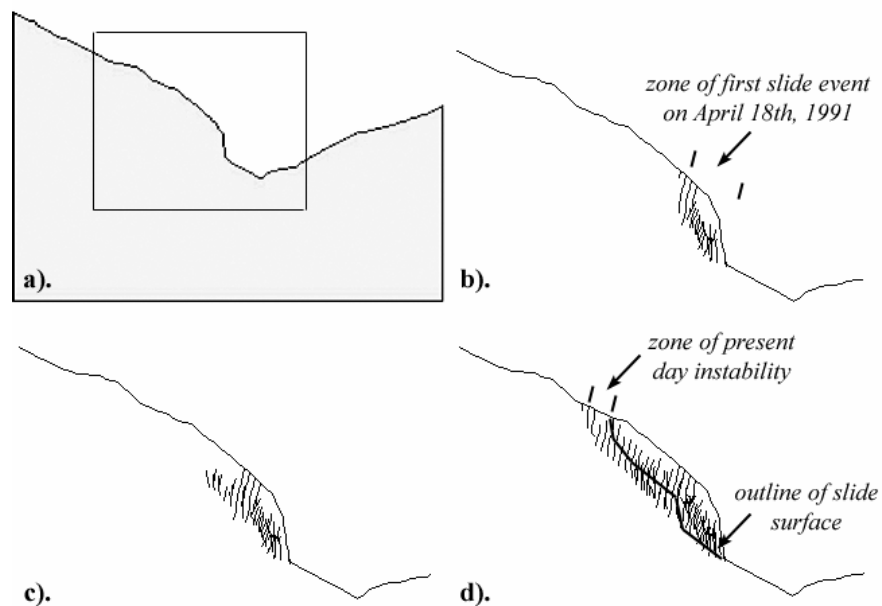


Figure D.4: Hybrid finite-/discrete-element model showing the progressive development of the failure surface superimposed with that of 1991 Randa rockslide events.

propagation driving the progressive development of the failure surface (as can be seen comparing Figure D.3 and Figure D.4). This leads to the formation of numerous subvertical

tension/extension cracks (i.e. normal to the direction of downslope strains). The presence of any low dipping natural discontinuities would further aid the process, aligning to form a stepped shear plane that could accommodate further movements and eventually kinematic release of the slide mass.

Remembering that this model started from an intact continuum, it can be reasoned that shear along a potential rock slope failure surface only becomes a factor once it's almost fully developed and mobilization becomes possible. In other words, the failure surface only becomes a "shear" surface once tensile extensional fracturing has progressed to the point where significant cohesion loss has occurred along the path of coalescing fractures and larger displacements become kinematically feasible (leading to mobilization).

In addition, the progressive failure approach also clearly predicts the development of the first phase of the Randa rock slope failure (i.e. April 18th, 1991 event), prior to that of the second major event (i.e. May 9th, 1991 event). Here failure appears to first involve the progressive development and collapse of the frontal region of the slope. The modelled slide boundaries for this first failure stage closely match those of the actual failure, and its progressively disintegrating nature would agree well with observations that the event lasted several hours and involved the tilting and falling of large blocks one after another (Bonnard et al. 1995). Such a mode of failure would require extensive internal deformation, fracturing and dilation, as demonstrated by the models.

D.6 MICROSEISMIC MONITORING

Based on the modelling results presented, it can be put forward that highly persistent natural discontinuities are not solely necessary for massive rock slope failure, but that extensional strain-induced brittle fracturing can also work towards progressively driving a rock slope to failure. As such, much can be gained from field based studies that similarly focus on brittle fracture indicators. On surface or in boreholes, these may take the form of open fractures that can be measured with respect to opening rates and displacements (Willenberg et al. 2003). Another potentially useful tool is the passive monitoring of microseismic activity to detect subsurface tensile fracturing and/or shear slip along internal fracture planes. Spatially clustered microseismic events in numerous fields (e.g. mining, geothermal energy, nuclear waste disposal, etc.) have provided critical information with respect to stress-induced fault plane locations, orientations and mechanisms.

In planning the design of the Randa Rockslide Laboratory, such a system was deemed essential (Eberhardt et al. 2001, Willenberg et al. 2002). To do so, an array of twelve three-component geophones was installed in 2001 (Figure D.5). Three 28 Hz geophones (labelled A5, B2, B5 in Figure D.5) were deployed near the bottom of three deep boreholes. Nine shallow geophones with 8 Hz resonance frequency complete the microseismic array. The spatial distribution of these sensors was chosen such that the array's resolution was concentrated to the active sliding area (shaded in Figure D.5a). This ensured that the hypocentre parameters generated from the seismic sources could be reliably constrained within the area of interest (Willenberg et al. 2002).

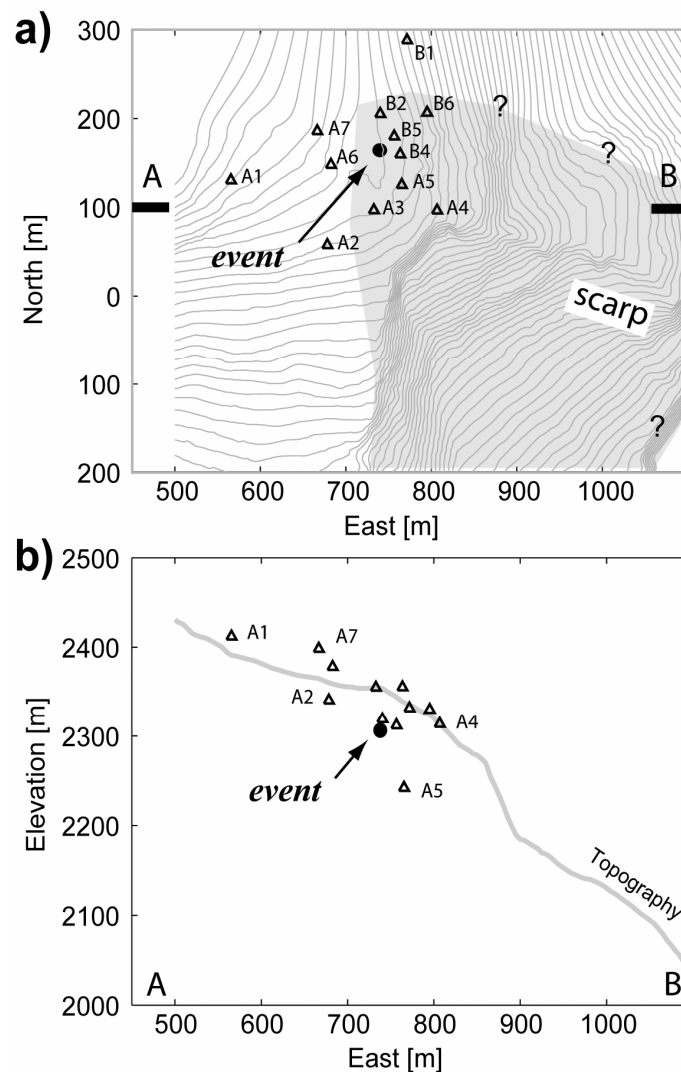


Figure D.5: a) Map view and b) cross-section of the Randa microseismic geophone array showing the location of a recorded event from a limited sample data set (March to May, 2002).

Following installation of the microseismic monitoring system in 2001, problems were encountered in the form of an unknown noise source that resulted in the frequent triggering of the system. These high frequency “noise bursts” generated exceptionally large volumes of data (>500 GBytes), requiring the testing of smaller data sets to improve event detection and develop efficient data processing routines. One such data set, for the period March to May 2002, revealed numerous microseismic events, but only one whose location fell within the projected moving volume (shown in Figure D.5b at 50 m depth). The remaining events were either related to seismic activity in the valley/region, unexplained events lying far outside the area of interest, noise, or provided such poor quality signals that accurate source location was not possible.

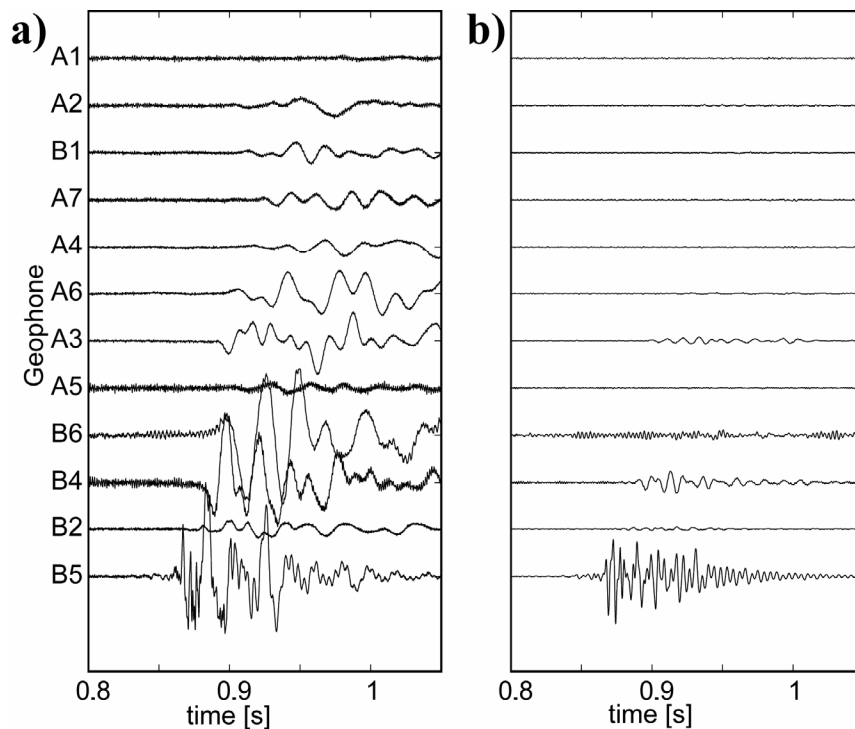


Figure D.6: Vertical components of a locatable microseismic event: a) raw; b) 100-500 Hz bandpass filtered signals. Signals are sorted according to the source-receiver distance, with sensor A1 being the farthest and B5 the closest. Absolute time scale is arbitrary.

The question of signal quality led to further analysis of the frequency content of the recorded events. Figure D.6a shows the vertical component of the seismograms for all twelve sensors for the locatable event (as noted in Figure D.6). The seismograms are sorted according to the source-receiver distance, with receiver A1 being the farthest from the source

and B5 the closest at 21 m. With the exception of B5, harmonic signals with dominant frequencies of 20 Hz and emergent first breaks characterize the seismograms. Figure D.6b shows a filtered version of the same event using a 100/500 Hz bandpass filter. This frequency range covers that which would be expected for the brittle fracture-induced microseismic events (i.e. higher frequency). However, as can be clearly seen in Figure D.6b, only the closest sensor B5 (21 m away from the source) was able to record significant amplitudes above 100 Hz. The high frequency information is strongly attenuated for the remaining sensors with source-receiver offsets between 40 and 200 m.

This and the poor signal quality of the other microseismic events point to the presence of large open fractures deep below surface, across which passing waves are strongly attenuated. These large open fractures are fully compatible with the geological model described in Willenberg et al. (2004). Larger low frequency events, such as those generated from natural seismic activity in the region, do not suffer as much from signal quality degradation. Based on these results, new algorithms must be devised that are capable of extracting more information on the subsurface deformation characteristics.

D.7 CONCLUSIONS

To explain and better predict the temporal evolution of massive rock slope instabilities and failures, subsurface processes involving rock mass strength degradation and progressive failure must be considered. Hybrid finite-/discrete-element models incorporating these processes were able, starting from a continuum, to reproduce both the shear surface outline and the staged nature of the failure of the 1991 Randa rockslide. The fractures generated through extensional strains were predominantly sub-vertical tensile fractures normal to the direction of downslope movement. As the density of these fractures increased, the shear plane progressively developed to form a failure surface typical of more ductile failures where the rock mass is heavily damaged.

These models help to reinforce conceptual models for which massive rock slope failure processes are largely driven by the initiation and propagation of brittle tensile fractures driven by extensional strain, which interact with natural pre-existing discontinuities to eventually form basal and internal shear planes. Shear failure only becomes a factor once enough tensile fracture damage was incurred to allow mobilization.

Microseismic data collected at the Randa Rockslide Laboratory, located over an unstable mass moving at rates of 1-2 cm/ year, suggest the presence of large open fractures, deep below surface. Although only a small data set sampled from the much larger data set collected has been analyzed, preliminary results show that the slope mass may be microseismically active. Difficulties arising due to poor signal quality and attenuation must be addressed though. Notwithstanding, it is believed that such mechanistically-based studies and analyses, combining state-of-the-art numerical modelling techniques, advanced instrumentation systems and multidisciplinary collaborations, will help to significantly advance current understanding of rock slope failure processes, from the early stages of development through to catastrophic failure.

Appendix E

High-resolution geophysical techniques for improving hazard assessments of unstable rock slopes

Alan G. Green, Hansruedi Maurer, **Thomas Spillmann**, Björn Heincke, and Heike Willenberg

The Leading Edge (2006)

Abstract

Unstable rock slopes are an increasing concern in mountainous regions worldwide. Significant expansions of human habitats and transport routes in mountain valleys, melting of alpine permafrost as a consequence of global warming, and exceptional climatic events are amplifying the risks of catastrophic mountain-slope failures. To minimize the effects of such failures, short-term predictions are required for the timely evacuation of vulnerable populations and medium-term forecasts are needed for the optimum design and construction of barriers that offer protection to lifelines (e.g., roads, railways and pipelines) and other expensive infrastructure. Moreover, long-term hazard assessments are necessary for prudent land-use planning. These tasks require detailed information on the extent and probable behavior of unstable rock. In this context, the locations and geometries of major fractures and faults are particularly important.

Investigations of potentially unstable mountain slopes typically involve geological mapping, strain measurements, remote sensing, and analyses of borehole logs. Since these methods only provide limited knowledge on the depth distribution of critical structures, there

is a growing awareness that geophysical techniques should play a role in such studies. Here, we demonstrate the utility of surface and borehole ground-penetrating radar (georadar), seismic tomography, and microseismicity studies for assessing the stability of mountain slopes.

E.1 RANDA STUDY SITE

Our study site lies immediately above a scarp created by the largest mass movement of rock in recent Swiss history (Figure E.1). During the spring of 1991, two major rockslides resulted in the release of 30 million m³ of crystalline rock and the formation of a debris cone that obliterated holiday apartments and barns close to the village of Randa and blocked the main transport route connecting the Rhône valley to the major tourist resort of Zermatt. The debris cone dammed the Matternispa River, causing flooding in upstream regions of the valley. Geodetic measurements suggest that ~9 million m³ of the remaining mountain slope are currently moving towards the valley at 1-2 cm/year. The continued instability of the mountain slope at Randa is of concern to the local population and responsible authorities.

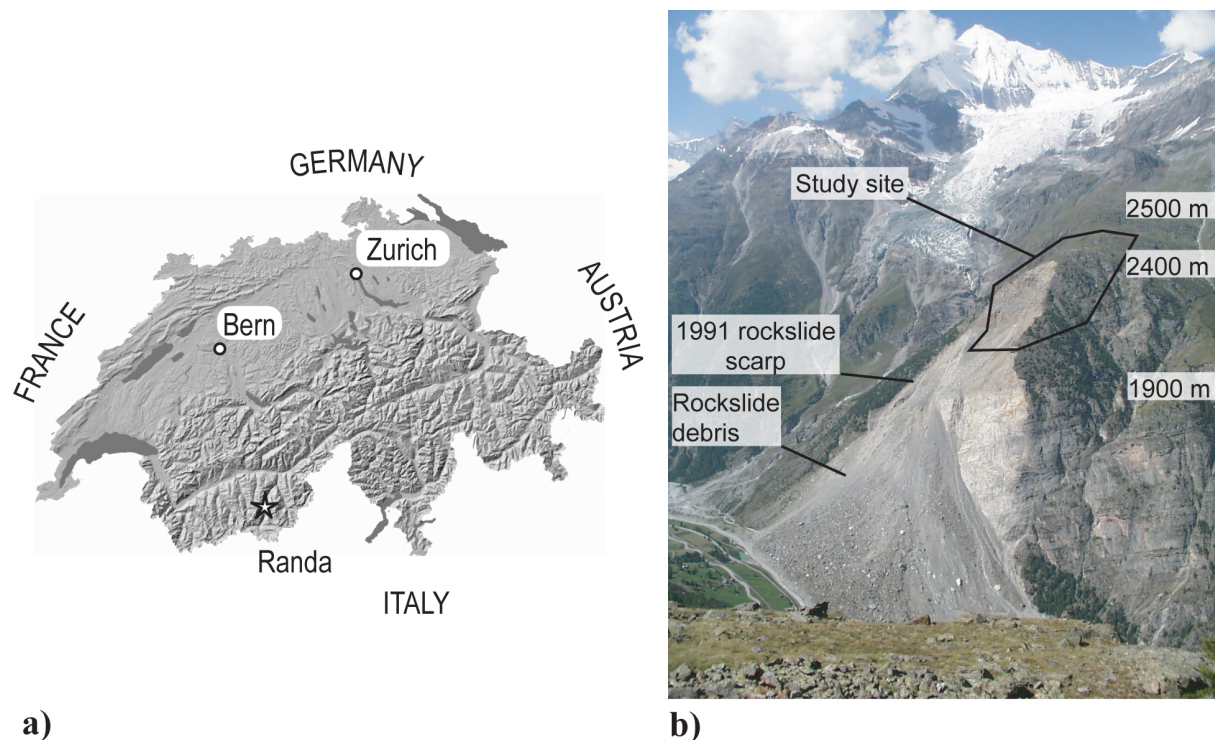


Figure E.1: (a) Randa (star) in the Matter Valley of southern Switzerland. (b) Photograph showing the Randa rockslide and study site.

Information on the geology in this region is based primarily on rock exposures (Figure E.2) and analyses of aerial photographs. The upper part of the mountain is composed of heterogeneous gneisses intersected by (i) shallow-dipping shear zones that parallel the

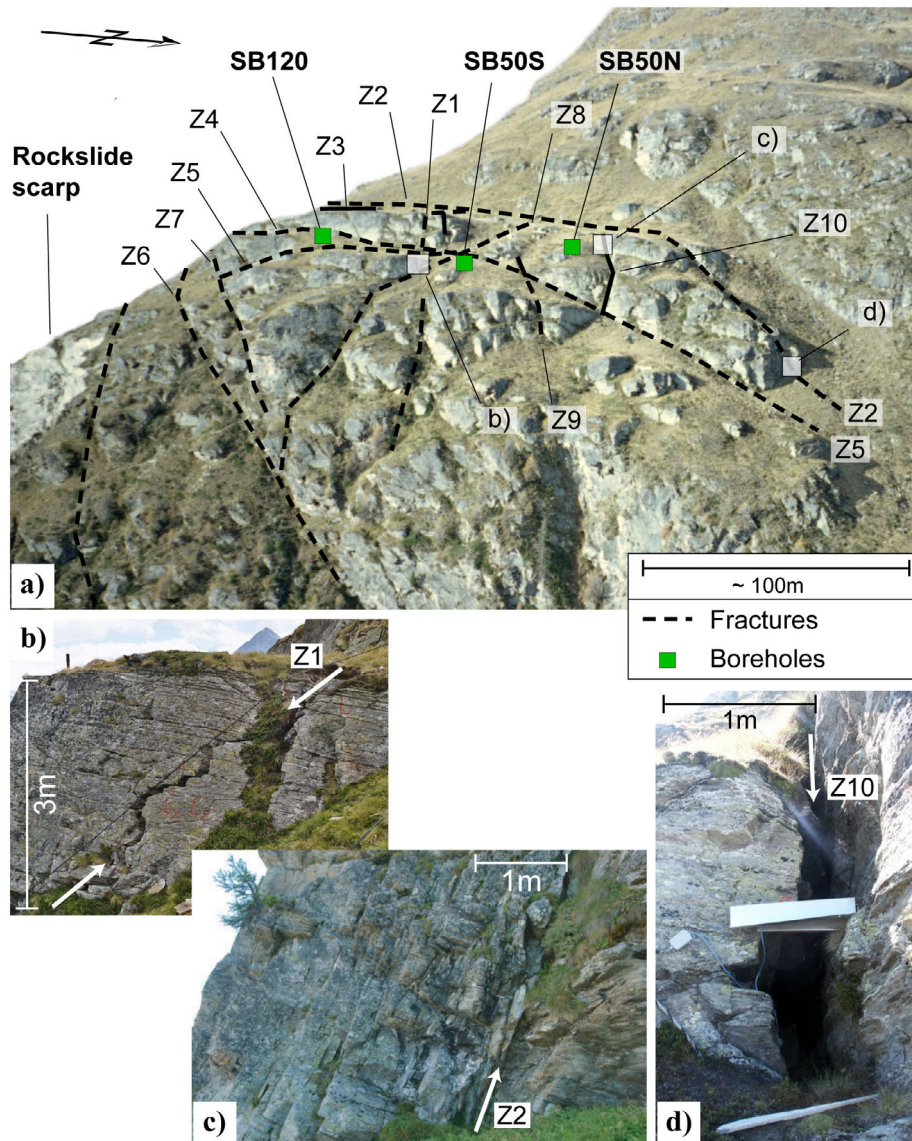


Figure E.2: (a) Perspective view showing the ruggedness of the terrain and the moraine and slope debris covering part of the study site. Green squares mark the positions of boreholes SB120 (120.8 m deep), SB50S (52.5 m deep) and SB50N (51.0 m deep). White squares locate the other photographs shown in the figure: (b) a jagged portion of open fracture Z1, (c) fracture Z2 and (d) open fracture Z10. Note the different scales of each photograph.

rock foliation and (ii) moderate- to steep-dipping fractures⁸ (Z1-Z10 in Figure E.2a) that range from jagged (Figure E.2b) to planar (Figure E.2c) and from closed (Figure E.2c) to open (Figure E.2d). A number of the moderate- to steep-dipping fractures buried beneath moraine and slope debris (Figure E.2a) can be delineated on the basis of lineaments, whereas others are not discernible at the surface. It is the moderate- to steep-dipping fractures, some of which have opening rates of 0.1-0.3 cm/year, that mostly influence the stability of the Randa mountain slope.

In an attempt to determine the subsurface geometries and minimum dimensions of fractures at Randa, we acquired 3-D georadar data across a 35 x 60 m area (Figure E.3 and Figure E.4) and recorded single-hole georadar and logging data in three boreholes (SB120, SB50S, SB50N; Figures E.3 and E.5). We also conducted a 3-D tomographic seismic survey across an extensive region (Figures E.6 and E.7) and monitored the local microseismicity for more than 3 years (Figures E.6, E.8, and E.9) to delineate potentially unstable parts of the rock mass.

E.2 MAPPING SHALLOW-DIPPING STRUCTURES USING SURFACE GEORADAR DATA

Georadar surveying across the rugged terrain at Randa (Figure E.2) and processing the resultant data were demanding tasks. We used a standard georadar unit connected to a semi-automatic self-tracking theodolite to collect coincident 3-D georadar and topographic data. Unshielded 100 MHz transmitter and receiver antennas separated by 1.0 m and a 2.15-m-high mast holding the theodolite target prism were mounted on a sled that was pulled across the surface. Georadar traces were acquired every ~0.25 m along approximately parallel straight lines separated by 0.15 - 0.25 m. Because attenuation and dispersion effects were insignificant in the dry crystalline rock mass, signal shapes varied little over the 1050 ns recording time.

⁸ Since differential motion has occurred across many of the brittle discontinuities at our study site, they are faults. However, for simplicity we will refer to all brittle discontinuities as fractures in this contribution.

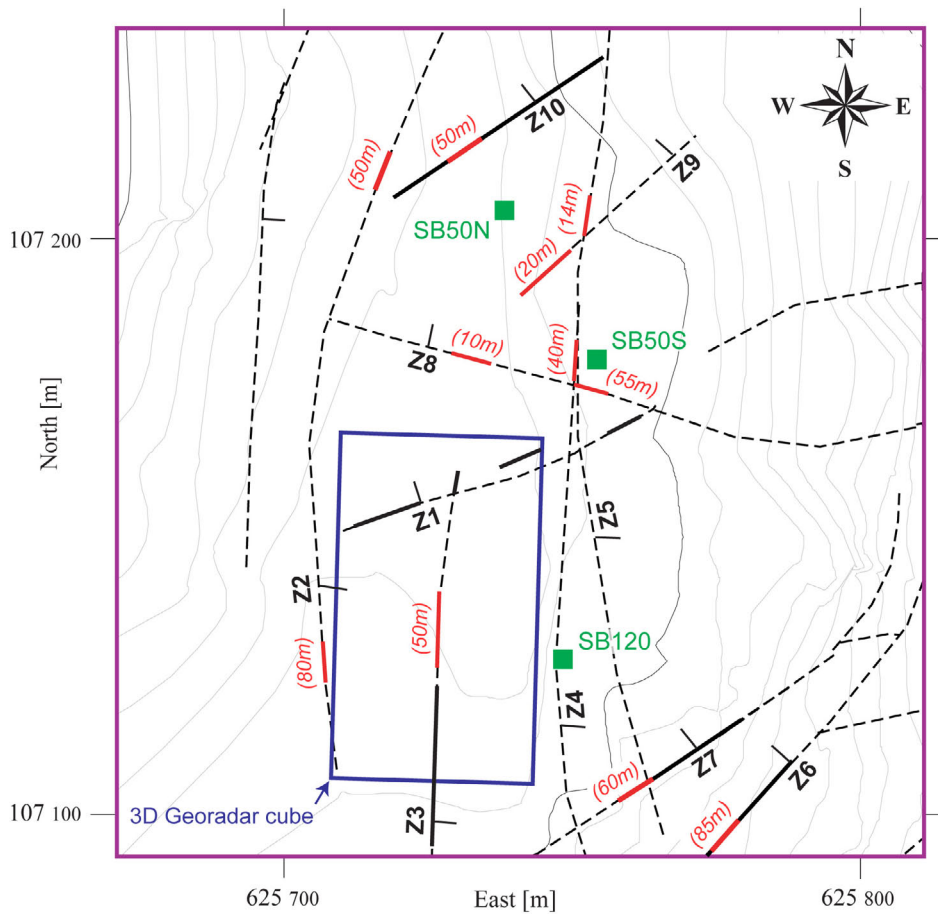


Figure E.3: Site of the surface and borehole georadar surveys. Green squares mark the positions of boreholes SB120, SB50S, and SB50N. The blue rectangle outlines the boundaries of the 3-D georadar survey area. Dashed and solid black lines delineate fractures (open parts of the fractures are highlighted by the solid lines). Ticks identify the dip directions. Red lines show coincident surface projections of georadar reflectors and known fractures and the numbers are the minimum down-dip lengths of the reflectors.

To obtain a meaningful subsurface image (Figure E.4), the 3-D georadar data were sequentially passed through gridding, amplitude-scaling, f-xy-deconvolution and f-k-filter routines before being migrated using a technique that accounted for the highly irregular topography. The shallowest reflector A is the boundary between the unconsolidated surface layer of moraine and debris and the underlying crystalline rock (Figure E.4). It approaches the surface along the eastern and northern edges of the survey site, where bedrock outcrops, and its migrated depth correlates with the depth to bedrock observed in the open fracture Z1 (Figure E.3). We interpret the shallow-dipping reflectors B and E as shear zones or

lithological contacts that parallel the rock foliation and the moderate-dipping C reflector as the depth extension of surface fracture Z2.

There is little evidence in the conventionally processed 3-D georadar data that the ubiquitous steep-dipping fractures produce reflections. This is not surprising, since the surface-based georadar method is not appropriate for the reflection imaging of steep-dipping features, primarily because of the unfavorable radiation patterns of most georadar antennas. This latter point is a fundamental shortcoming of the method, because it is the steep-dipping fractures that mostly influence the stability of the Randa rock mass and many other rocky mountain slopes.

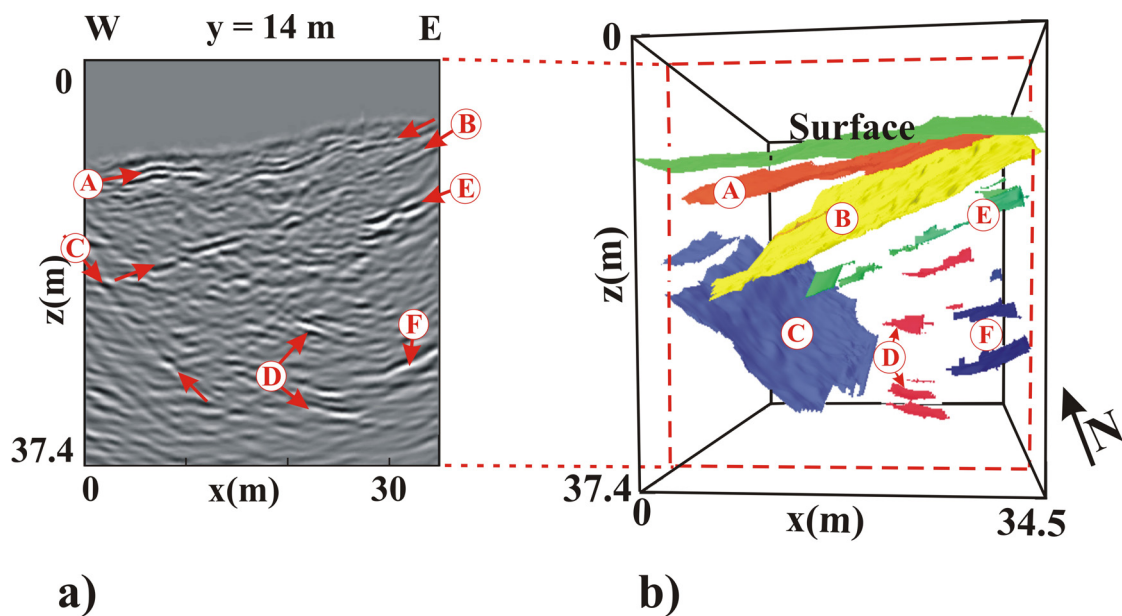


Figure E.4: (a) Cross-section extracted from the 3-D topographic-migrated georadar data set showing reflections A-C and E and diffractors D and F. (b) Three-dimensional image of the surface topography and semi-automatically picked reflectors and diffractors displayed in perspective view.

E.3 MAPPING STEEP-DIPPING FRACTURES USING BOREHOLE GEORADAR DATA

Compared to surface-based observations, georadar data recorded in near-vertical boreholes are well suited for imaging reflections from steep-dipping structures. Collection of single-hole georadar data at Randa involved pulling 100 MHz transmitter and receiver antennas slowly up the length of each borehole. The antennas were separated by a fixed

distance of 2.75 m and full-waveform traces were registered at 0.1 or 0.2 m intervals. Amplitude scaling, bandpass filtering, f-x deconvolution, and phase-shift migration were used to enhance the coherency of reflections.

Non-migrated and migrated versions of the borehole SB120 georadar section look much like surface seismic or georadar sections (Figures E.5a and c). They can be interpreted in a similar fashion, except the numerous reflections could have originated from any location around the borehole; due to the azimuthal invariance of the acquisition geometry, borehole georadar data on their own do not provide sufficient information to determine unambiguously the orientations and locations of reflectors. Nevertheless, it is clear that most of the prominent reflections originate from moderate- to steep-dipping structures. Based on the local geology, it is highly likely that the reflections are from fractures. Many fractures are air-filled structures that have large impedance contrasts relative to the adjacent intact rock. Although the openings of most fractures at this site are quite narrow relative to the ~1 m dominant wavelength of our 100 MHz georadar signal, georadar surveying at other locations has shown that damage zones around discontinuities in gneissic rock can be sufficiently wide to generate strong reflections.

To compensate for the directional ambiguity of our borehole data, we correlate the geometries of the georadar reflections with those of fractures observed in borehole televiewer logs and fractures discernible at the surface (Figure E.5b). We can relate some reflections to borehole fractures A10, A13, A16 and A26, but more importantly, four of the major reflection zones can be traced with reasonable confidence to surface fractures Z2, Z3, Z6, and Z7. Two prominent reflections (X1 and X2 in Figure E.5) that project close to the surface are not associated with any known fractures. Considering their high amplitudes, continuity and lengths, we infer that X1 and X2 are caused by fractures that have no surface expression.

Strong reflections were recorded from all but two (Z1 and Z5) of the named fractures (Figure E.3). In addition, our data contain significant reflections from at least five hidden fractures, the exact locations of which have yet to be determined. We note that the minimum depth dimensions of nearly all fractures are large fractions of their mapped lateral dimensions (Figure E.3). Consequently, the majority of important surface fractures extend deep into the mountain slope.

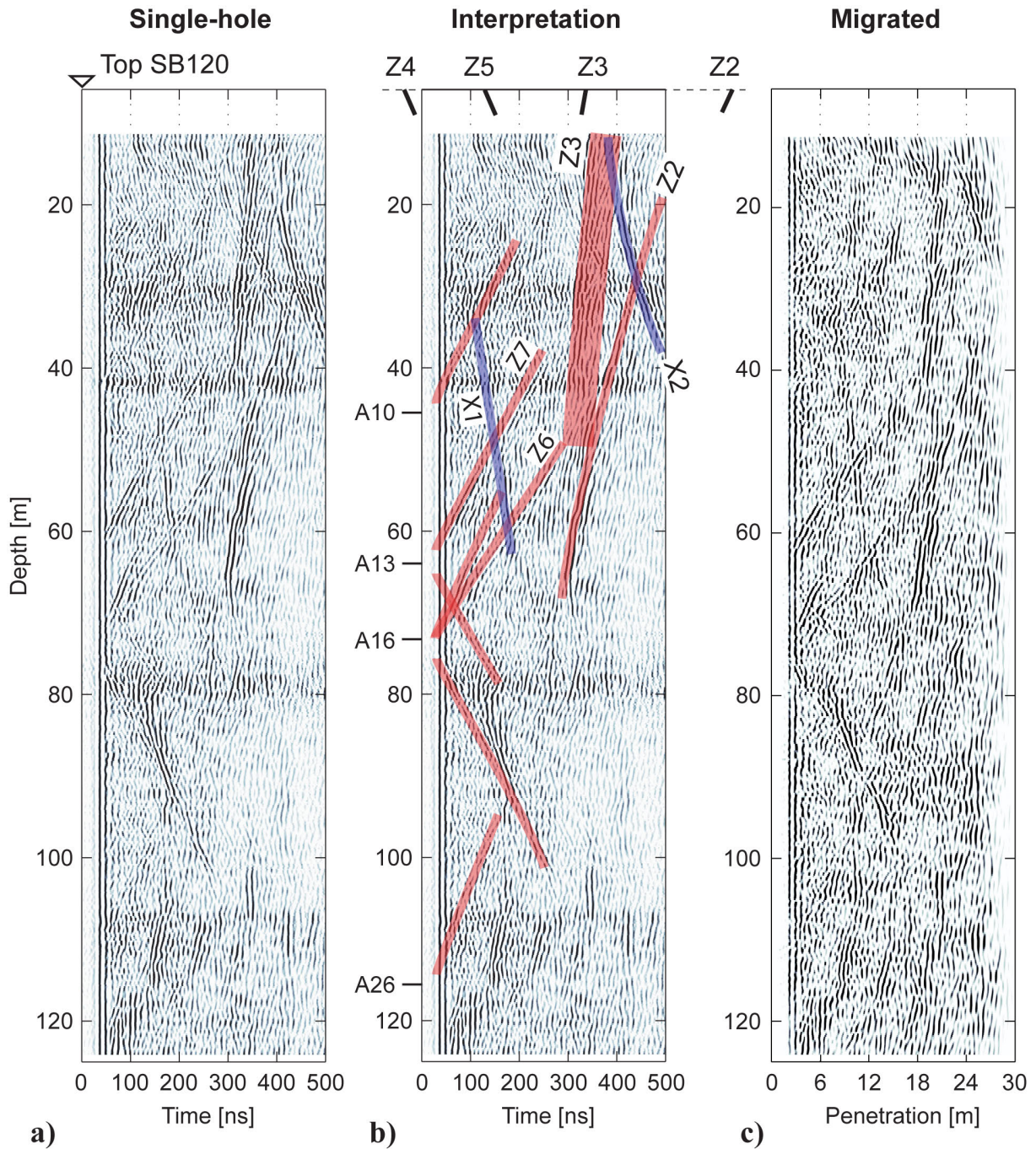


Figure E.5: (a) Processed (non-migrated) single-hole georadar section acquired in boreholes SB120. (b) As for (a), but showing our interpretation. The A's refer to fractures observed within the borehole, the X's refer to largely unexplained reflections, and the Z's refer to surface fractures. (c) Using a velocity of 0.12 m/ns (determined from crosshole observations), results of phase-shift migrating the georadar section shown in (a).

E.4 MAPPING ULTRA-LOW P-WAVE VELOCITIES USING TOMOGRAPHIC SEISMIC DATA

The goal of the 3-D tomographic seismic survey was to determine the broad-scale distribution of highly fractured rock, which we expected to be represented by low P-wave velocities. The primary layout of our survey included eight profiles, of which five were parallel (Q1-Q5) and three were perpendicular (H1-H3) to the general downslope direction (Figure E.6). Source and geophone spacings along the 126-324 m long profiles were 4 and 2 m, respectively. To avoid damaging the sensitive high alpine environment and possibly increasing mountain-slope instability, small shot charges of 5-50 g were detonated in shallow (0.5-0.7 m deep) holes. In addition to the shotholes along the profiles, we also drilled clusters of 8 shotholes (1 per profile) at 33 locations offset from the profiles. Signals generated by shots detonated at these clusters were received on geophones along all profiles, thus providing a relatively high degree of 3-D coverage. Furthermore, all inline and offset shots were recorded by the semi-permanent seismic network described in the next section (Figure E.6).

From the 99,031 registered traces, we were able to pick the traveltimes of 52,600 first arrivals with an accuracy of 1-4 ms. A 3-D tomographic inversion of these traveltimes revealed a broad zone of remarkably low seismic velocities along the edge of the mountain (Figure E.7a). Ultra-low velocities of < 1500 m/s were mapped throughout a large volume that extends over a 200 x 100 m area and a depth of ~ 25 m (Figure E.7b). Such low velocities in gneissic rock are extraordinary (intact gneissic rocks have velocities in the 3500 and 6500 m/s range). Velocities of < 1500 m/s in the Randa gneissic rock require ~ 17 % of the investigated volume to be air-filled voids. Ubiquitous dry cracks, fractures, and faults at a wide variety of scales seem to be the only plausible explanation for this observation.

Geodetic measurements have been used to determine the boundary between stable and unstable rock at Randa (Figure E.7). It is noteworthy that the zone of ultra-low P-wave velocities continues well beyond the estimated location of this boundary. Unfortunately, the geometry of our seismic survey (Figure E.6) precludes us from determining the full lateral extent of ultra-low velocity rock.

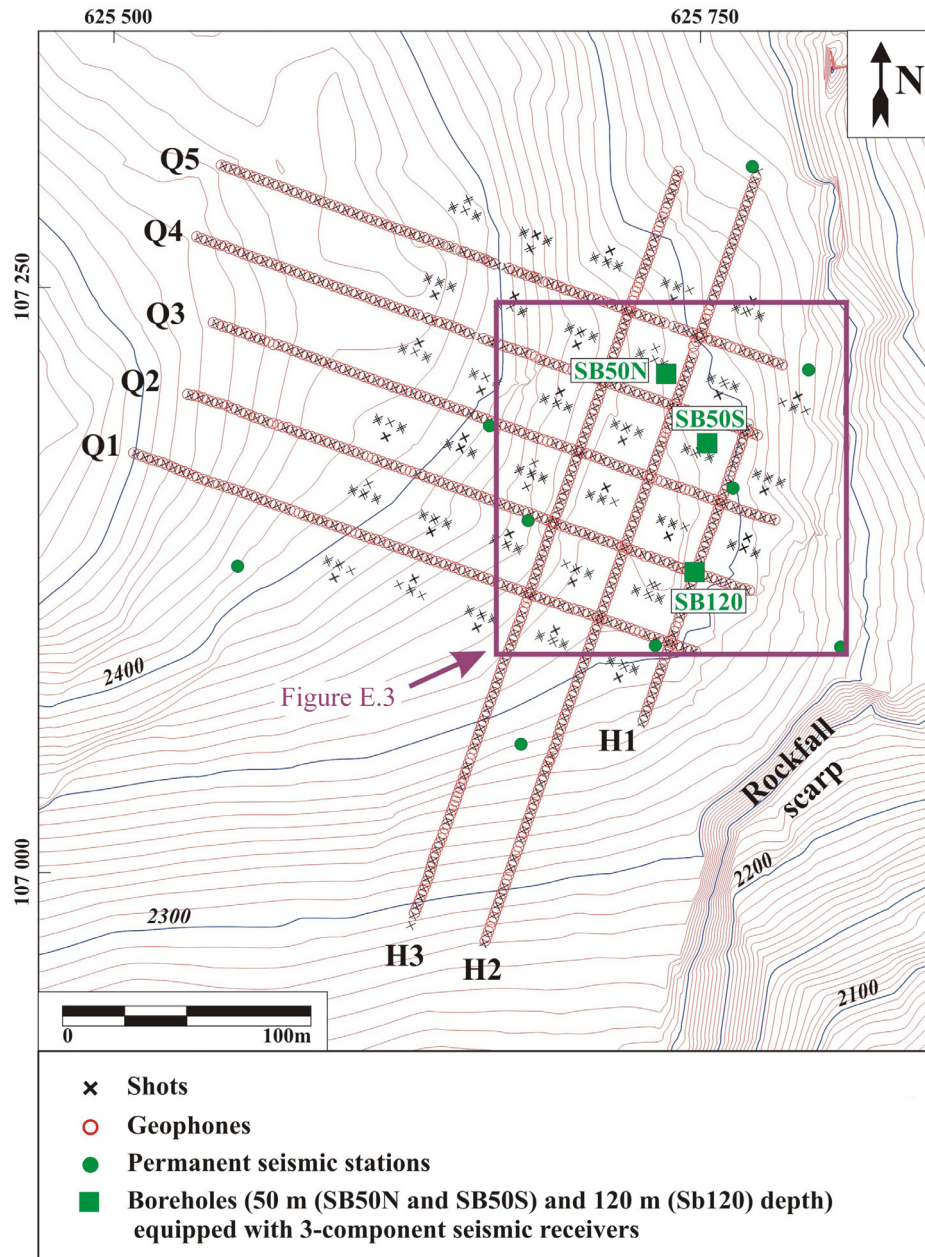


Figure E.6: Geometry of the seismic surveys. For the active and passive seismic surveys, the green dots indicate the positions of 9 semi-permanent geophones deployed in shallow holes and the green squares identify semi-permanent geophones deployed near the bottoms of boreholes SB50N, SB50S, and SB120. Black crosses and red circles show the source and additional geophone locations used for the active seismic survey. They are mostly arranged along 8 profiles approximately parallel (Q1-Q5) and perpendicular (H1-H3) to the mountain slope. Clusters of additional source locations are situated alongside the profiles; there are eight source locations per cluster (one for each profile). Contours are meters above sea-level. The site of the surface and borehole georadar surveys (Figure E.3) is shown by the purple square.

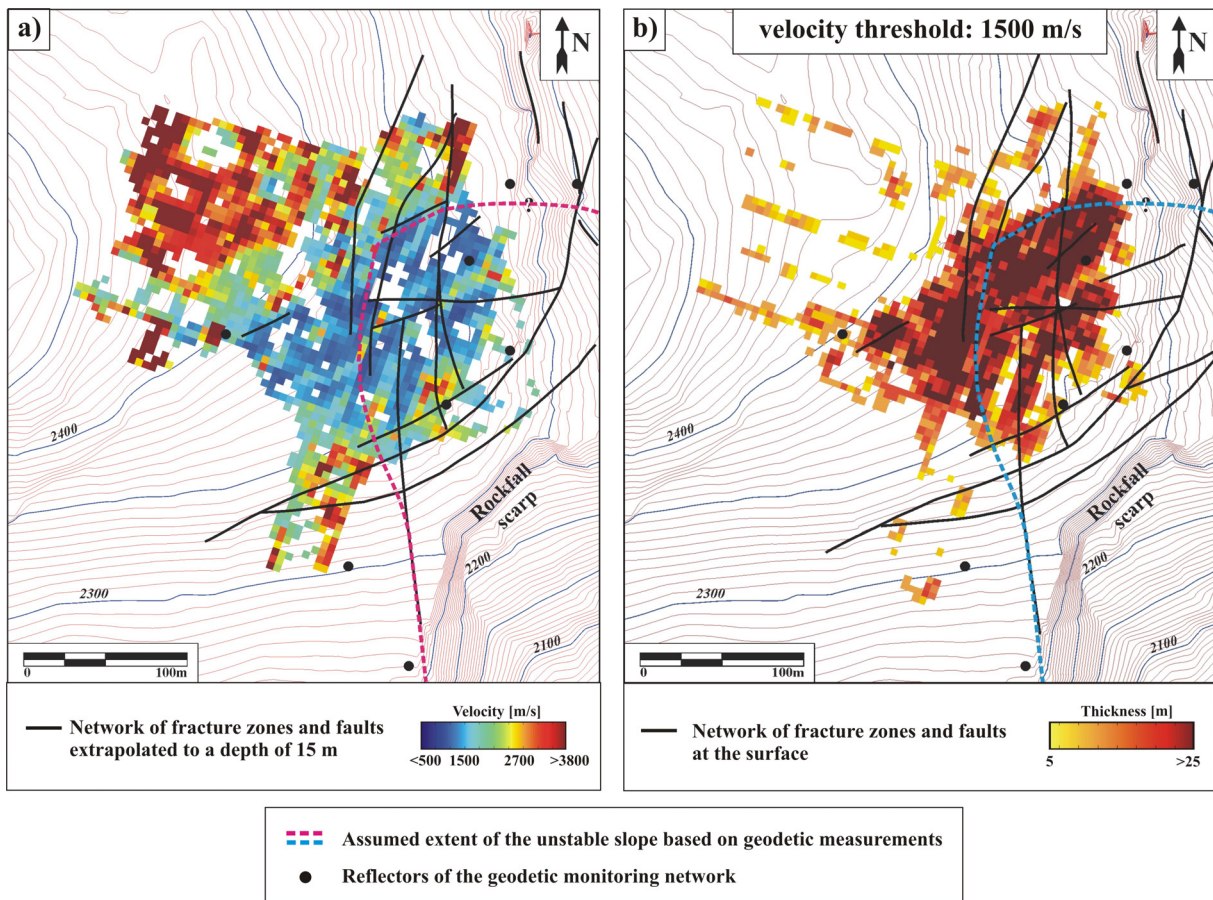


Figure E.7: (a) P-wave velocities extracted from the 3-D tomogram at 15 m depth below the surface. (b) Thicknesses of near-surface volumes with P-wave velocities <math><1500</math> m/s. In regions where the depth penetration of the seismic energy is limited, the thicknesses are minimum estimates. Fractures are marked by solid black lines and geodetic survey reflectors are marked by black dots in both figures. The unstable part of the rock mass based on geodetic measurements lies to the east of the dashed red line in (a) and the dashed blue line in (b). Contours are meters above sea-level.

E.5 MAPPING ROCK-SLOPE INSTABILITIES BASED ON MICROSEISMICITY

We have monitored the local microseismicity using a small seismic network comprising two 24-channel Geometrics Geodes operating in an event-trigger mode, nine 3-component geophones placed in shallow holes (green dots in Figure E.6) and three 3-component geophones located near the bottoms of the moderately deep boreholes (green squares in Figure E.6). Data temporarily stored on a field PC were transferred daily to a

computer located in the valley below via a 2-km-long wireless Ethernet connection. Both computers were accessible remotely from our headquarters in Zurich.

Operating a seismic network in an isolated high-mountain environment was challenging. Harsh weather conditions and difficult access imposed a variety of logistical constraints. Solar panels and a wind generator supplied the electrical power for the seismic network and other monitoring equipment. When there was neither sun nor wind, large battery packs ensured autonomous operation for approximately 10 days. The network was functional for more than three years between November 2001 and December 2004. In total, 66'440 events (1 TByte of data) were registered. To sort the events, we designed and implemented a semi-automated classification scheme. After identifying and eliminating spikes and "noise" created by human activities in the valley below, the remaining coherent signals were classified as: (i) single microearthquakes located within the mountain, (ii) multiple microearthquakes that were also caused by local disturbances of the ground, (iii) unexplained low frequency emergent events, and (iv) regional earthquakes that occurred at considerable distances from the unstable Randa mountain slope (Figure E.8).

Location errors of calibration blasts inside and outside of the seismic network using an optimum homogeneous velocity model and receiver corrections were unacceptably large (i.e., ± 50 -100m). Only after incorporating the tomographically derived 3-D velocity model in the earthquake location program were we successful in locating the vast majority of these blasts to within ± 15 -20m of their known locations. Analysis of our voluminous microseismicity data is underway. First results indicate a high concentration of microearthquakes within a small volume of rock near the edge of the mountain slope, but moderate levels of microearthquake activity occur throughout a region much larger than the geodetically defined unstable rock mass (Figure E.9). Current research activities are focused on possible correlations between the microearthquakes and fractures. In particular, we need to determine if the microseismic activity can be related to the largest fractures.

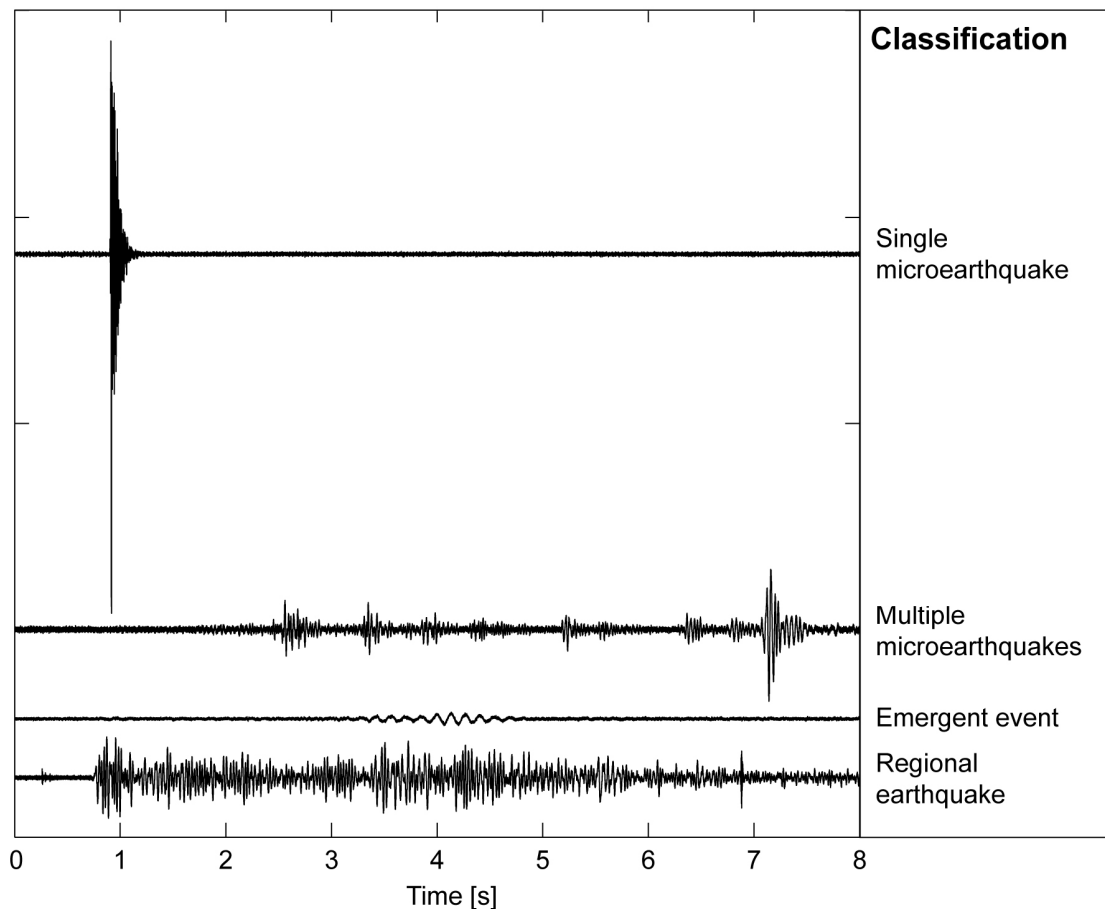


Figure E.8: Examples of earthquake seismograms recorded at the Randa study site. Most single and multiple earthquakes are likely related to rockslide activity. The origin of the emergent events is unknown. Numerous regional earthquakes also occur in the western Swiss Alps.

E.6 WHAT HAVE WE LEARNED ?

Applications of surface and borehole georadar techniques allowed us to determine the geometries and positions of significant shallow- to steep-dipping fractures within the Randa rock mass. The 3-D tomographic seismic image delineated a zone of remarkably low P-wave velocities that included the geodetically defined unstable part of the mountain slope and a large adjacent region. These low velocities were characteristic of low quality rock permeated by numerous dry cracks, fractures, and faults. Although the highest level of microseismicity occurred within a surprisingly small volume, microearthquakes were distributed over a large area of the mountain slope.

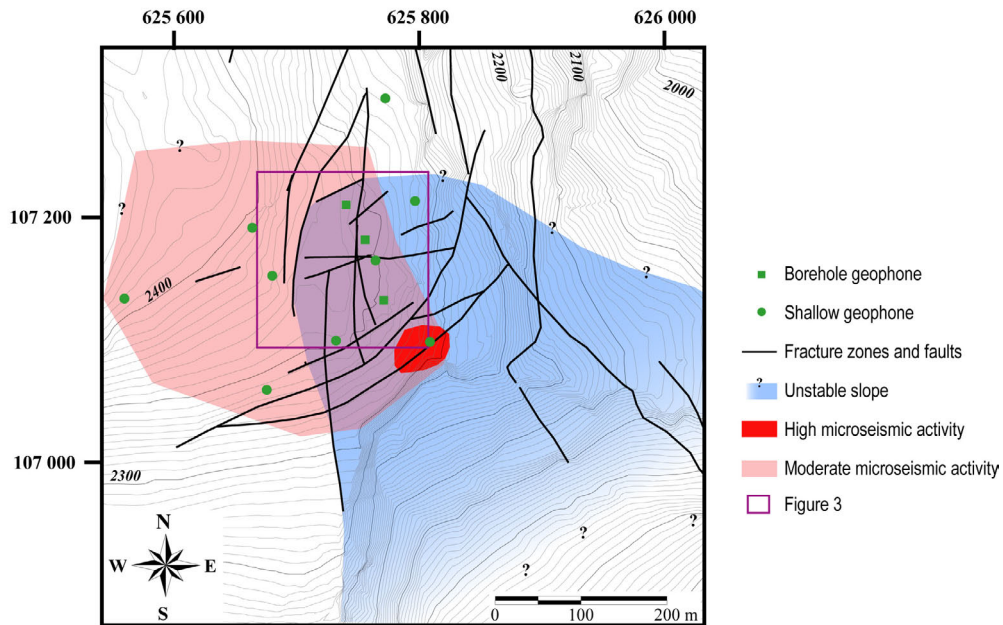


Figure E.9: Distribution of single microearthquakes (see Figure E.8). The site of the surface and borehole georadar surveys (Figure E.3) is shown by the purple square.

Surface-based geophysical techniques provided valuable knowledge on the state of the Randa rock mass. Nevertheless, we conclude that the three moderately deep boreholes were critical to the success of our investigation: the single-hole georadar data supplied important details on those fractures that strongly influence the stability of the mountain slope and the borehole seismometers yielded crucial data for constraining the 3-D P-wave velocity model and microearthquake hypocentral parameters.

We emphasize that our estimates for the down-dip lengths of the moderate- to steep-dipping fractures and the volume of ultra-low velocity rock are minimum values. The fractures likely project much deeper into the mountain and the low quality rock may continue well beyond the principal site of our investigations.

E.7 WHAT NEXT ?

We judge that the unstable mountain slope at Randa should be monitored using a seismic network that has a higher density of geophones within the area of moderate seismicity (to ensure more seismograms with a high frequency content for each event) and a greater aperture (to provide improved depth estimates). With an improved distribution of geophones, it should be possible to (i) determine reliable fault mechanism solutions, (ii)

study the kinematic and dynamic behavior of the mountain slope, and (iii) provide a predictive capability based on temporal changes in the rate of microseismic activity and/or temporal changes in the waveform characteristics.

E.8 SUGGESTED READING

Our surface georadar methods are described in "Semi-automated georadar acquisition in three dimensions" by Lehmann and Green (1999), "Topographic migration: Implications for acquisition and processing" by Lehmann and Green (2000), "3-D georadar images of an active fault: Efficient data acquisition, processing and interpretation strategies" by Gross et al. (2003). Our tomographic seismic methods are described in "Refraction tomography over a buried waste disposal site" by Lanz et al. (1998). More details on the geophysical experiments conducted at the Randa site can be found in "Acquisition and processing strategies for 3-D georadar surveying a region characterized by rugged topography" by Heincke et al. (2005), "Semblance-based topographic migration (SBTM): a method for identifying fractures in 3-D georadar data" by Heincke et al. (2006b), "Characterizing an unstable mountain slope using shallow 2- and 3-D seismic tomography" by Heincke et al. (2006a), and "Characterization of an unstable rock mass based on borehole logs and diverse borehole radar data " by Spillmann et al. (2006).

E.9 ACKNOWLEDGMENTS

The Randa rockslide project was financed by the Swiss National Science Foundation and ETH Zurich. We thank Keith Evans, Erik Eberhardt, and Simon Löw for their collaboration in this interdisciplinary project, J.D. Rouiller and colleagues at the Centre de Recherche sur l'Environnement ALPin (CREALP) for their logistical support, and Rick Miller for his constructive comments on the first draft of this manuscript.

Bibliography

- Abercrombie, R.E., 1995. Earthquake locations using single-station deep borehole recordings: Implications for microseismicity on the San Andreas fault in southern California. *Journal of Geophysical Research-Solid Earth* 100, 24003-24014.
- Aki, K. and Richards, P.G., 1980. *Quantitative seismology*. W.H. Freeman, New York, 932.
- Amitrano, D., Grasso, J.R., and Senfaute, G., 2005. Seismic precursory patterns before a cliff collapse and critical point phenomena. *Geophysical Research Letters* 32, Art. No. L08314.
- Antonello, G., Casagli, N., Farina, P., Leva, D., Nico, G., Sieber, A.J., and Tarchi, D., 2004. Ground-based SAR interferometry for monitoring mass movements. *Landslides* 1, 21-28.
- Arattano, M. and Marchi, L., 2005. Measurements of debris flow velocity through cross-correlation of instrumentation data. *Natural Hazards and Earth System Sciences* 5, 137-142.
- Bader, S. and Kunz, P., 2000. *Climate Risks - The Challenge for Alpine Regions*, Final Scientific Report NRP 31. vdf Hochschulverlag, Zurich.
- Bearth, P., 1964. *Geologischer Atlas der Schweiz - Erläuterungen zum Blatt Randa*. Kümmerly & Frey, Bern, 27.
- Benko, B. and Stead, D., 1998. The Frank slide: a reexamination of the failure mechanism. *Canadian Geotechnical Journal* 35, 299-311.
- Bichler, A., Bobrowsky, P., Best, M., Douma, M., Hunter, J., Calvert, T., and Burns, R., 2004. Three-dimensional mapping of a landslide using a multi-geophysical approach: the Quesnel Forks landslide. *Landslides* 1, 29-40.
- Bishop, A.W., 1967. Progressive failure - with special reference to the mechanisms causing it. *Proc. of the Geotechnical Conference on Shear Strength Properties of Natural Soils and Rock*. Oslo, Norway, 142-150.
- Bogoslovsky, V.A. and Ogilvy, A.A., 1977. Geophysical methods for investigation of landslides. *Geophysics* 42, 562-571.

- Bonnard, C., Noverraz, F., Lateltin, O., and Raetzo, H. 1995. Large landslides and possibilities of sudden reactivation. *Felsbau* 13: 401-407.
- Brodsky, E.E., Gordeev, E., and Kanamori, H., 2003. Landslide basal friction as measured by seismic waves. *Geophysical Research Letters* 30, Art. No. 2236.
- Brückl, E. and Brückl, J., 2006. Geophysical models of the Lesachriegel and Gradenbach deep-seated mass-movements (Schober range, Austria). *Engineering Geology* 83, 254-272.
- Brückl, E. and Parotidis, M., 2005. Prediction of slope instabilities due to deep-seated gravitational creep. *Natural Hazards and Earth System Sciences* 5, 155-172.
- Brune, J.N., 1970. Tectonic Stress and Spectra of Seismic Shear Waves from Earthquakes. *Journal of Geophysical Research* 75, 4997-&.
- Bruno, F. and Marillier, F., 2000. Test of high-resolution seismic reflection and other geophysical techniques on the Boup landslide in the Swiss Alps. *Surveys in Geophysics* 21, 335-350.
- Brunsdon, D. and Prior, D.B., 1984. *Slope Instability*. John Wiley & Sons, Chichester.
- Bulmer, M.H., Petley, D.N., Murphy, W., and Mantovani, F., 2006. Detecting slope deformation using two-pass differential interferometry: Implications for landslide studies on Earth and other planetary bodies. *Journal of Geophysical Research-Planets* 111, E06S16, doi:10.1029/2005JE002593.
- Burgmann, R., Hilley, G., Ferretti, A., and Novali, F., 2006. Resolving vertical tectonics in the San Francisco Bay Area from permanent scatterer InSAR and GPS analysis. *Geology* 34, 221-224.
- Canuti, P., Casagli, N., Ermini, L., Fanti, R., and Farina, P., 2004. Landslide activity as a geoinicator in Italy: significance and new perspectives from remote sensing. *Environmental Geology* 45, 907-919.
- Catani, F., Farina, P., Moretti, S., Nico, G., and Strozzi, T., 2005. On the application of SAR interferometry to geomorphological studies: Estimation of landform attributes and mass movements. *Geomorphology* 66, 119-131.
- Chiaraluce, L., Ellsworth, W.L., Chiarabba, C., and Cocco, M., 2003. Imaging the complexity of an active normal fault system: The 1997 Colfiorito (central Italy) case study. *Journal of Geophysical Research-Solid Earth* 108.

-
- Chichibu, A., Nakamura, K.J.M., and Kamata, M., 1989. Acoustic emission characteristics of unstable slopes. *Journal of Acoustic Emission* 8, 107-112.
- Chowdhury, R., 1992. Progressive failure considerations in slope stability analysis. 6th International Symposium on Landslides. Christchurch, 1659-1663.
- Cooke, R.U. and Doornkamp, J.C., 1990. *Geomorphology in environmental management: a new introduction*. Clarendon Press, Oxford, 410.
- Cummings, D., 2000. Transient electromagnetic survey of a landslide and fault, Santa Susanna Mountains, southern California. *Environmental & Engineering Geoscience* 6, 247-254.
- Curtis, A., Michelini, A., Leslie, D., and Lomax, A., 2004. A deterministic algorithm for experimental design applied to tomographic and microseismic monitoring surveys. *Geophysical Journal International* 157, 595-606.
- De Natale, G., Capuano, P., Troise, C., and Zollo, A., 1998. Seismicity at Somma-Vesuvius and its implications for the 3D tomography of the volcano. *Journal of Volcanology and Geothermal Research* 82, 175-197.
- Del Gaudio, V., Wasowski, J., Pierri, P., Mascia, U., and Calcagnile, G., 2000. Gravimetric study of a retrogressive landslide in southern Italy. *Surveys in Geophysics* 21, 391-406.
- Dillon, P.B. and Thomson, R.C., 1984. Offset source VSP surveys and their image reconstruction. *Geophysical Prospecting* 32, 790-811.
- Dunnicliff, J., 1988. *Geotechnical instrumentation for monitoring field performance*. Wiley & Sons Inc., New York, 577.
- Dussauge-Peisser, C., Wathelet, M., Jongmans, D., Hantz, D., Couturier, B., and Sintès, M., 2003. Investigation of a fractured limestone cliff (Chartreuse Massif, France) using seismic tomography and ground-penetrating radar. *Near Surface Geophysics* 1, 161-170.
- Eberhardt, E., Kaiser, P.K., and Stead, D. 2002. Numerical analysis of progressive failure in natural rock slopes. In C. Dinis da Gama & L. Ribeiro e Sousa (eds.), *EUROCK 2002 – Proc. of the ISRM Int. Sym. on Rock Engineering for Mountainous Regions, Madeira*. Lisboa: Sociedade Portuguesa de Geotecnia, 145-153.

- Eberhart-Phillips, D., and Michael, A.J., 1993. 3-Dimensional Velocity Structure, Seismicity, and Fault Structure in the Parkfield Region, Central California. *Journal of Geophysical Research-Solid Earth* 98, 15737-15758.
- Eberhardt, E., Spillmann, T., Maurer, H.R., Willenberg, H., Loew, S., and Stead, D., 2004b. The Randa Rockslide Laboratory: Establishing brittle and ductile instability mechanisms using numerical modelling and microseismicity. 9th International Symposium of Landslides. Rio de Janeiro, 481-487.
- Eberhardt, E., Stead, D., and Coggan, J.S., 2004a. Numerical analysis of initiation and progressive failure in natural rock slopes - the 1991 Randa rockslide. *International Journal of Rock Mechanics and Mining Sciences* 41, 69-87.
- Eberhardt, E., Willenberg, H., Loew, S., and Maurer, H.R., 2001. Active rockslides in Switzerland - understanding mechanisms and processes. *International Conference on Landslides - Causes, Impacts and Countermeasures*. Davos, 25-34.
- Einstein, H.H., Veneziano, D., Baecher, G.B., and O'Reilly, K.J., 1993. The effect of discontinuity persistence on rock slope stability. *International Journal of Rock Mechanics and Mining Sciences* 20, 227-236.
- Engheta, N., Papas, C.H., and Elachi, C., 1982. Radiation patterns of interfacial dipole antennas. *Radio Science* 17, 1557-1566.
- Erismann, T.H. and Abele, G., 2001. *Dynamics of rockslides and rockfalls*. Springer, Berlin.
- Evans, J.R., Hamstra, R.H., Kündig, C., Camina, P., and Rogers, H.A., 2005b. TREMOR: a wireless MEMS accelerograph for dense arrays. *Earthquake Spectra* 21, 91-124.
- Evans, K.F., Moriya, H., Niituma, H., Jones, R.H., Phillips, W.S., Genter, A., Sausse, J., Jung, R., and Baria, R., 2005a. Microseismicity and permeability enhancement of hydrogeologic structures during massive fluid injections into granite at 3 km depth at the Soultz HDR site. *Geophysical Journal International* 160, 388-412.
- Evans, S.G., Clague, J.J., Woodsworth, G.J., and Hungr, O., 1989. The Pandemonium Creek Rock Avalanche, British-Columbia. *Canadian Geotechnical Journal* 26, 427-446.
- Fehler, M., Jupe, A., and Asanuma, H., 2001. More than clouds: New techniques for characterizing reservoir structure using induced seismicity. *The Leading Edge* 20, 324-328.
- Fleming, R.W. and Johnson, A.M. 1989. Structures associated with strike-slip faults that bound landslide elements. *Eng. Geol.* 27, 39-114.

-
- Flinn, E.A., 1965. Signal analysis using rectilinearity and direction of particle motion. Proceedings of Institute of Electrical and Electronics Engineers (IEEE). 1874-1876.
- Geertsema, M., Clague, J.J., Schwab, J.W., and Evans, S.G., 2006. An overview of recent large catastrophic landslides in northern British Columbia, Canada. *Engineering Geology* 83, 120-143.
- Gibowicz, S.J., Young, R.P., Talebi, S., and Rawlence, D.J., 1991. Source parameters of seismic events at the Underground Research Laboratory in Manitoba, Canada - Scaling relations for events with moment magnitude smaller than -2. *Bulletin of the Seismological Society of America* 81, 1157-1182.
- Gili, J.A., Corominas, J., and Rius, J., 2000. Using Global Positioning System techniques in landslide monitoring. *Engineering Geology* 55, 167-192.
- Glade, T., Anderson, M., and Crozier, M.J., 2005a. *Landslide hazard and risk*. Wiley & Sons Ltd., Chichester.
- Glade, T., Stark, P., and Dikau, R., 2005b. Determination of potential landslide shear plane depth using seismic refraction - a case study in Rheinhessen, Germany. *Bulletin of Engineering Geology and the Environment* 64, 151-158.
- Glenn, N.F., Streutker, D.R., Chadwick, D.J., Thackray, G.D., and Dorsch, S.J., 2006. Analysis of LiDAR-derived topographic information for characterizing and differentiating landslide morphology and activity. *Geomorphology* 73, 131-148.
- Godio, A., Strobbia, C., and De Bacco, G., 2006. Geophysical characterisation of a rockslide in an alpine region. *Engineering Geology* 83, 273-286.
- Gomberg, J., Bodin, P., Savage, W., and Jackson, M.E., 1995. Landslide faults and tectonic faults, analogs? - the Slumgullion earthflow, Colorado. *Geology* 23, 41-44.
- Govi, M., Gullà, G., and Nicoletti, P.G., 2002. The Val Pola rock avalanche of July 28, 1987, in Valtellina (Central Italian Alps). In: S.G. Evans and J.V. DeGraff (Editors), *Catastrophic landslides: Effects, occurrence and mechanisms*. Geological Society of America, 71-89.
- Grasmueck, M., 1996. 3-D ground-penetrating radar applied to fracture imaging in gneiss. *Geophysics* 61, 1050-1064.

- Green, A.G., Maurer, H.R., Spillmann, T., Heincke, B., and Willenberg, H., 2006. High-resolution geophysical techniques for improving hazard assessments of unstable rock slopes. *The Leading Edge* 25, 311-316.
- Gross, R., Green, A.G., Horstmeyer, H., Holliger, K. and Baldwin, J., 2003. 3-D georadar images of an active fault: Efficient data acquisition, processing and interpretation strategies. *Subsurface Sensing Technologies and Applications*, 4, 19-40.
- Gruber, S. and Hoelzle, M., 2001. Statistical modelling of mountain permafrost distribution: Local calibration and incorporation of remotely sensed data. *Permafrost and periglacial processes* 12, 69-77.
- Hack, R., 2000. Geophysics for slope stability. *Surveys in Geophysics* 21, 423-448.
- Hanks, T.C. and Kanamori, H., 1979. Moment Magnitude Scale. *Journal of Geophysical Research* 84, 2348-2350.
- Hardage, B.A., 1983. Vertical seismic profiling, part A, principles. Geophysical Press, London.
- Hardt, M. and Scherbaum, F., 1994. The Design of Optimum Networks for Aftershock Recordings. *Geophysical Journal International* 117, 716-726.
- Hardy, H.R.J., 1989. Monitoring of rock and soil slopes and landslide areas using AE/MS techniques: A state-of-the art review. *Proceedings of the International Conference on Monitoring, Surveillance and Predictive Maintenance of Plants and Structures. Sicily*, 11-21.
- Havenith, H.-B., Jongmans, D., Abdrakhmatov, K., Trefois, P., Delvaux, D., and Torgoev, I.A., 2000. Geophysical investigations of seismically induced surface effects: case study of a landslide in the Suusamyр valley, Kyrgyzstan. *Surveys in Geophysics* 21, 351-370.
- Havenith, H.B., Jongmans, D., Faccioli, E., Abdrakhmatov, K., and Bard, P.Y., 2002. Site effect analysis around the seismically induced Ananevo, Rockslide, Kyrgyzstan. *Bulletin of the Seismological Society of America* 92, 3190-3209.
- Havenith, H.B., Vanini, M., Jongmans, D., and Faccioli, E., 2003. Initiation of earthquake-induced slope failure: influence of topographical and other site specific amplification effects. *Journal of Seismology* 7, 397-412.
- Heim, A., 1932. *Bergsturz und Menschenleben*. Translated in 1989 by N. Skemer as *Landslides and human lives*. Bitech Publishers, Vancouver, B.C.

-
- Heincke, B., Green, A.G., van der Kruk, J., and Horstmeyer, H., 2005. Acquisition and processing strategies for 3D georadar surveying a region characterized by rugged topography. *Geophysics* 70, K53-K61.
- Heincke, B., Green, A.G., van der Kruk, J., and Willenberg, H., 2006b. Semblance-based topographic migration (SBTM): a method for identifying fracture zones in 3-D georadar data. *Near Surface Geophysics* 4, 79-88.
- Heincke, B., Maurer, H.R., Green, A.G., Willenberg, H., Burlini, L., and Spillmann, T., 2006a. Characterizing an unstable mountain slope using shallow 2- and 3-D seismic tomography. *Geophysics* in press.
- Hervás, J., Barredo, J.I., Rosin, P.L., Pasuto, A., Mantovani, F., and Silvano, S., 2003. Monitoring landslides from optical remotely sensed imagery: the case history of Tessina landslide, Italy. *Geomorphology* 54, 63-75.
- Hilley, G.E., Burgmann, R., Ferretti, A., Novali, F., and Rocca, F., 2004. Dynamics of slow-moving landslides from permanent scatterer analysis. *Science* 304, 1952-1955.
- Holliger, K., Musil, M., and Maurer, H.R., 2001. Ray-based amplitude tomography for crosshole georadar data: a numerical assessment. *Journal of Applied Geophysics* 47, 285-298.
- Hufschmidt, G., Crozier, M., and Glade, T., 2005. Evolution of natural risk: research framework and perspectives. *Natural Hazards and Earth System Sciences* 5, 375-387.
- Husen, S. and Kissling, E., 2001. Local earthquake tomography between rays and waves: fat ray tomography. *Physics of The Earth and Planetary Interiors* 123, 127-147.
- Husen, S., Kissling, E., Deichmann, N., Wiemer, S., Giardini, D., and Baer, M., 2003. Probabilistic earthquake location in complex three-dimensional velocity models: Application to Switzerland. *Journal of Geophysical Research* 108, 2077, doi:10.1029/2002JB001778.
- Husen, S. and Smith, R.B., 2004. Probabilistic earthquake relocation in three-dimensional velocity models for the Yellowstone National Park Region, Wyoming. *Bulletin of the Seismological Society of America* 94, 880-896.
- Iannacchione, A.T., Esterhuizen, G.S., Bajpayee, T.S., Swanson, P.L., and Chapman, M.C., 2005. Characteristics of mining-induced seismicity associated with roof falls and roof

- caving events. In: G. Chen, S. Huang, W. Zhou and J. Tinucci (Editors), Proceedings of the 40th U.S. Rock Mechanics Symposium. Anchorage, AK, 1-10.
- Ischi, H., Keusen, H.R., and Scheller, E., 1991. Randa, Kt. Wallis, Bergsturz Grossgufer vom April/Mai 1991 - Zusammenfassender Bericht über die Aktivitäten der Geotest AG, Geotest AG, Martigny.
- Ito, A., Ucer, B., Baris, S., Nakamura, A., Honkura, Y., Kono, T., Hori, S., Hasegawa, A., Pektas, R., and Isikara, A.M., 2002. Aftershock activity of the 1999 Izmit, Turkey, earthquake revealed from microearthquake observations. *Bulletin of the Seismological Society of America* 92, 418-427.
- Jaboyedoff, M., Ornstein, P., and Rouiller, J.-D., 2004. Design of a geodetic database and associated tools for monitoring rock-slope movements: the example of the top of Randa rockfall scarp. *Natural Hazards and Earth System Sciences* 204, 187-196.
- Jeannin, M., Garambois, S., Grégoire, C. and Jongmans, D., 2006. Multiconfiguration GPR measurements for geometric fracture characterization in limestone cliffs (Alps). *Geophysics* 71, B85-B92.
- Jennings, J.E. 1970. A mathematical theory for the calculation of the stability of slopes in open cast mines. In: *Planning Open Pit Mines, Proc.*, Johannesburg. Cape Town: A.A. Balkema, 87-102.
- Jones, R.H., Beauce, A., Jupe, A., Fabriol, H., and Dyer, B.C., 1995. Imaging induced seismicity during the 1993 injection test at Soultz-sous-Forêts, France. *World Geothermal Congress. Florence, Italy*, 2665-2669.
- Jongmans, D., Hemroulle, P., Demanet, F., Renardy, F., and Vanbrabant, Y., 2000. Application of 2-D electrical and seismic tomography techniques for investigating landslides. *European Journal of Environmental and Engineering Geophysics* 5, 75-89.
- Joswig, M., 1995. Automated classification of local earthquake data in the BUG small array. *Geophysical Journal International* 120, 262-286.
- Jupe, A.J., Green, A.S.P., and Wallroth, T., 1992. Induced microseismicity and reservoir growth at the Fjällbacka hot dry rocks project, Sweden. *International Journal of Rock Mechanics and Mining Science & Geomechanics Abstracts* 29, 343-354.

-
- Kawakatsu, H., 1989. Centroid Single Force Inversion of Seismic-Waves Generated by Landslides. *Journal of Geophysical Research-Solid Earth and Planets* 94, 12363-12374.
- Kawamoto, T. and Takeda, N., 1979. An analysis of progressive failure in rock slopes. 3rd International Conference on Numerical Methods in Geomechanics. Aachen, 797-808.
- Kemeny, J. 2003. The time-dependent reduction of sliding cohesion due to rock bridges along discontinuities: A fracture mechanics approach. *Rock Mech. Rock Eng.* 36, 27-38.
- Keusen, H.R., 1997. Warn- und Überwachungssysteme (Frühwarndienste). FAN-Forum: Frühwarndienste - Stand der Kenntnisse und Anwendungen. Zollikofen, Switzerland, 1-34.
- Kilburn, C.R.J. and Petley, D.N., 2003. Forecasting giant, catastrophic slope collapse: lessons from Vajont, Northern Italy. *Geomorphology* 54, 21-32.
- Klumpen, E. and Joswig, M., 1993. Automated Reevaluation of Local Earthquake Data by Application of Generic Polarization Patterns for P-Onset and S-Onset. *Computers & Geosciences* 19, 223-231.
- Kovari, K., 1990. General report: Methods of monitoring landslides. In: C. Bonnard (Editor), Proc. of the 5th International Symposium on Landslides. Lausanne, Switzerland, 1421-1433.
- Lanz, E., Maurer, H.R., and Green, A.G., 1998. Refraction tomography over a buried waste disposal site. *Geophysics*, 63, 1414-1433.
- Lapenna, V., Lorenzo, P., Perrone, A., Piscitelli, S., Rizzo, E., and Sdao, F., 2005. 2D electrical resistivity imaging of some complex landslides in the Lucanian Apennine chain, southern Italy. *Geophysics* 70, B11-B18.
- Lee, W.H.K. and Stewart, S.W., 1981. Principles and applications of microearthquake networks. Academic Press, New York, New York, 293.
- Lehmann, F. and Green, A.G., 1999. Semiautomated georadar data acquisition in three dimensions. *Geophysics*, 64, 719-731.
- Lehmann, F. and Green, A.G., 2000. Topographic migration of georadar data: Implications for acquisition and processing. *Geophysics*, 65, 836-848.

- Lippitsch, R., White, R., and Soosalu, H., 2005. Precise hypocenter relocation of microearthquakes in a high-temperature geothermal field: the Torfajökull central volcano, Iceland. *Geophysical Journal International* 160, 370-387.
- Liu, S., Zhang, S.X., and Li, J.F., 2001. Investigation of a landslide in the new site of Badong County by integrated geophysical survey. *Science in China D: Earth Sciences* 44, 426-436.
- Lomax, A., 2005. A reanalysis of the hypocentral location and related observations for the great 1906 California earthquake. *Bulletin of the Seismological Society of America* 95, 861-877.
- Lomax, A., Virieux, J., Volant, P., and Thierry-Berge, C., 2000. Probabilistic earthquake location in 3D and layered models. In: C.H. Thurber and N.R. Rabinowitz (Editors), *Advances in seismic events location*. Kluwer Acad., Norwell, MA, USA, 101-134.
- Lomax, A., Zollo, A., Capuano, P., and Virieux, J., 2001. Precise, absolute earthquake location under Somma-Vesuvius volcano using a new three-dimensional velocity model. *Geophysical Journal International* 146, 313-331.
- Madariaga, R., 1976. Dynamics of an Expanding Circular Fault. *Bulletin of the Seismological Society of America* 66, 639-666.
- Malin, P.E., Blakeslee, S.N., Alvarez, M.G., and Martin, A.J., 1989. Microearthquake imaging of the Parkfield asperity. *Science* 244, 557-559.
- Mantovani, F., Soeters, R., and Van Westen, C.J., 1996. Remote sensing techniques for landslide studies and hazard zonation in Europe. *Geomorphology* 15, 213-225.
- Marcato, G., Mantovani, M., Pasuto, A., Silvano, S., Tagliavini, R., Zabuski, L., and Zannoni, A., 2006. Site investigation and modelling at "La Maina" landslide (Carnian Alps, Italy). *Natural Hazards and Earth System Sciences* 6, 33-39.
- Martin, C.D. and Kaiser, P.K. 1984. Analysis of rock slopes with internal dilation. *Can. Geotech. J.* 21, 605-620.
- Maurer, H.R., 1996. Systematic errors in seismic crosshole data: Application of the coupled inverse technique. *Geophysical Research Letters* 23, 2681-2684.
- Maurer, H.R., Burkhard, M., Deichmann, N., and Green, A.G., 1997. Active tectonism in the Central Alps; contrasting stress regimes north and south of the Rhone Valey. *Terra Nova* 9, 91-94.

-
- Maurer, H. and Kradolfer, U., 1996. Hypocentral parameters and velocity estimation in the western Swiss Alps by simultaneous inversion of P- and S-wave data. *Bulletin of the Seismological Society of America* 86, 32-42.
- Mauritsch, H.J., Seiberl, W., Arndt, R., Romer, A., Schneiderbauer, K., and Sendlhofer, G.P., 2000. Geophysical investigations of large landslides in the Carnic Region of southern Austria. *Engineering Geology* 56, 373-388.
- McCann, D.M. and Forster, A., 1990. Reconnaissance geophysical methods in landslide investigations. *Engineering Geology* 29, 59-78.
- McCauley, M.L., 1975. Monitoring slope stability with acoustic emission. In: H.R. Hardy and F.W. Leighton (Editors), 1st conference on acoustic emission/microseismic activity in geologic structures and materials. University Park - Pa.
- Mendecki, A.J., 1997. *Seismic Monitoring in Mines*. Chapman & Hall, London, 262.
- Mencl, V. 1966. Mechanics of landslides with non-circular slip surfaces with special reference to the Vaiont slide. *Géotechnique* 16, 329-337.
- Menke, W., 1984. The resolving power of cross-borehole tomography. *Geophysical Research Letters* 11, 105-108.
- Menke, W., 1989. *Geophysical data analysis: Discrete inverse theory*. International geophysics series, 45. Academic Press, Inc., San Diego, 290.
- Meric, O., Garambois, S., Jongmans, D., Wathélet, M., Chatelain, J.L., and Vengeon, J.M., 2005. Application of geophysical methods for the investigation of the large gravitational mass movement of Sechilienne, France. *Canadian Geotechnical Journal* 42, 1105-1115.
- Merrien-Soukatchoff, V., Clément, C., Senfaute, G., and Gunzburger, Y., 2005. Monitoring of a potential rockfall zone: The case of "Rochers de Valabres" site. *International Conference on Landslide Risk Management*. Vancouver.
- Metternicht, G., Hurni, L., and Gogu, R., 2005. Remote sensing of landslides: An analysis of the potential contribution to geo-spatial systems for hazard assessment in mountainous environments. *Remote Sensing of Environment* 98, 284-303.
- Montalbetti, J.F. and Kanasewich, E.R., 1970. Enhancement of Teleseismic Body Phases with a Polarization Filter. *Geophysical Journal of the Royal Astronomical Society* 21, 119-129.

- Moriya, H., Nakazato, K., Niitsuma, H., and Baria, R., 2002. Detailed fracture system of the Soultz-sous-Fortêts HDR field evaluated using microseismic multiplet analysis. *Pure and Applied Geophysics* 159, 517-541.
- Müller, L., 1968. New considerations on the Vaiont Slide. *Felsmechanik und Ingenieurgeologie* 6, 1-91.
- Munjiza, A., Owen, D.R.J., and Bicanic, N., 1995. A combined finite-discrete element method in transient dynamics of fracturing solids. *Engineering Computations* 12, 145-174.
- Musil, M., Maurer, H., Hollinger, K., and Green, A.G., 2006. Internal structure of an alpine rock glacier based on crosshole georadar traveltimes and amplitudes. *Geophysical Prospecting* 54, 273-285.
- Nolen-Hoeksema, R.C. and Ruff, L.J., 2001. Moment tensor inversion from the B-Sand propped hydrofracture, M-site, Colorado. *Tectonophysics* 336, 163-181.
- Norris, R.D., 1994. Seismicity of rockfalls and avalanches at three Cascade Range volcanoes; implications for seismic detection of hazardous mass movements. *Bull. seism. Soc. Am.* 84, 1925-1939.
- Oh, E., 1996. Development of a computer-based calibration facility for low-frequency acoustic emission transducers. In: H.R. Hardy (Editor), *Proceedings of 6th Acoustic Emission/Microseismic Activity in Geological Structures and Materials Conference*. Pennsylvania State University.
- Olsson, O., Falk, L., Forslund, O., Lundmark, L., and Sandberg, E., 1992. Borehole radar applied to the characterization of hydraulically conductive fracture zones in crystalline rock. *Geophysical Prospecting* 40, 109-142.
- Oye, V. and Roth, M., 2003. Automated seismic event location for hydrocarbon reservoirs. *Computers & Geosciences* 29, 851-863.
- Pezzo, E.D., Bianco, F., and Saccorotti, G., 2004. Seismic source dynamics at Vesuvius volcano, Italy. *Journal of Volcanology and Geothermal Research* 133, 23-39.
- Phillips, W.S., Rutledge, J.T., and Fairbanks, T.D., 1998. Reservoir fracture mapping using microearthquakes: Two oilfield case studies. *SPE Reservoir Evaluation & Engineering*. 114-121.

-
- Podvin, P. and Lecomte, I., 1991. Finite difference computation of traveltimes in very contrasted velocity models: a massively parallel approach and its associated tools. *Geophysical Journal International* 105, 271-284.
- Pratt, W., 2001. *Digital Image Processing*. John Wiley & Sons, Inc., New York.
- Presti, D., Troise, C., and De Natale, G., 2004. Probabilistic location of seismic sequences in heterogeneous media. *Bulletin of the Seismological Society of America* 94, 2239-2253.
- Rector III, J.W. and Washbourne, J.K., 1994. Characterization of resolution and uniqueness in crosswell direct-arrival traveltome tomography using the Fourier projection slice theorem. *Geophysics* 59, 1642-1649.
- Rockfield 2001. *ELFEN 2D/3D Numerical Modelling Package, v.3.0*. Swansea: Rockfield Software Ltd.
- Roth, M., Dietrich, M., Blikra, L.H., and Lecomte, I., 2005. Seismic monitoring of the unstable rock slope site at Åknes, Norway. 19th annual Symposium on the Application of Geophysics to Engineering and Environmental Problems (SAGEEP). Seattle, Washington.
- Rott, H. and Nagler, T., 2006. The contribution of radar interferometry to the assessment of landslide hazards, Natural hazards and oceanographic processes from satellite data. *Advances in Space Research*, 710-719.
- Rouse, C., Styles, P., and Wilson, S.A., 1991. Microseismic emissions from flowslide-type movements in South Wales. *Engineering Geology* 31, 91-110.
- Rutledge, J.T., Phillips, W., and Schuessler, B.K., 1998. Reservoir characterization using oil-production-induced microseismicity, Clinton County, Kentucky. *Tectonophysics* 289, 129-152.
- Sandersen, F., Bakkehoi, S., Hestnes, E., and Lied, K., 1996. The influence of meteorological factors on the initiation of debris flows, rockfalls, rockslides and rockmass stability. In: Senneset (Editor), *Proc. of the 7th International Symposium on Landslides*. Trondheim, 97-114.
- Sartori, M., Baillifard, F., Jaboyedoff, M., and Rouiller, J.-D., 2003. Kinematics of the 1991 Randa rockslides (Valais, Switzerland). *Natural Hazards and Earth System Sciences* 3, 423-433.

- Scavia, C. 1995. A method for the study of crack propagation in rock structures. *Géotechnique* 45, 447-463.
- Schaff, D.P., Bokelmann, G.H.R., Beroza, G.C., Waldhauser, F., and Ellsworth, W.L., 2002. High-resolution image of Calaveras Fault seismicity. *Journal of Geophysical Research-Solid Earth* 107.
- Scheikl, M., Angerer, H., Dözl Müller, J., Poisel, R., and Poscher, G., 2000. Multidisciplinary monitoring demonstrated in the case study of the Eiblschrofen rockfall. *Felsbau* 18, 24-29.
- Schepers, R., Rafat, G., Gelbke, C., and Lehmann, B., 2001. Application of borehole logging, core imaging and tomography to geotechnical exploration. *International Journal of Rock Mechanics and Mining Sciences* 3, 867-876.
- Schindler, C., Cuénod, Y., Eisenlohr, T., and Joris, C.-L., 1993. Die Ereignisse vom 18. April und 9. Mai 1991 bei Randa (VS) - ein atypischer Bergsturz in Raten. *Eclogae Geologicae Helveticae* 86, 643-665.
- Schmutz, M., Albouy, Y., Guérin, R., Maquaire, O., Vassal, J., Schott, J.-J., and Descloîtres, M., 2000. Joint electrical and time domain electromagnetism (TDEM) data inversion applied to the Super Sauze earthflow (France). *Surveys in Geophysics* 21, 371-390.
- Scholz, C.H., 1990. *The mechanics of earthquakes and faulting*. Cambridge University Press, Cambridge.
- Schorlemmer, D. and Wiemer, S., 2005. Microseismicity data forecast rupture area. *Nature* 434, 1086.
- Schuster, R.L., 1996. Socioeconomic Significance of Landslides. In: A.K. Turner and R.L. Schuster (Editors), *Landslides: investigation and mitigation*. National Academy Press, Washington, D.C., 12-35.
- Seol, S.J., Kim, J.-H., Cho, S.-J., and Chung, S.-H., 2004. A radar survey at a granite quarry to delineate fractures and estimate fracture density. *Journal of Environmental & Engineering Geophysics* 9, 53-62.
- Serzu, M.H., Kozak, E.T., Lodha, G.S., Everitt, R.A., and Woodcock, D.R., 2004. Use of borehole radar techniques to characterize fractured granitic bedrock at AECL's Underground Research Laboratory. *Journal of Applied Geophysics* 55, 137-150.

-
- Shibutani, T. and Katao, H., 2005. High resolution 3-D velocity structure in the source region of the 2000 Western Tottori Earthquake in southwestern Honshu, Japan using very dense aftershock observations. *Earth Planets and Space* 57, 825-838.
- Soeters, R. and van Westen, C., J., 1996. Slope instability recognition, analysis, and zonation. In: A.K. Turner and R.L. Schuster (Editors), *Landslides: investigation and mitigation*. National Academy Press, Washington, 129-177.
- Spillmann, T., Maurer, H.R., Willenberg, H., Evans, F.E., Heincke, B., and Green, A.G., 2006. Characterization of an unstable rock mass based on borehole logs and diverse borehole radar data. *Journal of Applied Geophysics*, in press.
- Stacey, T.R., 1981. A simple extension strain criterion for fracture of brittle rock. *Int. J. Rock Mech. Min. Sci. Geomech. Abstr.* 18, 469-474.
- Stacey, T.R., Xianbin, Y., Armstrong, R., and Keyter, G.J., 2003. New slope stability considerations for deep open pit mines. *The Journal of the South African Institute of Mining and Metallurgy* 103, 373-389.
- Stead, D., Eberhardt, E., and Coggan, J.S., 2006. Developments in the characterization of complex rock slope deformation and failure using numerical modelling techniques. *Engineering Geology* 83, 217-235.
- Stead, D., Eberhardt, E., Coggan, J., and Benko, B. 2001. Advanced numerical techniques in rock slope stability analysis – Applications and limitations. In M. Kühne et al. (eds.), *UEF Int. Conf. on Landslides – Causes, Impacts and Countermeasures*, Davos. Essen: Verlag Glückauf GmbH, 615-624.
- Steinberg, D.M., Rabinowitz, N., Shimshoni, Y., and Mizrachi, D., 1995. Configuring a seismographic network for optimal monitoring of fault lines and multiple sources. *Bulletin of the Seismological Society of America* 85, 1847-1857.
- Suriñach, E., Vilajosana, I., Khazaradze, G., Biescas, B., Furdada, G., and Vilaplana, J.M., 2005. Seismic detection and characterization of landslides and other mass movements. *Natural Hazards and Earth System Sciences* 5, 791-798.
- Talebi, S., Boone, T.J., and Eastwood, J.E., 1998. Injection-induced Microseismicity in Colorado Shales. *Pure and Applied Geophysics* 153, 95-111.
- Tanaka, Y., 1998. Rock slope stability assessment incorporating fissure effects. In: t.I.I. Congress (Editor), Vancouver. 3005-3009.

- Tarantola, A. and Valette, B., 1982. Inverse problems = Quest for information. *Journal of Geophysics* 50, 159-170.
- Tarchi, D., Casagli, N., Moretti, S., Leva, D., and Sieber, A.J., 2003. Monitoring landslide displacements by using ground-based synthetic aperture radar interferometry: Application to the Ruinon landslide in the Italian Alps. *Journal of Geophysical Research-Solid Earth* 108, 2387, doi:10.1029/2002JB002204.
- Terzaghi, K., 1950. Mechanism of landslides. *Geological Society of America (Berkeley Volume)*, 83-123.
- Thurber, C.H., 1983. Earthquake Locations and 3-Dimensional Crustal Structure in the Coyote Lake Area, Central California. *Journal of Geophysical Research* 88, 8226-8236.
- Trifu, C.I. and Urbancic, T.I., 1996. Fracture coalescence as a mechanism for earthquakes: Observations based on mining induced microseismicity. *Tectonophysics* 261, 193-207.
- Troncke, J. and Knoll, M.D., 2005. Vertical radar profiling: influence of survey geometry on first-arrival traveltimes and amplitudes. *Journal of Applied Geophysics* 57, 179-191.
- Turner, A.K. and Schuster, R.L., 1996. Landslides: Investigation and Mitigation, 247. National Research Council, Transportation Research Board Special Report, Washington, D.C.
- Uhrhammer, R.A., 1980. Analysis of small seismographic station networks. *Bulletin of the Seismological Society of America* 70, 1369-1379.
- van Westen, C.J., van Asch, T.W.J., and Soeters, R., 2006. Landslide hazard and risk zonation - why is it still so difficult? *Bulletin of Engineering Geology and the Environment* 65, 167-184.
- Vécsey, G., Holliger, K., Pratt, R.G., Dyer, B.C., and Green, A.G., 1998. Anisotropic seismic tomography of a potential hot dry rock reservoir before and during induced pressurization. *Geophysical Research Letters* 25, 1991-1994.
- Vidale, J.E., 1986. Complex Polarization Analysis of Particle Motion. *Bulletin of the Seismological Society of America* 76, 1393-1405.
- Vilardo, G., DeNatale, G., Milano, G., and Coppa, U., 1996. The seismicity of Mt Vesuvius. *Tectonophysics* 261, 127-138.

-
- Wagner, A., 1991. Bergsturz Grossguger Randa - Etude structurale et géomécanique., Sion.
- Waldhauser, F. and Ellsworth, W.L., 2000. A double-difference earthquake location algorithm: Method and application to the northern Hayward fault, California. *Bulletin of the Seismological Society of America* 90, 1353-1368.
- Wänstedt, S., Carlsten, S., and Tirén, S., 2000. Borehole radar measurements aid structure geological interpretations. *Journal of Applied Geophysics* 43, 227-237.
- Washbourne, J.K., Rector, J.W., and Bube, K.P., 2002. Crosswell travelttime tomography in three dimensions. *Geophysics* 67, 853-871.
- Weichert, D., Horner, R.B., and Evans, S.G., 1994. Seismic signatures of landslides - the 1990 Brenda Mine collapse and the 1965 Hope rockslides. *Bulletin of the Seismological Society of America* 84, 1523-1532.
- Willenberg, H., 2004. Geologic and kinematic model of a landslide in crystalline rock (Randa, Switzerland), Ph.D. thesis, ETH Zurich, Zürich, <http://e-collection.ethbib.ethz.ch/show?type=diss&nr=15581>.
- Willenberg, H., Evans, K.F., Eberhardt, E., and Loew, S., 2003. Monitoring of complex rock slope instabilities - correction and analysis of inclinometer/extensometer surveys and integration with surface displacement data. In: Myrvoll (Editor), 6th International Symposium on Field Measurements in Geomechanics. Oslo, 393-400.
- Willenberg, H., Evans, K.F., Eberhardt, E., Loew, S., Spillmann, T., and Maurer, H.R., 2004. Geological, geophysical and geotechnical investigations into the internal structure and kinematics of an unstable, complex sliding mass in crystalline rock., *Proceedings of the 9th International Symposium on Landslides*. Rio de Janeiro.
- Willenberg, H., Ladner, F., Spillmann, T., Loew, S., Sambeth, U., Evans, K., and Eberhardt, E., 2002. Aufbau eines Multi-Parameter-Überwachungssystems für Felsrutschungen. *Felsbau* 20, 44-51.
- Willenberg, H., Spillmann, T., Eberhardt, E., Evans, K., Loew, S., and Maurer, H.R., 2002. Multidisciplinary monitoring of progressive failure processes in brittle rock slopes - Concepts and system design. *Proceedings of the 1st European Conference on Landslides*. Prague, 477-483.
- Zhou, H. and Sato, M., 2000. Application of vertical radar profiling technique to Sendai Castle. *Geophysics* 65, 533-539.

Acknowledgements

This thesis benefited from the support, help and thoughts of many people and it would not have been finished without them.

Foremost I would like to thank my supervisors Dr. Hansruedi Maurer and Prof. Dr. Alan Green for offering this challenging and interesting topic to me and for supporting and motivating me throughout the duration of this work. I wish to thank Dr. Hansruedi Maurer for his support during all phases of this thesis, from fieldwork to data analysis and publishing – and during bike and ski-excursions. I am in debt to Prof. Dr. Alan Green who contributed significantly to the quality of this thesis. His enthusiasm and experience in science greatly improved the quality of my publications.

I also want to acknowledge Prof. Dr. Erik Eberhardt and Prof. Dr. Simon Löw for initiating this multidisciplinary project and Dr. Keith Evans for generously providing his knowledge on borehole logging and data analysis.

My colleagues Björn Heincke and Heike Willenberg are thanked for the joint field work and the many nice evenings we spent on the Randa mountain slope. Björn Heincke is also acknowledged for contributing his 3-D velocity model. Heike Willenberg is greatly thanked for becoming my wife.

Installation of the monitoring network would not have been possible without the Institute of Geophysic's electronics lab, with a lot of extra commitment from Beat Rinderknecht and Christoph Bärlocher. Fieldwork would have been much less entertaining without them. I am grateful to all of my enthusiastic field companions: Rolf Sidler, Remco Mujs, Cedric Schmelzbach, Mohammed Metwaly, Christian Haug, Jens Tronicke, Franz Gönner. A big thank you goes as well to André Blanchard for all organisational support.

Heinrich Horstmeyer's tremendous knowledge on computer systems and data processing helped me during many critical phases. Thanks to him, Jacques Ernst, and Peter Hetely for maintaining and repairing the AUG computer facilities.

I am grateful to Stefan Husen, and Nicholas Deichmann for advice and discussion on seismology, computing magnitudes, and for providing earthquake catalogues.

I am grateful for having met so many nice colleagues in the AUG group and in the Institute of Geophysics. I will miss deep philosophical disputes and chats with Jacques Ernst, Christian Schmid, Rolf Sidler, Peter Stummer, Cedric Schmelzbach, and Bill Fry's UCAR. Gavin Winsborrow will be remembered and missed.

Baptiste Dafflon and Simon Lloyd assisted me in data analysis during their semester works. I benefited from Giovanni Piffaretti's and Felix Akeret's help.

I also want to mention those outside ETH who contributed to the Rockslide Research Project. Specifically, Arge ISR Injectobohr SA & SIF Groutbor SA, Stump Foratec AG, Terratec GmbH, and AirZermatt valuably contributed to the project. Special thanks to Ewald Gruber and Svenya Nanzer from the Randa authorities for changing data tapes.

During the ups and downs of my thesis, I was happy for constant generosity, encouragement and distraction from my family and friends.

Thanks to Heike for love and patience.

Curriculum vitae

Personal

Name	Thomas Spillmann
Date of birth	14 / 12 / 1969
Place of birth	Niederhasli, Switzerland
Nationality	Swiss

Education

2001 – 2006	Ph.D. position at the <i>Applied and Environmental Geophysics Group</i> , ETH Zurich, Switzerland
1996 – 2001	Diploma in Geophysics at ETH Zurich
1993 – 1994	Study of Mathematics and Physics, University Zurich
1990 – 1993	Kantonale Maturitätsschule für Erwachsene, Zurich

Work Experience

1994 – 1996	Trainer, MALUCO AG, Faulensee, Switzerland
1985 – 1990	Apprenticeship and employee in Geomatics, Wilhelm+Müller, Dielsdorf, Switzerland